Fermilab

FERMILAB-THESIS-1996-15

OBSERVATION OF TOP QUARK PAIR PRODUCTION IN THE DILEPTON DECAY CHANNEL FROM PROTON-ANTIPROTON COLLISIONS AT $\sqrt{s} = 1.8\,TeV$

A Thesis

Submitted to the Faculty

of

Purdue University

by

Mark Charles Kruse

In Partial Fulfillment of the

Requirements for the Degree

of

Doctor of Philosophy

May 1996

ACKNOWLEDGMENTS

It is a pleasure to thank the many people who through their knowledge, guidance, support and friendship, have contributed to the completion of this analysis. I would like to thank my major professors, Daniela Bortoletto and Arthur Garfinkel, who introduced me to this exciting topic, and always generously gave their support.

I owe a special appreciation to Jacobo Konigsberg for his guidance and friendship. We worked extremely well and productively together on many aspects of this analysis, and I learned a great deal from his knowledge and intuition through our frequent discussions.

To the people from the CDF Top Dilepton group, who worked towards the understanding of the many facets involved in this analysis, I would like to express my gratitude. In particular, to Milciades Contreras, who always had a good sense of what was important, and helped with many useful suggestions and ideas.

Finally I would like to thank my parents and my brother, who although far away, always seemed to be there.

TABLE OF CONTENTS

APPENDICES

LIST OF TABLES

Appendix
Table

LIST OF FIGURES

Figure Page

Appendix
Figure

ABSTRACT

Kruse, Mark Charles, Ph.D., Purdue University, May 1996. Observation of Top Quark Pair Production in the Dilepton Decay Channel from Proton-Antiproton Collisions at $\sqrt{s} = 1.8\,TeV$. Major Professors: Daniela Bortoletto, Arthur Garfinkel.

This thesis presents the results of a search for the top quark using data obtained at the Collider Detector at Fermilab (CDF) in $p\overline{p}$ collisions at a center-of-mass energy of $\sqrt{s} = 1.8\,TeV$. The data represents an integrated luminosity of $109\,pb^{-1}$. The search includes the Standard Model $t\overline{t}$ decays with final states in the dilepton channel; $t\overline{t} \rightarrow \ell^+\nu_\ell b\ell^-\overline{\nu}_\ell\overline{b}$, where $\ell = e$ or μ. Such events are characterized by 2 high momentum leptons, 2 b quark jets, and missing energy from the undetected neutrinos. Nine events were observed to pass the selection based on these characteristics, with an estimated background of 2.1 ± 0.4 events. The probability for an upward fluctuation of the background to produce the observed signal is 6.3×10^{-4}, which corresponds to an excess of 3.2σ. The excess is identified as $t\overline{t}$ production, and gives a measured cross-section of $\sigma_{t\overline{t}} = 8.2^{+4.3}_{-3.3}\,pb$.

In the midst of the word he was trying to say,
  In the midst of his laughter and glee,
He softly and suddenly vanished away,
  For the Snark *was* a Boojum, you see.

Lewis Carroll, *The Hunting of the Snark*

1. INTRODUCTION

1.1 Overview

One of the cornerstones of our understanding of nature has been the identification of three generations of each of two kinds of fundamental constituents of matter : the leptons,

$$\begin{bmatrix} e \\ \nu_e \end{bmatrix} \begin{bmatrix} \mu \\ \nu_\mu \end{bmatrix} \begin{bmatrix} \tau \\ \nu_\tau \end{bmatrix},$$

and the quarks,

$$\begin{bmatrix} u \\ d \end{bmatrix} \begin{bmatrix} c \\ s \end{bmatrix} \begin{bmatrix} t \\ b \end{bmatrix}.$$

A theory of the strong and electroweak forces, often referred to as *the Standard Model* [1], has been extremely successful in describing the properties and interactions of these fundamental particles. The top quark, though predicted by the Standard Model (SM), remained unobserved for a long time, and was the final parton to be seen. The following chapter discusses the importance of the top quark in the SM, and what is expected from its production and decay.

This thesis describes the observation of the top quark in the *dilepton* SM decay channel: $t\bar{t} \to W^+bW^-\bar{b} \to \ell^+\nu_\ell b\ell^-\overline{\nu}_\ell\bar{b}$, where $\ell = e$ or μ. Such events are characterized by 2 highly energetic leptons, 2 jets from the fragmentation of the b quarks, and a large missing energy from the unobserved neutrinos. Chapter 4 explains the method used in selecting such events while minimizing background contributions.

In order to measure the $t\bar{t}$ cross-section using the selection for the dilepton decay channel, 4 components are required :

(1) The dilepton channel acceptance, which is the subject of Chapter 5, gives the probability for $t\bar{t}$ Monte Carlo events to pass the dilepton selection.

(2) The expected contributions from the various background (non-$t\bar{t}$) sources of dilepton events, which is discussed and calculated in Chapter 6.

(3) The number of signal events, that is, the total number of events observed in the data to pass the dilepton selection. This is presented in Chapter 7.

(4) The total integrated luminosity from which the data was accumulated, which is given below in the following section.

Given these components, the significance of the dilepton signal, and the $t\bar{t}$ cross-section measured from the dilepton channel, are calculated in Chapter 8.

The analysis presented here contributed to the CDF discovery of the top quark in April, 1995 [2], which used a search in the *lepton + jets* and *dilepton* decay channels, from an integrated luminosity of $67\,pb^{-1}$. This thesis presents the *dilepton* analysis using the full dataset of $109\,pb^{-1}$, and concludes that $t\bar{t}$ production has been observed in the dilepton decay channel alone, giving a $t\bar{t}$ production cross-section in good agreement with measurements in the *lepton + jets* channel.

1.2 The CDF dataset

Data was collected from $p\bar{p}$ collisions at the Tevatron Collider, at a center-of-mass energy of $\sqrt{s} = 1.8\,TeV$, using the Collider Detector at Fermilab (CDF). The Tevatron and the CDF detector are discussed in Chapter 3, together with the process of data acquisition.

The 109 pb^{-1} of integrated luminosity at CDF, on which the results presented in this thesis are based, was accumulated during *Run 1*, which was broken up into 2 parts as follows :

	Run 1A	**Run 1B**
Period of operation	August 1992 - May 1993	January 1994 - July 1995
Total Integrated Luminosity	$19.3\,pb^{-1}$	$90.1\,pb$

The luminosity numbers are still not quite finalized for Run 1B, but will not differ from the above value by more than $1\,pb^{-1}$. At present the estimated error in the Run 1B luminosity is 8% [3], and for the Run 1A luminosity the error is 3.6%. Therefore, the data used in this thesis represents a total integrated luminosity at $\sqrt{s} = 1.8\,TeV$ of,

$$\mathcal{L} = 109.4 \pm 7.2\,pb^{-1} \ .$$

The main differences between Run 1B and Run 1A were the replacement of the CDF Silicon Vertex Detector (see subsection 3.2.1), and the higher instantaneous luminosities attained by the Tevatron (see section 3.1).

1.3 Conventions

The following conventions will be employed in this thesis.

Units : For convenience *Natural Units* will be used, that is, with $\hbar = c = 1$. Hence all masses, momenta, and energies will have the same units.

Coordinate system : CDF employs a right-handed coordinate system with the z axis along the beam line. It is more convenient to express particle track coordinates in the detector by $\eta = -\ln(\tan\frac{\theta}{2})$, and ϕ, where θ is the polar angle, and

ϕ the azimuthal angle. The CDF coordinate system is discussed in more detail in section 3.2.

Transverse energy and momentum : The momentum in the plane perpendicular to the beam axis (see section 3.2), is referred to as the transverse momentum, $P_t = P \sin\theta$, and is measured by the Central Tracking Chamber (see section 3.2.1). The transverse energy, $E_t = E \sin\theta$, is essentially the same except the measurement comes from the calorimeters. In this sense, although E_t is referred to as an energy, it is in this definition a vector quantity in the transverse plane. Therefore, the momenta of jets and electrons will usually be referred to with E_t, since their measurements come from the calorimeters, and the momenta of muons with P_t, since their measurements come from the tracking chambers.

2. PHENOMENOLOGY OF TOP QUARK PRODUCTION AND DECAY

Following the discovery of the b quark at Fermilab in 1977 through the production of the $\Upsilon = b\bar{b}$ states [4], searches were launched for a partner to complete the third known family of quarks in the Standard Model. The search proved unavailing until 1994, when the CDF collaboration of Fermilab announced the first evidence for $t\bar{t}$ production [5], followed soon after in 1995 by the announcement of the *top* quark discovery by both the CDF and D0 collaborations [2, 6]. The purpose of this chapter is to introduce some of the history and motivation behind the *top* discovery, in addition to explaining the phenomenology of its production in hadronic collisions and its subsequent decay.

2.1 The truth is out there

Before the direct observation of the top quark, there were many compelling experimental results that indirectly implied its existence. Some of these are discussed in the following subsections.

2.1.1 The weak isospin of the *b* quark

There is no purely theoretical reason why the top quark must exist, however if it did not, the b quark would be a weak isospin singlet with the third component of its weak isospin, T^b_{3L}, being equal to zero. The subscript L is a reminder that

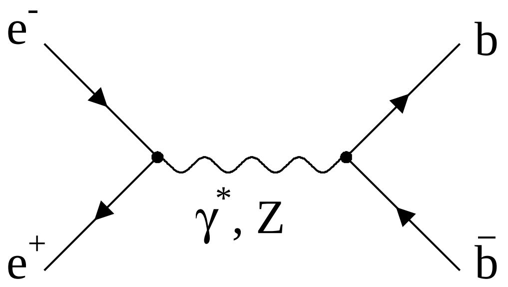

Figure 2.1

Bottom quark pair production from e^+e^- scattering.

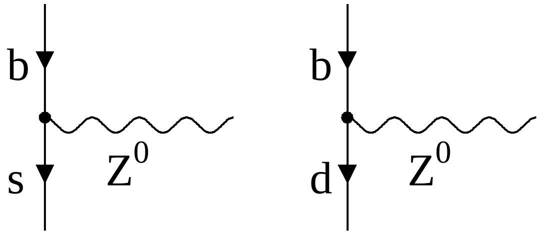

Figure 2.2

Flavor changing neutral currents (FCNC) in b decay.

the weak isospin current couples only to fermions in left-handed doublets. However, the weak isospin of the b quark, $T_L^b = \frac{1}{2}$, implies that there exists a weak isospin partner. This has been inferred from the forward-backward asymmetry, A_{FB}^b, in the scattering process $e^+e^- \to Z^0 \to b\bar{b}$ (see Figure 2.1). This asymmetry is defined by:

$$A_{FB}^b = \frac{\int_0^{+1} \frac{d\sigma}{d(\cos\theta)} d(\cos\theta) - \int_{-1}^0 \frac{d\sigma}{d(\cos\theta)} d(\cos\theta)}{\int_{-1}^{+1} \frac{d\sigma}{d(\cos\theta)} d(\cos\theta)} = \frac{\mathrm{N(forward)} - \mathrm{N(backward)}}{\mathrm{N(forward)} + \mathrm{N(backward)}},$$

where, θ is the b quark angle relative to the e^- direction in the center-of-mass frame, and σ is the $e^+e^- \to b\bar{b}$ cross-section. Within the Standard Model, the asymmetry can be written in terms of the vector and axial couplings of the fermions to the Z^0 boson, v_f and a_f respectively. At the Z^0 resonance ($\sqrt{s} = M_Z$), it has the approximate form * :

$$A_{FB}^b \approx \frac{3}{4} \frac{2v_e a_e}{v_e^2 + a_e^2} \frac{2v_b a_b}{v_b^2 + a_b^2} \equiv \frac{3}{4} A_e A_b \ .$$

The couplings are functions of the weak isospin, T_{3L}^f, the fermion charge, Q_f,

---

*See, for example, Barger and Phillips, *Collider Physics*, page 118.

and the weak mixing angle, θ_W. Their values are:

$$v_f = T^f_{3L} - 2Q_f \sin^2\theta_W \ , \quad \text{and,} \quad a_f = T^f_{3L} \ .$$

Therefore, if the b quark is a weak isospin singlet the forward-backward asymmetry, $A^b_{FB} = 0$. If indeed it is a member of a weak isospin doublet, with its partner by definition being the top quark, then a Standard Model asymmetry of 0.0997 is expected. This expected value assumes $\sin^2\theta_W = 0.2321$ [7]. The asymmetry was first measured by the JADE collaboration at PETRA [8] (at $\sqrt{s} = 35\,GeV$) with a result consistent with the b quark being a member of an isospin doublet. Recent measurements at LEP (at the Z^0 resonance) find $A^b_{FB} = 0.107 \pm 0.011$ from the DELPHI collaboration [9], and $A^b_{FB} = 0.0963 \pm 0.0077$ from the OPAL collaboration [10], implying the existence of top in the Standard Model.

2.1.2 The absence of Flavor Changing Neutral Currents (FCNC)

FCNC decays of the b quark via the Z^0 boson (see Figure 2.2) can be searched for by looking for lepton pairs from the Z^0 decay. It has been shown [11] that if the b quark were a left-handed singlet and decayed via the conventional gauge bosons, $W^\pm$ and Z^0, then the ratio of partial widths (or branching ratios), , $(b \to \ell^+\ell^- X)/$, $(b \to \ell\nu X)$, must exceed 0.12. This implies a branching ratio(BR) of greater than 1.3×10^{-2} for $b \to \ell^+\ell^- X$. If each family has the same singlet/doublet isospin structure (that is, left-handed doublets and right-handed singlets), then FCNC decays are suppressed by the GIM mechanism [12], giving a value for the above ratio well below the given limit. A 90% confidence limit of $BR(b \to \ell^+\ell^- X) < 1.2 \times 10^{-3}$ was obtained by the CLEO experiment [13], ruling out the possibility of a five-quark standard model.

2.1.3 The absence of anomalies

It can be shown that in order to have a renormalizable gauge theory of the weak interactions, anomalies arising from so-called *triangle* diagrams (in which three external gauge bosons are attached to a triangular fermion loop), must cancel for every fermion contribution. This requires $\sum_f a_f Q_f^2 = 0$, where the sum is over all fermions in a given generation, which implies $\sum_f Q_f = 0$. This demands the existence of the top quark to complete the cancellation of triangle anomalies in the third generation.

2.1.4 The top quark mass from electroweak precision measurements

The mass of the top quark, m_t, can be inferred from electroweak precision measurements [14, 15]. Recall that at the tree-level, any electroweak observable in the Minimal Standard Model (MSM) can be calculated in terms of three basic parameters (commonly denoted g, g', v), which are determined from three precisely measured quantities: α, G_F, and M_Z. Precise measurements of other electroweak observables (e.g. M_W, A_{LR}, etc.) constitute tests of the MSM. However, the tree-level results are modified by loop-level corrections which depend on all couplings and masses in the MSM. These corrections are incorporated into the relationship for G_F by the factor Δr:

$$\frac{G_F}{\sqrt{2}} = \frac{g^2}{8M_W^2}(1+\Delta r) \ .$$

Therefore, assuming α, G_F, and M_Z are used as inputs, one can calculate the W boson mass by:

$$M_W^2 = \frac{1}{2}\left\{1+\left[1-\frac{4\pi\alpha(1+\Delta r)}{\sqrt{2}G_F M_Z^2}\right]^{\frac{1}{2}}\right\} M_Z^2 \ .$$

(Note that this can also be written in terms of the weak mixing angle through the relation $\sin^2\theta_W \equiv 1 - M_W^2/M_Z^2$.) So one needs to calculate Δr from the one-loop

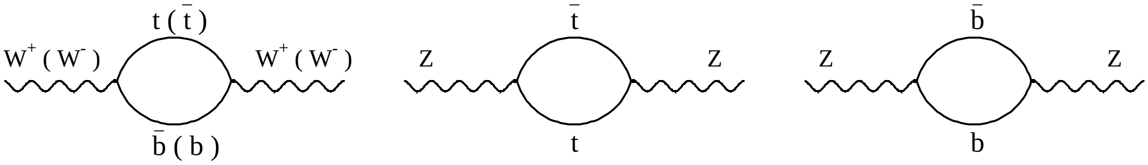

Figure 2.3

Loop diagrams leading to the different mass shifts for W and Z^0 bosons.

diagrams to predict M_W. The loop diagram corrections to M_W and M_Z which involve the top quark are shown in Figure 2.3. In evaluating the leading one-loop correction diagrams (the loop diagrams involving the lighter quarks and leptons can be ignored since they appear in Δr with an M_f^2 dependence), Δr can be expressed in terms of M_W, M_Z, M_H, and m_t, where M_H is the unknown Higgs mass (appearing from Higgs loop corrections which lead to a logarithmic M_H dependence). Therefore, a precise measurement of M_W, and some assumptions about M_H, gives a prediction of the top mass.

A fit to the electroweak measurements made at LEP from the 1989-1993 data yields [7]:

$$m_t = 177^{+11}_{-11}{}^{+18}_{-19}\,GeV \ ,$$

where, the second error reflects the uncertainty in the Higgs mass (a range from 60 to 1000 GeV was used to estimate this error). Such electroweak measurements then, not only require top, but also have some predictive power over its properties. Note also, that a precise measurement of the top mass leads to a prediction of the Higgs mass [14], but as yet the errors in the measurements of M_W and m_t are too large to give a useful mass range in which to look for the Higgs boson [16].

The above examples are only a few selected from the body of experimental results that require the existence of the top quark. Others of note include the decay rate for $Z^0 \to b\bar{b}$ which depends on the weak isospin of the b quark, and the observation of $B^0\overline{B^0}$ mixing which includes a significant contribution from the exchange of virtual top quarks. Together these build a strong case for the top quark, so its observation in 1995 was of particular importance in maintaining the foundations of the Standard Model of nature.

2.2 A recent history of top at $p\overline{p}$ colliders

A brief account will be given of some previous top quark analyses that led to the eventual discovery of the top quark. This is by no means an exhaustive list, but is intended to at least give a backdrop for the present analysis.

In 1988, the UA1 collaboration at the CERN $p\overline{p}$ collider published a lower limit on the top quark mass of, $m_t > 44\,GeV/c^2$ at the 95% confidence level [17]. This was the result from data collected during 1983 to 1985, corresponding to an integrated luminosity of $700\,nb^{-1}$. Centre of mass energies of $546\,GeV$ and $630\,GeV$ were used, with the sources of top quarks, $p\overline{p} \to W + X\,(W \to t\bar{b})$, $p\overline{p} \to Z + X\,(Z \to t\bar{t})$, and $p\overline{p} \to t\bar{t} + X$, being considered in the search.

From the 1988-1989 run at Fermilab, which accumulated $4.1\,pb^{-1}$ of integrated luminosity, the top mass limit was increased by the CDF collaboration, first to $m_t > 77\,GeV/c^2\,(95\%\,c.l.)$ in early 1991 using a search in the *electron + jets* channel [18], and later in early 1992, to $m_t > 91\,GeV/c^2\,(95\%\,c.l.)$ using the *dilepton* channel ($t\bar{t} \to \ell\nu b\ell\nu\bar{b}$, where $\ell = e$ or μ) [19]. In 1994 the D0 collaboration at Fermilab, using $15\,pb^{-1}$ of Run 1A data, searched for the top quark in both the *dilepton* and *lepton + jets* channels to set a lower limit of $m_t > 131\,GeV/c^2$ at the 95% confidence level [20]. Later that year the CDF collaboration published the first evidence for top quark production [5], using $19.3\,pb^{-1}$ of data collected during Run 1A. The search was carried out in the *dilepton* and *lepton + jets* channels, and, assuming the excess yield over background was due to $t\bar{t}$ production, a top mass of $174 \pm 10(\mathrm{stat})^{+13}_{-12}(\mathrm{syst})\,GeV/c^2$, and $t\bar{t}$ cross-section of $13.9^{+6.1}_{-4.8}\,pb$, were measured. After about half of the Run 1B data had been collected, the statistics from Run 1A alone were tripled, and the evidence for top quark production was now incontrovertible. In April of 1995 both the CDF and D0 collaborations published the top quark discovery [2, 6]. CDF, using $67\,pb^{-1}$ of integrated luminosity, measured the top quark mass to be $176 \pm 8(\mathrm{stat}) \pm 10(\mathrm{syst})\,GeV/c^2$, and the $t\bar{t}$ production cross-section to be $6.8^{+3.6}_{-2.4}\,pb$, with the signal being inconsistent with the background prediction by 4.8σ. D0, using $\sim 50\,pb^{-1}$ of integrated luminosity, measured a top quark mass of $199^{+19}_{-21} \pm 22\,GeV/c^2$, and a $t\bar{t}$ cross-section of $6.4 \pm 2.2\,pb$, with a signal to background significance of 4.6σ.

2.3 Top quark production

In hadronic collisions which involve large momentum transfer (high Q^2 as compared to the QCD energy scale Λ^2), the processes contributing to the cross-section are short-distance interactions which can be described by the parton model. The heavy top quark mass necessarily involves a large Q^2, thereby ensuring short range interactions, and therefore a small enough α_s for perturbation theory to be valid. The total inclusive cross-section for heavy quark production in perturbative QCD can be written as:

$$\sigma(s) = \sum_{i,j} \int_0^1 dx_1 \int_0^1 dx_2 f_i(x_1,\mu) f_j(x_2,\mu) \hat{\sigma}_{ij}(\hat{s}, m_Q, \alpha_s(\mu)), \tag{2.1}$$

where, the sum is over the initial parton states, and the integrations are over the two parton momentum fractions. The terms in equation 2.1 have the following meanings.

$f_i(x_1,\mu)$ is the momentum density (or structure function) for parton i. That is, it represents the probability that parton i is carrying a fraction of the incident hadron momentum between x_1 and x_1+dx_1. Similarly for $f_j(x_2,\mu)$.

$\hat{\sigma}_{ij}$ is the total short distance cross-section for the production of a heavy quark pair from the incident partons i and j. It is calculated from the appropriate Feynman diagrams representing the production of the heavy quark pair.

μ^2 is the renormalization (or factorization) scale which necessarily results from the inclusion of Feynman diagrams higher than leading order. Essentially, μ^2 defines a reference α_s ($\alpha_s(Q^2=\mu^2)$) which avoids the infinities appearing in loop diagrams.

α_s is the strong running coupling constant. It decreases with increasing Q^2 and is therefore small in short-distance interactions.

$\hat{s}$ is the square of the center-of-mass energy in the i-j parton system, and is related to the $p\overline{p}$ center-of-mass energy, s, by $\hat{s}=x_1x_2s$.

m_Q is the heavy quark mass.

The leading order, or Born, diagrams for $t\overline{t}$ production are given in Figure 2.4. The cross-sections calculated from these diagrams can be written in terms of the top quark mass, m_t, and $\hat{s}$ as follows.

$q\overline{q}$ annihilation:

$$\hat{\sigma}_{q\overline{q}}=\frac{8\pi\alpha_s^2}{27\hat{s}}\left(1-\frac{4m_t^2}{\hat{s}}\right)^{\frac{1}{2}}\left(1+\frac{2m_t^2}{\hat{s}}\right)$$

gluon-gluon fusion:

$$\hat{\sigma}_{gg}=\frac{\pi\alpha_s^2}{12\hat{s}}\left[\left(\frac{4m_t^4}{\hat{s}^2}+\frac{16m_t^2}{\hat{s}}+4\right)\ln y-\left(7+\frac{31m_t^2}{\hat{s}}\right)\left(1-\frac{4m_t^2}{\hat{s}}\right)^{\frac{1}{2}}\right]$$

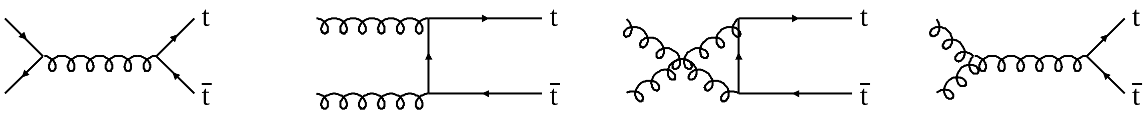

Figure 2.4

Leading order (α_s^2) diagrams for $t\bar{t}$ production in $p\bar{p}$ collisions. The first diagram represents the $q\bar{q}$ annihilation mechanism, and the remaining three, gluon-gluon fusion.

where,

$$y \equiv \frac{1 + \left(1 - \frac{4m_t^2}{\hat{s}}\right)^{\frac{1}{2}}}{1 - \left(1 - \frac{4m_t^2}{\hat{s}}\right)^{\frac{1}{2}}}$$

The relative importance of the quark and gluon diagrams depends on the top quark mass, m_t. At threshold ($\hat{s} \sim 4m_t^2$), the partonic cross-sections become;

$$\hat{\sigma}_{q\bar{q}} = \frac{4\pi\alpha_s^2}{9\hat{s}} \left(1 - \frac{4m_t^2}{\hat{s}}\right)^{\frac{1}{2}}$$

$$\hat{\sigma}_{gg} = \frac{59\pi\alpha_s^2}{48\hat{s}} \left(1 - \frac{4m_t^2}{\hat{s}}\right)^{\frac{1}{2}}$$

giving;

$$\hat{\sigma}_{q\bar{q}} : \hat{\sigma}_{gg} \approx 1 : 3.$$

However, the $t\bar{t}$ cross-section also depends on the parton luminosities* (or equivalently, the parton structure functions), which were neglected in calculating the above ratio. A high top mass requires large x_1x_2, and, since the gluon to quark ratio decreases with increasing x, the gluon-gluon luminosity decreases relative to

---

*See, for example, Barger and Phillips, *Collider Physics*, page 159, for a definition of parton luminosity. It is essentially just an integral of the structure functions over the parton momentum fractions.

the quark-quark luminosity for high top mass. This effect should be properly taken into account by the structure functions in equation 2.1 when calculating the total $t\bar{t}$ production cross-section. It turns out that after folding in the relative effects of the parton luminosities the $q\bar{q}$ annihilation mechanism dominates for $m_t >\sim 100\,GeV$ for the conditions present at the Tevatron. For $\sqrt{\hat{s}} \approx 4m_t$, the relative contribution to the total $t\bar{t}$ cross-section from $\hat{\sigma}_{q\bar{q}}$ with respect to $\hat{\sigma}_{gg}$ is about $5:1$ for a top mass in the region of $175\,GeV$.

The cross-section for heavy quark production is rather sensitive to higher order corrections to the leading order Born approximation, the $\mathcal{O}(\alpha_s^3)$ corrections to the cross-section being in the order of 25%. Some next to leading order (NLO) diagrams for the $q\bar{q}$ annihilation process are shown in Figure 2.5. Similar corrections also exist for gluon-gluon fusion. Initial state gluon bremsstrahlung dominates the NLO corrections [21]. Other corrections to the partonic cross-section at the α_s^3 level include quark-gluon fusion processes in which the final state gluon splits into a $t\bar{t}$ pair. Electroweak corrections which include loops with couplings to H, Z, γ, W are not included in standard calculations, in particular those shown in this section. Such corrections are very small for $\hat{s}$ close to threshold. Figure 2.6 shows the NLO calculation of Laenen, Smith and van Neerven, which includes *soft gluon resummation* [22]. It was shown in reference [22] that logarithmic contributions from the emission of soft initial state gluons significantly enhance the NLO cross-section result. At top masses around $175\,GeV$ the resummed NLO calculation is about 20% higher than the full NLO matrix element calculation of Ellis [23]. The dashed lines in Figure 2.6 represent the lower and upper $\sigma_{t\bar{t}}$ limits, the latter depending on the choice of scale at which to stop the resummation. A more recent calculation by Berger and Contopanagos [24], using a different resummation technique, yields results about 10% higher than the Laenen *et. al.* calculation, giving for a top mass

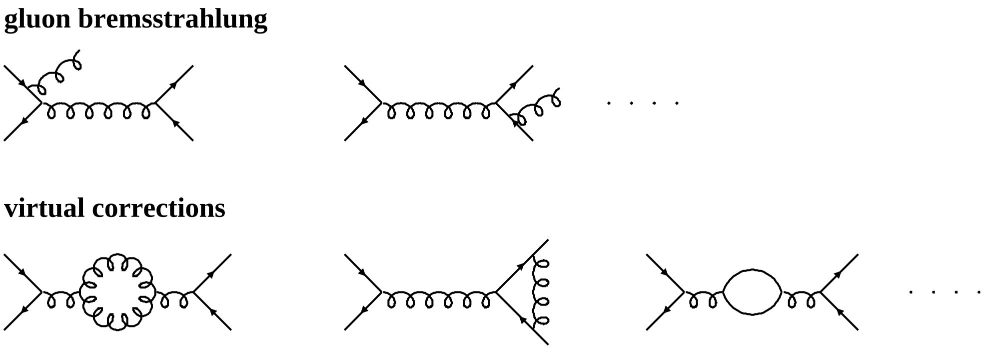

Figure 2.5

Diagrams for some next to leading order (NLO) corrections (order α_s^3) to $\hat{\sigma}_{t\bar{t}}$.

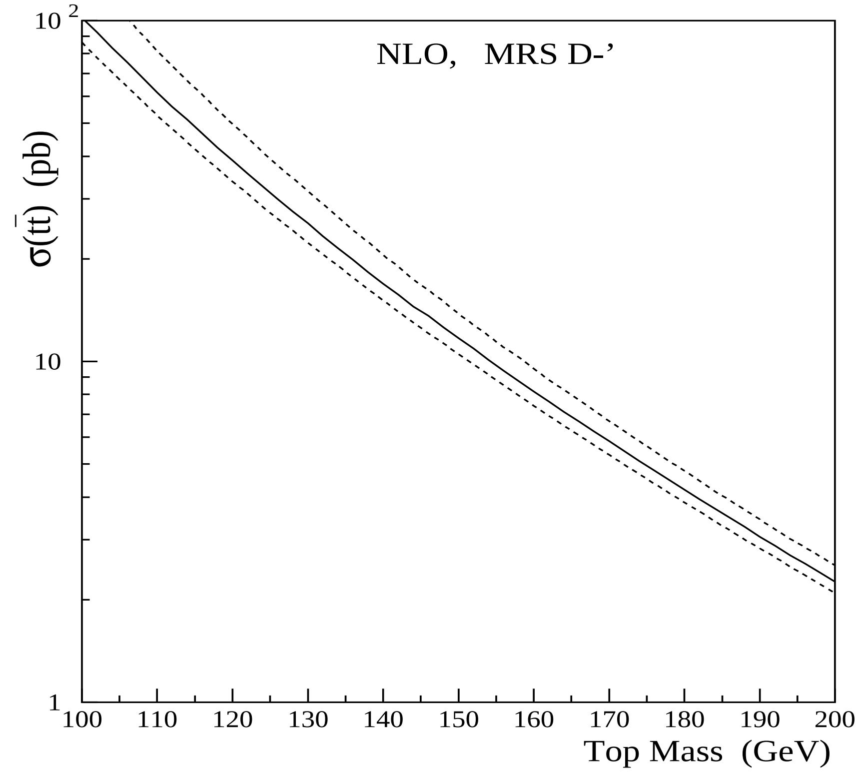

Figure 2.6

Next to leading order (NLO) calculation of the $t\bar{t}$ cross-section as a function of the top mass. The MRSD-' parton distribution functions were used.

of $175\,GeV$, $\sigma_{t\bar{t}} = 5.52^{+0.07}_{-0.45}\,pb$. It should also be noted that in a paper yet to be published [25] at the time of this writing, the effects of soft gluon resummation are found to be much smaller than previously thought, the cross-section result at a top mass of $175\,GeV$ being $\sigma_{t\bar{t}} = 4.75^{+0.63}_{-0.68}\,pb$.

2.4 Top quark decay

In the Standard Model the top quark decays by the charged weak current into a real W boson and a b quark with a branching fraction close to unity*. Assuming a $V-A$ coupling with a CKM mixing parameter V_{tb} for the $t \rightarrow bW$ decay vertex, one obtains for the partial width [26]:

$$\Gamma(t \rightarrow bW) = \frac{G_F M_W^2}{8\pi\sqrt{2}} \frac{1}{m_t^2} |V_{tb}|^2 \left[\frac{(m_t^2 - m_b^2)^2}{M_W^2} + m_t^2 + m_b^2 - 2M_W^2 \right] \times 2k \ , \qquad (2.2)$$

where,

$$k = \frac{\sqrt{(m_t^2 - (M_W + m_b)^2)\,(m_t^2 - (M_W - m_b)^2)}}{2m_t}$$

denotes the W momentum in the t rest frame. It is more instructive to see how the width scales as a function of the top mass, m_t, by assuming $|V_{tb}| = 1$, and m_t, $m_W \gg m_b$, from which one gets:

$$\Gamma(t \rightarrow bW) \approx 175\,MeV \left(\frac{m_t}{m_W} \right)^3 \ .$$

Substituting into equation 2.2 a W mass of $m_W = 80.4\,GeV$ [27], a b quark mass of $m_b = 5\,GeV$, and a top quark mass of $m_t = 175\,GeV$, one obtains for the decay rate and the top quark lifetime $(\tau_t = 1/\Gamma_t)$:

$$\Gamma(t \rightarrow bW) \approx 1.55\,GeV \quad \Rightarrow \quad \tau_t \sim 4 \times 10^{-25}\,s.$$

---

*The present 90% confidence limit on the CKM matrix element magnitude V_{tb} is 0.9988 to 0.9995, assuming 3 generation CKM unitarity.

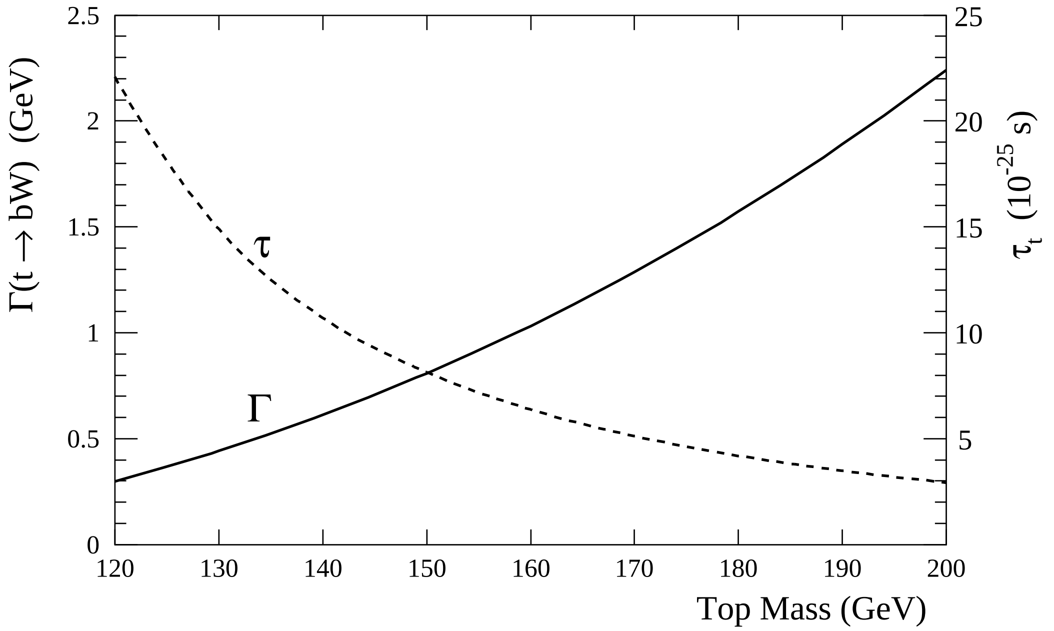

Figure 2.7

Partial width (solid curve, left scale) and lifetime (dashed curve, right scale), for the decay $t \to bW$ as a function of top mass.

If QCD radiative corrections are included, the partial width as determined by equation 2.2 is reduced by about 10% [28].

The $t \to bW$ decay rate and lifetime are shown in Figure 2.7 as a function of the top quark mass. The curves drawn correspond to the values from reference [28] in which QCD radiative corrections are accounted for, together with the finite W width and electroweak corrections (both in the order of $1-2\%$). A width of $1.55\,GeV$ means the top quark is produced and decays like a *free* quark. That is, the top quark is so transient that there is not enough time to allow it to fragment and form mesons. Hadronization is characterized by the typical hadronic time scale,

$\tau_{HAD} = (fm)/c = (200\,MeV)^{-1}$, which is about 10 times longer than the top quark lifetime. Therefore, the top decay will *remember* its original spin-$\frac{1}{2}$ state, in that its spin will be manifest in the angular distribution of its decay products [29]. This is in contrast to the expected isotropic angular distribution of the b quark decay products as a result of b quark fragmentation, typically to a spin 0 meson, before decaying. It is also worth mentioning that the Standard Model top decay is dominated by longitudinally polarized W bosons, a measurement of which could be sensitive to new physics. It is expected that for the decay $t \rightarrow bW$, longitudinal W bosons ($helicity = 0$) are favored over left-handed W bosons ($helicity = -1$) by a factor of $m_t^2/2M_W^2$ [30]. (The $helicity = +1$ amplitude for W bosons is essentially zero, as right-handed W bosons are forbidden from top decay if one assumes $m_b \approx 0$.) For a top mass of $175\,GeV$ it is expected that 70% of the W bosons emitted from top decay will be longitudinally polarized. If X_L is the fraction of longitudinally polarized W bosons, then the decay angular distribution of the leptons in the W rest frame is given by :

$$\frac{dN}{d(\cos\theta^*)} \;\propto\; (1 - X_L)(1 - \cos\theta^*) + 2X_L \sin^2\theta^* \;,$$

where, θ^* is the angle between the lepton momentum vector in the W rest frame and the W momentum vector in the top rest frame. The first term comes from the $helicity = -1$ decay amplitude for $W \rightarrow \ell\nu_\ell$, and the second term from the $helicity = 0$ amplitude.

As already mentioned the Standard Model predicts a branching fraction for the top decay $t \rightarrow bW$ to be close to unity, with all other decays strongly suppressed. Rare decays associated with the FCNC vertices $Z\bar{t}c$ and $\gamma\bar{t}c$, have estimated Standard Model branching fractions in the order of 10^{-10} [31]. Such decays would only be observable in the present CDF dataset if very strong top-quark couplings beyond

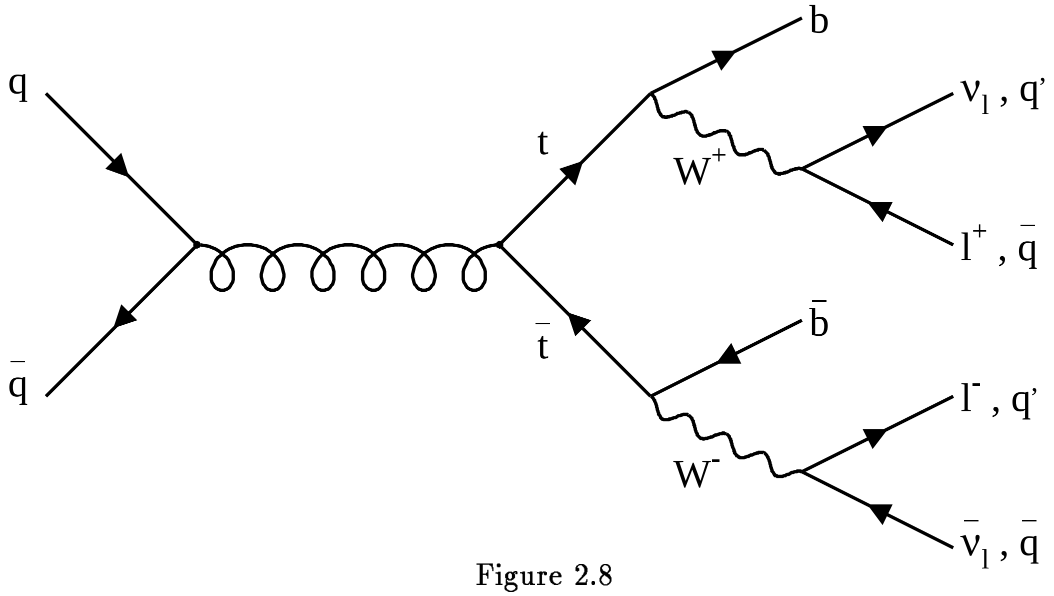

Figure 2.8

Tree level $q\overline{q} \longrightarrow t\overline{t}$ production followed by the SM $t\overline{t}$ decay.

the Standard Model were to exist [32]. Using the present CDF data ($109\,pb^{-1}$) a 95% confidence limit on the $t \longrightarrow q\gamma$ ($q = c$ or u) branching fraction of $BF(t \longrightarrow q\gamma) < 2.9\%$ has been set [33], based on one observed event.

2.5 SM $t\overline{t}$ decay channels

The $t\overline{t}$ decays can be characterized by the W^+W^- decays, as shown in Figure 2.8. Explicitly, each W boson can decay in the following ways:

$$W^+ \longrightarrow (e^+\nu_e)(\mu^+\nu_\mu)(\tau^+\nu_\tau)(u\overline{d})(c\overline{s})$$

$$W^- \longrightarrow (e^-\overline{\nu}_e)(\mu^-\overline{\nu}_\mu)(\tau^-\overline{\nu}_\tau)(\overline{u}d)(\overline{c}s).$$

The hadronic decay pairs can each appear in 3 different color combinations ($R\overline{R}, G\overline{G}, B\overline{B}$), giving 9 final state degrees of freedom for each W decay. The $t\overline{t}$ analyses naturally fall into 3 different categories depending on whether the W decay is leptonic or hadronic. These are summarized in Table 2.1. The *dilepton* category for $t\bar{t}$ decay is represented by the case in which both W bosons decay leptonically, the *lepton + jets* category by the case in which one W decays leptonically and the other hadronically, and the *all-hadronic* category by the case in which both W bosons decay hadronically. Leptonic decays to τ's are normally excluded in the standard analyses because of the added difficulty in identifying a τ decay from either its leptonic or hadronic decay products above background sources. However, analyses in CDF have been carried out, with some still in progress, that include the τ channels in the dilepton $t\bar{t}$ decay modes [34].

The *all-hadronic* decay channel, with 6 jets expected in the final state, has the highest branching ratio, however, it suffers from a large QCD background making it difficult to extract a $t\bar{t}$ signal. However recent success has been achieved in observing a $t\bar{t}$ signal by requiring tight kinematical cuts on the jets, and with at least one jet required to be tagged as originating from a b quark [35]. A separate CDF analysis requiring *double tagged* events and a large $\sum E_t(jets)$ event cut, has also had success in observing a $t\bar{t}$ signal [36].

The lepton + jets channel is characterized by a final state with a high-P_t lepton, missing transverse energy ($\not{E}_t$, see section 4.9) from the undetected neutrino, and four jets, two from the b quarks, and two from the hadronic W decay. The *lepton + jets* analysis requires events to have at least one *b-tagged* jet [5], and a total of least three jets, in association with the high-P_t lepton and $\not{E}_t$.

The cleanest channel with respect to signal over background (with an expected ratio of $\sim 2.5 : 1$) is the dilepton channel, though its branching ratio is the smallest. The $t\bar{t}$ dilepton signature is characterized in events by two high-P_t leptons, large missing transverse energy ($\not{E}_t$) from the neutrinos, and two jets from the fragmen-

Category	Decay mode	Branching ratio	
Dilepton	$t\bar{t} \rightarrow e\nu b e\nu\bar{b}$	1/81	4/81 (5%)
	$t\bar{t} \rightarrow \mu\nu b\mu\nu\bar{b}$	1/81	
	$t\bar{t} \rightarrow e\nu b\mu\nu\bar{b}$	2/81	
	$t\bar{t} \rightarrow e\nu b\tau\nu\bar{b}$	2/81	
	$t\bar{t} \rightarrow \mu\nu b\tau\nu\bar{b}$	2/81	
	$t\bar{t} \rightarrow \tau\nu b\tau\nu\bar{b}$	1/81	
Lepton + jets	$t\bar{t} \rightarrow q\bar{q}be\nu\bar{b}$	12/81	24/81 (30%)
	$t\bar{t} \rightarrow q\bar{q}b\mu\nu\bar{b}$	12/81	
	$t\bar{t} \rightarrow q\bar{q}b\tau\nu\bar{b}$	12/81	
All-Hadronic	$t\bar{t} \rightarrow q\bar{q}bq\bar{q}\bar{b}$	36/81	36/81 (44%)

Table 2.1

$t\bar{t}$ decay modes and their associated branching ratios. The τ decay modes are not considered in the standard $t\bar{t}$ analysis categories.

tation of the b quarks. The search for this signature is the topic of this thesis, and the requirements imposed for its selection are discussed in chapter 4.

3. THE TEVATRON AND COLLIDER DETECTOR

3.1 The Tevatron Collider

The Fermilab Tevatron is a $p\overline{p}$ superconducting collider which, for Runs 1A and 1B, operated with 6 proton on 6 antiproton bunches at a center-of-mass energy of $\sqrt{s} = 1.8\,TeV$. The Fermilab tunnel is $1\,km$ in radius, and is occupied by both the Tevatron and the *Main Ring*, the predecessor to the Tevatron which can accelerate protons or antiprotons to $400\,GeV$. Proton bunches begin as an H_2 gas which is ionized to make H^-. The H^- ions are then accelerated by a Cockcroft-Walton electrostatic accelerator and then a *Linac* to $200\,MeV$. Before they are injected into the circular *Booster* accelerator, the ions strike a thin carbon foil which strip the electrons off, leaving the proton nucleus. In the Booster the protons attain an energy of $8\,GeV$ and are formed into bunches before being injected into the Main Ring. There the bunches are accelerated to $150\,GeV$, then coalesced into one bunch before entering the Tevatron where the protons are accelerated to an energy of $900\,GeV$ and circulate in $5.7\,T$ superconducting dipole magnets. For 6 bunch operation this procedure is done 6 times.

The antiproton bunches are a lot more difficult and time consuming to produce. Protons of $120\,GeV$ from the Main Ring are collided with an external Tungsten target to produce secondary particles, some of which are $\overline{p}$'s which are focussed with a Lithium lens. The antiprotons are then stochastically cooled to very low momentum in the *Antiproton Debuncher*, before entering the *Accumulator* loop (which is the same size as the proton Booster) which creates $8\,GeV$ bunches of antiprotons.

Their path to maximum energy is then similar to the protons. They are injected into the Main Ring where they reach an energy of $150\,GeV$, then into the Tevatron with the protons, but in a different orbit and in the opposite direction, where they are accelerated to $900\,GeV$.

The luminosity attainable by the accelerator is determined by:

$$\mathcal{L} = \frac{N_p N_{\overline{p}} B f_0}{4\pi\sigma^2}$$

where, $N_p(N_{\overline{p}})$ is the number of protons(antiprotons) per bunch, B is the number of bunches of each type in the accelerator, f_0 is the revolution frequency of the bunches, and, σ is the transverse cross-sectional area of the bunches. The revolution frequency is about $50\,kHz$, implying the bunches are separated by $\sim 3.5\,\mu s$. The number of bunches is 6, and typically (for Run 1B) $\sigma \sim 5 \times 10^{-5}\,cm^2$, $N_p \sim 2 \times 10^{11}$, and, $N_{\overline{p}} \sim 6 \times 10^{10}$ [37]. Typical and best instantaneous luminosities for Run 1A were $0.54 \times 10^{31}\,cm^{-2}s^{-1}$ and $0.92 \times 10^{31}\,cm^{-2}s^{-1}$ respectively, while for Run 1B they were $1.6 \times 10^{31}\,cm^{-2}s^{-1}$ and $2.8 \times 10^{31}\,cm^{-2}s^{-1}$ respectively.

3.2 The Collider Detector

The Collider Detector at Fermilab (CDF) has been designed to maximally exploit the physics resulting from high energy $p\overline{p}$ collisions from the Tevatron collider. The detector, shown schematically in Figure 3.1, is cylindrically symmetric, and, forward-backward symmetric about the transverse plane passing through the interaction point. In Figure 3.1 the interaction point is along the beamline in the lower right corner. The detector can be viewed in three main functional sections, going radially outwards from the beamline, as follows.

- The tracking system, located in a $1.5\,m$ radius superconducting solenoid which produces a $1.4\,T$ axial magnetic field, is used for particle charge and momentum

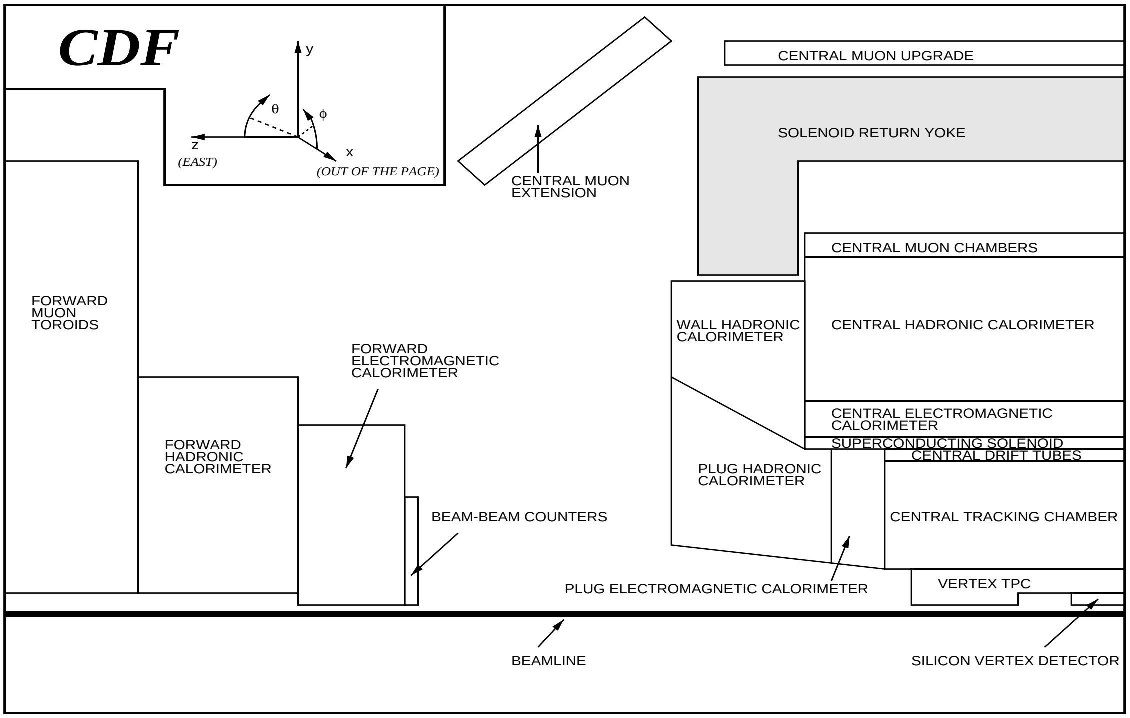

Figure 3.1

Side view cross section of quarter of the CDF detector. To get an idea of scale, the radial distance from the beamline to the inner surface of the Central Electromagnetic Calorimeter is 1.73 m.

measurements.

- The calorimetry system, which surrounds the tracking chambers, is used to measure the electromagnetic and hadronic energy of electrons, photons and jets.
- The muon drift chambers, which surround the calorimeters, serve to cleanly detect muons by using the calorimeters together with layers of steel as hadronic absorbers.

This section will overview the components of the detector important to the top analyses. A more complete description of CDF as used in the 1989 run can be found elsewhere [38]. The coordinate system used for CDF is based in $\phi-\eta$ space. ϕ is the azimuthal angle with the positive z direction being defined as the direction of the proton beam, the positive y direction pointing vertically upward, and the positive x direction pointing radially outward from the Tevatron. η is the *pseudorapidity* defined as a function of the polar angle (θ) by:

$$\eta = -\ln(\tan\frac{\theta}{2}).$$

3.2.1 The tracking system

The detector's tracking components are, going outwards from the 1.9 cm radius beampipe, the Silicon Vertex Detector (SVX), the Vertex Time Projection Chamber (VTX), and the Central Tracking Chamber (CTC), all enclosed within the solenoid.

The SVX of Run 1A [39], was replaced in Run 1B by SVX$'$ (*SVX prime*) [40], due to the radiation damage it had sustained which resulted in increased leakage currents and a significant degradation in hit efficiency by the end of Run 1A. The designs were very similar, the major differences being that the single sided DC coupled silicon microstrip detectors of SVX were replaced in SVX$'$ by AC coupled devices to reduce leakage current and coherent noise, the readout chips were upgraded to be radiation hard for the increased luminosity of Run 1B, and the inner radius was reduced from 3.00 cm to 2.86 cm to eliminate some geometrical cracks in the innermost layer. The SVX consists of two identical barrels, located either side of $z=0$, giving a total active length of 51 cm. Due to the $\sigma \sim 30\,cm$ spread of the z location of the interaction point, this active length converts into a track acceptance of about 60% for $p\overline{p}$ collisions. A schematic of one barrel is shown in Figure 3.2. Each barrel is divided azimuthally into 12 wedges (each having a ϕ range of 30°), and radially into 4 concentric layers, the inner layer being at a radius of 2.86 cm from the

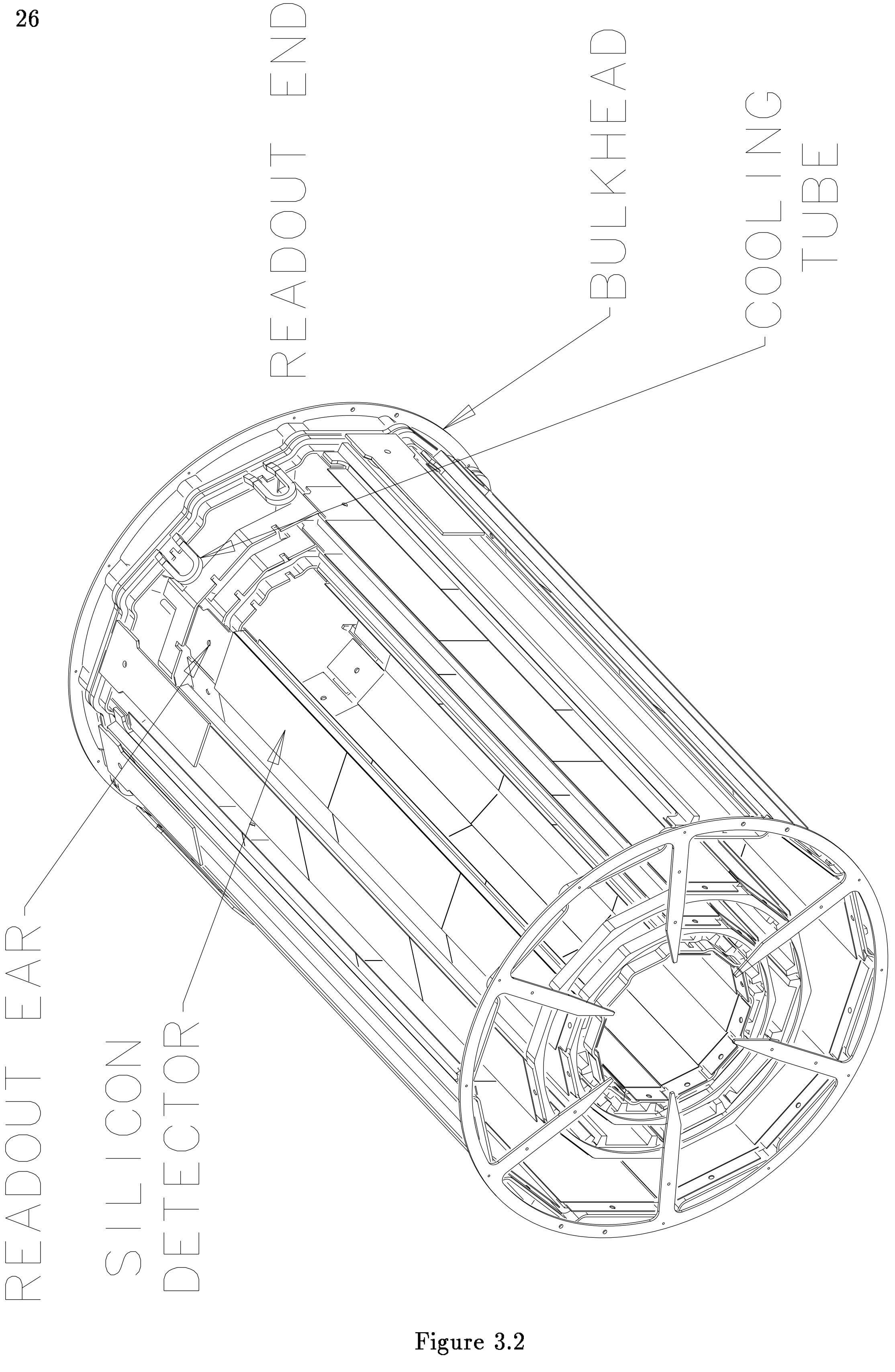

Figure 3.2

Schematic view of a single barrel of the SVX detector.

beamline, and the outer layer at a radius of $7.87\,cm$. This implies a pseudorapidity coverage of $|\eta| < 1.9$. Each layer consists of silicon microstrip detectors, bonded in groups of three (called a *ladder*) along the beam direction. Each wedge consists of four such ladders with increasing width from the innermost to outermost layer. The axial readout strips of each detector have a pitch of $60\,\mu m$, except for the outermost layer which has detectors of $55\,\mu m$ pitch. The ladders are read out by *readout chips*[*], each responsible for 128 *channels* (or readout strips). The number of readout chips per ladder depends on the layer, being 2 for the innermost layer, then 3,4 and 6 out to the outermost layer. This gives a total of 46080 channels for the whole SVX detector, each wedge of 1920 channels being read out in parallel and in *sparse mode*, meaning only those channels which register a *hit* are read out (typically about 5% of the total number of channels). Even so, the SVX has one of the longest readout times of CDF, taking about $2\,ms$ for a typical event. The SVX provides invaluable vertex information for the detection of secondary vertices from b quark decays, which have a mean decay length of, $c\tau \approx 480\,\mu m$. The individual hit resolution for the SVX depends on the layer, but is typically, $\sigma \sim 10\,\mu m$ in the transverse plane (measured from data).

The SVX is mounted inside the VTX which extends out to a radius of $22\,cm$ and has a pseudorapidity coverage of $|\eta| < 3.25$. The VTX is a gas chamber of 8 modules (each segmented azimuthally into 8 wedges), the endcaps of which consist of wires perpendicular to the beam line and the radial centerline of the wedges. The main purpose of the VTX is to provide an accurate z position of the event vertex to compliment the tracking information provided by the surrounding CTC. The axial drift in a VTX module provides information in the $r-z$ view, the wire position giving radial information on the particle track and the time of arrival to each wire position

---

[*] The so-called SVXD chips for SVX, and the rad-hard SVXH chips for SVX$'$.

yields the track position along the z direction. This enables the determination of the $p\overline{p}$ interaction vertex along the z direction with a resolution of about $1\,mm$, which supplies the seed for the 3-dimensional CTC track reconstruction.

Surrounding both the SVX and VTX is the CTC [41], a $3.2\,m$ long cylindrical drift chamber with 84 layers of sense wires, and an outer radius of $1.32\,m$ which corresponds to a pseudorapidity coverage of $|\eta| < 1.0$. The 84 layers of wires are arranged into cells of two types, axial and stereo, which in turn are arranged into 9 *superlayers*, numbered from 0 to 8 (0 being the innermost superlayer). A transverse view of this arrangement is shown in Figure 3.3. The 5 axial superlayers (0,2,4,6 and 8) are composed of cells of 12 sense wires running along the length of the CTC parallel to the beam line and give tracking information in the $r - \phi$ plane. They alternate with 4 stereo superlayers which are composed of cells of 6 sense wires offset by $\pm 3^\circ$ for tracking in the $r - z$ plane. Stereo superlayers 1 and 5 have a stereo angle of $+3^\circ$, and superlayers 3 and 7 a stereo angle of -3°. The axial and stereo cells are tilted by 45° with respect to the radial direction, in order to compensate for the Lorentz angle of the drift electrons in the crossed $1.4\,T$ magnetic field and $1350\,V/cm$ electric drift field, giving the drift electrons trajectories perpendicular to the radial direction. CTC track reconstruction comprises fitting a track's *hits* to the arc of a helix. The resulting momentum resolution in the transverse plane for the CTC alone is, $\frac{\delta P_t}{P_t^2} \approx 0.002\,GeV^{-1}c$. When information from the SVX is additionally used in the track reconstruction the transverse momentum resolution improves to, $\frac{\delta P_t}{P_t^2} \approx 0.001\,GeV^{-1}c$.

3.2.2 The CDF calorimeters

Particles with transverse momentum greater than about $350\,MeV$ will have a sufficiently stiff trajectory to escape the solenoid's magnetic field and be detected

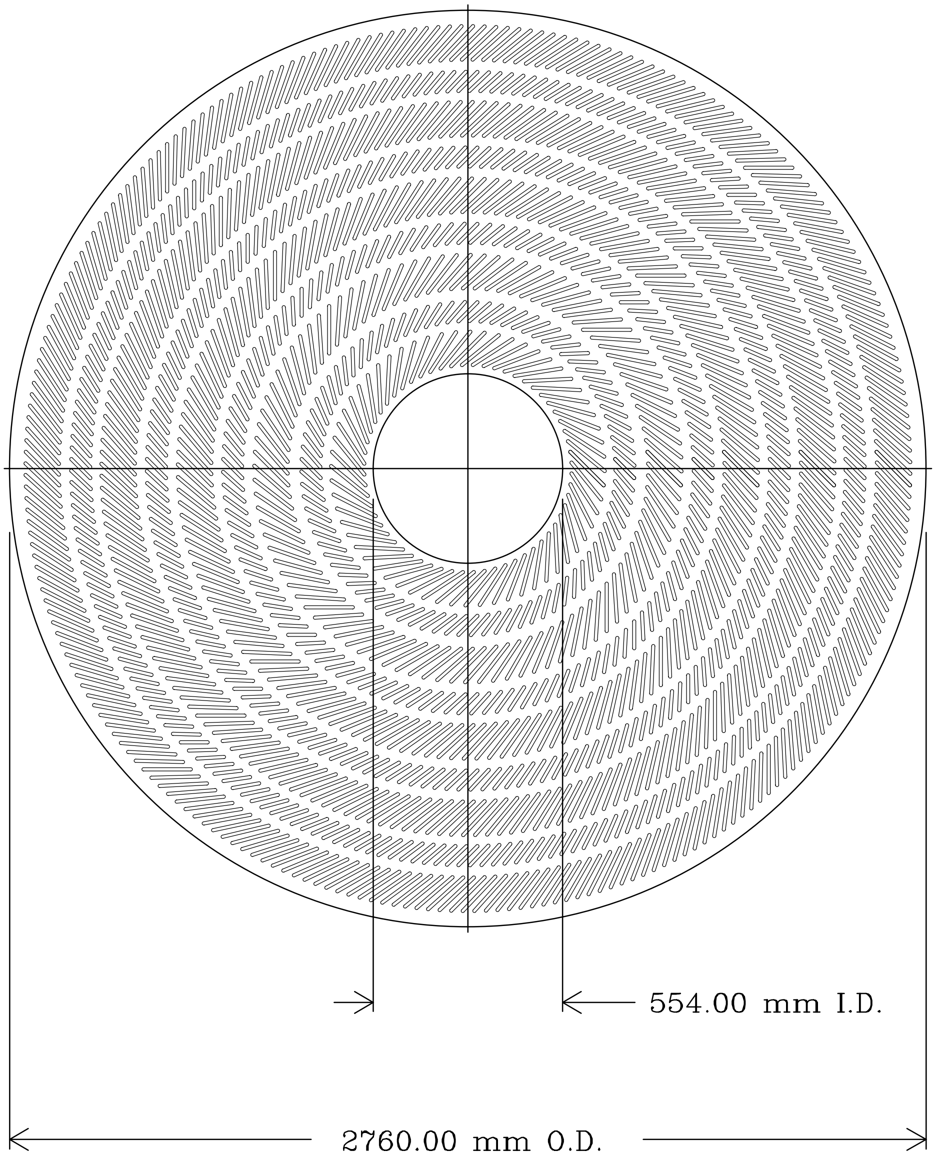

Figure 3.3

The end view of the Central Tracking Chamber showing the grouping of stereo and axial cells into 9 superlayers.

by the calorimeters surrounding the solenoid. Together the calorimeters offer a 2π azimuthal coverage and a pseudorapidity coverage of $|\eta| < 4.2$. They are separated into three regions; central, plug and forward; each region having an electromagnetic and hadronic calorimeter. Only the central region calorimeters [42, 43] are used in this analysis. They include the Central Electromagnetic Calorimeter (CEM), the Central Hadronic Calorimeter (CHA), and the Wall Hadronic Calorimeter (WHA). The pseudorapidity coverages for each of these is $|\eta| < 1.1$, $|\eta| < 0.9$, and $0.7 < |\eta| < 1.3$ respectively. The *plug* region calorimeters cover the ranges $1.1 < |\eta| < 2.4$ and $1.3 < |\eta| < 2.4$ for the electromagnetic (PEM) and hadronic (PHA) components respectively. The forward calorimeters (FEM, FHA) extend the $|\eta|$ coverage out to 4.2.

The central calorimeters are divided azimuthally into 24 wedges, each covering 15° of azimuthal angle, and extending about $250\,cm$ along the beam axis either side of $z = 0$. The CEM begins at a radius of $173\,cm$ and is $35\,cm$ thick, after which begins the CHA. The segmentation in pseudorapidity forms calorimeter *towers* which project back to the nominal interaction point. Each tower covers $\Delta\eta = 0.11$, with each tower in the CHA directly behind and matching each tower in the CEM, allowing the ratio of electromagnetic to hadronic energy to be measured for any individual tower. A schematic of a single central calorimeter wedge, showing both the CEM and the CHA, and the tower geometry, is shown in Figure 3.4. The central region is defined by towers 0 to 8, with towers 6 to 8 sharing their hadronic portion with the endwall calorimeter.

The CEM is composed of $5\,mm$ thick layers of scintillator as the sampling medium, interleaved with $3\,mm$ layers of lead absorber. The CHA is composed of 32 sampling-absorber layers. The sampling medium is scintillator and the absorber is steel, arranged in $1.0\,cm$ and $2.5\,cm$ layers respectively. The thickness

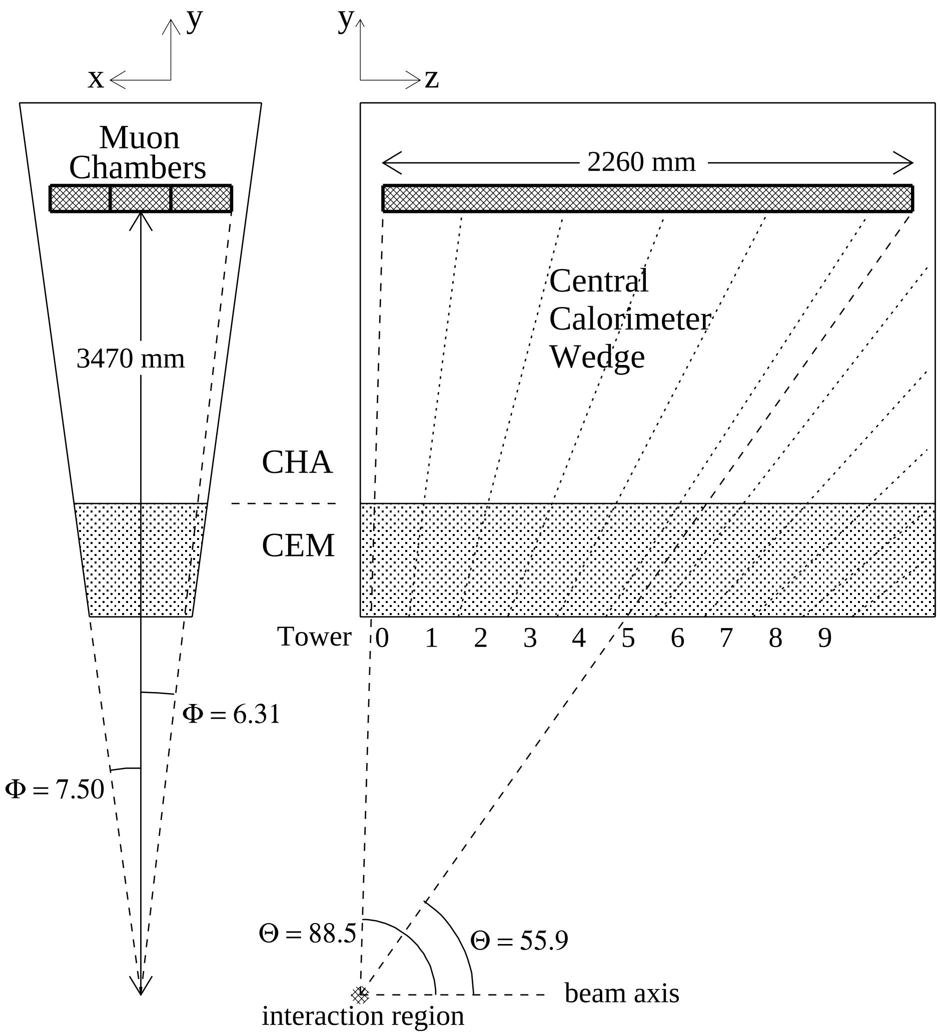

Figure 3.4

Geometry of a central calorimeter wedge and its towers, showing the location of the central muon chambers.

of the CEM is about 18 *radiation lengths*, and its energy resolution (for incident electrons and photons) is:

$$\frac{\sigma(E)}{E} = \frac{13.5\%}{\sqrt{E_t}} \oplus 2\%,$$

where $\oplus$ means that the constant term is added in quadrature. The CHA is about 4.5 *attenuation lengths* thick, with its energy resolution (for incident isolated pions) being,

$$\frac{\sigma(E)}{E} = \frac{75\%}{\sqrt{E_t}} \oplus 3\%.$$

A proportional strip chamber (CES) is inserted in each CEM wedge, at a depth corresponding to the maximum average transverse electromagnetic shower development (about 6 radiation lengths). The proportional chambers have orthogonal strip and wire readout for position measurements in the transverse and z directions. The position resolution in both the strip and wire views for high P_t electrons ($> 40\,GeV$) is typically $2\,mm$, and worsens somewhat at lower energies. The position resolution is improved by the positioning of similar chambers, the central pre-radiator (CPR), between the CEM and the solenoid to detect early shower development.

3.2.3 Muon detection

Outside the layers of steel and scintillator, each central calorimeter wedge contains 4 layers of single wire drift cells, which form the central muon detection system (CMU) [44]. The coverage of the CMU is $|\eta| < 0.6$, for muons with sufficient energy to make it to the muon chambers ($P_t >\sim 1.5\,GeV/c$). The CMU is segmented into 12.6° wedges, each comprising 3 *towers*, with a 2.4° gap between each CMU wedge. The geometrical relationship between a CMU wedge and a central calorimeter wedge is shown in Figure 3.4. Figure 3.5 shows a muon chamber tower consisting of 4 layers of 4 drift cells. Located at the center of each drift cell is a sense wire running the length of the wedge ($2260\,mm$). Pairs of sense wires are offset from each other by $2\,mm$, in order to resolve the ambiguity as to which side of the wire the muon passed, by determining which sense wire was hit first. The azimuthal angle between a muon track and the radial line passing through the sense wires, can be determined by measuring the differences in the arrival times of the drift electrons. A track can be measured in the $r - \phi$ plane with an intrinsic resolution of $250\,\mu m$. Information about the position of the track along the z direction is obtained by comparing the pulse heights at each end of the sense wires. A resolution of $1.2\,mm$ can be obtained in the z direction. Tracks which are measured in at least 3 of the 4 layers form a track segment called a *muon stub*.

Outside of the CMU are steel absorbers for further hadron absorption, and 4 additional layers of drift cells which make up the central muon upgrade (CMP). Two $60\,cm$ walls of steel running along the sides of the detector at $x = \pm \sim 540\,cm$ provide the extra hadron absorption for the CMP chambers in the 2 ϕ regions $(315°, 45°)$ and $(135°, 225°)$. The absorbers for the CMP chambers running along the top $(45° < \phi < 135°)$ and bottom $(225° < \phi < 315°)$ of the detector are provided by the steel return yoke of the solenoid at $y = \pm \sim 480\,cm$, which is roughly the same thickness as the side walls of steel. The ϕ gaps in the return yoke mean that the CMP has gaps in the regions $80° < \phi < 100°$ and $260° < \phi < 280°$. This is perhaps seen better pictorially in an event display, for example that of Figure 4.15. The CMP offers roughly the same η coverage as the CMU and provides coverage over most of the CMU ϕ gaps. The muon coverage is extended by additional muon chambers in the pseudorapidity range $0.6 < |\eta| < 1.0$, which constitute the central muon extension (CMX). Scintillators on both sides of the CMX (referred to as the CSX) are used in the CMX muon trigger (see next section).

Figure 3.5

A transverse view of a muon chamber tower showing sense wire positions along radial lines.

3.3 Event triggers

With a luminosity of $2 \times 10^{31}\, cm^{-2} s^{-1}$ (typical during run 1B), and with the total inelastic cross-section, $\sigma \sim 5 \times 10^{-26}\, cm^2$, for $p\overline{p}$ collisions at $\sqrt{s} = 1.8\, TeV$, a typical interaction rate of $1\, MHz$ is observed at the Tevatron. With a bunch crossing rate of $280\, kHz$, this translates to an average of over 3 interactions per bunch crossing. It is therefore the bunch crossing rate that defines the maximum rate at which events are produced.

The object of a trigger system is to maximize the total rate of interesting events, and minimize the dead time incurred while making a decision. Because not all the information from the detector is immediately available, in order to make a fast decision a 3 level trigger system is employed at CDF to select events with electrons, muons or jets. This system reduced the initial $280\,kHz$ rate to an output event rate to magnetic tape of $\sim 8\,Hz$ during run 1B (for run 1A the rate from level 3 was typically 3 to $5\,Hz$). The level 3 output rate is governed by the maximum rate at which events can be written to tape. Each trigger level processes fewer events than the level preceding it, but it processes them with greater sophistication and hence takes more time per event. The level 1 and 2 trigger decisions were made by hardware processors, while the level 3 decision was made with software on a farm of Silicon-Graphics computers.

The lowest level triggers are those of level 1 which are based on the energy deposition in $\Delta\eta \times \Delta\phi = 0.2 \times 15^\circ$ trigger towers for the calorimetry triggers, and on the presence of muon track segments for the muon triggers. There is no tracking information available to the level 1 decision. The level 1 triggers incur no dead time, the decisions being made in the $3.5\,\mu s$ between beam crossings. During run 1B, the level 1 calorimetry trigger for inclusive electrons and jets required single towers above a threshold of $8\,GeV$ for the CEM, $11\,GeV$ for the PEM, $12\,GeV$ for the CHA, and $51\,GeV$ for the PHA, FEM and FHA. The level 1 inclusive muon triggers require hits on two radially aligned sense wires in the CMU or CMX chambers. The P_t of the track segment is then determined from the difference in drift times caused by the track's deflection in the magnetic field. The CMU trigger requires a track segment with $P_t > 6\,GeV$ to be matched with hits in the CMP. If there are no CMP chambers corresponding to the CMU track segment, then the CMU hits are required to be in time with the hadron calorimeter TDC's. The CMX trigger requires a $P_t > 10\,GeV$ track segment in coincidence with the CSX response and the hadron TDC's.

The level 1 triggers reduce the event rate down to a few kHz, these remaining events being passed on to the level 2 triggers. The level 2 decision takes about $20\,\mu s$ and incurs a dead time in the order of a few percent due to the fact that the detector ignores subsequent beam crossings until a level 2 decision is made. Level 2 trigger decisions are based on calorimeter clusters, central stiff tracks and muon candidates. A hardware calorimeter cluster finder provides a list of clusters by searching for seed towers above a threshold, and then all the nearest neighbor towers above a lower threshold, repeating the procedure until no new seed towers are found. For each cluster the E_t is determined together with an average η and ϕ. Stiff CTC tracks are provided by the Central Fast Tracker (CFT) [45], a hardware processor that finds high P_t, $r-\phi$ tracks with high efficiency and computes the P_t with a resolution of $\delta P_t/P_t^2 = 3.5\%$. The muon track segments from the CMU, CMP and CMX which triggered level 1 are also available to the level 2 triggers. Level 2 central electron candidates are required to have energy clusters in the CEM with $E_t > 9\,GeV$ matched to CFT tracks with $P_t > 9.2\,GeV$, and a ratio of CHA/WHA to CEM cluster energies less than 0.125. The electromagnetic clusters are formed by requiring a seed trigger tower in the CEM above a threshold of $9\,GeV$ and then looking for adjoining towers above a threshold of $7\,GeV$. Likewise, level 2 muons require a CFT track match to the muon track segments that triggered level 1.

Events accepted by level 2 are passed onto the software trigger of level 3 which runs much of the same FORTRAN reconstruction algorithms as used in offline analyses. Electrons and muons from level 2 have their tracks fully reconstructed in 3 dimensions, and are required to match a reconstructed electromagnetic cluster or a muon stub. If the event is accepted by level 3, it will be written to tape to make the inclusive electron and muon samples from which the Run 1B dilepton analysis begins. The Run 1A sample used was somewhat different, requiring at least 2 leptons in an event. The level 3 trigger requirements for the samples used in the dilepton analysis are discussed in more detail in section 4.1.

4. DILEPTON EVENT SELECTION

A typical $t\bar{t}$ decay in the dilepton channel will contain 2 high-P_t leptons, 2 high-E_t jets, and 2 neutrinos which provide a large missing transverse energy ($\not{E}_t$). The dilepton event selection begins by looking for events with at least two high-P_t leptons that pass the lepton identification requirements. Missing E_t and 2-jet requirements, in combination with topological and kinematical cuts, enhance the dilepton signal from $t\bar{t}$ decay to that from background processes. The sections of this chapter are organised as follows. The lepton identification and P_t requirements are first described, followed by the discussion and motivation for each of the dilepton event selection cuts; “same-sign”, “isolation”, “invariant mass”, “missing transverse energy”, and finally “2-jet”. Jet identification is also discussed in the section describing the 2-jet cut. The impact of these cuts on the dilepton data will be shown, together with their expected effect on $t\bar{t}$ dilepton events with $m_{top} = 175\,GeV$. The latter will, however, be discussed in more detail in Chapter 5. The background processes, for which these cuts are designed to reduce, are introduced and discussed fully in Chapter 6, though reference will be made to them in this chapter as a means to motivate the dilepton selection process.

4.1 Data sample

The starting point for any analysis is a sample of events that has been selected to include all the events of relevance to the analysis, while at the same time be of manageable size. The data samples used in Runs 1A and 1B had different selection criteria and so will be discussed separately.

The Run 1A data sample was created by selecting events with at least 2 leptons with, $P_t > 15\,GeV$ for muons, and for electrons, $E_t > 15\,GeV$ and $P_t > 10\,GeV$*. In addition, one lepton was required to satisfy tighter cuts which were†; for electrons, $E_{HAD}/E_{EM} < 0.055 + 0.045 \times E_t/100$ and $\chi^2_{strip} < 15$, and, for muons; $E_{EM} < 2\,GeV$ and $E_{HAD} < 6\,GeV$. This "dilepton" data sample was selected from almost 2 million events written to tape during data collection, and consisted of about 90 000 events.

The data sample used for the dilepton analysis in Run 1B was acquired somewhat differently. The samples originated from the so-called *Stream A* inclusive high P_t central electron and muon data sets [46], which require at least one lepton passing the level 3 trigger requirements listed in Table 4.1. The level 1 and 2 trigger requirements which feed level 3 were discussed in section 3.3. These Run 1B inclusive samples contain about 750 000 electrons and 570 000 muons. From these samples tighter cuts were made on the primary lepton in the event to give the final inclusive electron and muon samples from which the top dilepton analysis begins [47]. These tighter cuts are the same as those required by the lepton selection in Tables 4.2 and 4.3, and reduced the electron sample size to 130 000 events, and the muon sample size to 90 000 events.

4.2 Electron selection

This analysis only considers electrons in the central calorimeter region ($|\eta| < 1.1$), with $E_t > 20\,GeV$. Electrons are expected to deposit most of their energy in a single electromagnetic calorimeter tower. In addition they will have a CTC

---

*Recall that P_t is measured by the Central Tracking Chamber, and E_t by the calorimeters.

†The cut variables are introduced in sections 4.2 and 4.3.

MUONS
$P_t > 18\,GeV$, $E_{HAD} < 6\,GeV$, ($\lvert\Delta x\rvert_{CMU} < 5\,cm$ OR $\lvert\Delta x\rvert_{CMP} < 10\,cm$ OR $\lvert\Delta x\rvert_{CMX} < 10\,cm$)

ELECTRONS
$E_t > 18\,GeV$, $P_t > 13\,GeV$, $L_{shr} < 0.2$, $E_{HAD}/E_{EM} < 0.125$, $\lvert\Delta x\rvert < 3\,cm$, $\lvert\Delta z\rvert < 5\,cm$, $\chi^2_{strip} < 10$
OR
$E_t > 22\,GeV$, $P_t > 13\,GeV$, $E_{HAD}/E_{EM} < 0.125$, $\not\!\!E_t > 22\,GeV$
OR
$E_t > 22\,GeV$, $L_{shr} < 0.2$, $E_{HAD}/E_{EM} < 0.05$, $E_{border} < 2.5\,GeV$, $\not\!\!E_t > 25\,GeV$, $\chi^2_{strip} < 20$
OR
First electron: $E_t > 18\,GeV$, $P_t > 13\,GeV$ Second electron: $E_t > 20\,GeV$, $P_t > 10\,GeV$
OR
$E_t > 50\,GeV$, $P_t > 25\,GeV$

Table 4.1

Level 3 trigger requirements for the Stream A high P_t inclusive muon and electron datasets. The level 3 electron trigger is broken up into triggers for; high E_t e with tight cuts, central W, tight W with no track required, $Z^0 \rightarrow ee$, and, very high E_t e with loose cuts, respectively.

track pointing to the electromagnetic cluster, with a well defined shower profile in the proportional strip chambers (CES). These characteristics are used in designing a set of cuts on variables (see below) to distinguish electrons from other tracks and calorimeter objects.

Two classes of electrons are defined :

- Tight Central Electrons (TCE)
- Loose Central Electrons (LCE)

Both TCE and LCE electrons use the same variables in their identification, with LCE electrons having somewhat looser requirements, and included to increase the dielectron acceptance. Electrons in the *plug* region of the detector are not included in this analysis. This is because dilepton events containing plug electrons do not contribute significantly to the overall $t\bar{t}$ dilepton acceptance (about 4%), in addition to the fact that the probability to fake an electron is much greater in the plug region due to limited tracking information at higher η.

4.2.1 Central electron geometrical requirements

In order for the energy of the electron to be well measured the electron shower must deposit most of its energy in the active volume of the central electromagnetic calorimeter. To ensure this, the shower position as measured by the CES is required to be away from CEM wedge boundaries and known inactive regions [*]. The following geometrical cuts are applied to central electrons (these are often referred to as the electron fiducial cuts).

- The CES shower position in the transverse plane must be at least $3.2\,cm$ from a CEM wedge boundary in ϕ. The width of a CEM wedge at the CES radius is

---

[*] The electron fiducial requirements were performed by the routine FIDELE, in the CDF offline package.

48.5 cm, implying about 13% of electrons will be lost by this requirement.

- The cluster position in the z direction, must be at least 9 cm from the transverse plane at $z = 0$, in order to avoid the gap between the two cylindrical halves of the central calorimeters. This cuts about 5% of electrons in the central region.
- The seed tower (see section 2.3) of the electromagnetic cluster must not be tower 9, the tower at largest pseudorapidity (see Figure 3.4)
- One wedge module is cut away to allow access to the CDF superconducting solenoid. In this wedge, commonly referred to as the chimney module, there are only 7 normal towers, with one partial tower (tower 7), and with towers 8 and 9 completely missing. The seed tower of the cluster is required not to be tower 7 of the chimney module.

Note that the cluster finding algorithm, discussed in section 3.3, does allow electrons to cross boundaries in η. Also considered as part of the electron fiducial requirements is the condition that *at least* 1 3-D track be pointing to the cluster. For this requirement to be met the track must have gone through sufficient stereo superlayers in the CTC to enable its reconstruction in 3 dimensions. This is almost always the case for central electrons, with this cut essentially being 100% efficient.

4.2.2 Electron identification requirements

The variables used to identify electrons are defined as follows:

- E_t : The transverse energy deposited in the electromagnetic calorimeter (CEM) towers of the cluster corresponding to the track direction. In this analysis corrections to the electron energy to account for variations in tower-to-tower response were *not* applied.
- P_t : The transverse momentum of the track as measured by the track curvature

in the CTC.

- E/P : The ratio of the electromagnetic calorimeter energy to the track momentum.
- E_{HAD}/E_{EM} : The ratio of the hadronic (CHA or WHA) calorimeter energy to the CEM calorimeter energy for the cluster.
- L_{shr} : The lateral shower profile for electrons. This variable compares the energy in adjacent CEM calorimeter towers to the cluster's seed tower. It is required to be consistent with that of test beam electrons. Explicitly:

$$L_{shr} = 0.14 \sum_i \frac{E_i^{obs} - E_i^{exp}}{\sqrt{(0.14\sqrt{E})^2 + \sigma^2_{E_i^{exp}}}}$$

where the sum is over the towers adjacent to the seed tower, E_i^{obs} is the electromagnetic energy observed in tower i, with E_i^{exp} being that expected from test beam electrons, $0.14\sqrt{E}$ is the CEM calorimeter energy resolution, and $\sigma^2_{E_i^{exp}}$ the uncertainty in E_i^{exp}.

- $|\Delta x|$: the distance in the $r-\phi$ plane between the extrapolated CTC track position and the CES chamber position.
- $|\Delta z|$: as for $|\Delta x|$ but in the $r-z$ plane.
- χ^2_{strip} : the χ^2 resulting from the comparison of the CES shower profile in the z view between the electron candidate and test beam electrons.
- z-vertex match : the distance along the beam(z) axis between the primary vertex (interaction point) and the reconstructed track. If there is more than 1 vertex in the event (caused by multiple interactions), the distance to the closest vertex is used. In addition the closest vertex is required to be less than $60\,cm$ from $z = 0$.

Distributions of these variables for electrons in the data are given in Figure 4.1. The distributions come from the second leg of $Z^0 \rightarrow ee$ events where the first leg

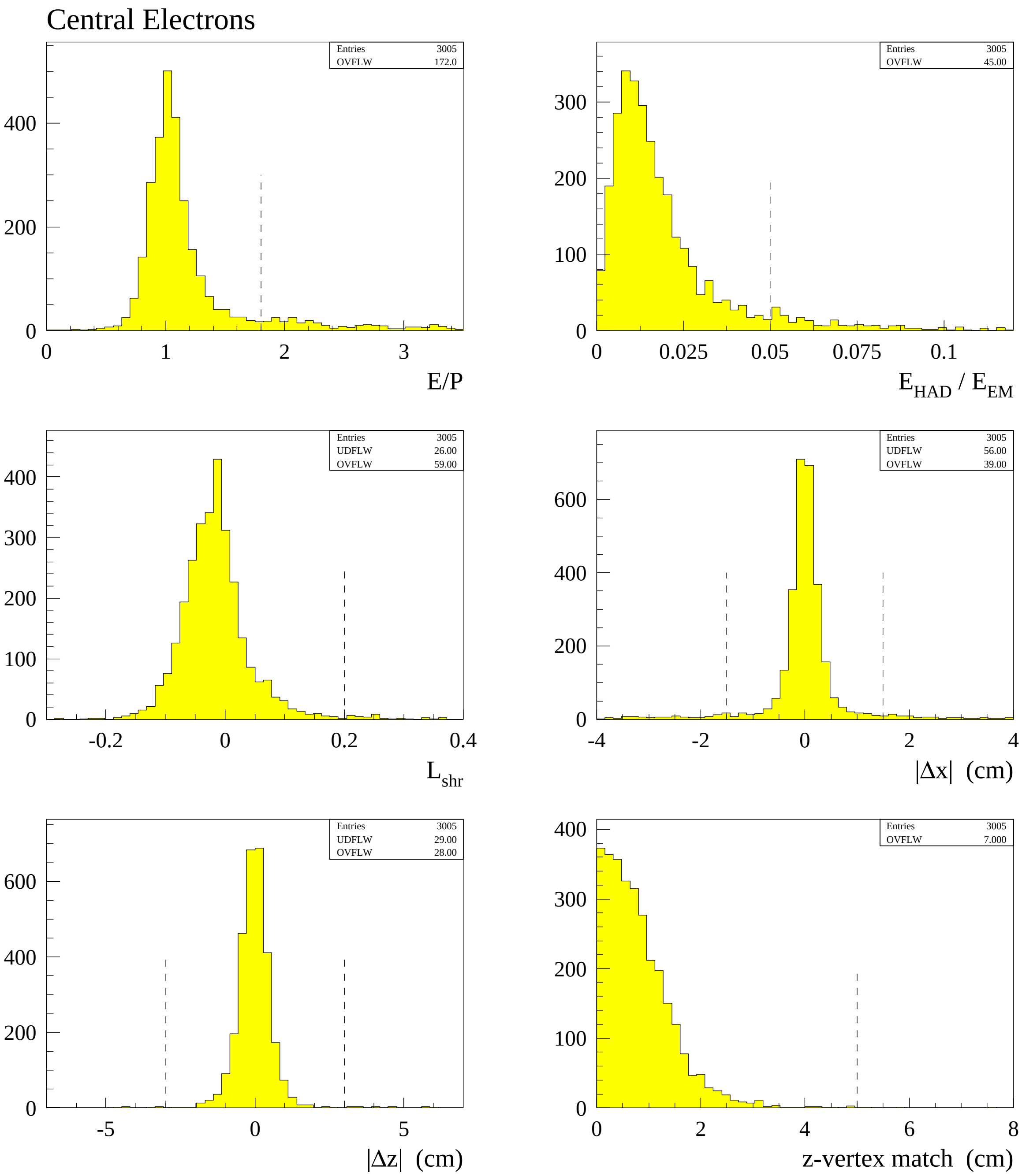

Figure 4.1

Distributions of central electron identification variables. The dashed lines indicate the cut values.

is required to pass the TCE requirements and the second leg must have passed the fiducial and $E_t > 20\,GeV$ requirements. The dashed lines represent the electron identification cuts.

Table 4.2 shows the cuts used for the selection of electrons. The LCE cuts differ from the TCE cuts in the E/P, E_{HAD}/E_{EM} and χ^2_{strip} variables as indicated in the table. Higher energy electrons have more leakage into the hadronic calorimeter and so to keep the E_{HAD}/E_{EM} cut efficient a linear term in the energy is added for the LCE class.

In addition to the above fiducial and ID requirements for electrons, an algorithm is applied to remove those electrons coming from photon conversions [48, 49]. The algorithm is 91% efficient at removing such electrons [48]. The effect of the conversion removal on the $t\bar{t}$ acceptance in the dilepton channel is discussed in section 5.2.

4.3 Muon selection

Muons are required to have CTC tracks with $P_t > 20\,GeV$. Since they are minimum ionizing, they can be recognized by high-P_t tracks pointing to very little energy deposition in the calorimeters, and matching to hits in the muon chambers if the extrapolated track is in the muon chamber fiducial region.

There are three classes of muons defined in this analysis:

- Tight Central Muon (TCM)
- Tight Extension Muon (CMX)
- Minimum Ionizing Track (CMI)

The CMI class of muon is considered *loose* in dilepton categories (section 4.5). CMI's are high P_t tracks which do not pass through the fiducial region of the muon chambers but which deposit very little energy in the calorimeters. The TCM muon class can be either CMU only (a muon stub only in the CMU chambers), CMP only

Variable	Cut	comments
E_t	$> 20\, GeV$	
P_t	$> 10\, GeV/c$	
E/P	< 1.8	for TCE
E/P	< 4.0	for LCE
E_{HAD}/E_{EM}	< 0.05	for TCE
E_{HAD}/E_{EM}	$< 0.055 + \frac{0.045 \times E}{100}$	for LCE
L_{shr}	< 0.2	
$\|\Delta x\|$	$< 1.5\, cm$	
$\|\Delta z\|$	$< 3.0\, cm$	
z-vertex match	$< 5.0\, cm$	
χ^2_{strip}	< 10.0	for TCE (not applied for LCE)

Table 4.2

Selection cuts for Central Electrons (TCE and LCE). TCE electrons differ from LCE electrons in the cuts on E/P, E_{HAD}/E_{EM}, and χ^2_{strip}.

(a muon stub only in the CMP chambers), or, CMU and CMP (matching stubs in both the CMU and CMP chambers). These are all discussed further in the next section.

4.3.1 Central muon geometrical requirements

TCM and CMX muons are by definition fiducial since they have already passed the requirement of having a stub in the muon chamber active volume at the level 1 muon trigger. The muon trigger requires a muon stub, however, muons that miss the fiducial region of the muon chambers can still come in on other triggers and be counted in the analysis. These are referred to as CMI's, which are characterized by a high-P_t track pointing to energy in the calorimeter consistent with a minimum ionizing particle. Because CMI's do not have muon chamber confirmation more stringent tracking and isolation requirements are imposed to reduce the rate of objects faking a CMI (see Table 4.4). Furthermore, CMI's must satisfy the following fiducial requirements.

- $|\eta_{det}| < 1.2$, where η_{det} is the *detector pseudorapidity*, measured from the $z = 0$ in the detector*.
- Similar calorimeter fiducial requirements as applied to electrons, but using the track position instead of the CES position. Explicitly :

\- the extrapolated track position must be at least $9\,cm$ in z from the $z = 0$ central calorimeter boundary.

\- the distance of the extrapolated track from the nearest 15° wedge ϕ boundary

---

*This is the only meaning that η has hitherto implied. However, when talking about tracks, a distinction is made between η_{det}, and η_{ev}, the *event pseudorapidity*, measured from the z position of the track, which is a more intuitive variable in defining the track direction.

must be greater than 2.5 *cm*.

- the extrapolated CTC track does not pass through the chimney region defined above for electrons.

- The track must not pass through the corner region of the plug electromagnetic calorimeter, where the PEM shares a boundary with the solenoid. This region covers the η range : $1.06 < |\eta| < 1.12$.

In addition all muon types are required to have a track in the CTC that can be fully reconstructed in 3-D, for which sufficient CTC stereo superlayer hits are required. The results of the muon fiducial requirements are shown in Figure 4.2, where η and ϕ were calculated from the muon track parameters. Because CMI's must be associated with another object passing the trigger requirements, their contribution to the inclusive muon distributions is relatively small and so their scale in these plots has been magnified by a factor of 10. The ϕ distributions show the azimuthal segmentation of the CMU chambers within the calorimeter wedges, and also the ϕ range of the CMX chambers. Note an increase in the CMI contribution in the CMX ϕ gaps. In both plots a CMI contribution is indicative of gaps in the CMU, CMP or CMX fiducial region. Also visible is the effect of the plug corner cut on the CMI $|\eta|$ distribution. As mentioned above, the TCM muon type can be *CMU only*, *CMP only*, or *CMU and CMP*. CMU only muons are mainly those that go through the ϕ gaps of the CMP chambers. Figure 4.3 shows the η and ϕ distributions for the 3 fiducial regions comprising the TCM muon type. These can be seen most clearly in Figure 4.15 of section 4.10, in which the outer "square" of chambers are the CMP, the "circle" of chambers inside those are the CMX, and within those is the CMU. The ϕ gaps shown in this diagram are clearly visible in Figures 4.2 and 4.3.

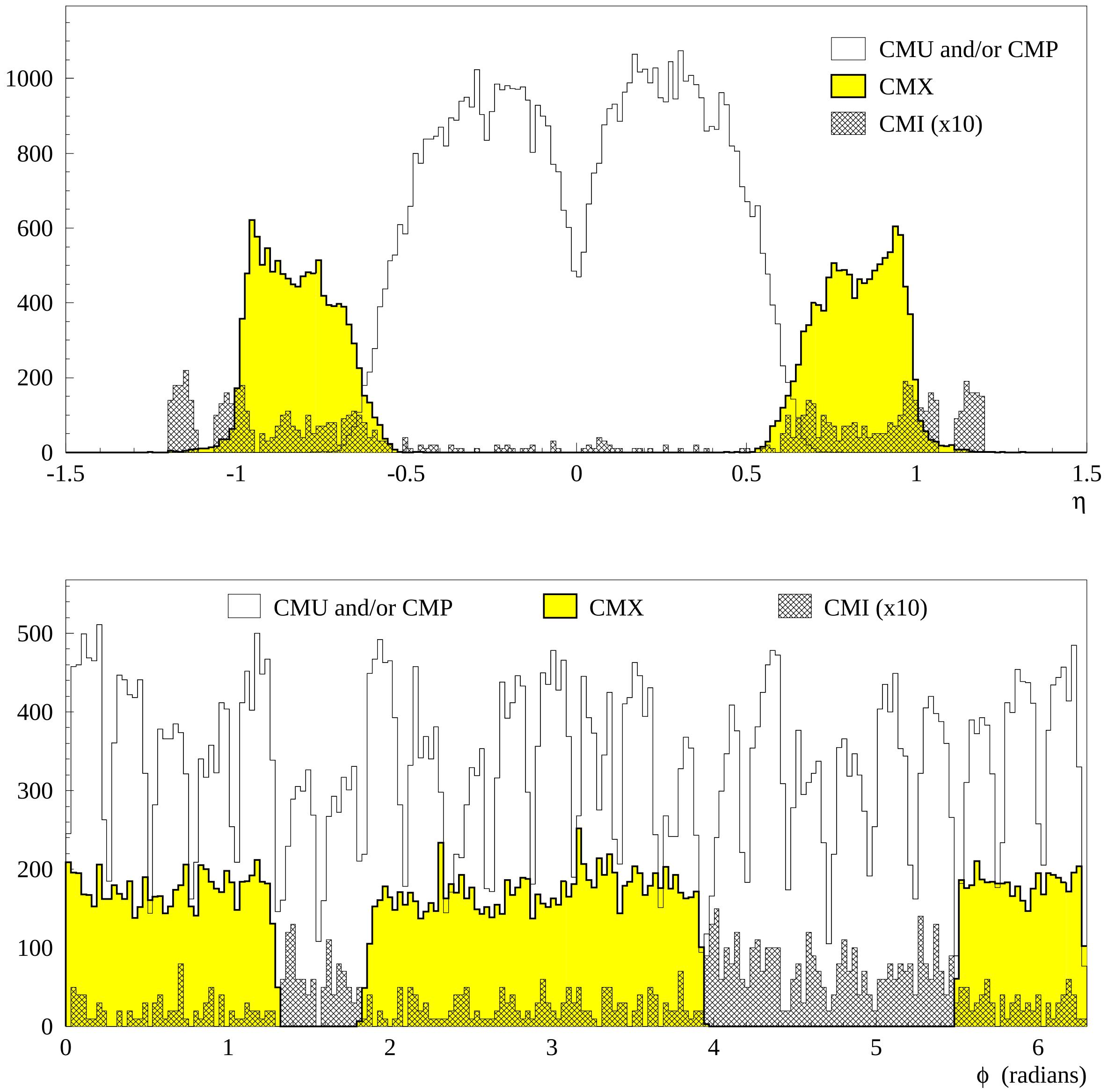

Figure 4.2

Pseudorapidity and azimuthal angular distributions for all inclusive muons in the data passing the identification requirements of subsection 4.3.2. Shown are TCM, CMX and CMI muons, with the CMI muon distributions scaled up by a factor of 10.

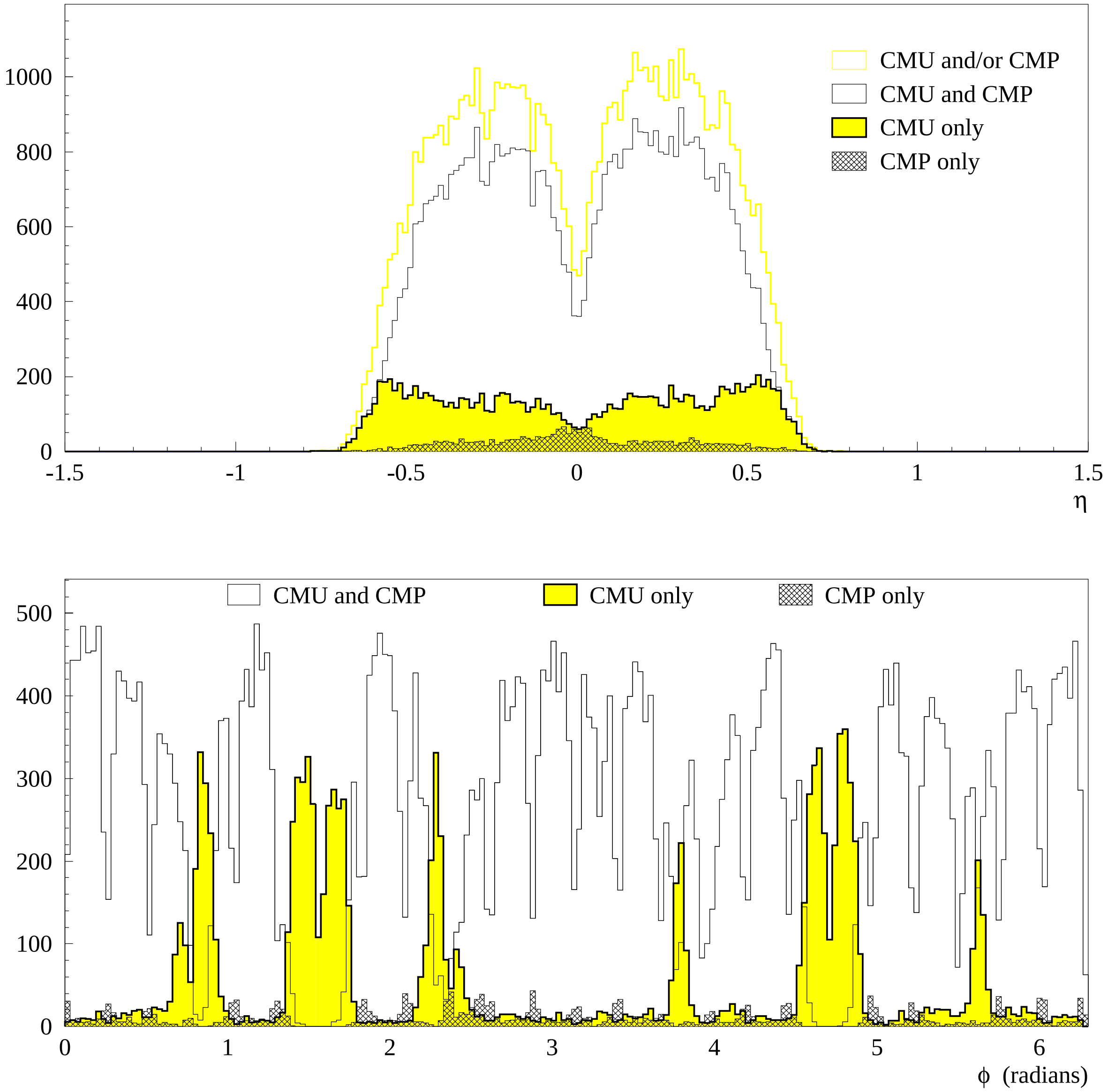

Figure 4.3

Pseudorapidity and azimuthal angular distributions for TCM muons showing the separation of the different muon chamber requirements.

4.3.2 Muon identification requirements

The TCM and CMX muon classes have identical requirements except for the matching requirement between the muon stub and the extrapolated CTC track (see below), which is chamber dependent. Tables 4.3 and 4.4 list the cuts used to select muons. The variables used in the identification of central muons (TCM and CMX) are:

- P_t : The transverse momentum of the track as measured by the CTC. The variable cut on is the *beam constrained* P_t, for which the track is refit with the added constraint that it pass through the $x - y$ beam position.
- E_{EM} and E_{HAD} : The energy deposited in the electromagnetic and hadronic calorimeters respectively. This energy is required to be consistent with that from a minimum ionizing particle.
- $d0$: The impact parameter, that is, the distance of closest approach between the reconstructed muon track and the beam axis in the $r - \phi$ plane.
- z-vertex match : the distance along the beam(z) axis between the primary vertex (interaction point) and the reconstructed track.
- $|\Delta x|_{CM}$: the distance in the $r - \phi$ plane between the extrapolated CTC track and the track segment in the relevant muon chamber.

Distributions of these variables are shown in Figures 4.4 and 4.5. In addition to the variables used for TCM and CMX class muons, the following are used in the identification of CMI muons.

- I_{cal} and I_{trk} : calorimeter and track isolation respectively, defined as the ratio of *excess* transverse energy (or momentum for track isolation) in a cone of 0.4 around the track direction, to the beam constrained transverse momentum of the muon

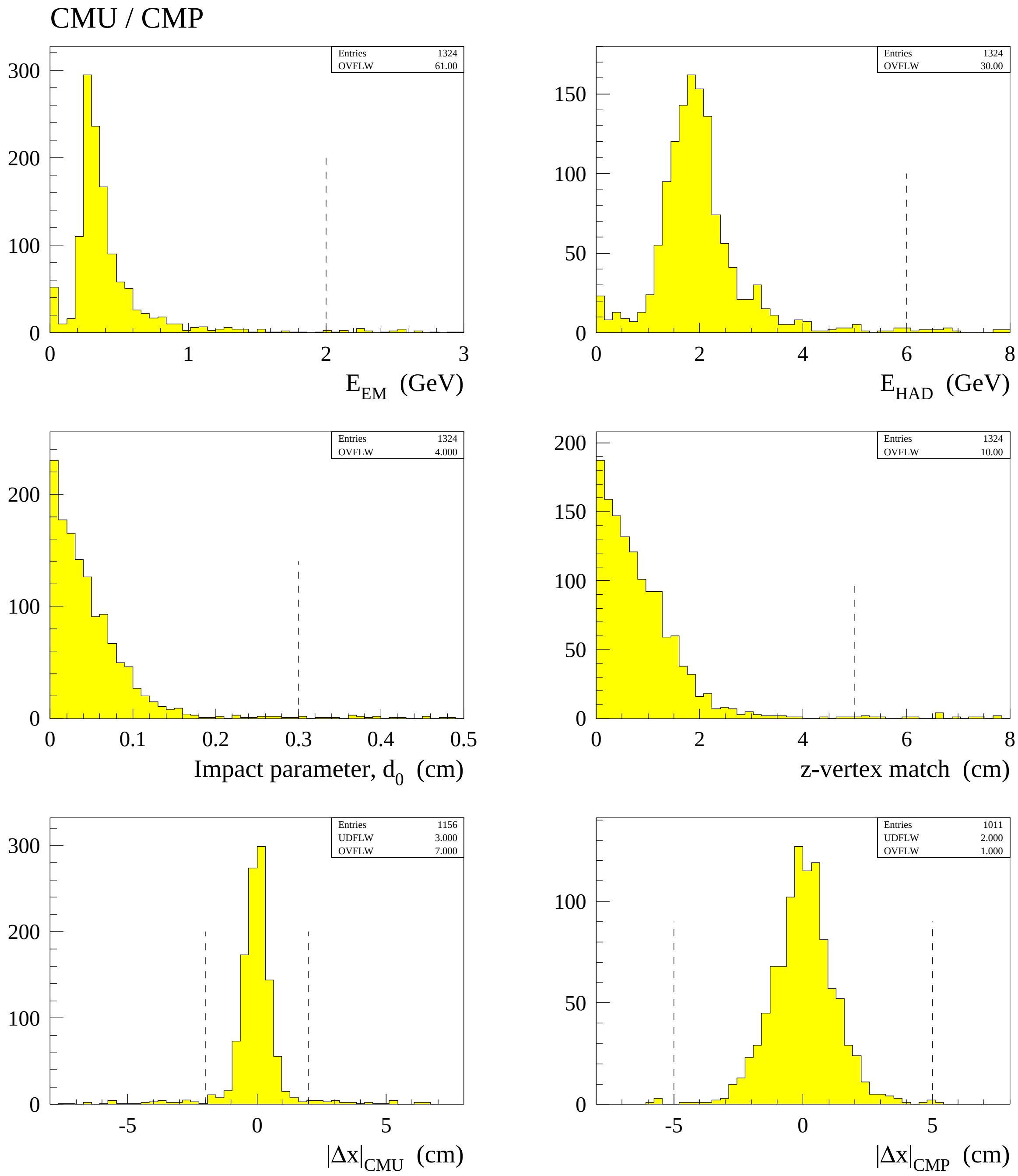

Figure 4.4

Distributions of central muon (CMU/CMP) identification variables.

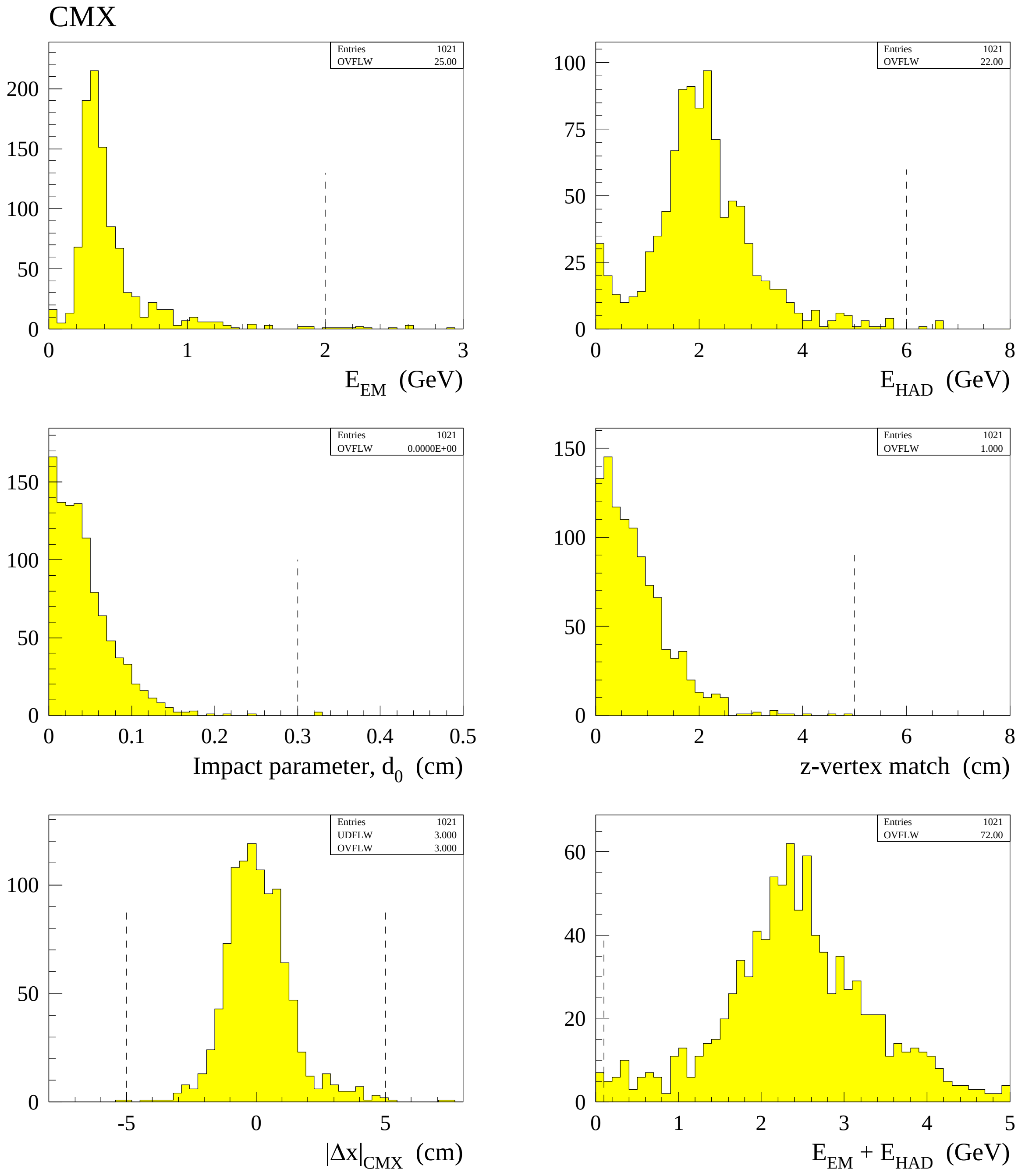

Figure 4.5

Distributions of muon extension (CMX) identification variables.

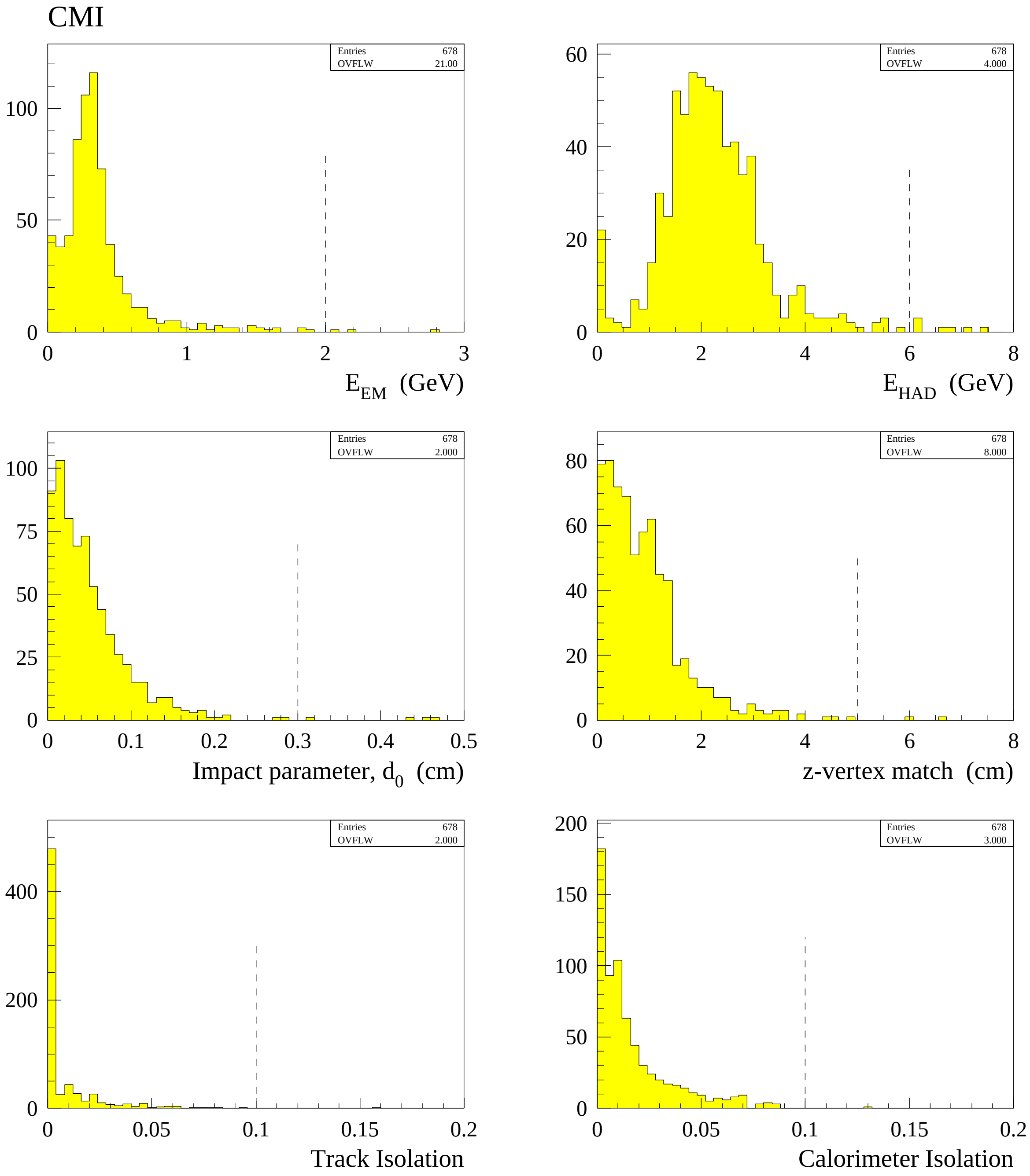

Figure 4.6

Distributions of central minimum ionizing particle (CMI) identification variables.

Variable	Cut	comments
P_t	$> 20\,GeV$	beam constrained
E_{EM}	$< 2\,GeV$	
E_{HAD}	$< 6\,GeV$	
$E_{EM} + E_{HAD}$	$> 0.1\,GeV$	
Impact parameter (d0)	$< 3\,mm$	
z-vertex match	$< 5\,cm$	
$\|\Delta x\|_{CMU}$	$< 2\,cm$	for TCM
$\|\Delta x\|_{CMP}$	$< 5\,cm$	for TCM
$\|\Delta x\|_{CMX}$	$< 5\,cm$	for CMX

Table 4.3

Selection cuts for Central Muons (TCM and CMX).

track. Isolation is also discussed, in somewhat more depth, in section 4.7.

- Number of axial and stereo superlayers (SL) : to increase the quality of the track, requirements are made on the number of CTC superlayers that contain *hits*.

Distributions of CMI identification variables are shown in Figure 4.6. In addition to the muon ID cuts in Tables 4.3 and 4.4, and the fiducial cuts of subsection 4.3.1, a very efficient cosmic ray filter is applied to remove muons from cosmic ray events.

Variable	Cut	comments
P_t	$> 20\,GeV$	beam constrained
E_{EM}	$< 2\,GeV$	
E_{HAD}	$< 6\,GeV$	
$E_{EM} + E_{HAD}$	$> 0.1\,GeV$	
Impact parameter (d0)	$< 3\,mm$	
z-vertex match	$< 5\,cm$	
I_{cal} and I_{trk}	< 0.1	
Number of axial SL	≥ 3	
Number of stereo SL	≥ 2	
Total number of SL	≥ 6	

Table 4.4

Selection cuts for Central Minimum Ionizing (CMI) particles.

If a cosmic ray muon passes close to the beam line it can look like a dimuon event. Such events are characterised by two extremely back-to-back tracks, which are out of time as measured by the hadron calorimeter TDC's, because they don't originate at a vertex along the z-axis. Often the momentum of one of the tracks (the *entering* track) is very badly mismeasured because of difficulties associated with reconstructing a track that appears to be going backwards in time. This will often lead to a large $\not{E}_t$ measurement once the correction for muons has been applied (see section 4.9). Such events will always fail the 2-jet requirement*, however, it is still desirable to remove them, if for nothing but aesthetical reasons. To remove cosmic ray events the following algorithm is applied:

- Tight back-to-back cut: remove any $\mu\mu$ event which passes,

$$|\eta_{\mu 1} + \eta_{\mu 2}| < 0.1 \quad and \quad |180^\circ - \Delta\phi| < 1.5^\circ \ .$$

- Looser back-to-back cut with track timing requirements: remove any $\mu\mu$ event which falls outside the above cone but within the looser cone:

$$|\eta_{\mu 1} + \eta_{\mu 2}| < 0.25 \quad and \quad |180^\circ - \Delta\phi| < 3.0^\circ \ ,$$

and, whose muon tracks are out of time. Explicitly, *out of time* means that the difference in time measured by the hadronic calorimeter TDC's for both muons is; $|\Delta TDC| > 14\,ns$, *or*, the individual TDC of either muon is outside the range $-10\,ns < TDC < 22\,ns$*.

This cosmic ray removal algorithm removes 6.5% of $\mu\mu$ events in the data after lepton ID cuts, and 2.5% of $Z^0 \rightarrow \mu\mu$ events ($\mu\mu$ events in the Z^0 mass window; $75\,GeV < M_{\mu\mu} < 105\,GeV$.

4.4 Lepton detection efficiencies

The lepton cuts in Tables 4.2, 4.3, and 4.4, were chosen to identify leptons with a high efficiency while keeping the probability extremely small for a hadron to fake a lepton signature (see section 6.4). Given a lepton that has satisfied the fiducial requirements of sections 4.2.1 and 4.3.1, and has a transverse energy (or

---

*Unless, by a freak coincidence, they overlap with a 2-jet event.

*For Run 1B only. For Run 1A the range was $-14\,ns < TDC < 18\,ns$.

momentum) greater than $20\,GeV$, it is important to know the probability for that lepton to pass its identification cuts, in order to understand part of the dilepton acceptance (chapter 5). These probabilities are commonly referred to as the lepton detection efficiencies. The methods for calculating these efficiencies using $Z^0 \rightarrow ee$ and $Z^0 \rightarrow \mu\mu$ events, are explained in Appendix A. The results for each of the 5 lepton types used in this analysis are given in Table 4.5. The efficiencies given in this table do not include any corrections due to the trigger bias explained in section A.3. In calculating the lepton efficiencies, the dilepton invariant mass was required to be; $80\,GeV < M_{\ell\ell} < 100\,GeV$. The lepton efficiencies crucially depend on the event activity close to the lepton direction, and so will be different for leptons from Z^0 decay than for leptons in $t\bar{t}$ events, where the lepton source can be from W, τ, b, or c decay. Nevertheless, the efficiencies of leptons in Z^0 events provide an important basis for determining the lepton efficiencies in $t\bar{t}$ events. This is discussed at some length in chapter 5.

The lepton efficiencies calculated as a function of calorimeter isolation (defined in section 4.7) is discussed in section 5.3. As seen in Figure 5.5 of that section, the efficiencies are higher after requiring the lepton be isolated from other calorimeter activity.

4.4.1 Effect of luminosity on lepton efficiencies

During the course of Runs 1A and 1B there was a wide range of instantaneous luminosities attained. It might be conjectured that an increase in instantaneous luminosity would decrease the lepton detection efficiencies, because of the corresponding increase of multiple interactions in each beam crossing. To check this, Run 1B data was used and the lepton efficiencies calculated separately for runs in which the initial instantaneous luminosity was, $L < 7 \times 10^{30}\,cm^{-2}s^{-1}$, and also

	Run 1B		Run 1A	
	Method 1	Method 2	Method 1	Method 2
TCE	0.815 ± 0.007	0.818 ± 0.009	0.832 ± 0.013	0.841 ± 0.017
LCE	0.896 ± 0.005	0.889 ± 0.007	0.902 ± 0.010	0.905 ± 0.013
TCM	0.917 ± 0.007	0.922 ± 0.009	0.922 ± 0.014	0.938 ± 0.017
CMX	0.897 ± 0.018	0.914 ± 0.010	—	0.923 ± 0.021
CMI	—	0.913 ± 0.013	—	0.927 ± 0.025

Table 4.5

Lepton identification efficiencies in Run 1A and Run 1B data. Shown are the two methods for calculating the efficiency described in Appendix A. Errors are statistical only.

	$<L>= 4.8 \times 10^{30}\ cm^{-2}s^{-1}$	$<L>= 10.6 \times 10^{30}\ cm^{-2}s^{-1}$
TCE	0.811 ± 0.012	0.815 ± 0.008
LCE	0.894 ± 0.008	0.897 ± 0.006
TCM	0.926 ± 0.010	0.910 ± 0.009
CMX	0.906 ± 0.017	0.917 ± 0.012
CMI	0.934 ± 0.017	0.895 ± 0.018

Table 4.6

Lepton identification efficiencies for two different average values of the instantaneous luminosity. Errors are statistical only.

for runs in which $L > 7 \times 10^{30}\, cm^{-2}s^{-1}$. These runs give the following average instantaneous luminosities, $<L>$, and integrated luminosities, $\mathcal{L}$.

	Average L	Integrated L, $\mathcal{L} = \int L\, dt$
Runs where $L < 7 \times 10^{30}\, cm^{-2}s^{-1}$	$4.8 \times 10^{30}\, cm^{-2}s^{-1}$	$34\, pb^{-1}$
Runs where $L > 7 \times 10^{30}\, cm^{-2}s^{-1}$	$10.6 \times 10^{30}\, cm^{-2}s^{-1}$	$59\, pb^{-1}$

The lepton detection efficiencies obtained from these two sets of different luminosity runs are given in Table 4.6. The efficiencies quoted for TCE, LCE and TCM leptons are from “method 1”, and those for CMX and CMI muons, from “method 2”. Within the statistical errors shown, there is no significant dependence of the lepton detection efficiencies on the instantaneous luminosity, except possibly for the CMI efficiency which decreased by more than 4% with a doubling of $<L>$.

4.5 Dilepton selection

Events are selected which contain at least one *tight* electron or muon (TCE, TCM or CMX) as defined in the previous sections. The LCE and CMI lepton types are considered *loose*. This creates the *tight-tight* and *tight-loose* dilepton categories shown in Table 4.7.

In addition to the z-vertex matching requirements on each lepton, both leptons must be found to come from the same event vertex. This requirement decreases the number of ee events by about 0.8% and the number of $\mu\mu$ events by about 1.6%, after the lepton ID cuts.

For each category it is required that at least one *tight* lepton be isolated (see section 4.7). The event is then subjected to the kinematical and topological cuts discussed in the following sections, to determine the dilepton top candidates. The

	Dilepton Category
$e-e$	TCE-TCE TCE-LCE
$\mu-\mu$	TCM-TCM TCM-CMX CMX-CMX TCM-CMI CMX-CMI
$e-\mu$	TCE-TCM TCE-CMX TCE-CMI TCM-LCE CMX-LCE

Table 4.7

Dilepton categories used for the ee, $\mu\mu$ and $e\mu$ channels. Each dilepton category requires at least one tight lepton (TCE, TCM or CMX).

cuts are made in the order in which they are discussed below. Events with 3 or more leptons are considered a separate category which will be discussed separately following the event selection cuts.

4.6 Same-Sign cut

Both leptons in the event are required to have opposite charge. This reduces the *Fake Dilepton* background by 2, while preserving most of the top dilepton acceptance. Same-sign dilepton $t\bar{t}$ decays have one lepton from a W decay and the other from the decay of one of the b quarks. From $t\bar{t}$ Monte-Carlo, with $m_t = 175\,GeV$, about 3% of the dilepton signal comes from same-sign events. The same-sign acceptance is discussed in more detail in section 7.6, together with the same-sign events seen in the data.

4.7 Isolation cut

Each dilepton event is required to have at least 1 tight lepton (TCE, TCM or CMX) that is isolated. The same isolation requirement is already part of the CMI definition, so in dilepton events containing CMI's both leptons must be isolated. The isolation requirement is two-fold, consisting of a calorimeter isolation (I_{cal}) cut, and, a track isolation (I_{trk}) cut. Track isolation is defined as:

$$I_{trk} = \frac{P_t^{04}}{P_t} \ ,$$

where, P_t^{04} is the sum of the transverse track momenta (excluding the lepton P_t) inside a cone of radius $\Delta R = \sqrt{\Delta\eta^2 + \Delta\phi^2} = 0.4$ with axis as the lepton direction. Calorimeter isolation is defined likewise as:

$$\text{For electrons :} \quad I_{cal} = \frac{E_t^{04}}{E_t} \ , \qquad \text{For muons :} \quad I_{cal} = \frac{E_t^{04}}{P_t} \ ,$$

where, E_t^{04} is the sum of the calorimeter transverse energy inside a cone of radius $\Delta R = 0.4$ with axis as the lepton direction, excluding the calorimeter transverse energy of the lepton. For the case of muons in these definitions, P_t is beam constrained. The isolation requirement is for at least one tight lepton in the event to satisfy both:

$$I_{cal} < 0.1 \quad \text{AND} \quad I_{trk} < 0.1 \ .$$

The calorimeter isolation distributions for leptons with $P_t > 20\,GeV$ in $t\bar{t}$ events from W, τ, and b decays are shown in Figures 4.7 and 4.8. Distributions from both HERWIG and PYTHIA[*] $t\bar{t}$ samples are plotted for a top mass of $175\,GeV$. These plots were made before any lepton identification and dilepton selection cuts, with the only requirements being that the lepton is in the fiducial region of the detector, and, $P_t(\mu)$ or $E_t(e)$ is greater than $20\,GeV$. Note the difference in scale for the distributions from b decay. The difference in the shapes of the electron and muon isolation distributions from b decay is a manifestation of the different definitions of I_{cal} for electrons and muons (see above).

The isolation cut drastically reduces the background from $b\bar{b}$ production since leptons from semi-leptonic b decay are generally surrounded by jet activity, while being about 95% efficient for the $t\bar{t}$ signal (see section 5.4). Most of the inefficiency in $t\bar{t}$ dilepton events is due to the dilepton acceptance in the *lepton + jets* channel, where one lepton comes from b decay, which is discussed further in chapter 5.

4.8 Invariant Mass cut

The Drell-Yan background from Z^0 decay dominates the dielectron and dimuon events after the lepton ID, same-sign, and isolation cuts. To remove Z^0's from the

---

[*] Monte Carlo generators are introduced in Appendix B.

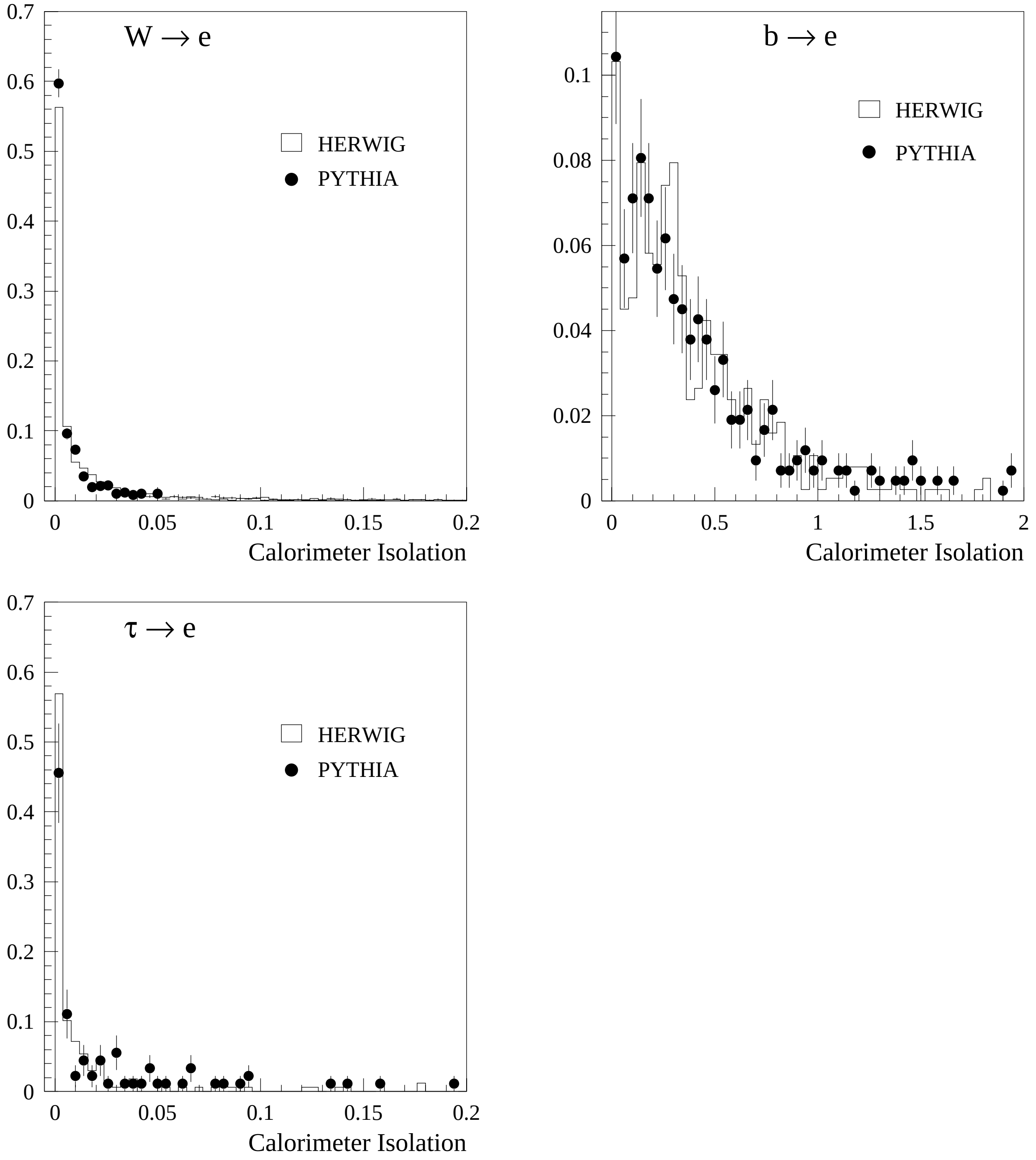

Figure 4.7

Calorimeter isolation distributions for electrons from three sources in $t\bar{t}$ Monte Carlo events with a top mass of $175\,GeV$.

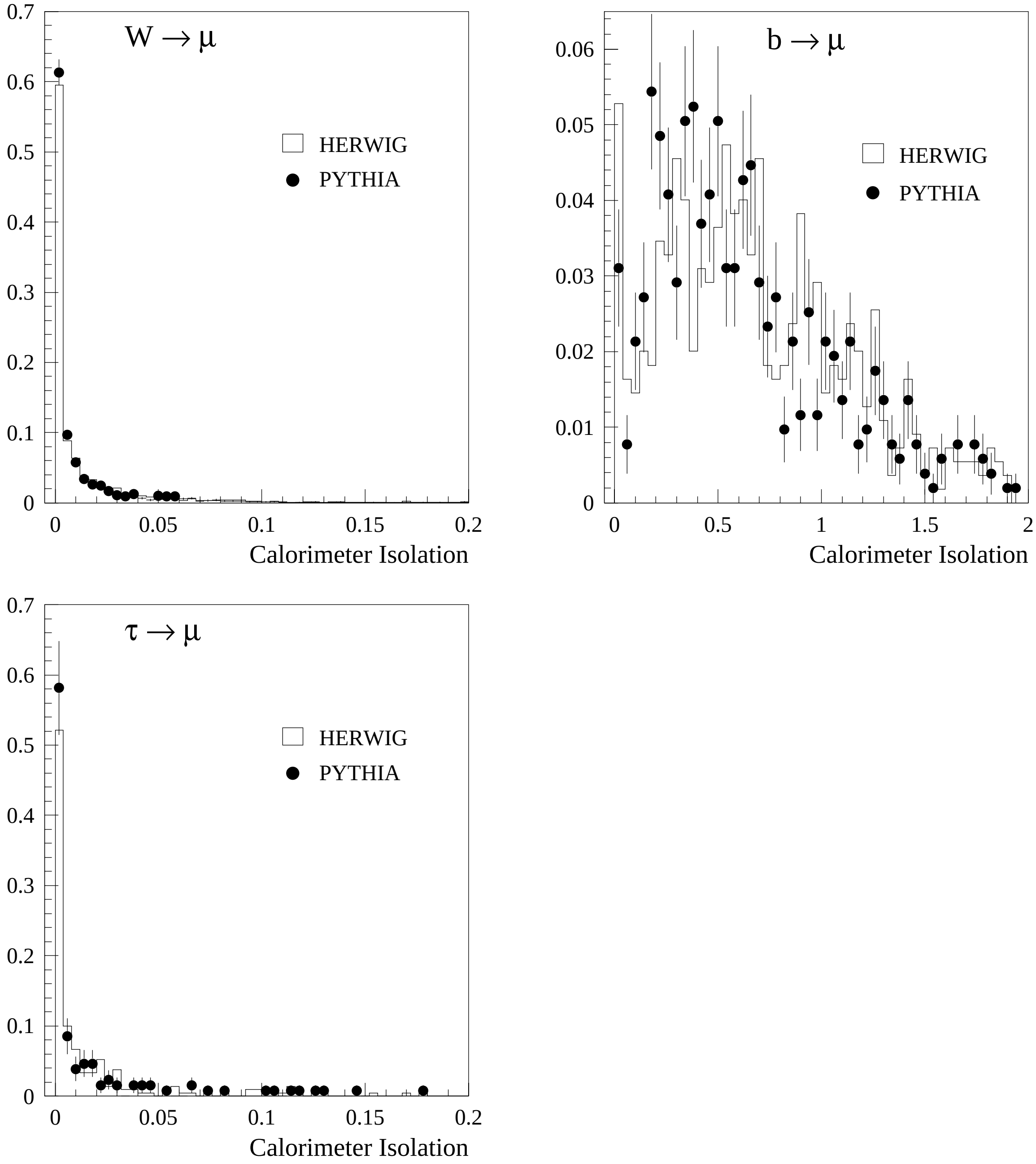

Figure 4.8

Calorimeter isolation distributions for muons from three sources in $t\bar{t}$ Monte Carlo events with a top mass of $175\,GeV$.

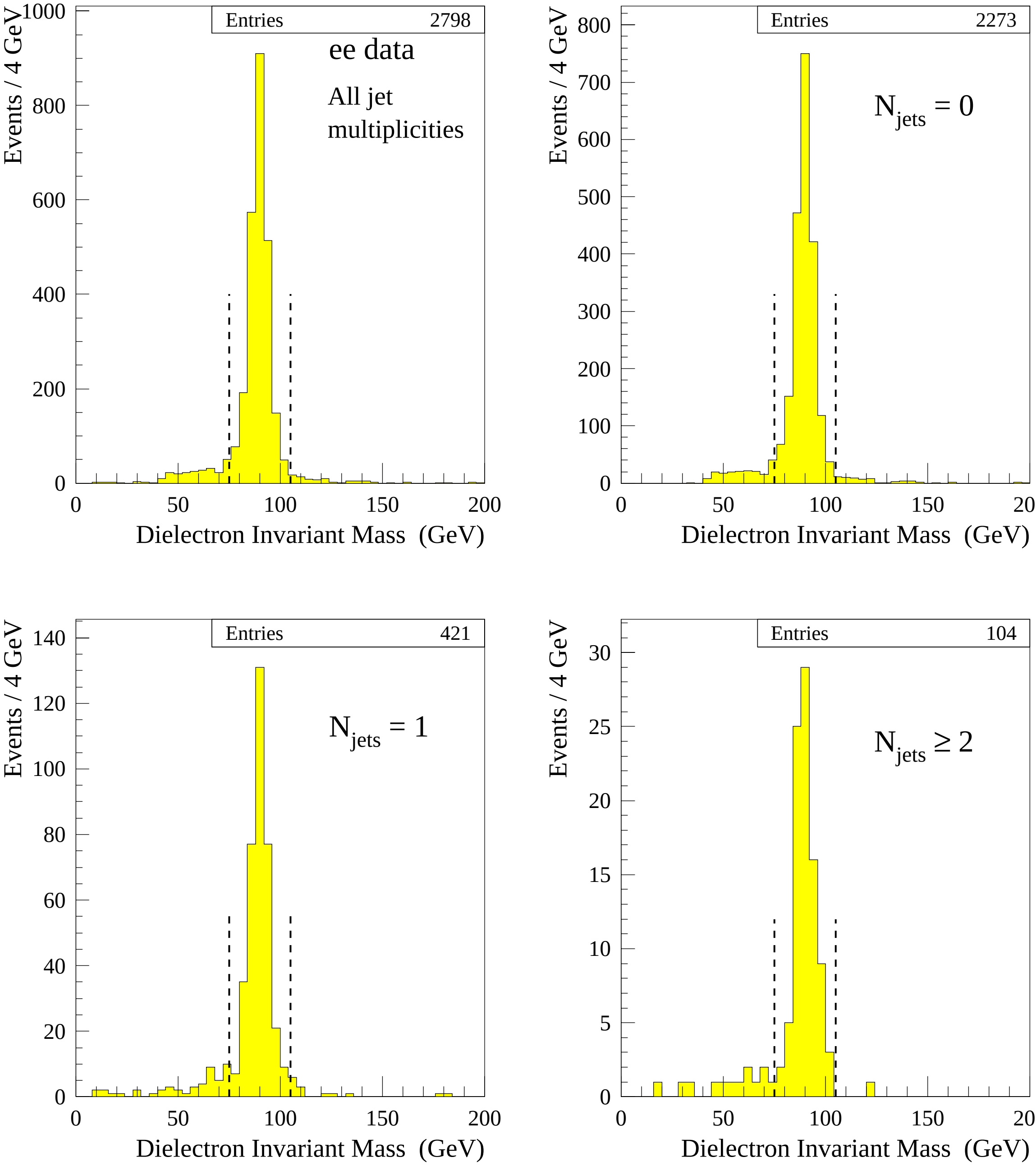

Figure 4.9

Dielectron (ee) invariant mass distributions for the $109\,pb^{-1}$ of data before the invariant mass cut, but after the lepton ID, same-sign, and isolation cuts. The ee data has been separated according to jet multiplicity. The dashed lines define the Z^0 mass window.

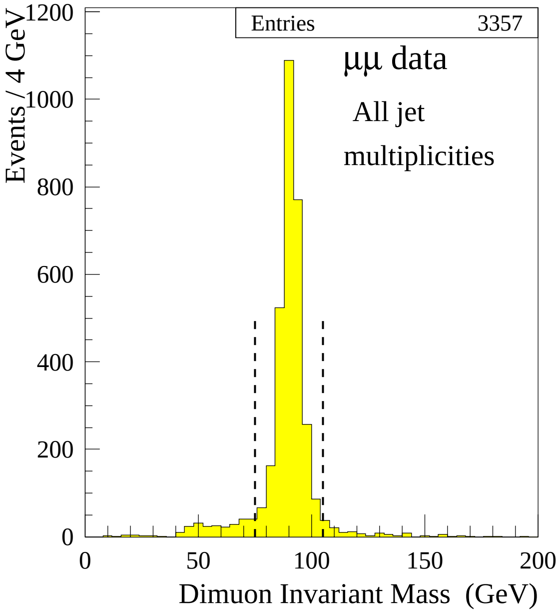

Figure 4.10

Dimuon ($\mu\mu$) invariant mass distributions for the $109\,pb^{-1}$ of data before the invariant mass cut, but after the lepton ID, same-sign, and isolation cuts. The $\mu\mu$ data has been separated according to jet multiplicity. The dashed lines define the Z^0 mass window.

sample, events are rejected if the dielectron or dimuon invariant mass is in the region $75\,GeV \leq M_{\ell\ell} \leq 105\,GeV$. About 90% of the ee and $\mu\mu$ data fall inside this Z^0 mass window before the invariant mass cut. The dielectron and dimuon invariant masses are defined respectively as:

$$M_{ee} = \sqrt{(E^{e1}_{tot} + E^{e2}_{tot})^2 - (E^{e1}_x + E^{e2}_x)^2 - (E^{e1}_y + E^{e2}_y)^2 - (E^{e1}_z + E^{e2}_z)^2}$$

$$M_{\mu\mu} = \sqrt{(P^{\mu1}_{tot} + P^{\mu2}_{tot})^2 - (P^{\mu1}_x + P^{\mu2}_x)^2 - (P^{\mu1}_y + P^{\mu2}_y)^2 - (P^{\mu1}_z + P^{\mu2}_z)^2}\ ,$$

where, the E_i for the 2 electrons ($e1$ and $e2$) are the electromagnetic calorimeter energies, and the P_i for the 2 muons ($\mu1$ and $\mu2$) are the beam constrained track momenta. The dielectron and dimuon data before the invariant mass cut (but after the lepton ID, same-sign and isolation cuts) is displayed in the invariant mass distributions of Figures 4.9 and 4.10. These figures present the data in the various jet multiplicity bins, with the dashed lines indicating the invariant mass cut values. From the PYTHIA 175 sample, this cut is $(76 \pm 4)\%$ efficient for dielectrons and dimuons from $t\bar{t}$ decay. The denominator in this calculation is all dielectron and dimuon events that have passed the lepton ID, same-sign, and isolation cuts, and the numerator those events that have also passed the subsequent Z^0 mass cut. When $e\mu$ events are included, for which the invariant mass cut is not applied, the efficiency of this cut for dilepton events is $(88 \pm 3)\%$.

The effect of the invariant mass cut in dilepton events from $t\bar{t}$ decay is illustrated in Figure 4.11 for a top mass of $175\,GeV$. The effect of this cut on some background distributions is shown in Figures 6.9 and 6.11 in chapter 6.

4.9 Missing $\mathbf{E}_t$ cuts

The undetected neutrinos in a $t\bar{t}$ dilepton channel event will usually engender a large missing transverse energy ($\not{E}_t$) measurement. The so called *raw* $\not{E}_t$ is the

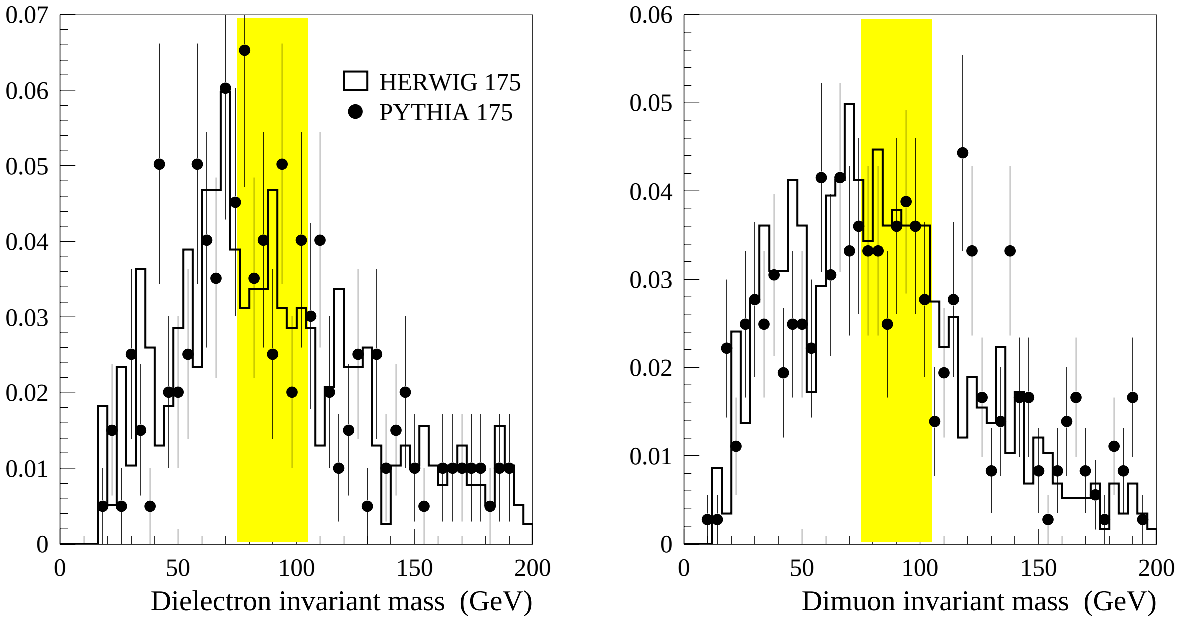

Figure 4.11

Dilepton invariant mass distributions for ee and $\mu\mu$ events from $t\bar{t}$ Monte Carlo samples with a top mass of $175\,GeV$. The shaded area represents the region excluded by the invariant mass cut.

negative of the vector sum of all the transverse energy in the calorimeter. This undergoes two corrections to give the final $\not{E}_t$ measurement.

- A correction is made for all muons that have passed one of the 3 muon categories, TCM, CMX or CMI. The beam constrained muon P_x and P_y are subtracted from the respective components of the $\not{E}_t$, with the x and y components of the CEM and CHA energies of the muon added back in.
- A correction is made for jets in the event, with the definition of a jet being that in section 2.9, with the only difference being that for the $\not{E}_t$ correction jets are used out to $|\eta| < 2.4$, instead of $|\eta| < 2.0$ as is used in jet counting. As explained in

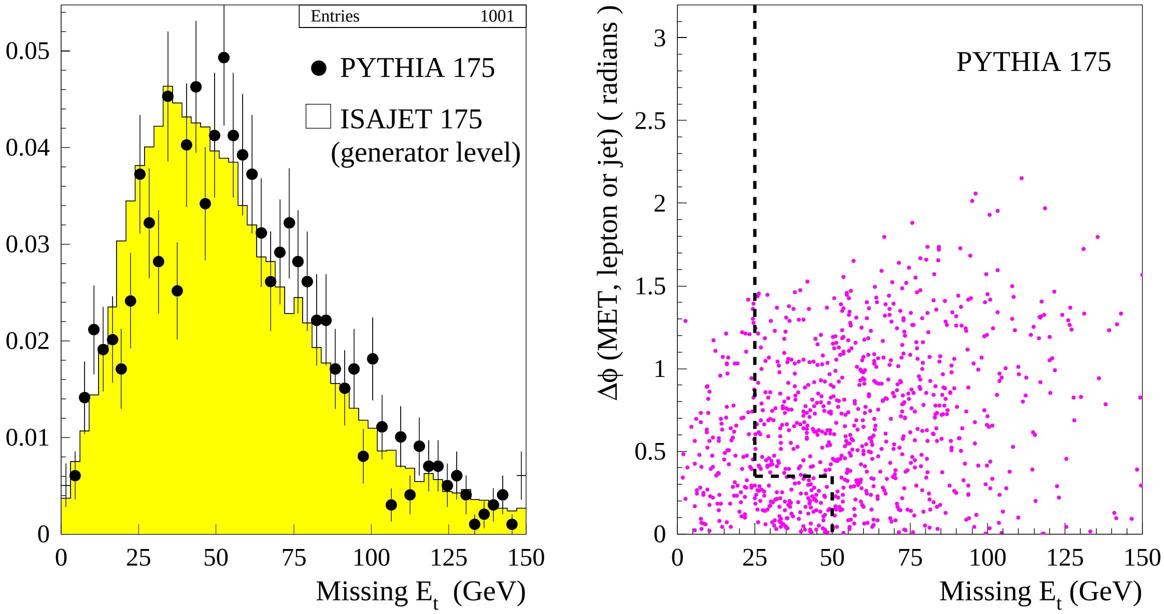

Figure 4.12

The $\not{E}_t$ distribution (left plot, normalized to 1), and the azimuthal angle between the $\not{E}_t$ and the nearest lepton or jet versus the $\not{E}_t$ (right plot), expected from $t\bar{t}$ Monte Carlo with $m_t = 175\,GeV$. The PYTHIA+QFL simulated events have passed the lepton ID, same-sign, isolation, invariant mass, and 2-jet cuts. For comparison an ISAJET generator level $\not{E}_t$ distribution is shown (see text).

section 2.9 jet energies are corrected for detector effects. The difference between the corrected and uncorrected jet E_t's are used to correct the $\not{E}_t$.

Henceforth the term $\not{E}_t$ will refer to the corrected missing transverse energy, unless explicitly stated otherwise. Figure 4.12 shows the $\not{E}_t$ distributions expected for $t\bar{t}$ decay in the dilepton channel for $m_t = 175\,GeV$. The PYTHIA+QFL distributions originate from a sample of 80 000 unforced $t\bar{t}$ decays in which the events have passed all dilepton cuts except the $\not{E}_t$ cuts (see below). The ISAJET distribution is from 20 000 $t\bar{t}$ events forced to decay to the dilepton channel. Detector effects have not been taken into account (i.e. the events were not run through QFL). The $\not{E}_t$ was calculated from the x and y components of the neutrino momenta, and is plotted simply to show the comparison between a $\not{E}_t$ measurement and the actual neutrino momenta.

There are two requirements made on the $\not{E}_t$. The magnitude, $|\not{E}_t|$, is required to be greater than $25\,GeV$. This has the greatest reduction power for the Drell-Yan background as is most clearly seen in Figure 6.2 of section 6.1. It also significantly reduces the number of dilepton events from $Z^0 \rightarrow \tau\tau$, $b\bar{b}$ and *fakes* (see chapter 6). The second requirement rejects events if $\not{E}_t < 50\,GeV$ and the azimuthal angle between the $\not{E}_t$ and the nearest (in ϕ) lepton or jet $(\Delta\phi(\not{E}_t, \ell \ or \ j))$ is less than $20°$. If $\not{E}_t > 50\,GeV$ no angular cut is placed. These cuts are best seen in the second diagram of Figure 4.12, which shows the expected distribution from dilepton $t\bar{t}$ events, with $m_t = 175\,GeV$, in the $\Delta\phi(\not{E}_t, \ell \ or \ j) - \not{E}_t$ plane. The dashed lines represent the cut values.

Drell-Yan events (see section 6.1) have no neutrinos, and so any $\not{E}_t$ in the event is expected to come predominantly from the energy mismeasurement of a jet. In this case the $\not{E}_t$ vector is expected to point along a direction close to the jet direction. This is the premise behind the angular cut on $\Delta\phi(\not{E}_t, nearest\ jet)$. Figure 4.13 shows the distributions of $\Delta\phi(\not{E}_t, nearest\ jet)$ versus $\not{E}_t$ for Drell-Yan $Z^0 + jets$ events in the data. The $\Delta\phi(\not{E}_t, nearest\ lepton)$ cut was primarily to reduce dileptons from $Z^0 \rightarrow \tau\tau$ decay in which the $\not{E}_t$ often points close to the direction of one of the leptons. Distributions of $\Delta\phi(\not{E}_t, nearest\ lepton)$ versus $\not{E}_t$ expected from $Z^0 \rightarrow \tau\tau$ are shown in Figure 4.14. This cut will be dropped in future dilepton analyses (see Appendix D) and still exists largely for historical reasons. Once the 2-jet requirement is made there is no longer any obvious correlation between the $\not{E}_t$ and lepton directions.

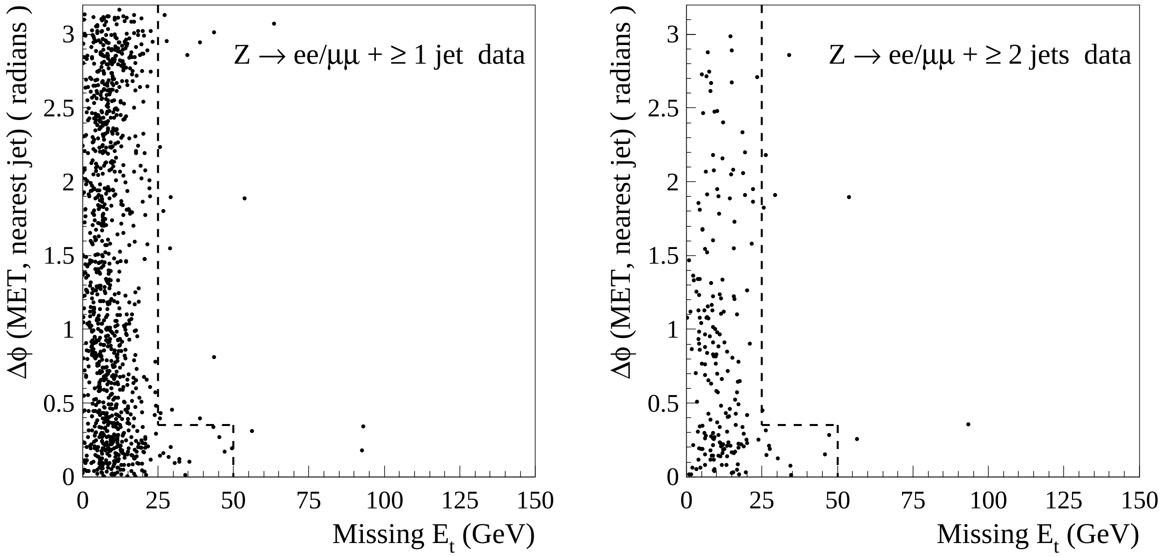

Figure 4.13

Distributions of the azimuthal angle between the $\not\!\!E_t$ and the nearest jet versus $\not\!\!E_t$, for dimuon and dielectron $Z^0+ \geq 1\,jet$ and $Z^0+ \geq 2\,jet$ events from the $109\,pb^{-1}$ of data.

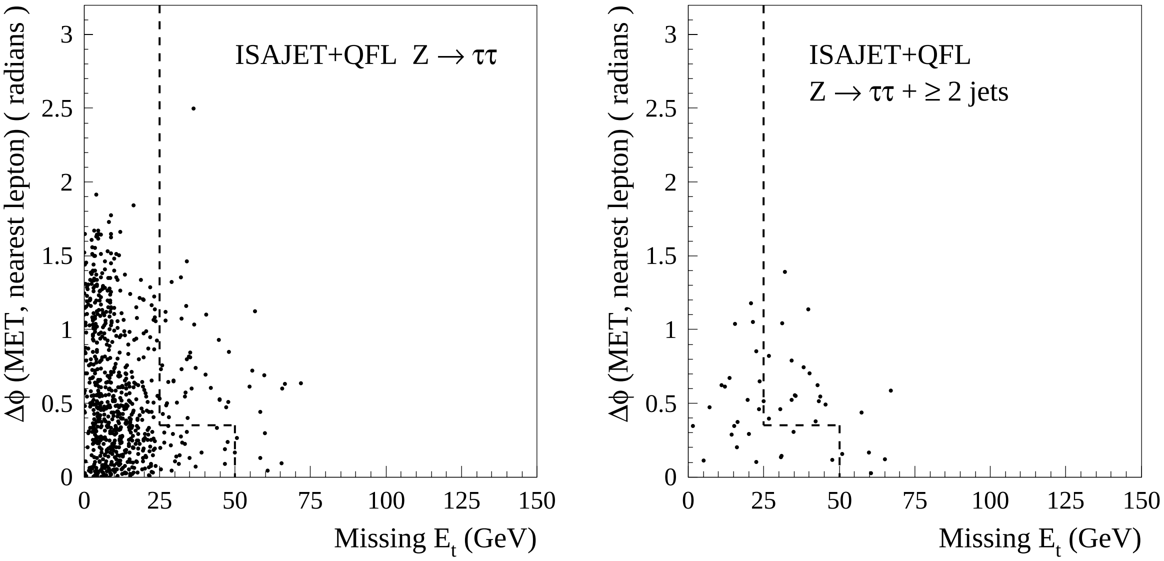

Figure 4.14

Distributions of the azimuthal angle between the $\not\!\!E_t$ and the nearest lepton versus $\not\!\!E_t$, for $Z^0 \rightarrow \tau^+\tau^-$ simulated events, both for no jet requirement (left plot), and for the 2-jet requirement (right plot).

4.10 Jet requirements

4.10.1 Jet corrections and definitions

Colored quarks and gluons created from hard $q\bar{q}$ collisions will experience fragmentation (or hadronization), due to the color force field, and form colorless hadrons which exit the interaction region as a narrow stream of particles referred to as *jets*. Various fragmentation functions exist which try to parameterize this process as a function of the initial parton energy and the energy fractions of the resulting hadrons, for example those by Field and Feynman [50] (used in the ISAJET Monte Carlo generator), and the more sophisticated modeling of Webber et al. [51] (used in the HERWIG Monte Carlo). Jets are expected to deposit their energy in a localized group of calorimeter towers, and so the energy of the initial parton can be approximated by summing the tower energies inside a cone of specified size. The cone size is defined in η-ϕ space by its radius, $R = \sqrt{\Delta\eta^2 + \Delta\phi^2}$, and is centered at the largest calorimeter energy tower. The cone size must be chosen so as to encompass most of the jet energy without allowing a significant contribution from other activity in the event. The cone concept is best illustrated by an example. Figure 4.15 is an event picture which shows the transverse view of the tracks as measured in the CTC which constitute one of the top dilepton candidates, the $\mu\mu$ event 272140 from run 63700. The muon tracks are at $\phi = 147^\circ$ and $\phi = 292^\circ$, and the tracks of the 2 jets in the event are centered at $\phi = 77^\circ$ and $\phi = 249^\circ$. The group of tracks at about $\phi = 45^\circ$ do not have enough combined energy to be considered a jet (see below). Below the CTC event display is Figure 4.16, the so called *lego plot* for the event, which displays the energy deposited in the calorimeter towers in a *flattened* η-ϕ coordinate system. The height of each lego tower is proportional to the total energy deposited in the corresponding electromagnetic and hadronic calorimeter tower. Drawn around each calorimeter cluster centroid are 3 cones of sizes $R = 0.4$, $R = 0.7$, and $R = 1.0$. For

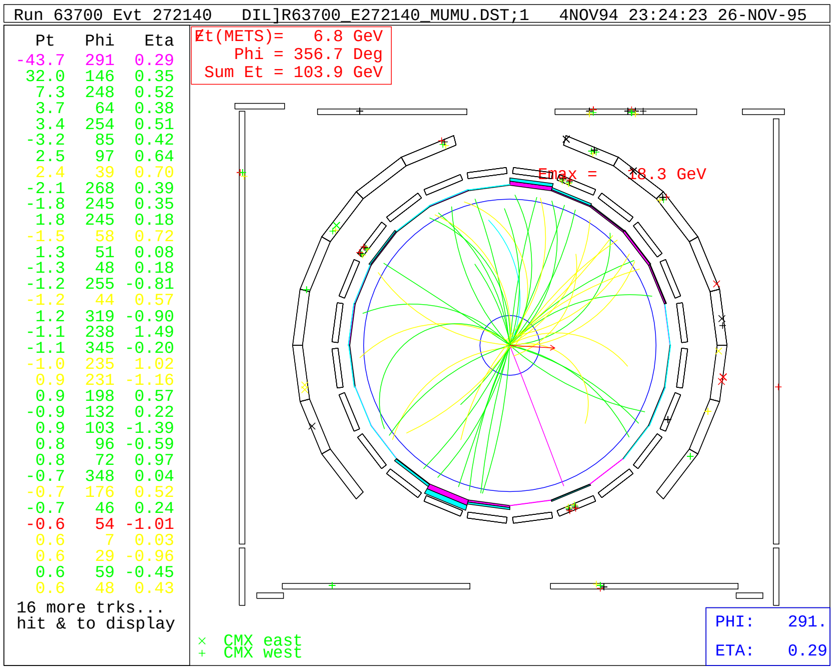

```
Run 63700 Evt 272140   DIL]R63700_E272140_MUMU.DST;1   4NOV94 23:24:23 26-NOV-95

   Pt   Phi   Eta
-43.7   291  0.29
 32.0   146  0.35
  7.3   248  0.52
  3.7    64  0.38
  3.4   254  0.51
 -3.2    85  0.42
  2.5    97  0.64
  2.4    39  0.70
 -2.1   268  0.39
 -1.8   245  0.35
  1.8   245  0.18
 -1.5    58  0.72
  1.3    51  0.08
 -1.3    48  0.18
 -1.2   255 -0.81
 -1.2    44  0.57
  1.2   319 -0.90
 -1.1   238  1.49
 -1.1   345 -0.20
 -1.0   235  1.02
  0.9   231 -1.16
  0.9   198  0.57
 -0.9   132  0.22
  0.9   103 -1.39
  0.8    96 -0.59
  0.8    72  0.97
 -0.7   348  0.04
 -0.7   176  0.52
 -0.7    46  0.24
 -0.6    54 -1.01
  0.6     7  0.03
  0.6    29 -0.96
  0.6    59 -0.45
  0.6    48  0.43
16 more trks...
hit & to display

Et(METS)=    6.8 GeV
   Phi = 356.7 Deg
 Sum Et = 103.9 GeV

PHI:   291.
ETA:   0.29
```

Figure 4.15

Transverse view of the CDF detector with the CTC enlarged, showing the tracks contributing to the $\mu\mu$ candidate 63700/272140. Going radially outwards beyond the CTC are the chambers of the CMU, CMX and CMP muon systems.

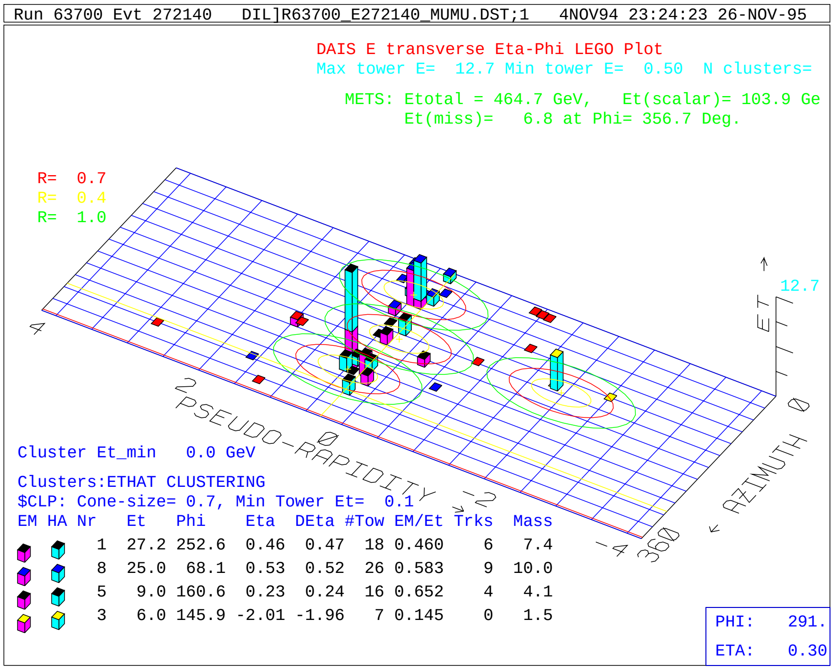

```
Run 63700 Evt 272140   DIL]R63700_E272140_MUMU.DST;1   4NOV94 23:24:23 26-NOV-95

DAIS E transverse Eta-Phi LEGO Plot
Max tower E=  12.7 Min tower E=  0.50  N clusters=

  METS: Etotal = 464.7 GeV,   Et(scalar)= 103.9 Ge
        Et(miss)=   6.8 at Phi= 356.7 Deg.

R=  0.7
R=  0.4
R=  1.0

Cluster Et_min   0.0 GeV

Clusters:ETHAT CLUSTERING
$CLP: Cone-size= 0.7, Min Tower Et=  0.1
EM HA Nr    Et   Phi    Eta  DEta #Tow EM/Et Trks  Mass
         1  27.2 252.6  0.46  0.47   18 0.460    6   7.4
         8  25.0  68.1  0.53  0.52   26 0.583    9  10.0
         5   9.0 160.6  0.23  0.24   16 0.652    4   4.1
         3   6.0 145.9 -2.01 -1.96    7 0.145    0   1.5

PHI:   291.
ETA:   0.30
```

Figure 4.16

The *lego* plot corresponding to the CTC view above, showing the transverse energy deposition in the calorimeter towers.

this analysis jets are defined to be within a cone of radius $R = 0.4$. The algorithm used to cluster jets within a specified cone size is explained in detail in reference [52]. The sum of the individual tower transverse energies in a cone of 0.4 will be referred to as the *raw transverse energy*, E_t^{raw}, of the jet. This will tend to be a low estimate of the initial parton energy for several reasons: (*i*) a fraction of the jet energy may lie outside the cone, referred to as out-of-cone losses, (*ii*) the lack of a uniform response for the boundary regions between calorimeter towers and wedges, (*iii*) the sweeping out of low momentum tracks by the solenoidal field, and, (*iv*) energy that is not detected by the calorimeter due to the presence of muons and neutrinos in the jet. Also effects due to the nonlinearities between calorimeter tower responses, and the contribution from the *underlying event* (energy not associated with the hard parton-parton scattering process, but from the soft interactions between spectator partons in the event), introduce an additional uncertainty in the jet energy measurement. The methods used to determine the extent of these corrections to the jet energy is discussed in references [52, 53].

For this analysis only corrections due to detector effects are applied. Out-of-cone and underlying event corrections are not applied. Jet energies which have been corrected in this fashion will be referred to as *corrected transverse energies*, E_t^{corr}, of the jet. Typically the uncertainty in the jet energy scale is taken to be 10% [52, 53, 5, 54]. The effect of the applied corrections is to increase the jet energy by $\sim$ 30%. It should be noted that the corrections referred to above were developed from QCD jet studies in which the jets predominantly originate from light quarks. However, the fragmentation of heavy quarks (in particular b quarks) is somewhat different than for the lighter quarks [*]. To accommodate this an improved set of corrections was developed for b quarks [5](page 3017). These corrections are of more

---

[*] See, for example, Barger and Phillips, *Collider Physics*, page 177.

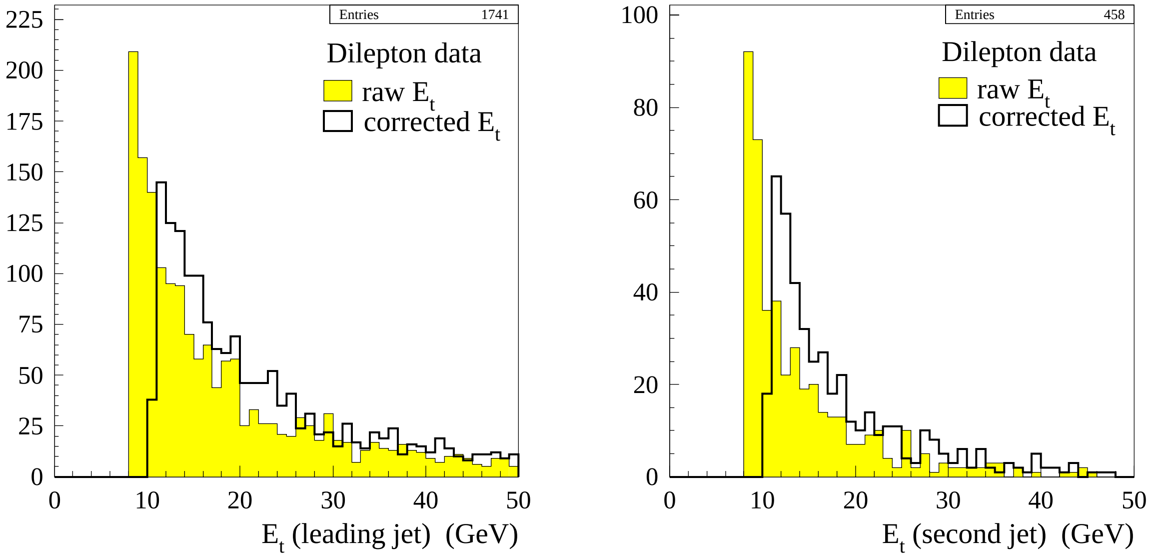

Figure 4.17

Transverse energy distribution of the two highest E_t^{raw} jets in data events that have passed the lepton ID, same-sign, and isolation requirements. The jet E_t^{raw} threshold used was $8\,GeV$.

relevance for a mass analysis where the best possible determination of the jet energy is more important, and are not applied in this analysis.

The effect of applying jet corrections to the jets in the dilepton data is demonstrated in Figure 4.17. The dilepton events used here are those after the lepton ID, same-sign, and isolation cuts, and therefore will be largely Drell-Yan Z^0 events with the jets originating from initial and final state radiation. The jets used in this plot were required to have $E_t^{raw} > 8\,GeV$ and $|\eta_{det}| < 2.4$.

4.10.2 Jet identification

For the purposes of jet counting in a dilepton event the following criteria are

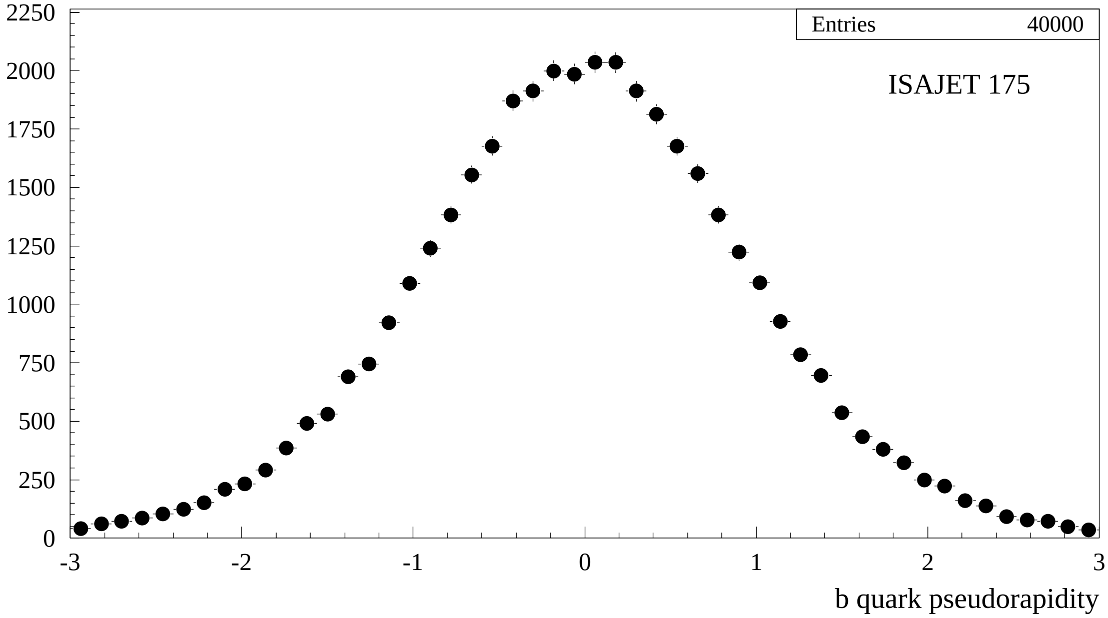

Figure 4.18

Pseudorapidity (η) distribution of b quarks in a Monte Carlo sample of 20 000 $t\bar{t}$ dilepton channel events with $m_{top} = 175\,GeV$. Detector effects and interaction point smearing have not been taken into account.

employed.

- A jet is not considered if it is within a cone of $\Delta R < 0.4$ from any electron passing the TCE or LCE requirements. This is necessary because electrons are also *jet objects* in that they form calorimeter clusters of energy, albeit highly electromagnetic and narrow. There is not the same problem for muons which are minimum ionizing in the calorimeter. This has the implication that real electrons failing the TCE and LCE identification requirements may be counted as jets.
- The jet has a pseudorapidity, as measured from the cluster position with respect to the detector origin (as opposed to the jet direction), of $|\eta_{det}| < 2.0$. Note that this is in slight contrast to the definition of jets used in the $\not{E}_t$ jet correction described in

the previous subsection, which uses jets measured out to a pseudorapidity of ± 2.4. Recall that pseudorapidity is defined as $\eta = -\ln(\tan\frac{\theta}{2})$. Figure 4.18 shows the η distribution expected for b quarks in a Monte Carlo sample of top dilepton events. Detector effects have not been taken into account (which will not have a significant effect on the η distribution), nor has smearing of the interaction point. Nevertheless, it is of interest to observe that at the generator level, $(2.4 \pm 0.1)\%$ of b quarks have $|\eta| > 2.4$, and $(4.3 \pm 0.1)\%$ have $|\eta| > 2.0$, implying the probability that at least one b *jet* fail the η requirement is 0.084 (this should not be used as an estimate of the η effect on the 2-jet efficiency because as shown in Figure 7.4 there is quite a large probability of a third jet in the event).

- The jet has a raw transverse energy of $E_t^{raw} > 10\,GeV$. Jet energy corrections are not used for this cut (though are used in the $\not{E}_t$ correction). Note that this cut would be roughly equivalent to a $13\,GeV$ cut on the corrected transverse energy. Figure 4.19 displays both the raw and corrected jet energy distributions of the leading two jets in a $t\bar{t}$ sample for $m_{top} = 175\,GeV$. For comparison Figure 4.20 shows the momenta distributions of b quarks before detector simulation in $t\bar{t}$ dilepton channel events, showing that the corrected jet energies are a better measure of the original b quark momenta.

4.10.3 The 2-jet cut

With the above jet definitions, dilepton events are required to contain at least 2 jets. This will substantially reduce all major background contributions while preserving $(84 \pm 4)\%$ of $t\bar{t}$ events in the dilepton channel, after all other cuts have been applied, for a top mass of $175\,GeV$ (see section 5.4).

Figures 4.21, 4.22 and 4.23 represent the data after the lepton ID, same-sign, isolation, and invariant mass cuts in the $\Delta\phi(\not{E}_t, \ell\ or\ j) - \not{E}_t$ plane. In each plot the

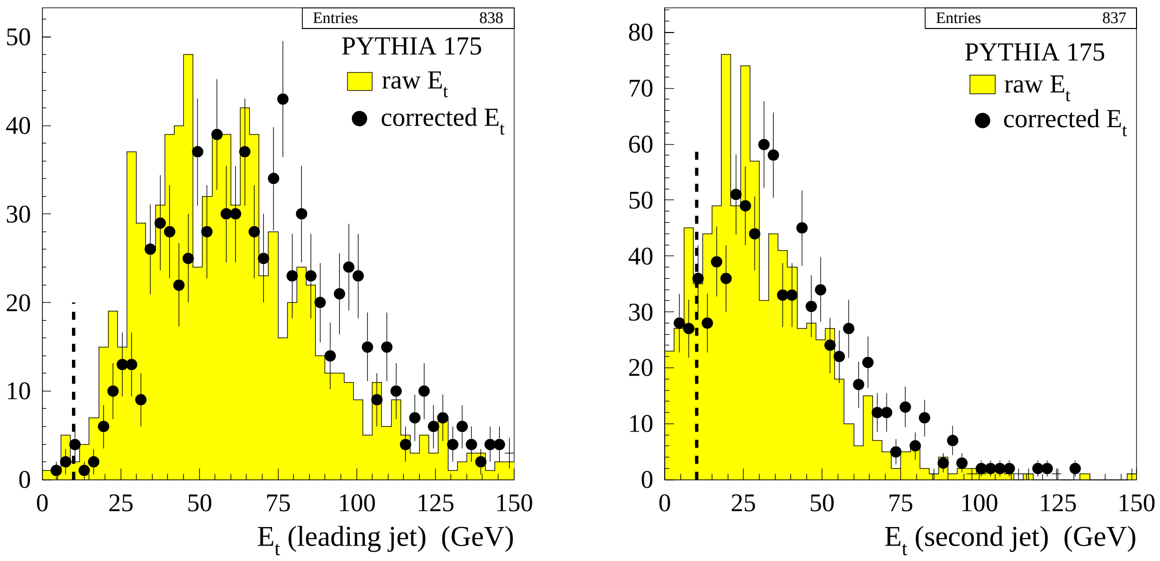

Figure 4.19

Detector simulated transverse energy distributions of the two highest E_t^{raw} jets with $|\eta| < 2.4$ in events that have passed all dilepton selection criteria except the 2-jet cut, in a Monte Carlo sample of 80 000 $t\bar{t}$ events. The dashed lines represent the jet $E_t^{raw} > 10\,GeV$ cut.

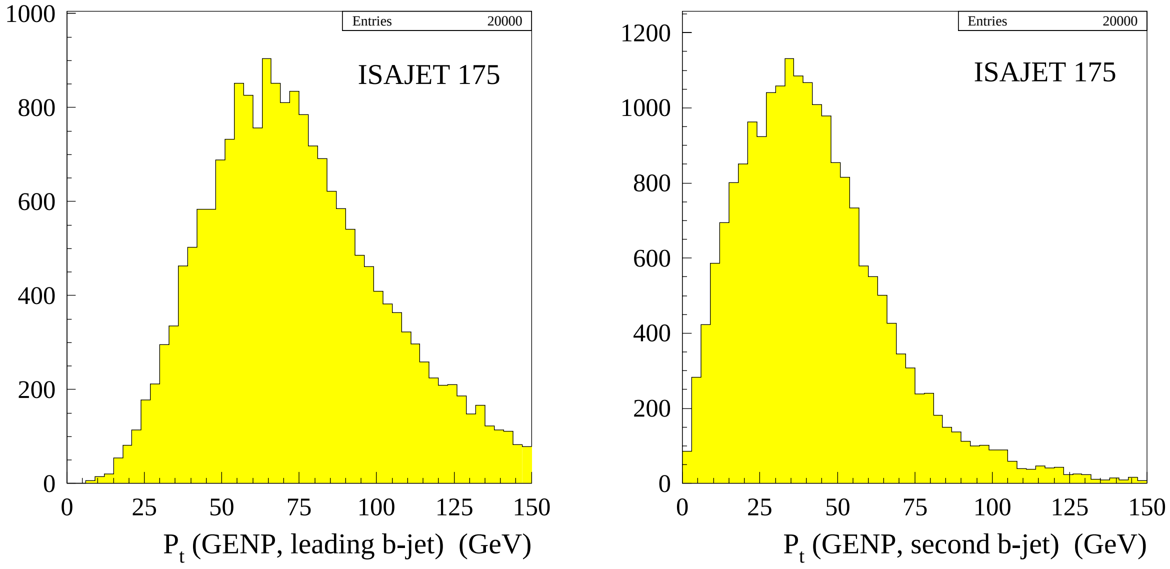

Figure 4.20

Transverse momenta distributions of the two b quarks at the generator level in a Monte Carlo sample of 20 000 $t\bar{t}$ dilepton channel events with $m_{top} = 175\,GeV$.

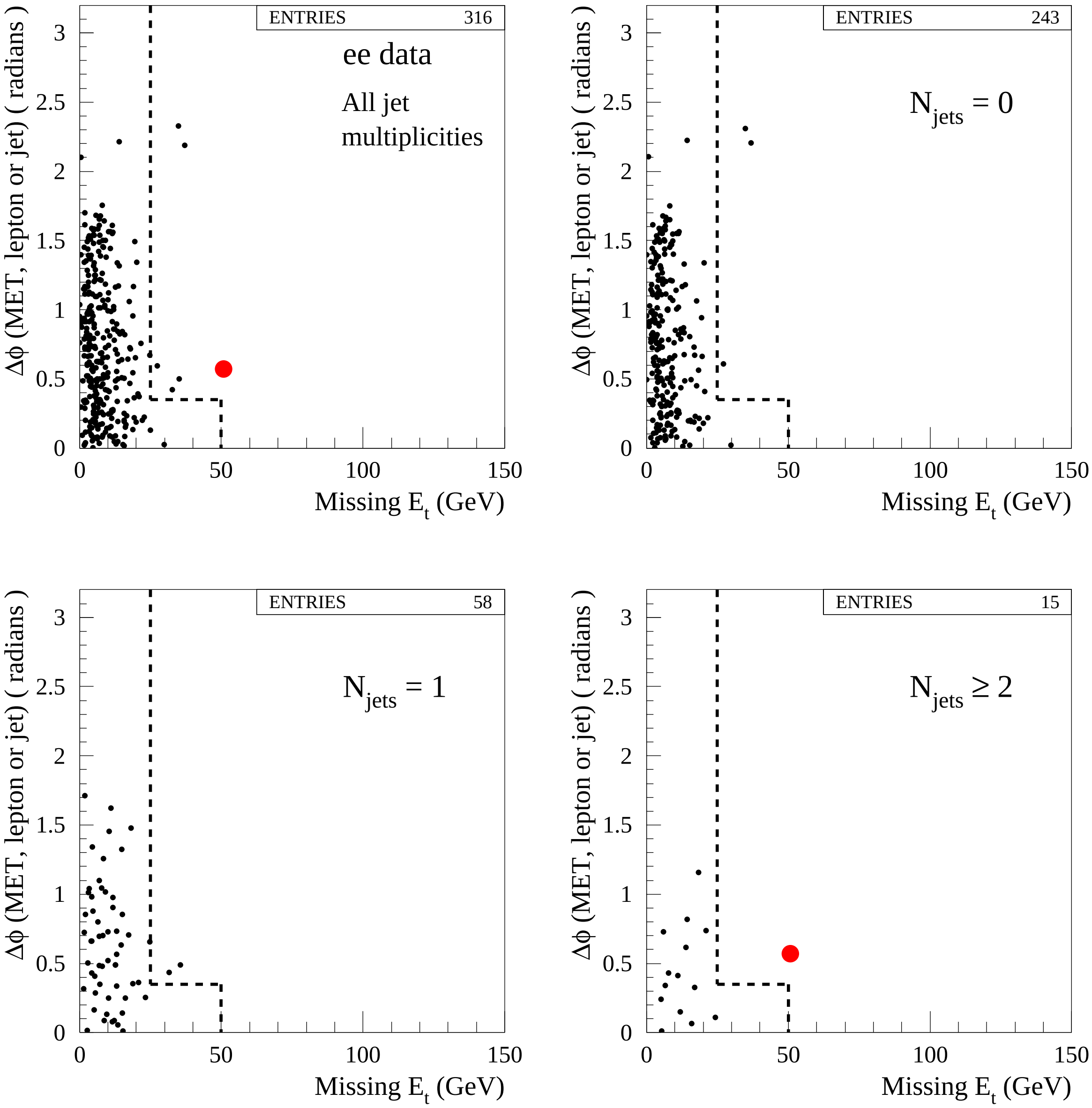

Figure 4.21

Azimuthal angle between the $\not{E}_t$ and the nearest lepton or jet versus the $\not{E}_t$, for $109\,pb^{-1}$ of *ee* data after the lepton ID, same-sign, isolation and invariant mass cuts. The *ee* data has been separated according to jet multiplicity. The dashed lines represent the $\not{E}_t$ magnitude and angular cuts. Candidate events are shown by the larger dots.

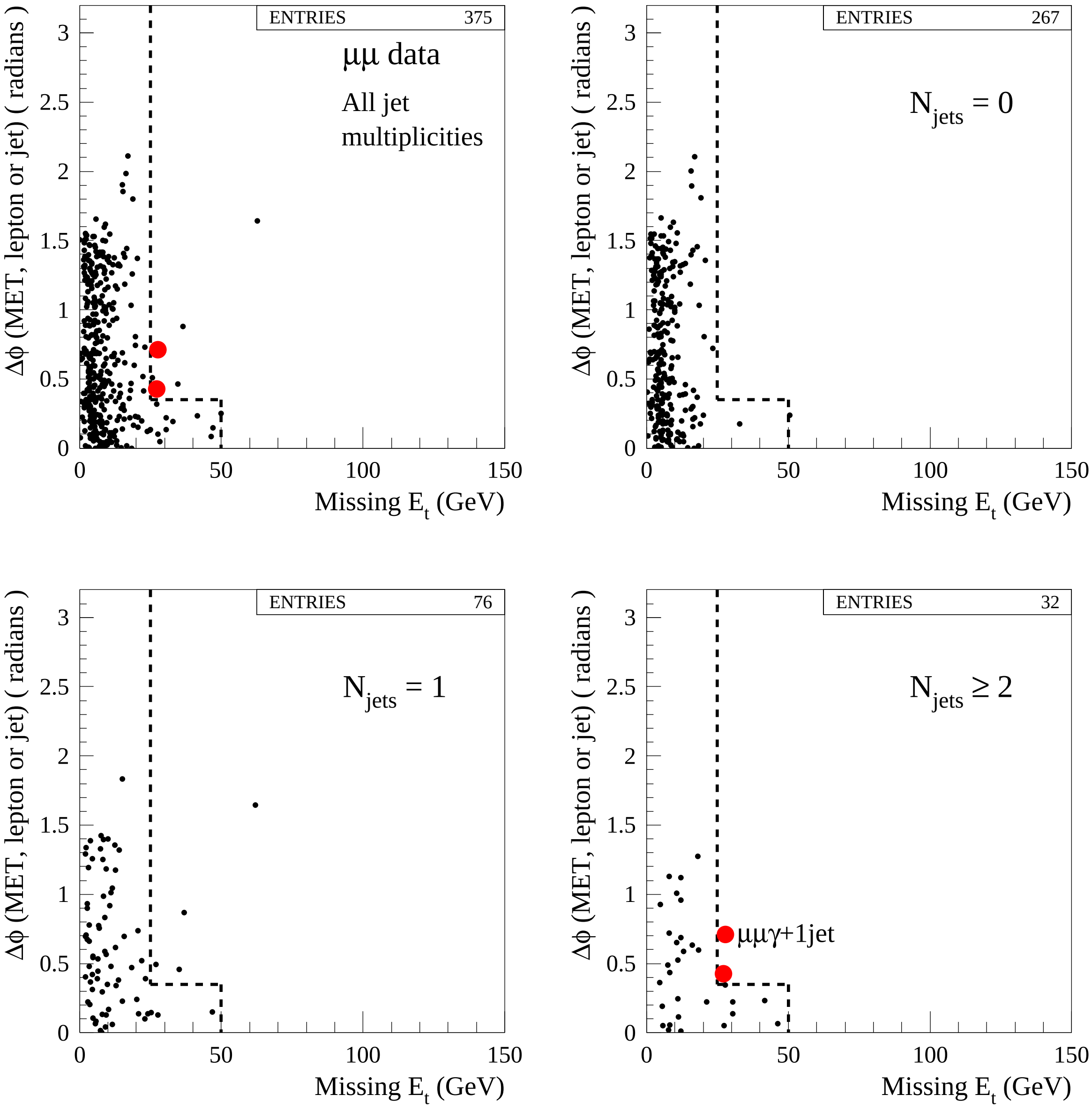

Figure 4.22

Azimuthal angle between the $\not\!\!E_t$ and the nearest lepton or jet versus the $\not\!\!E_t$, for $109\,pb^{-1}$ of $\mu\mu$ data after the lepton ID, same-sign, isolation and invariant mass cuts. The $\mu\mu$ data has been separated according to jet multiplicity. The dashed lines represent the $\not\!\!E_t$ magnitude and angular cuts. Candidate events are shown by the larger dots.

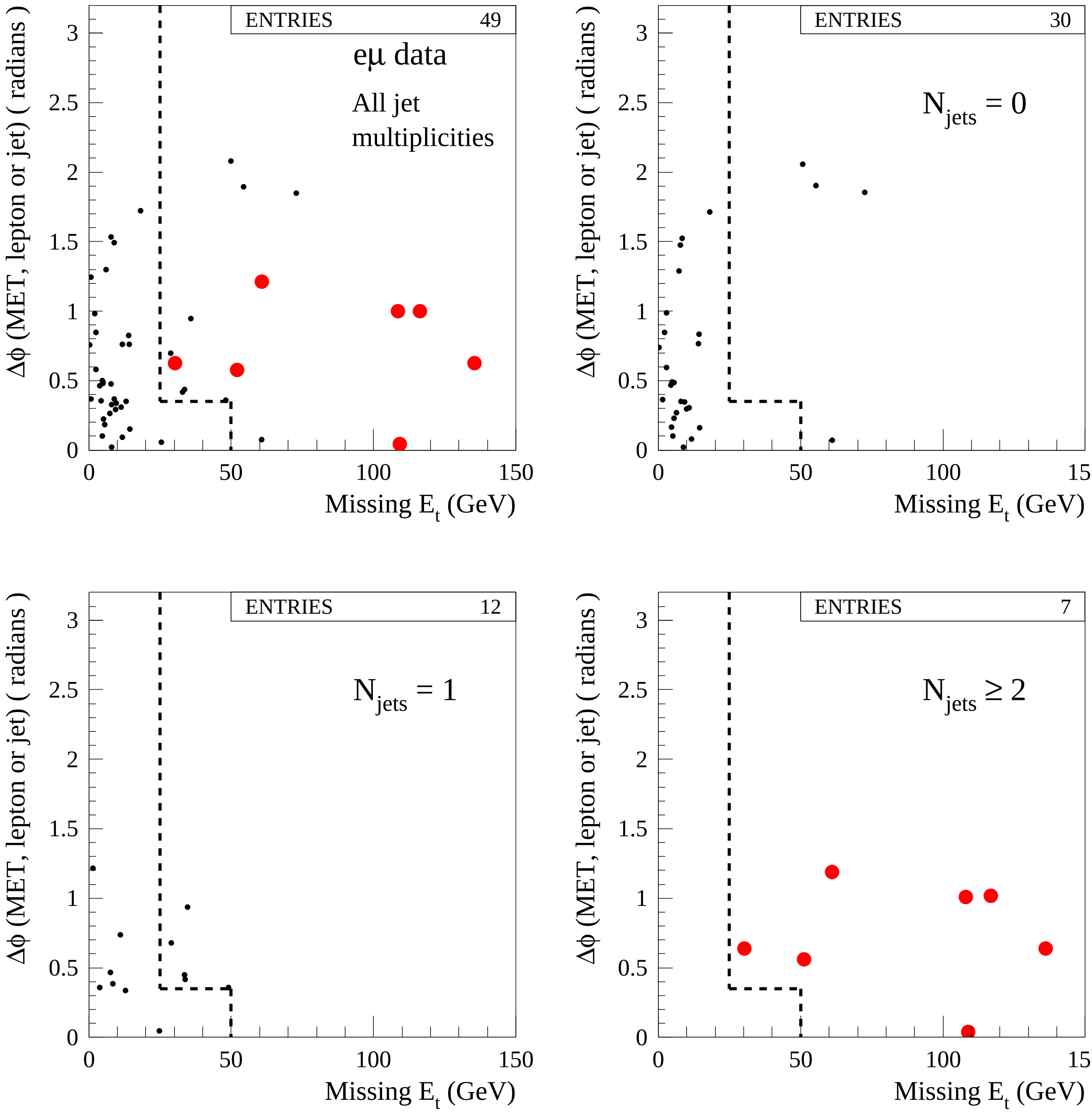

Figure 4.23

Azimuthal angle between the $\not\!\!E_t$ and the nearest lepton or jet versus the $\not\!\!E_t$, for $109\,pb^{-1}$ of $e\mu$ data after the lepton ID, same-sign, isolation and invariant mass cuts. The $e\mu$ data has been separated according to jet multiplicity. The dashed lines represent the $\not\!\!E_t$ magnitude and angular cuts. Candidate events are shown by the larger dots.

signal region is that in the 2-jet bin outside the $\not{E}_t$ cuts represented by the dashed lines. Events in this region are represented by the larger point size. As can be seen, after the 2-jet cut 10 dilepton events remain, 1 ee, 2 $\mu\mu$, and 7 $e\mu$. These are the $t\bar{t}$ dilepton channel candidates in the $109\,pb^{-1}$ of data, and will be discussed in depth in Chapter 7.

4.10.4 The jet vertex requirement

In a $t\bar{t}$ event all leptons and partons are expected to originate from the same vertex (at least within the resolution of the z vertex measurement). Section 4.5 discussed the requirement for the leptons to come from the same event vertex. It is more difficult to precisely determine the z position from which jets originate, but it would be clearly beneficial to additionally require that any jet in the event be consistent with coming from the same vertex as the 2 leptons. This becomes particularly relevant for the high instantaneous luminosities achieved during Run 1B. For example, an instantaneous luminosity of $\sim 2 \times 10^{31}\, cm^{-2}s^{-1}$ implies an average of about 3 interactions per event (or bunch crossing). In such circumstances it is desirable to remove the possibility of 2 separate interactions in the same event creating the signature for $t\bar{t}$ dilepton decay (e.g. 1 interaction producing $Z^0 \rightarrow \ell\ell$, and another a di-jet).

A lot of work still needs to be done in understanding the effect of multiple interactions, and how to best measure the z position of jets, however, for now a somewhat simple method is adopted for requiring jets come from the same vertex as the leptons. This will be improved in future analyses (see Appendix D). The requirement is made just before the 2-jet cut, and simply looks for a loose consistency between the z positions of the jets, and the vertex from which the leptons originate. Jets with $|\eta_{det}| < 2.4$ are required to be within $20\,cm$ of the event vertex of the leptons. Jets are always assumed to come from the best vertex in the event (since they will in general define the vertex with the most tracks), and so it is always events which contain jets and in which the leptons come from a second vertex which are removed by this requirement. This assumption also needs further study. The effect of this requirement will be discussed more in section 6.7.

The $t\bar{t}$ dilepton candidate events (see chapter 7) were all scanned, and found to contain a single vertex from which all leptons and jets originated, so this requirement has no effect on the signal region. However, it has been observed to be important for the understanding of the data in the 0 and 1-jet bins after the $\not{E}_t$ cuts (see section 7.2).

4.11 Trilepton events

Events containing at least 3 leptons passing the identification requirements of sections 4.2 and 4.3 are extremely rare, and so will not be granted a separate category in the data. The dilepton category in which they are put is therefore somewhat arbitrary, however, they will be given special mention in chapter 7. In calculating the $t\bar{t}$ acceptance in the dilepton channel, trilepton events *are* considered a separate category in order to understand how many such events are expected. This will be discussed further in chapter 5.

The next three chapters apply the $t\bar{t}$ dilepton selection, described in this chapter, to; (1) $t\bar{t}$ Monte Carlo events, in order to calculate the $t\bar{t}$ dilepton acceptance for the analysis; (2) the expected sources of background to estimate the level of non-$t\bar{t}$ dilepton contributions, and; (3) the data, to look for an excess of dilepton events over the background that is consistent with a $t\bar{t}$ dilepton signal.

5. DILEPTON CHANNEL ACCEPTANCE

The absolute top acceptance in the dilepton channel, ϵ_{dil}, is defined as the fraction of $t\bar{t}$ events that pass all the dilepton selection cuts. It can therefore be viewed as the probability that any given $t\bar{t}$ event will, (a) produce 2 oppositely charged leptons that pass the fiducial, P_t, lepton identification, isolation and Z^0 mass cuts, (b) produce neutrinos such that the $\not{E}_t$ requirements are satisfied, and (c) produce at least 2 jets passing the jet requirements. In the context of cross-sections, the visible cross-section in the dilepton channel, σ_{dil} (the number of observed $t\bar{t}$ dilepton events divided by the integrated luminosity), is the fraction ϵ_{dil} of the total $t\bar{t}$ cross-section, $\sigma_{t\bar{t}}$ (i.e. $\sigma_{dil} = \epsilon_{dil}\sigma_{t\bar{t}}$). Note that in the above definition, the dilepton acceptance is not calculated relative to the branching ratio of $\frac{4}{81}$, as is sometimes the case. The dilepton acceptance is dominated by events in which both W bosons decay leptonically ($t\bar{t} \rightarrow \ell^+\nu\ell^-\bar{\nu}b\bar{b}$, $\ell = e$ or μ), but also includes contributions from other $t\bar{t}$ decays, most notably from events in which one W boson decays to a τ which subsequently decays leptonically, and also from events in the *Lepton + Jets* channel in which one of the b quarks decays to a high-P_t electron or muon*. The $\ell^+\ell^-$ dilepton signal from $t\bar{t}$ decay can include contributions from W^+W^-, W^+b, $W^-\bar{b}$, $W^+\tau^-$, $W^-\tau^+$, $\tau^+\tau^-$, and $b\bar{b}$.

The dilepton acceptance is required for the calculation of the $t\bar{t}$ cross-section using the dilepton decay channel (see chapter 8). Using $t\bar{t}$ Monte Carlo samples,

---

*Unless explicitly stated otherwise, b decay to a lepton will be taken to imply $b \rightarrow c\ell\nu_\ell$ and/or the cascade decay $b \rightarrow c \rightarrow s\ell\nu_\ell$.

the first step is to calculate the geometrical and kinematical acceptance, $\epsilon_{geom \cdot P_t}$. This is essentially the probability that both leptons pass through the fiducial regions of the detector defined for central electrons and muons, and that each lepton have a transverse momentum, $P_t > 20\,GeV$. This is discussed further in section 5.2. For Monte Carlo events in which these requirements are satisfied, the efficiency of the event triggers ($\epsilon_{trigger}$) and the efficiencies of the dilepton selection cuts (lepton ID, same-sign, isolation, invariant mass, missing E_t, and 2-jet), then determine the total dilepton acceptance, ϵ_{dil}. The dilepton acceptance can be written in terms of these efficiencies:

$$\epsilon_{dil} = \epsilon_{geom \cdot P_t}\, \epsilon_{trigger}\, \epsilon_{ID}\, \epsilon_{SS}\, \epsilon_{iso}\, \epsilon_{mass}\, \epsilon_{\not{E}_t}\, \epsilon_{2-jet} \tag{5.1}$$

Each of the terms in equation 5.1 will be discussed further in the following sections.

5.1 Monte Carlo samples

For the acceptance studies presented here, two main Monte Carlo samples* were used, which will be referred to extensively throughout this chapter.

- A PYTHIA+QFL sample of 80 000 $t\bar{t}$ events [55], with a top mass of $175\,GeV$, was used to calculate the dilepton acceptance for $m_t = 175\,GeV$, and to calculate the various contributions to the acceptance. It was created with no forced decays, that is, both the t and $\bar{t}$ were allowed to decay through any of their decay channels. The default PYTHIA CTEQ2L structure functions were used. This sample will be referred to as the PYTHIA top 175 sample in what follows. This PYTHIA sample was obtained using version 5.6 of the PYTHIA code, which does not include the effects of W polarization from top decay. Version 5.7, which does include these effects, had not been installed at CDF at the time these studies were done. However,

---

*The Monte Carlo generators are discussed in Appendix B.

once version 5.7 was available the dilepton acceptance was recalculated using a sample of 84 000 $t\bar{t}$ PYTHIA v5.7 events with a top mass of $175\,GeV$, and found to be consistent with the v5.6 value (see section 5.4).

- HERWIG+QFL samples at different top masses [56], using MRS D0′ structure functions, were used to calculate the dilepton acceptance as a function of the top mass, and to compare with the PYTHIA result at $m_t = 175\,GeV$. The HERWIG samples were created by requiring at least 2 generator level leptons with $P_t > 18\,GeV$ per event, in order to significantly reduce the sample size. For all HERWIG samples the CLEO QQ Monte Carlo was used to decay bottom and charm particles in the events (see Appendix B).

5.2 Geometrical and kinematical acceptance

The *geometrical and kinematical* acceptance in the dilepton channel, $\epsilon_{geom \cdot P_t}$, is the ratio of dilepton events to the total number of generated $t\bar{t}$ events, in which both leptons have passed following criteria:

- The extrapolated tracks go through the fiducial (or active) regions of the detector (see subsections 4.2.1 and 4.3.1).
- Each ELES bank object[*] has $E_t > 20\,GeV$, and for each CMUO and CMIO bank object[†], $P_t > 20\,GeV$ (beam constrained).
- *Track Quality* cuts are satisfied as explained in Sections 4.2 and 4.3.
- Each Monte Carlo ELES, CMUO and CMIO track must lie within a cone of $\Delta R <$

---

[*] An ELES data bank is generated for every central calorimeter cluster with $E_t > 5\,GeV$ and $E_{HAD}/E_{EM} < 0.125$.

[†] A CMUO data bank is generated for every muon chamber *stub* that is matched to a single track in the central tracking chamber. All tracks above $10\,GeV$ that are not matched become CMIO data banks.

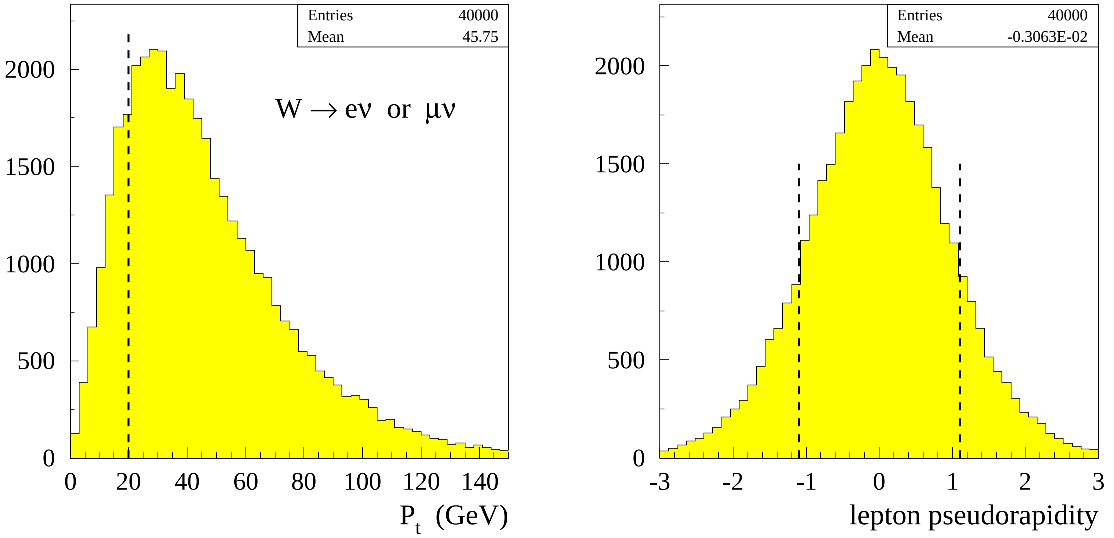

Figure 5.1

Distributions of P_t and η for leptons from W decay in an ISAJET $t\bar{t}$ Monte Carlo sample of 20 000 events, with $m_t = 175\,GeV$. The leptons have not been detector simulated.

0.04 around the momentum direction of a generator level (GENP) electron or muon, where $\Delta R = \sqrt{\Delta\eta^2 + \Delta\phi^2}$.

- The photon conversion removal algorithm used in the data (see section 4.2) is applied to electrons. and the cosmic ray removal algorithm (see section 4.3) applied to muons.

That is, $\epsilon_{geom \cdot P_t}$ is the acceptance before the lepton identification requirements have been imposed. It will be shown that after all dilepton selection cuts, about 86% of the acceptance comes from both W bosons decaying leptonically. Therefore, to get a better feeling for $\epsilon_{geom \cdot P_t}$, consider Figure 5.1 which shows the P_t and η distributions for leptons from the decay of W bosons in $t\bar{t}$ events ($m_t = 175\,GeV$), before detector simulation. The probability for a given generator level lepton from a W to pass the P_t requirement is about 0.85, and the probability to be in the $|\eta| < 1.1$ region* is about 0.75. Therefore, given the branching ratio for $WW \rightarrow \ell\nu\ell\nu$ of $\frac{4}{81}$, the percentage of $t\bar{t}$ events in which both W bosons decay to leptons that pass the geometrical and P_t requirements, is roughly 2% ($\frac{4}{81} \times (0.85)^2 \times (0.75)^2$), assuming no correlation between P_t and η of the leptons). This is a somewhat cursory estimate for $\epsilon_{geom \cdot P_t}$ for the $t\bar{t} \rightarrow WWb\bar{b} \rightarrow \ell\nu\ell\nu b\bar{b}$ decay channel, but gives the essential meaning behind the calculation lest it get mired in the details that follow. As will be shown, after only these geometrical and P_t requirements a significant contribution (about half) to $\epsilon_{geom \cdot P_t}$ for the dilepton channel comes from the situation in which one W decays hadronically, with the second lepton coming from b decay. However, after imposing the lepton ID cuts this contribution is drastically reduced. This is discussed further below.

The matching requirement of a fully simulated lepton (that is, one for which an ELES, CMUO or CMIO bank has been created after the event has been run through the detector simulation, QFL), to a GENP lepton is very efficient as shown in Figure 5.2. The distributions in this figure come from leptons in the PYTHIA top 175 sample (see section 5.1) that are in the fiducial region with at least $20\,GeV$ of transverse energy. The long tail in the ΔR distribution for central electrons is due to both the effect of bremsstrahlüng radiation on the electron direction (affects roughly 20% of electrons), and also due to the small fraction of jets in the events that pass the requirements for the formation of an ELES bank, and hence will not be matched to a GENP electron. The latter effect extends the tail all the way out

---

*This is roughly the detector η region for central leptons, ignoring the inactive regions between detector components.

to $\Delta R \sim \pi$.

The transverse energy distributions of leptons in $t\bar{t}$ events are shown in Figures 5.3 and 5.4. The distributions are from the PYTHIA sample mentioned above. Four sources of leptons in $t\bar{t}$ events are considered separately : leptonic decay of a W boson ($W \rightarrow \ell\nu_\ell$, $\ell = e$ or μ); $W \rightarrow \tau\nu_\tau$ followed by leptonic τ decay; semi-leptonic b decay ($b \rightarrow \ell\nu_\ell c$); and, $b \rightarrow c$ followed by semi-leptonic charm decay. For all leptons in the fiducial region and for which a generator level (GENP) lepton is matched with a fully simulated lepton, both the GENP lepton transverse energy and the fully simulated lepton transverse energy are plotted. The E_t and P_t cut at $20\,GeV$ is placed on the latter.

There are some notable differences between the electron E_t and muon P_t distributions when the leptons are not from W decay. First note that for each lepton for which the transverse energy is plotted, both a reconstructed lepton data bank (ELES, CMUO or CMIO), and a corresponding generator level lepton must exist. The requirement for the creation of an ELES bank of $E_{HAD}/E_{EM} < 0.125$, greatly reduces the number of electrons in the detector simulated $t\bar{t}$ sample that are not isolated, that is, for which the surrounding jet activity significantly contributes to the hadronic energy in the electron calorimeter cluster. This is most often the case for electrons from b and c decay, as is reflected in the difference between the number of entries in the plots of Figures 5.3 and 5.4. To a much lesser extent this also affects the lower energy electrons from W and τ decay. Muons are not affected because simulated muon data banks at most require a muon chamber *stub* to match to a track in the central tracking chamber. Hence the muon energy spectra are more representative of the distributions expected from leptons in $t\bar{t}$ events before detector simulation. Note also the shift in the detector simulated energies of electrons from b and c decay due to their non-isolation, from jets which contribute mostly

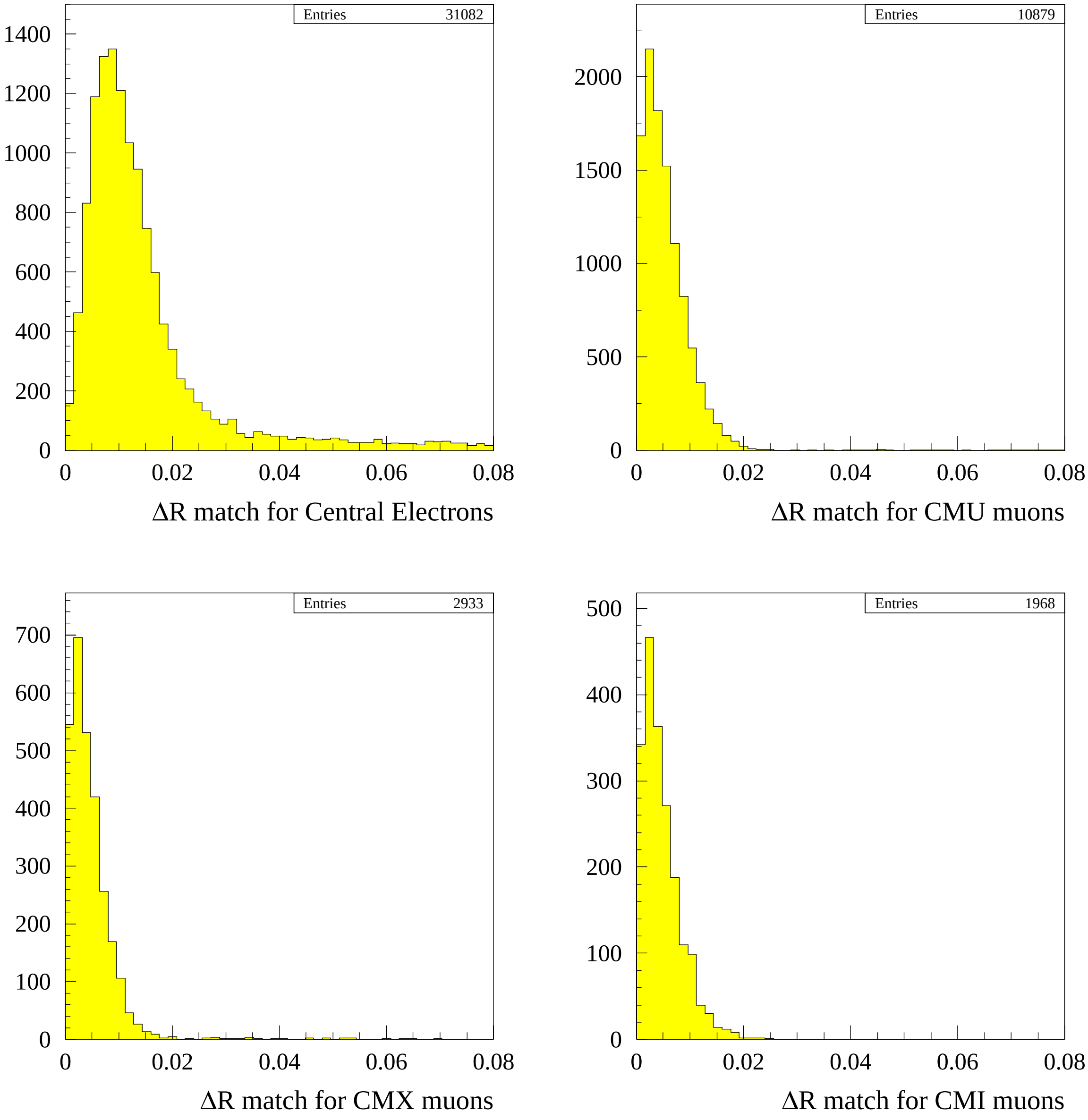

Figure 5.2

Distributions of ΔR between fully simulated leptons and generator level leptons.

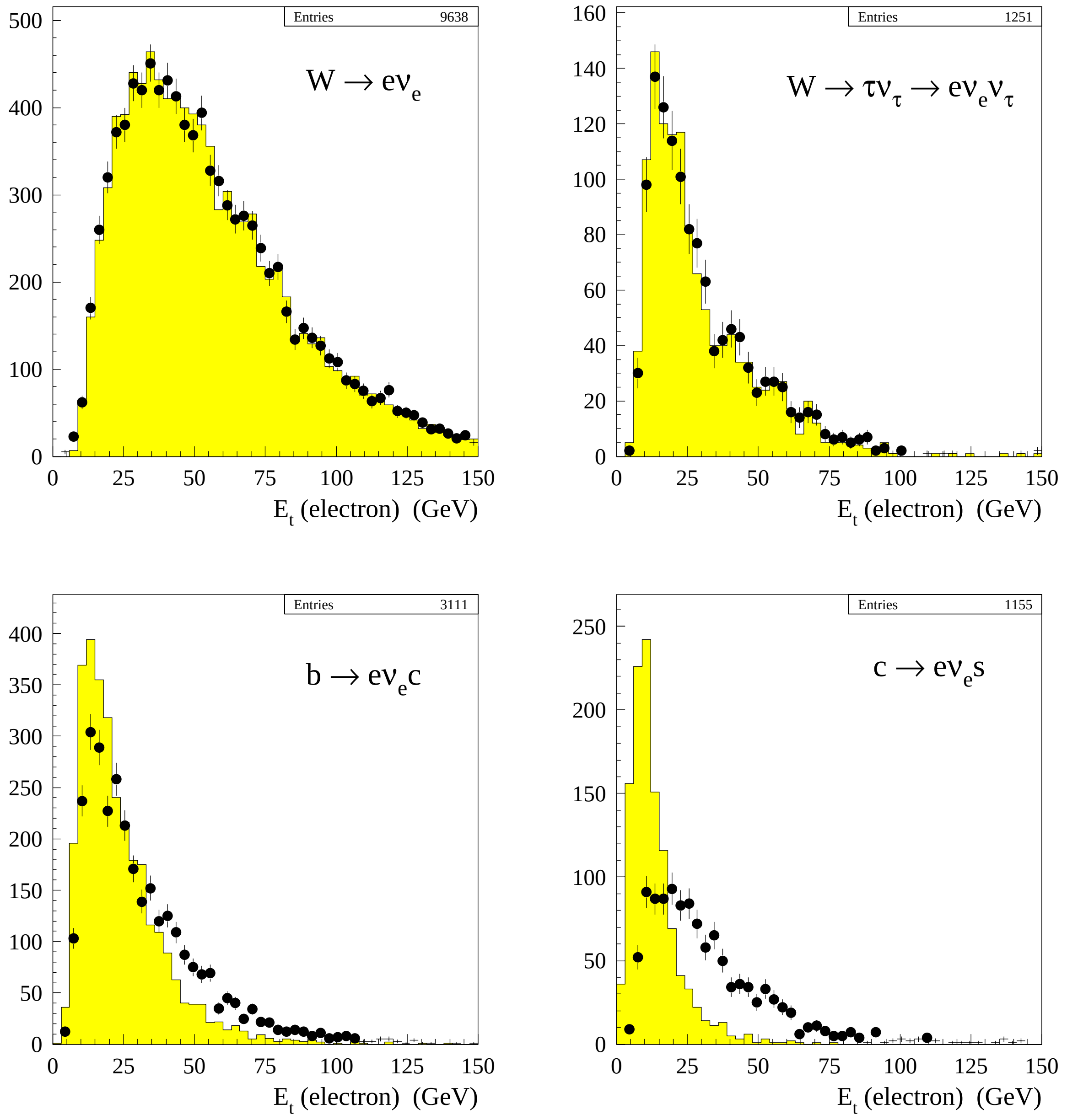

Figure 5.3

Transverse energy distributions for electrons in a $t\bar{t}$ Monte Carlo sample with $m_t = 175\,GeV$, that are in the fiducial region and have satisfied the GENP matching requirement. Shown is the generator level (GENP) E_t (histogram) and the detector reconstructed E_t (points), for the 4 main sources of electrons in $t\bar{t}$ events.

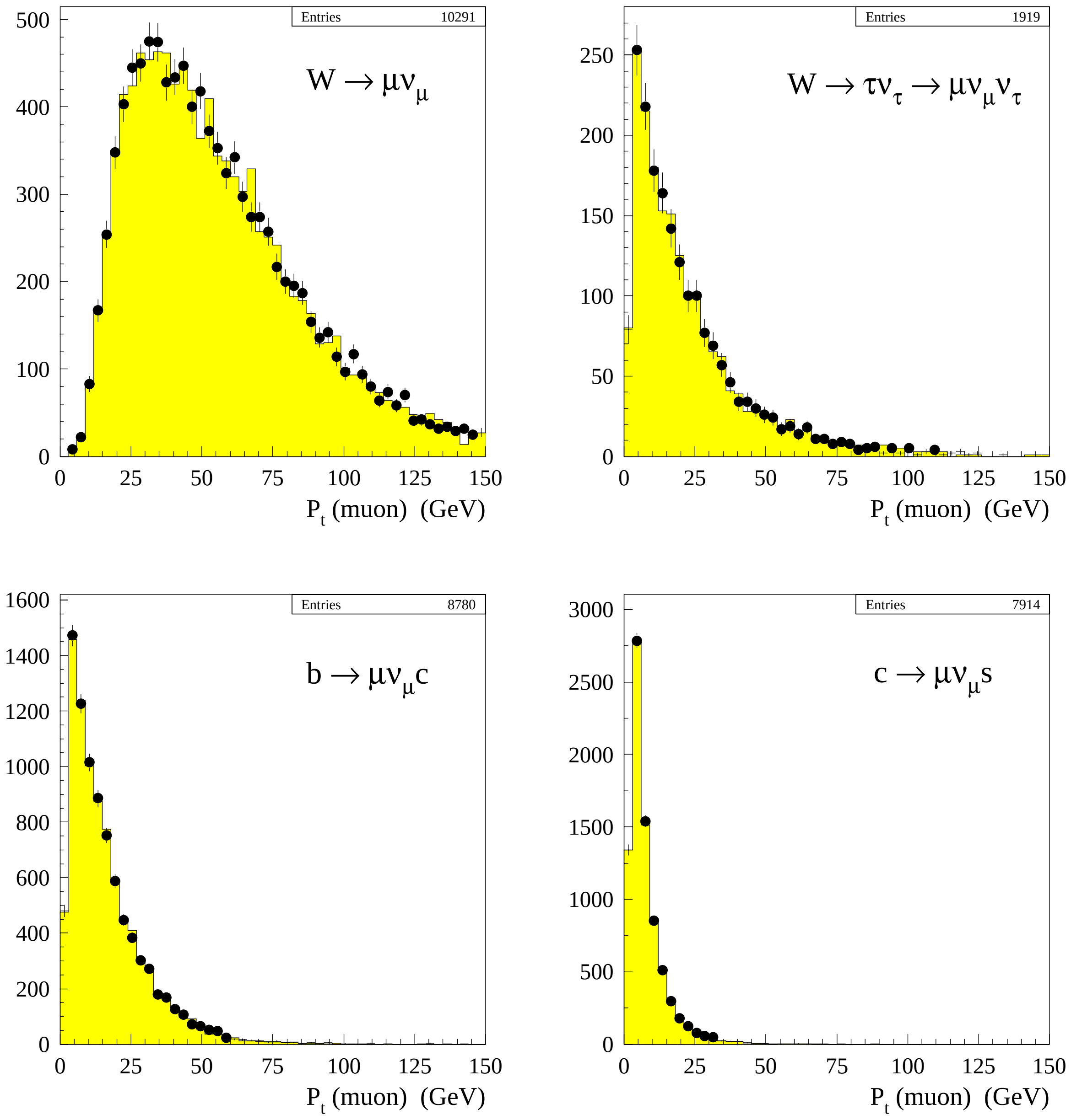

Figure 5.4

Transverse momentum distributions for muons in a $t\bar{t}$ Monte Carlo sample with $m_t = 175\,GeV$, that are in the fiducial region and have satisfied the GENP matching requirement. Shown is the generator level (GENP) P_t (histogram) and the detector reconstructed P_t (points), for the 4 main sources of muons in $t\bar{t}$ events.

electromagnetic energy to the electron cluster.

The P_t and E_t cut at $20\,GeV$ is designed to be efficient for leptons from W decay, while reducing the backgrounds from low P_t dilepton sources (for example $p\overline{p} \rightarrow b\overline{b}$). As Figures 5.3 and 5.4 show, this cut is also effective in reducing the contribution to the dilepton acceptance from $t\overline{t}$ events in which one lepton is not from W decay.

The geometrical and kinematical acceptance results for a top mass of $175\,GeV$ from the aforementioned PYTHIA (80 000 events) and HERWIG (130 000 events) $t\overline{t}$ Monte Carlo samples are as follows (errors are statistical only).

	$\epsilon_{geom \cdot P_t}$	$\epsilon_{geom \cdot P_t}$ relative to the BR $\frac{4}{81}$
PYTHIA top 175	$(3.56 \pm 0.07)\%$	$(72.1 \pm 1.4)\%$
HERWIG top 175	$(2.91 \pm 0.05)\%$	$(58.9 \pm 1.0)\%$

These results were calculated before the application of the muon trigger simulation to the event. After applying the trigger simulation, which gives a trigger efficiency, $\epsilon_{trigger}$, of about 0.95 (see below), the PYTHIA and HERWIG values for $\epsilon_{geom \cdot P_t}$ are $(3.34 \pm 0.06)\%$ and $(2.77 \pm 0.05)\%$ respectively. There are two main reasons for the difference between the PYTHIA and HERWIG results [*]. The lepton E_t and P_t spectra are somewhat softer in HERWIG, particularly from b decay, giving a lower acceptance from the transverse energy requirements. The second reason is somewhat artificial, being caused by the method in creating the HERWIG samples. As mentioned above these samples are created with the requirement that each event have at least 2 leptons with GENP $P_t > 18\,GeV$. However, it is possible that electrons from b or c decay with $P_t < 18\,GeV$ will have a fully simulated

---

[*] A possible third reason that has not yet been fully investigated is the fact that the PYTHIA sample does not include polarization of W bosons from top decay, whereas the HERWIG sample does.

energy of $E_t > 20\,GeV$ as a result of contributions to the electron CEM cluster energy from other nearby jet activity (as discussed above and seen in Figure 5.3). Such electrons are not likely to pass the tight lepton identification requirements, and so the HERWIG sample selection will not affect the final dilepton acceptance result. This was verified by applying a $P_t > 18\,GeV$ cut on all GENP leptons in the PYTHIA sample. The geometrical and kinematical acceptance was reduced by 7%, to $(3.30 \pm 0.07)\%$, and the total dilepton acceptance ϵ_{dil} (see following sections) was unchanged. Therefore, this only need be kept in mind for the HERWIG results at the geometrical and kinematical level; the differences in $\epsilon_{geom \cdot P_t}$ between HERWIG and PYTHIA do *not* significantly manifest themselves in the overall acceptance results.

As mentioned before, although most of the dilepton acceptance, $\epsilon_{geom \cdot P_t}$, is due to events in which both W bosons decay leptonically, a significant part is due to $t\bar{t}$ events in which one lepton is from a W decay with the second from a b quark decay. Table 5.1 gives the relative contributions from all the possible sources to $\epsilon_{geom \cdot P_t}$, separately for the ee, $\mu\mu$ and $e\mu$ channels. These results are also displayed graphically in Figure 5.11 together with the contributions to the total dilepton acceptance, ϵ_{dil}. The $lepton + jet$ channels are denoted by ejj, μjj and τjj, with the special case in which one of the leptons comes from direct b decay given as a subset to these. In the $lepton + jet$ events where the second lepton does not come from a b decay (that is, in the differences between the $WW \rightarrow \ell jj$ and $WW \rightarrow \ell jj (b \rightarrow \ell)$ contributions to the acceptance), it almost always comes from a charm decay. Section 5.4 gives further details on the dilepton acceptance before the lepton identification cuts have been applied, in particular the dependence on top mass.

Finally, a note on the photon conversion and cosmic ray removal algorithms used.

$t\bar{t}$ dilepton source : $WW \rightarrow$	Dilepton Category (after Geom/P_t cuts only)		
	ee	$\mu\mu$	$e\mu$
ee	$44 \pm 3\%$	0	$1.0 \pm 0.3\%$
$\mu\mu$	0	$49 \pm 3\%$	$0.7 \pm 0.2\%$
$\tau\tau$	0	$0.4 \pm 0.2\%$	$0.5 \pm 0.2\%$
$e\mu$	$1.6 \pm 0.6\%$	$1.7 \pm 0.5\%$	$49 \pm 2\%$
$e\tau$	$9.6 \pm 1.4\%$	0	$5.6 \pm 0.7\%$
$\mu\tau$	0	$12.2 \pm 1.3\%$	$5.6 \pm 0.7\%$
ejj	$37 \pm 3\%$	$0.4 \pm 0.2\%$	$16 \pm 1\%$
μjj	$1.0 \pm 0.4\%$	$31 \pm 2\%$	$17 \pm 1\%$
τjj	$2.9 \pm 0.7\%$	$3.1 \pm 0.7\%$	$2.7 \pm 0.5\%$
$ejj\ (b \rightarrow e)$	$26 \pm 2\%$	$0.4 \pm 0.2\%$	$13 \pm 1\%$
$\mu jj(b \rightarrow \mu)$	$1.0 \pm 0.4\%$	$25 \pm 2\%$	$11 \pm 1\%$
$\tau jj(b \rightarrow \tau)$	$2.5 \pm 0.7\%$	$2.5 \pm 0.6\%$	$2.1 \pm 0.4\%$
$jjjj$	$3.3 \pm 0.8\%$	$1.8 \pm 0.5\%$	$2.4 \pm 0.4\%$

Table 5.1

Relative acceptances to the $t\bar{t}$ dilepton signal (for the ee, $\mu\mu$ and $e\mu$ categories separately) from the various top decay modes ($WW \rightarrow ee, \mu\mu, ...$), after only the geometrical and P_t requirements, using the PYTHIA top 175 Monte Carlo sample. Errors are statistical only.

The cosmic ray removal algorithm decreases the acceptance in the $\mu\mu$ channel only, by less than 0.5% (using an average from the PYTHIA and HERWIG samples at $m_t = 175\,GeV$), and so will not be considered further in the following discussions on the acceptance. The photon conversion removal algorithm has somewhat more of an effect, which contributes to the systematic error estimate for the total acceptance. As such, it will be discussed quantitatively in section 5.5.

5.3 Applying lepton ID cuts

If one had a perfect Monte Carlo simulation of the detector response to the particles passing through it, then the dilepton acceptance would simply be calculated from running the $t\bar{t}$ Monte Carlo samples through the dilepton analysis and counting the number of events that pass. However, the Monte Carlo detector simulation (QFL) does not model every lepton identification variable sufficiently well to enable one to do this. Table 5.2 gives the lepton identification efficiencies from Run 1B $Z^0 \rightarrow \ell\ell$ data, and from ISAJET+QFL $Z^0 \rightarrow \ell\ell$ Monte Carlo (100 000 events), to illustrate the difference between the data and the Monte Carlo. The method for calculating the efficiencies, using $Z^0 \rightarrow \ell\ell$ events, is discussed in Appendix A. A dilepton invariant mass window of $80 < M_{\ell\ell} < 100\,GeV$ was used in selecting Z^0 events for the efficiency calculations. The efficiencies from Z^0 data are discussed in section 4.4. The Monte Carlo Z^0 efficiencies were calculated after the geometrical and kinematical requirements listed in section 5.2.

The number of Monte Carlo $t\bar{t}$ events passing the dilepton analysis could be scaled by the appropriate ratios of efficiencies from Table 5.2 to roughly account for the difference in data and Monte Carlo lepton efficiencies. However, this would neglect the fact that the efficiencies were calculated using leptons from Z^0 decay, whereas leptons in $t\bar{t}$ events typically result from the decay of W bosons, b quarks,

Lepton Type	Lepton Efficiencies, ϵ_{ID}	
	Data	Monte Carlo
TCE	0.818 ± 0.009	0.892 ± 0.003
LCE	0.889 ± 0.007	0.936 ± 0.003
TCM	0.922 ± 0.009	0.978 ± 0.002
CMX	0.914 ± 0.010	0.972 ± 0.002
CMI	0.913 ± 0.013	0.962 ± 0.003

Table 5.2

Lepton identification efficiencies from $Z^0 \rightarrow \ell\ell$ Run 1B data, and ISAJET+QFL Monte Carlo.

or τ's. It would also neglect the effect of the jet activity in the event on the lepton efficiency. The jet activity in $t\bar{t}$ events is very different than in Z^0 events. Higher jet activity decreases the chances of a lepton being isolated, and non-isolated leptons have a lower detection efficiency (see below). In addition the $Z^0 \rightarrow \ell\ell$ Monte Carlo sample does not replicate the jet activity seen in the data, which would affect the comparison of the numbers in Table 5.2. In order to alleviate the concern of jet activity, the lepton efficiencies from Z^0 data and Monte Carlo are calculated and compared for 3 different isolation bins. This is shown in Figure 5.5. The method for calculating these efficiencies is discussed in Appendix A (section A.2). The efficiencies calculated are those *after* the isolation requirement. The discrepancy between data and Monte Carlo is greatest for non-isolated leptons, which will mostly affect leptons from b and c decays. The detection efficiencies for CMI muons were not calculated as a function of isolation as for the other lepton types, because isolation is part of the CMI identification (see section 4.3), implying only the first 2 isolation bins would be relevant. Therefore, without loss of precision, all CMI muons use the same efficiency comparison independent of isolation, that is, the numbers from Table 5.2.

As mentioned above, a Z^0 mass window of width $20\,GeV$ (about $\pm 2\sigma$) was used in calculating the efficiencies. This was made narrow in order to reduce the background under the Z^0 peak, which was expected to be greatest for Z^0 events with non-isolated leptons. To check the effect of the Z^0 window width, the efficiencies were recalculated using the narrower mass window $85 < M_{\ell\ell} < 95\,GeV$. In the first 2 isolation bins ($0 < I_{cal} < 0.02$ and $0.02 < I_{cal} < 0.1$), the isolated lepton efficiencies agreed to within $\sim 1\%$, and in the last isolation bin ($I_{cal} > 0.1$) the non-isolated lepton efficiencies increased by $\sim 5\%$, but were still well within the statistical errors.

The prescription for applying the correct lepton ID efficiencies to leptons in $t\bar{t}$ Monte Carlo samples is therefore as follows. Each lepton is passed through the same lepton selection as is used for the data (sections 4.2 and 4.3), and the calorimeter isolation for each lepton is determined. Each lepton is then assigned a scale factor, $s(type,\, I_{cal})$, depending on its type (TCE, LCE, TCM, CMX or CMI) and isolation, which is simply the data to Monte Carlo ratio of efficiencies in the isolation bins of Figure 5.5. If a dilepton event passes all the dilepton analysis cuts it is then assigned a weight, $w = s(lepton\,1,\; I_{cal}) \times s(lepton\,2,\; I_{cal})$. The dilepton acceptance is finally calculated using the weighted number of dilepton events passing all cuts (see section 5.4). The effect of scaling the Monte Carlo lepton efficiencies to those

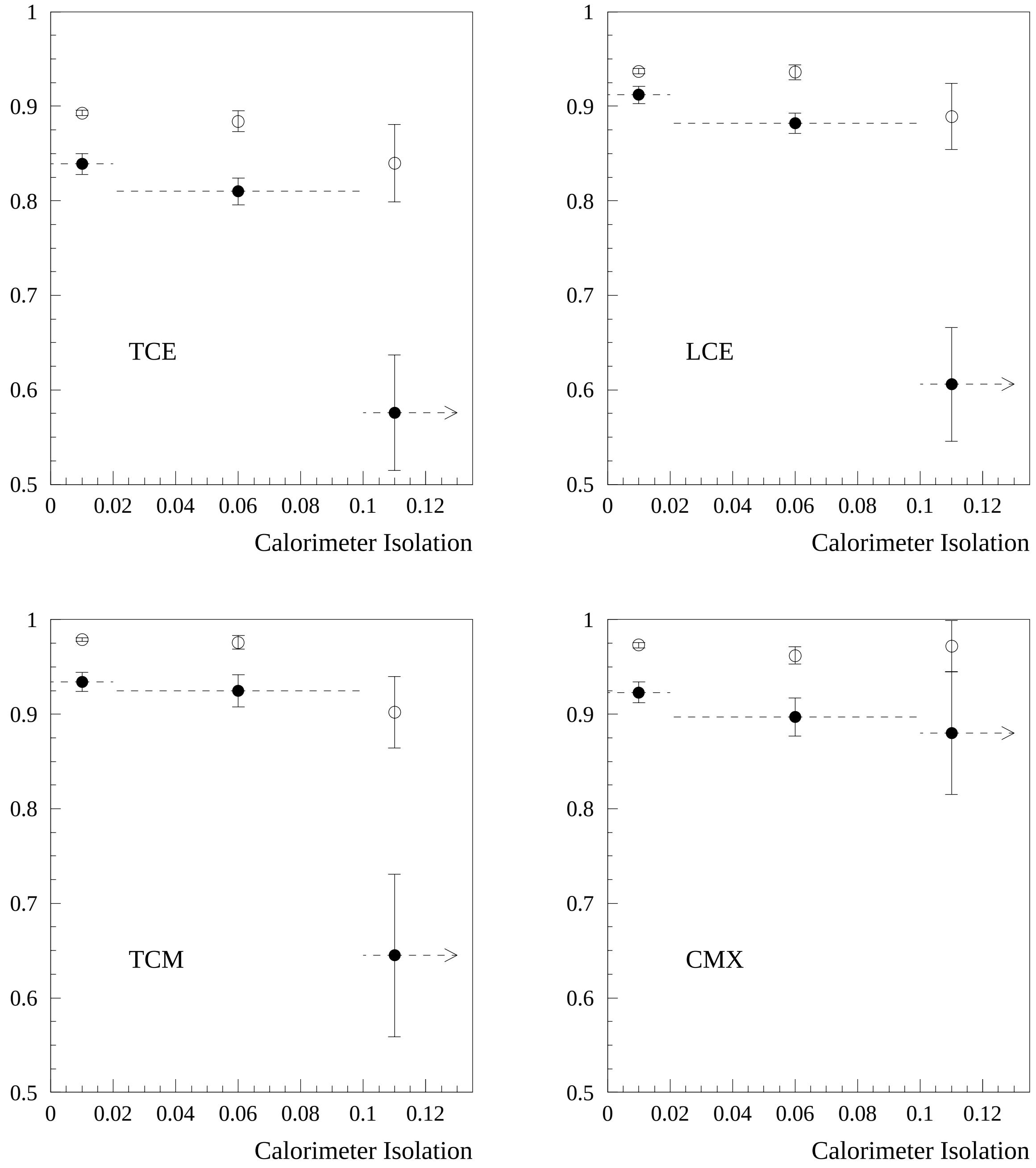

Figure 5.5

TCE, LCE, TCM and CMX identification efficiencies versus calorimeter isolation from $Z^0 \rightarrow \ell\ell$ data (closed points) and Monte Carlo (open points). The dashed lines represent the 3 isolation bins used, with the last point representing non-isolated ($I_{cal} > 0.1$) leptons. The error bars are statistical only.

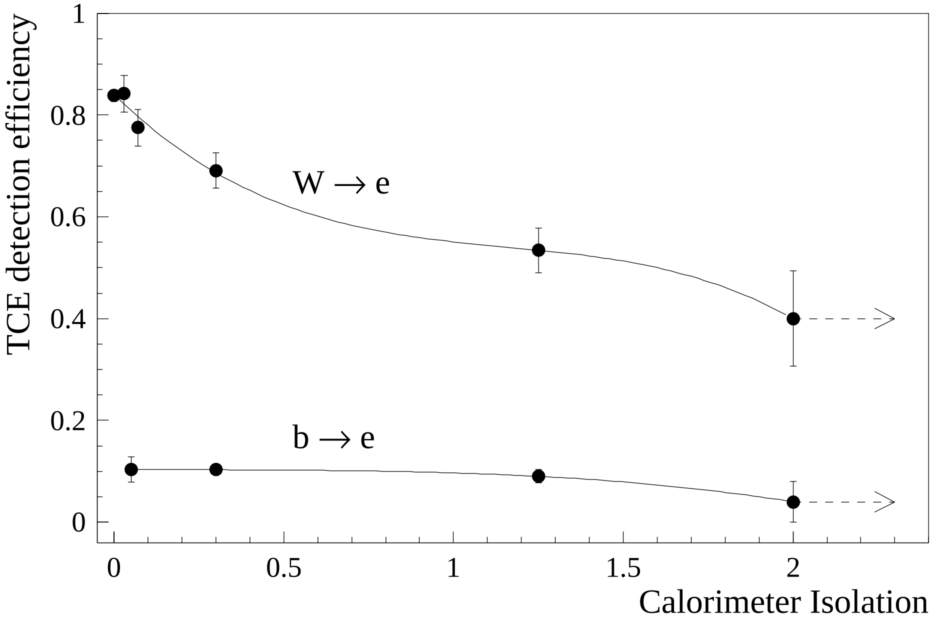

Figure 5.6

Efficiencies for Tight Central Electrons (TCE) from the decay of W's and b's ($b \rightarrow e\nu_e c$ only) in $t\bar{t}$ Monte Carlo events as a function of isolation.

measured in the data, is to reduce the overall dilepton acceptance by about 13%.

This method still neglects the effect on the efficiencies from the source of leptons. Figure 5.6 shows the considerable difference in the efficiencies as a function of isolation for TCE electrons from W's and b's in $t\bar{t}$ events. Note the difference in scale between this figure and Figure 5.5 (there were not enough statistics from non-isolated leptons in the Z^0 sample to make a similar plot for Z^0). Essentially, the difference is due to the very different physics reasons that leptons from W's and b's are non-isolated. A lepton from W decay will generally be non-isolated because of one or two tracks from a nearby jet entering the 0.4 cone around the lepton direction without significantly disrupting the lepton identification variables. Whereas leptons from b decays are generally immersed in the b jet itself, with many close tracks disrupting the clean identification of the lepton. Leptons in Z^0 events will be non-isolated for similar reasons to the W's in $t\bar{t}$ events, that is, because of spurious tracks from an uncorrelated jet. Therefore, since most of the leptons in $t\bar{t}$ events will come from W decay, the scaling factors obtained from the Z^0 events are expected to give a good approximation to reality. The assumption that the same scaling factors also apply for leptons from τ, b, and c decay introduces a systematic error discussed in section 5.4.

5.4 Acceptance results and dependence on top mass

The PYTHIA top 175 sample was run through the dilepton analysis with the results for each dilepton category (see section 4.5) given in Table 5.3. Trilepton events are treated as a separate category, but if only two of the three leptons pass the lepton ID cuts, then the event is put into the appropriate dilepton category. The events that pass the missing transverse energy ($\not{E}_t$) cuts (subsection 4.4.4) are segregated according to jet multiplicity. The dilepton analysis requires at least two jets with $E_t^{raw} > 10\, GeV$ and $|\eta| < 2.0$ (see section 4.10). The final column is the number of 2-jet events corrected for lepton ID efficiency differences between Monte Carlo and data (see Figure 5.5) as discussed in the previous section. This last column represents the expected number of dilepton candidates from $t\bar{t}$ Monte Carlo with a top mass of $175\, GeV$.

The first column of numbers, those dilepton events passing the geometrical and kinematical requirements discussed in section 5.2, include the effect of the trigger efficiency, $\epsilon_{trigger}$, in that the muon trigger simulation [57] has been applied. The effect of the electron trigger efficiencies in dilepton events has been neglected, since

	Dilepton Cut						$N_j(> 10\,GeV)$			
Category	Geom/P_t	lepton ID	Same-Sign	Isolation	Z^0 mass	$\not{E}_t$	0	1	≥ 2	
TCE-TCE	512	212	202	192	142	111	2	17	92	79.1
TCE-LCE	0	33	25	21	11	9	0	3	6	5.2
ee	512	245	227	213	153	120	2	20	98	84.2
TCM-TCM	400	215	204	192	151	107	0	12	95	82.9
TCM-CMX	159	97	92	88	64	51	0	10	41	35.7
CMX-CMX	30	15	14	14	10	7	0	0	7	6.2
TCM-CMI	97	77	75	70	54	35	0	5	30	27.1
CMX-CMI	26	18	16	16	14	10	0	1	9	8.1
$\mu\mu$	712	422	401	380	293	210	0	28	182	160.0
TCE-TCM	914	438	425	412	412	313	5	44	264	225.9
TCE-CMX	237	122	116	112	112	84	2	11	71	61.8
TCE-CMI	161	92	90	84	84	65	1	6	58	51.8
TCM-LCE	0	48	39	33	33	29	0	5	24	21.2
CMX-LCE	0	8	7	5	5	4	0	1	3	2.4
$e\mu$	1312	708	677	646	646	495	8	67	420	363.2
$\ell\ell\ell$	135	16	16	15	12	9	0	5	4	2.4
Total	2671	1391	1321	1254	1104	834	10	120	704	609.8

Table 5.3

Results from the dilepton selection on the PYTHIA top 175 sample (80 000 events). The second to last column is multiplied by the appropriate weighting factors, discussed in text, to give the last column which is the expected number of dilepton candidates.

the central electron trigger has been measured to be greater than 99% efficient [58]. The trigger simulation is applied before the lepton identification, and predicts for the PYTHIA top 175 sample, a reduction of $(19 \pm 2)\%$ in the number of $\mu\mu$ events. This gives an overall trigger efficiency of $\epsilon_{trigger} = 0.94$, before lepton ID cuts have been applied. After lepton identification and all other dilepton cuts, the muon trigger is found to decrease the number of $\mu\mu$ candidates by $\sim 7\%$, and the total number of dilepton candidates by 2.0%.

As an aside, if the plug electron (PEL) categories were included (TCE-PEL, TCM-PEL, CMX-PEL), as they were in the standard dilepton analysis of Run 1A [59], the dilepton acceptance would increase by about 4%.

From the results presented in Table 5.3, the various efficiencies contributing to ϵ_{dil} in equation 5.1 are given in Table 5.4. The efficiencies in this table are those of the dilepton cuts in Table 5.3 and are calculated assuming all previous cuts have been passed. Consequently the order in which the efficiencies are written in Table 5.4 and equation 5.1 is of importance. The efficiency of the Z^0 mass cut is given for all dilepton events, though it is only applied to ee and $\mu\mu$ events. The efficiency of this cut for only ee and $\mu\mu$ events is, $\epsilon_{mass}(ee,\, \mu\mu) = 0.75 \pm 0.02$. Recall that the 2-jet cut requires there be at least 2 jets with $E_t^{raw} > 10\, GeV$ and $|\eta_{det}| < 2.0$ (see section 4.10). If instead the jet energy requirement was $E_t^{corr} > 20\, GeV$, ϵ_{2-jet} becomes 0.764 ± 0.017, for a top mass of $175\, GeV$ (from the PYTHIA sample*). Below, all the efficiencies will be calculated as a function of top mass using the HERWIG samples, and can be compared with the PYTHIA results in Table 5.4. The total dilepton efficiency predicted for a top mass of $175\, GeV$ from the PYTHIA

---

*HERWIG top 175 gives $\epsilon_{2-jet} = 0.769 \pm 0.013$ with $20\, GeV$ corrected jets.

$\epsilon_{geom \cdot P_t}$ (%)	3.56 ± 0.07
$\epsilon_{trigger}$	0.937 ± 0.005
ϵ_{ID}	0.451 ± 0.013
ϵ_{SS}	0.950 ± 0.006
ϵ_{iso}	0.949 ± 0.006
ϵ_{mass}	0.880 ± 0.010
$\epsilon_{\not{E}_t}$	0.755 ± 0.015
ϵ_{2-jet}	0.844 ± 0.014
ϵ_{dil} (%)	0.762 ± 0.031

Table 5.4

The geometrical and kinematical acceptance, $\epsilon_{geom \cdot P_t}$, followed by the efficiencies which give the total dilepton acceptance, ϵ_{dil}, from the PYTHIA top 175 sample. Each efficiency is calculated from the events that have passed all the preceding cuts. All errors are statistical only.

sample[†], is:

$$\epsilon_{dil} = (0.762 \pm 0.031)\% \qquad \text{(PYTHIA top 175)}$$

where the error is statistical only. The corresponding result from the HERWIG

[†] Recall from section 5.1 that version 5.6 of PYTHIA was used for these results, which does not include W polarization effects. A sample of PYTHIA v5.7 $t\bar{t}$ events predicts $\epsilon_{dil} = (0.74 \pm 0.03)\%$.

	After Geom/P_t cuts only		After all dilepton selection cuts	
	PYTHIA (%)	HERWIG (%)	PYTHIA (%)	HERWIG (%)
ee	18.0 ± 0.8	18.0 ± 0.7	13.8 ± 1.5	16.8 ± 1.3
$\mu\mu$	30.8 ± 1.0	31.9 ± 0.9	26.2 ± 2.1	26.6 ± 1.6
$e\mu$	46.2 ± 1.3	46.2 ± 1.1	59.6 ± 3.1	56.3 ± 2.4
$\ell\ell\ell$	4.9 ± 0.4	3.9 ± 0.3	0.39 ± 0.25	0.24 ± 0.15

Table 5.5

The relative acceptances in the ee, $\mu\mu$, $e\mu$ and $\ell\ell\ell$ channels both before lepton identification and trigger, and, after all dilepton selection cuts.

sample of 130 000 events is:

$$\epsilon_{dil} = (0.784 \pm 0.025)\% \qquad \text{(HERWIG top 175).}$$

These results give an average overall dilepton acceptance (with statistical error only) of:

$$\boxed{\epsilon_{dil} = (0.77 \pm 0.02)\% \qquad (\text{ for } m_t = 175\, GeV\ )}$$

The acceptances expected from the ee, $\mu\mu$, $e\mu$ and $\ell\ell\ell$ channels relative to $\epsilon_{geom \cdot P_t}$ and ϵ_{dil} are given in Table 5.5 for a top mass of $175\, GeV$.

The differences in the ee, $\mu\mu$ and $e\mu$ contributions to the acceptance after only the geometrical and P_t cuts, and after all the dilepton selection cuts, is mostly attributable to; the Z^0 mass cut on ee and $\mu\mu$ events, the 20% reduction of $\mu\mu$

events by the trigger before the lepton identification cuts, and, the difference in the electron and muon identification efficiencies. Also, the trilepton ($\ell\ell\ell$) events are drastically reduced by the lepton identification efficiencies, because at least one lepton must come from a b (or c) decay for which the detection efficiency is very low (see Figure 5.6). Events with 3 leptons after the geometrical and P_t cuts, in which only one lepton fails the lepton identification cuts are kept and put into the appropriate dilepton category.

The various $t\bar{t}$ contributions to the dilepton acceptance are given in Table 5.6, separately for the ee, $\mu\mu$ and $e\mu$ channels, analogous to the $\epsilon_{geom \cdot P_t}$ contributions given in Table 5.1. The information contained in tables 5.1 and 5.6 is presented more visually in Figure 5.7.

The dilepton acceptance, ϵ_{dil}, was found to almost double over the top quark mass range of $130\,GeV$ to $220\,GeV$, using the acceptances predicted by the HERWIG samples mentioned in section 5.1.

Figure 5.8 shows the increase of $\epsilon_{geom \cdot P_t}$ and ϵ_{dil} with top mass, m_t, as well as the dependence of the dilepton selection cut efficiencies on m_t. As m_t increases so to does the energy available to the W bosons, b quarks, and τ's in the event, thus providing any leptons from their decay with a greater probability of passing the geometrical and kinematical requirements that define $\epsilon_{geom \cdot P_t}$. This is particularly true for leptons from b decay, which tend to be non-isolated and therefore require a large P_t to be distinguished from the surrounding jet activity. This can be seen in Figure 5.9, where the fraction of ϵ_{dil} from $Wb \rightarrow \ell\nu_\ell \ell\nu_\ell c$ events* more than doubles over the mass range (implying the acceptance for the Wb source only, increases

---

*Events in which one lepton comes from c decay are not included in the plots of Figure 5.9.

$t\bar{t}$ dilepton source : $WW \rightarrow$	Dilepton Category (after all selection cuts)		
	ee	$\mu\mu$	$e\mu$
ee	$83 \pm 10\%$	0	$0.2 \pm 0.2\%$
$\mu\mu$	0	$83 \pm 7\%$	$0.2 \pm 0.2\%$
$\tau\tau$	0	0	$0.7 \pm 0.4\%$
$e\mu$	0	0	$84 \pm 5\%$
$e\tau$	$13.5 \pm 4.0\%$	0	$5.0 \pm 1.2\%$
$\mu\tau$	0	$14.5 \pm 3.0\%$	$5.6 \pm 1.2\%$
ejj	$2.9 \pm 1.9\%$	0	$1.8 \pm 0.7\%$
μjj	0	$2.4 \pm 1.2\%$	$1.7 \pm 0.7\%$
τjj	$0.8 \pm 0.8\%$	$0.4 \pm 0.4\%$	$0.5 \pm 0.4\%$
$ejj\ (b \rightarrow e)$	$0.8 \pm 0.8\%$	0	$0.8 \pm 0.5\%$
$\mu jj(b \rightarrow \mu)$	0	$1.8 \pm 1.1\%$	$1.1 \pm 0.5\%$
$\tau jj(b \rightarrow \tau)$	$0.8 \pm 0.8\%$	$0.4 \pm 0.4\%$	$0.2 \pm 0.2\%$
$jjjj$	0	0	0

Table 5.6

Relative acceptances to the $t\bar{t}$ dilepton signal from the various top decay modes after all dilepton selection cuts, using the PYTHIA top 175 Monte Carlo sample. Errors are statistical only.

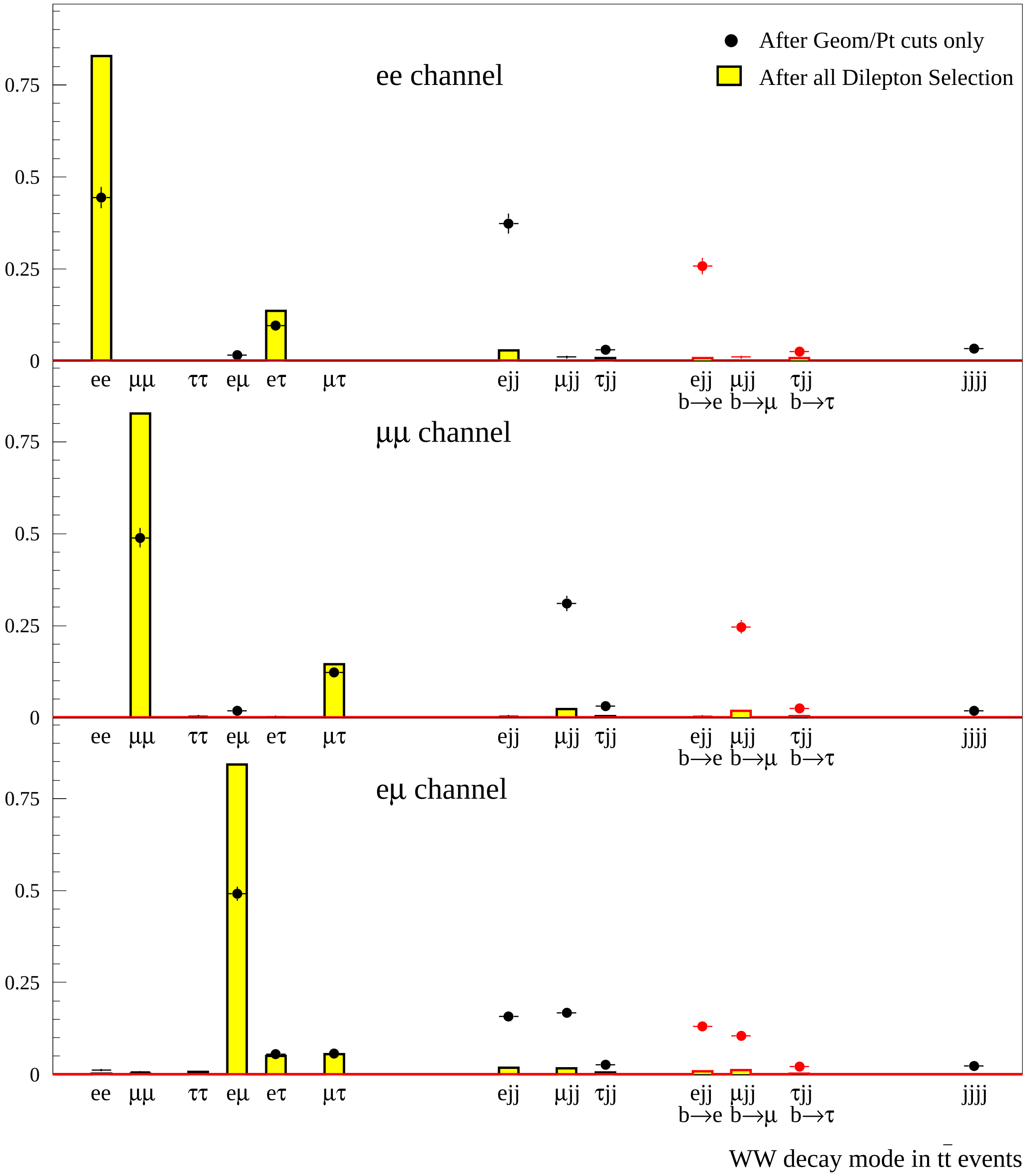

Figure 5.7

The fractional contribution to the ee, $\mu\mu$ and $e\mu$ acceptances from the various possible $t\bar{t}$ decay modes, for a top mass of $175\,GeV$. See text for further explanation.

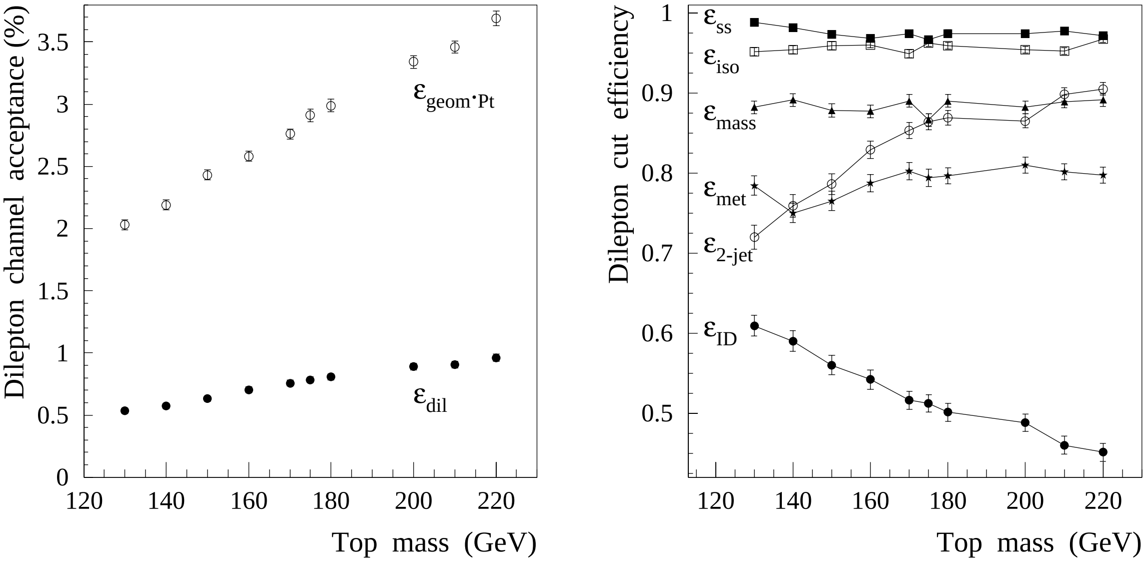

Figure 5.8

Graphical representation of the terms in equation 1.1 as a function of top mass. Not shown is the trigger efficiency, $\epsilon_{trigger}$, which is constant at 0.95 ± 0.01 over the range of top masses shown.

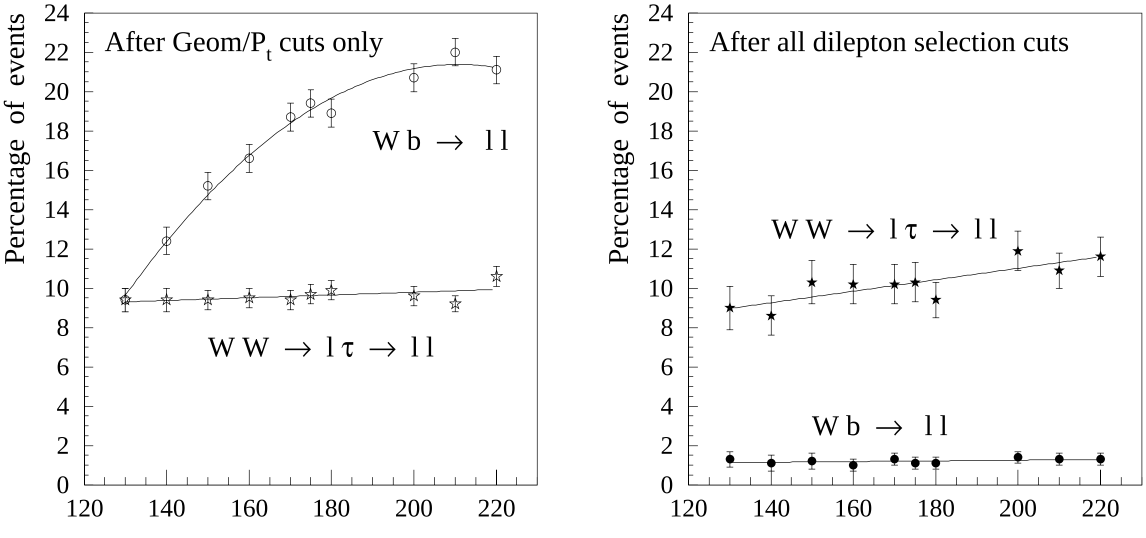

Figure 5.9

Contribution to $\epsilon_{geom \cdot P_t}$ (left plot) and to the total dilepton acceptance, ϵ_{dil} (right plot), from the $t\bar{t}$ dilepton sources $WW \rightarrow \ell\tau \rightarrow \ell\ell$, and $Wb \rightarrow \ell\ell$ (the second W decays hadronically), as a function of top mass ($\ell = e$ or μ).

more than four fold). The fraction of events in which one lepton comes from τ decay stays more or less constant at 10% (though, since $\epsilon_{geom \cdot P_t}$ doubles over the range of masses, so to does the acceptance of events in which on lepton is given by a τ decay). The decrease in the lepton identification efficiency, ϵ_{ID}, over the m_t range is due to the increase in the fraction of leptons from b decay, for which, as already discussed, the detection efficiency is small. Therefore, the lepton identification cuts eliminate most of the events in which one lepton is the result of b (or c) decay. After all dilepton selection cuts the contribution of such events to ϵ_{dil} is less than 2%[†], and does not vary much over the m_t range shown. The contribution to ϵ_{dil} from $W \rightarrow \tau\nu_\tau \rightarrow \ell\nu_\ell\nu_\tau\nu_\tau$ decay chains also does not vary appreciably over the m_t range, being about 10% at $m_t = 175\, GeV$. These numbers can be compared to those predicted by PYTHIA for a $175\, GeV$ top in tables 5.1 and 5.6. The results are consistent, except for the PYTHIA prediction of a higher Wb contribution to $\epsilon_{geom \cdot P_t}$ because of the GENP filter used to create the HERWIG samples as discussed above.

The increase in ϵ_{dil} with m_t is therefore a result of the increase in acceptance of the $WW \rightarrow \ell\ell$ and $WW \rightarrow \ell\tau \rightarrow \ell\ell$ sources with mass (recall the Wb contribution is largely eliminated by the lepton identification cuts), together with the increase in efficiency of the 2-jet cut. The dilepton acceptance as a function of m_t is plotted separately in Figure 5.10.

The relative acceptances in the ee, $\mu\mu$, $e\mu$ and $\ell\ell\ell$ channels, given in Table 5.5 for a top mass of $175\, GeV$, are seen in Figure 5.11 to remain essentially constant with m_t after all dilepton selection cuts.

[†] From direct b decay only; events with leptons from c decay contribute an additional $\sim 1\%$.

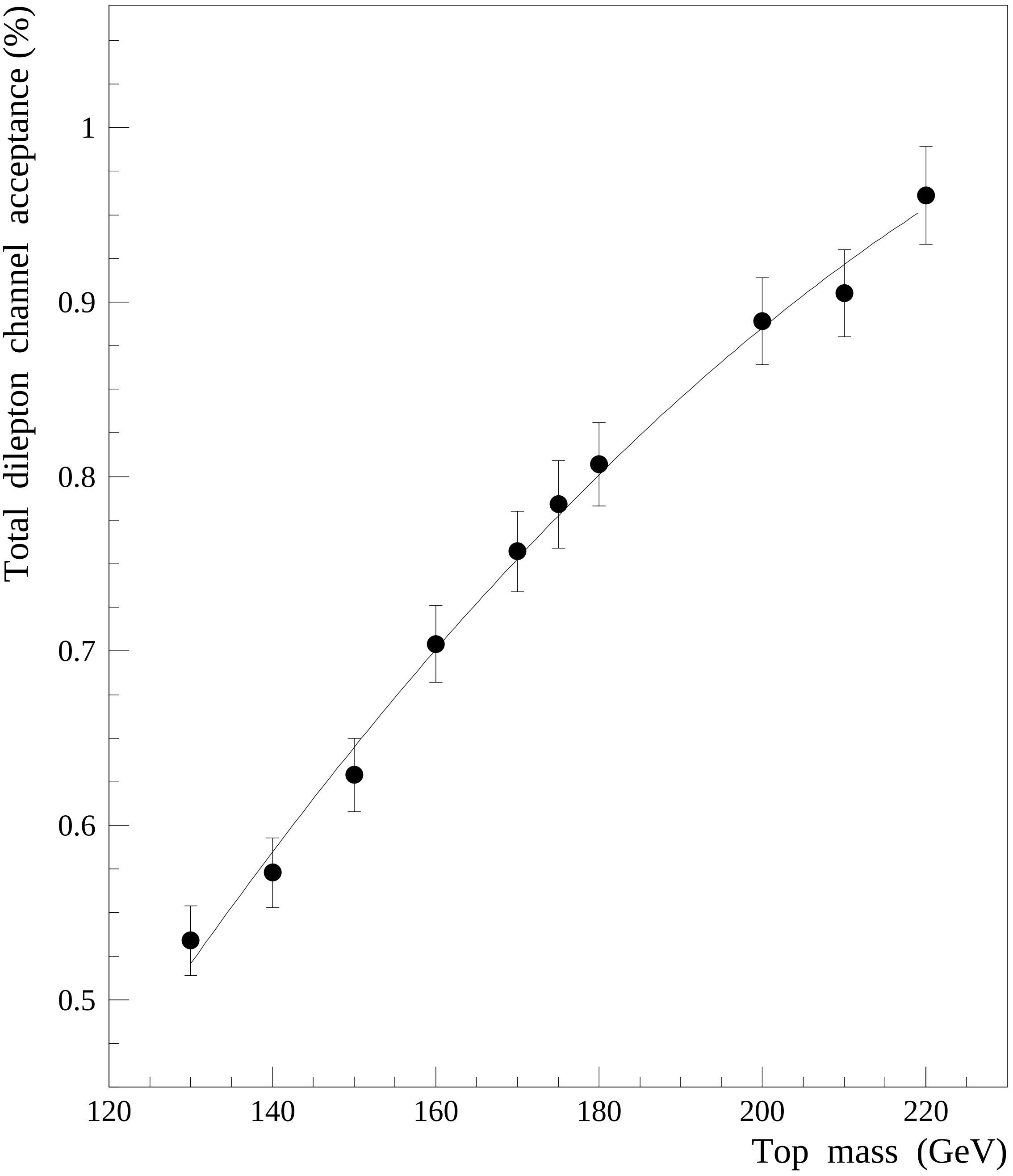

Figure 5.10

The $t\bar{t}$ dilepton channel acceptance, ϵ_{dil}, versus the top mass. Errors are statistical only.

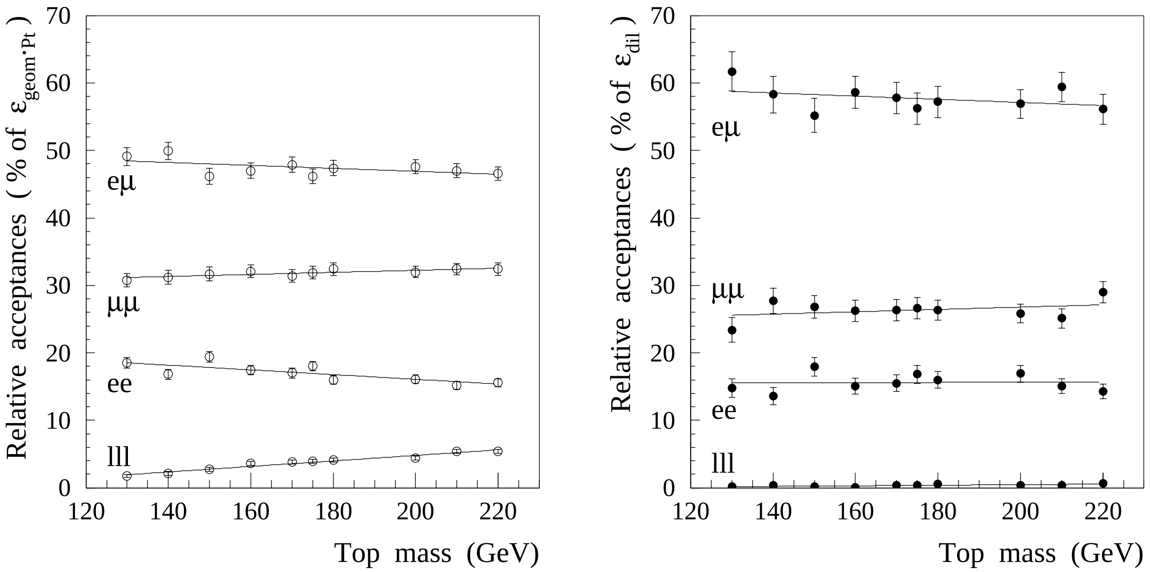

Figure 5.11

The relative contributions to $\epsilon_{geom \cdot P_t}$ (left plot, before trigger) and ϵ_{dil} (right plot) from the ee, $\mu\mu$, $e\mu$ and trilepton channels, as a function of top mass.

5.5 Systematic uncertainty in the acceptance

Each source of systematic uncertainty in the dilepton acceptance calculation is briefly discussed below, and summarized in Table 5.7.

- Lepton ID efficiencies contribute the largest systematic error to ϵ_{dil}. As discussed in section 5.3, the fast detector simulation QFL, does not satisfactorily reproduce the lepton efficiencies measured from the Z^0 data, and so the probability for a given lepton to pass the identification cuts is scaled according to the difference seen between Z^0 data events and Monte Carlo events (see Figure 5.5). It is not clear how accurate this scaling is because of the differences in the lepton sources and isolation properties between Z^0 events and $t\bar{t}$ events. To estimate the systematic error in applying the lepton identification procedure, discussed in section 5.3, to $t\bar{t}$ events, the dilepton acceptance was recalculated using the Z^0 data efficiencies in Figure 5.5 plus or minus half the difference between the Monte Carlo and data efficiencies. The resulting uncertainty was estimated to be ±7%.

- The systematic uncertainty resulting from which Monte Carlo generator is used was estimated at ±3%. This is simply calculated from the range of ϵ_{dil} values from using PYTHIA v5.6 (0.76 ± 0.03), PYTHIA v5.7 (0.74 ± 0.03), HERWIG (0.78 ± 0.03), and ISAJET (0.78 ± 0.05), all at a top mass of $175\,GeV$.
- The uncertainty in how well the Monte Carlo generator simulates initial state (IS) and final state (FS) gluon radiation, was estimated using 3 PYTHIA top 170 samples; one with the IS radiation turned off, one with the FS radiation turned off, and one with both IS and FS radiation turned on (the default). The differences in the acceptances from these samples result in a systematic error of ±3%.
- The choice of structure functions used with a given generator is estimated to result in a systematic error of ±2%. The HERWIG samples described in section 5.1 use the MRS D0′ structure functions. A sample of 50 000 $t\bar{t}$ events, with a top mass of $175\,GeV$, was generated with the HERWIG Monte Carlo using the latest CTEQ structure functions (CTEQ2pL) [56], in order to compare with the MRS D0′ result. The acceptances after the geometrical, P_t and trigger requirements are:

$$\epsilon_{geom\cdot P_t} = (2.77 \pm 0.05)\% \qquad (\mathrm{MRS\,D0'})$$

$$\epsilon_{geom\cdot P_t} = (2.84 \pm 0.08)\% \qquad (\mathrm{CTEQ2pL})$$

and, after all the dilepton selection cuts:

$$\epsilon_{dil} = (0.784 \pm 0.025)\% \qquad (\mathrm{MRS\,D0'})$$

$$\epsilon_{dil} = (0.816 \pm 0.040)\% \qquad (\mathrm{CTEQ2pL}).$$

These numbers are consistent within their statistical errors, however a systematic error of 2% is assigned due to the choice of structure functions.

- At CDF the uncertainty in jet energies has been estimated to be ±10% for the jets typically found in $t\bar{t}$ events [54]. To estimate the effect of the jet energy scale uncertainty, the jet energies, after QFL simulation, were increased and decreased by 10% before applying the $\not{E}_t$ and 2-jet cuts, and the dilepton acceptance measured for both cases. The HERWIG top 175 sample gives:

$$\epsilon_{dil} = (0.794 \pm 0.025)\% \quad (E_t(jet) = E_t(jet) + 10\%)$$

$$\epsilon_{dil} = (0.767 \pm 0.024)\% \quad (E_t(jet) = E_t(jet) - 10\%).$$

Taking half the difference gives a systematic uncertainty of ±2% in ϵ_{dil} due to the jet energy uncertainties.

- The photon conversion removal algorithm used in the data analysis was discussed briefly in section 4.2. Photon conversions will not be a significant source of high-E_t electrons in $t\bar{t}$ events, however the over-efficiency of the conversion removal algorithm will decrease the dilepton $t\bar{t}$ acceptance, and the uncertainty in this effect will contribute to the systematic uncertainty in ϵ_{dil}. The PYTHIA top 175 sample predicts a decrease in $\epsilon_{geom \cdot P_t}$ of $(5.6 \pm 0.4)\%$ due to the conversion removal algorithm (a $(11.6 \pm 1.4)\%$ decrease in the ee acceptance, and a $(5.8 \pm 0.6)\%$ decrease in the $e\mu$ acceptance), and a $(4.0 \pm 0.7)\%$ decrease in ϵ_{dil} (a $(7.0 \pm 2.5)\%$ decrease in ee, and a $(4.7 \pm 1.1)\%$ decrease in $e\mu$). The HERWIG top 175 sample predicts a $(4.0 \pm 0.3)\%$ decrease in $\epsilon_{geom \cdot P_t}$ ($(7.2 \pm 1.0)\%$ from ee, and $(5.1 \pm 0.5)\%$ from $e\mu$), and a $(1.8 \pm 0.4)\%$ decrease in ϵ_{dil} ($(2.9 \pm 1.3)\%$ from ee, and $(2.2 \pm 0.6)\%$ from $e\mu$). There is clearly a difference in these predictions, which has hitherto not been investigated further. A systematic uncertainty in ϵ_{dil} of 2% is assigned due to the uncertainty of the effect of the photon conversion removal algorithm on Monte

Carlo $t\bar{t}$ events.

- The efficiency of the isolation cut (section 4.7) in the dilepton analysis for $t\bar{t}$ events depends on the correct modeling of the isolation variables (I_{cal} and I_{trk}) by the Monte Carlo simulation. This is more critical for leptons from b (and c) decays, than it is for leptons from W and τ decays for which the isolation cut is extremely efficient (see figures 4.7 and 4.8). The isolation cut efficiency, ϵ_{iso} for $t\bar{t}$ events is 0.95, where essentially all the inefficiency is due to events in which one lepton comes from b decay. In an extreme situation where the Monte Carlo underestimates the isolation by a factor of 2, ϵ_{dil} was recalculated (by halving the isolation cuts to 0.05) for the HERWIG top 175 sample. The resulting acceptance was, $\epsilon_{dil} = (0.769 \pm 0.024)\%$, 2% lower than the original value. This is taken to be the estimate of the systematic uncertainty resulting from the Monte Carlo modeling of isolation.
- The degradation in the CTC tracking efficiency during Run 1B, is expected to affect mostly low momentum tracks and not influence the top dilepton acceptance significantly. However, until its affect on high-P_t tracks is better understood, a systematic of 2% is assigned due to tracking efficiency uncertainties.
- As discussed in section 5.4, the effect of the muon triggers is to reduce the $t\bar{t}$ dilepton acceptance by about 2%. The effect of the central electron triggers has been neglected due to their high efficiency. Because of the small overall effect of the triggers, uncertainties in their accurate modeling are not expected to effect the dilepton acceptance significantly. The systematic uncertainty associated with the trigger is expected to be $< 1\%$.

The total systematic error in ϵ_{dil} is therefore estimated to be $\pm 9\%$. Some of the sources of systematic error estimated above will be correlated, and so the 9% error is considered to be a conservative estimate. However, the error in the cross-section

Source	% error
Lepton ID efficiencies	7%
Monte Carlo generator	3%
IS and FS radiation	3%
Structure functions	2%
Jet energy scale	2%
Conversion removal	2%
Isolation efficiency	2%
Tracking efficiency	2%
Trigger efficiency	1%
TOTAL	9%

Table 5.7

Contributions to the systematic uncertainty in the dilepton acceptance calculation.

calculation of chapter 8, is not greatly affected by the error in ϵ_{dil}, but rather is statistically dominated by the number of $t\bar{t}$ dilepton candidates found.

5.6 Dilepton acceptance summary

Using the average of the PYTHIA and HERWIG results, the $t\bar{t}$ dilepton acceptance for this analysis with a top mass of $175\,GeV$ is:

$$\epsilon_{dil} = (0.77 \pm 0.02(stat) \pm 0.07(syst)\,)\%$$

The results from this chapter are summarized in Table 5.8.

Total $t\bar{t}$ dilepton channel acceptance	
$\epsilon_{dil} = (0.77 \pm 0.08)\%$	
Percentage contributions to ϵ_{dil} by dilepton category	
ee	$(15.3 \pm 1.0)\%$
$\mu\mu$	$(26.4 \pm 1.3)\%$
$e\mu$	$(58.0 \pm 2.0)\%$
$\ell\ell\ell$	$(0.3 \pm 0.2)\%$
Percentage contributions to ϵ_{dil} by dilepton source	
$WW \to \ell\ell$	$(86 \pm 3)\%$
$WW \to \ell\tau \to \ell\ell$	$(11 \pm 1)\%$
$WW \to \ell jj \;\; (b,\, c \to \ell)$	$(3 \pm 1)\%$

Table 5.8

Summary of the contributions to ϵ_{dil}. The numbers represent an average of the PYTHIA and HERWIG results with a top mass of $175\,GeV$.

6. DILEPTON BACKGROUNDS

There are various sources of lepton pairs which can potentially resemble $t\bar{t}$ decays in the dilepton channel. Such lepton pairs must be accompanied by at least 2 jets and so typically involve higher order QCD processes beyond the tree level lepton pair production process. This alone substantially reduces the cross-section for background sources. The dilepton event selection discussed in Chapter 4 was designed to further reduce the background contribution to the $t\bar{t}$ signal by requiring 2 high-P_t leptons and large $\not{E}_t$. Nevertheless, in order to preserve a good acceptance for $t\bar{t}$ decay in the dilepton channel, one necessarily allows contributions to the signal from other sources. In this chapter the main background sources are discussed and their contribution to the dilepton signal is estimated.

6.1 Drell-Yan lepton pair production

Electrons and muons can be pair produced by the Drell-Yan process [60] in which $q\bar{q}$ annihilation produces a virtual photon, or a Z (at, or away from, the Z^0 pole), which decays to a lepton pair as illustrated in Figure 6.1. The Drell-Yan cross-section is dominated by the Z contribution at the Z^0 resonance. Higher order processes which involve a QCD contribution of at least 2 jets to the lepton pair event can mimic the $t\bar{t}$ dilepton decay signal. Drell-Yan events involving *on-shell* (or real) Z^0 decays are removed by the Z^0 *mass cut* (see section 4.8), so the Drell-Yan background contribution comes from the dilepton invariant mass continuum outside the Z^0 mass window of $75 < M_{\ell\ell} < 105\,GeV$.

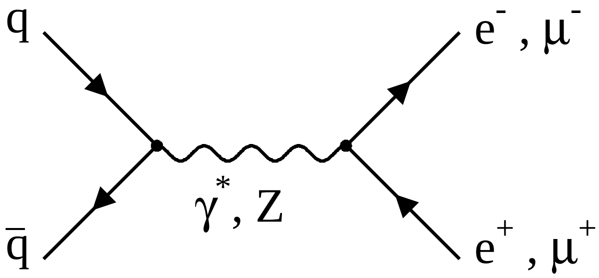

Figure 6.1

Lowest order diagram for Drell-Yan production of lepton pairs at hadron colliders.

Since there are no neutrinos in a Drell-Yan event, the lepton and jet energies must be mismeasured in such a way as to produce a $\not{E}_t$ that satisfies the magnitude and direction requirements of the top dilepton analysis. The level of this background depends crucially on the tail of the $\not{E}_t$ distribution in *Drell-Yan + multijet* events. A $500\,pb^{-1}$ sample of ISAJET+QFL* $Z^0 \rightarrow ee/\mu\mu$ was generated to compare the Monte Carlo modeling of jet energies and $\not{E}_t$ to that seen in the Z^0 data. This comparison is shown in Figure 6.2 for both $Z^0+1\,jet$ and $Z^0+\geq 2\,jet$ events. There is good agreement between the distributions from Monte Carlo and data, however the statistics are low in the $\not{E}_t$ tails which are of primary interest, particularly for the $\geq 2\,jet$ case. Note that there will be small contributions from other sources in the data distributions, most notably in the large $\not{E}_t$ region (such as from $t\bar{t}$). Since there is some uncertainty in the Monte Carlo modeling of the large $\not{E}_t$ tails, $Z^0+\geq 2\,jet$

---

*References to all Monte Carlo generators can be found in Appendix B.

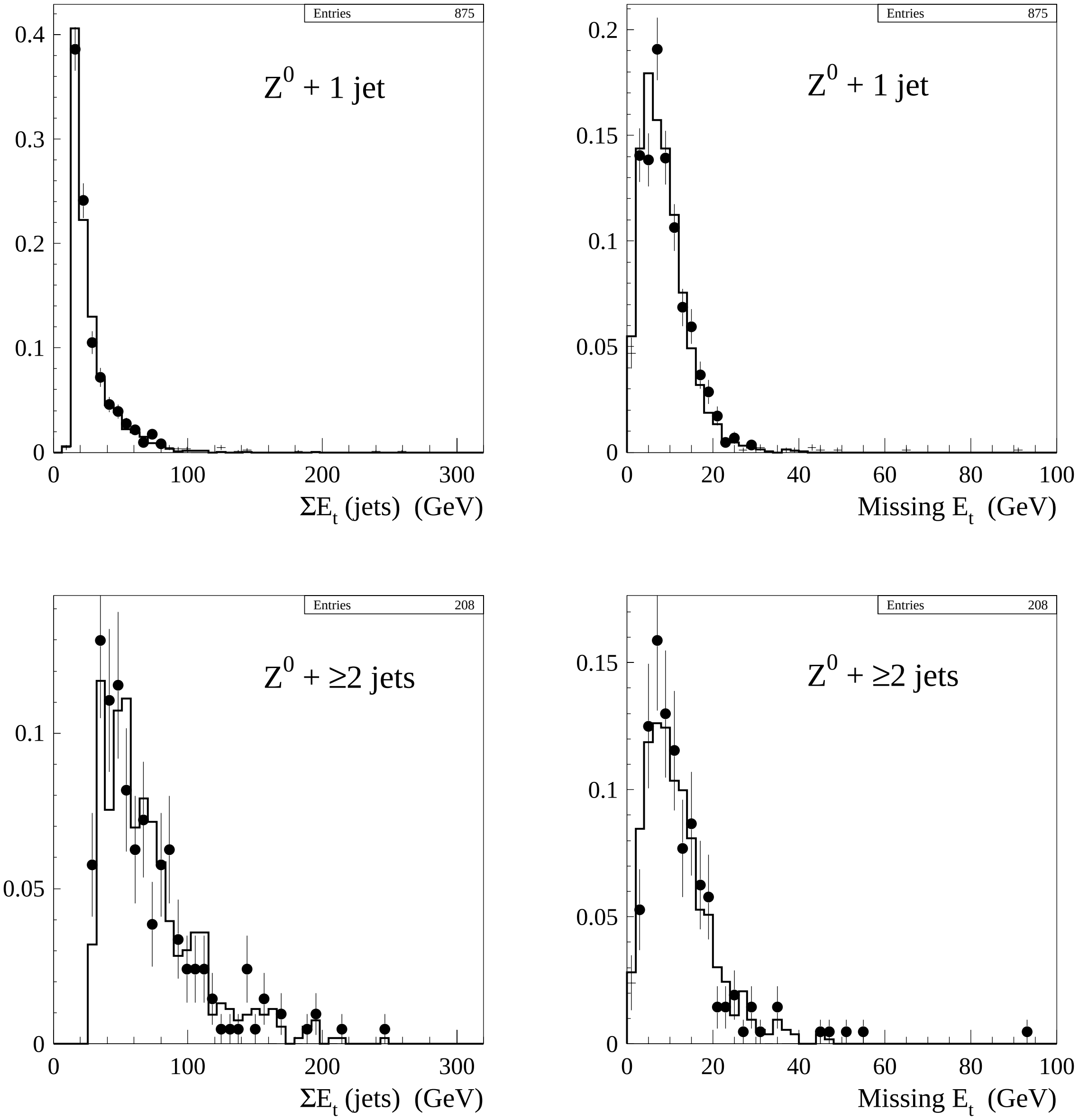

Figure 6.2

Comparison of the $\sum E_t(jets)$ and $\not{E}_t$ distributions in $Z^0 + multijet$ events between data (points) and Monte Carlo (histogram). All distributions have been normalized to 1, with the number of entries referring to the number of data events. The $\not{E}_t$ has been corrected for muons and jets.

events in the data are used to estimate the Drell-Yan background[†]. Results from the Monte Carlo sample will nevertheless be used for comparative purposes.

A naive estimate of the Drell-Yan background ($\hat{N}_{bg}^{DY}$) would simply be to count the number of Z^0 events (the events inside the Z^0 mass window) that pass the $\not{E}_t$ and 2-jet requirements (N_Z^{pass}), and scale that number by the ratio of the number of events in the continuum to the number inside the Z^0 mass window. That is;

$$\hat{N}_{bg}^{DY} = N_Z^{pass}\frac{N_{lo}+N_{hi}}{N_Z} \tag{6.1}$$

where, N_{lo} (N_{hi}) is the number of continuum events with $M_{\ell\ell} < 75\,GeV$ ($M_{\ell\ell} > 105\,GeV$), and, N_Z is the number of events in the Z^0 window. In fact to first order this is a good approximation. However, a correction is required to account for the dependence of the 2-jet rejection factor (or, the efficiency of the 2-jet cut) on the dilepton invariant mass[*]. This dependence has been calculated using a $Z + 2\ jet$ matrix element Monte Carlo [62]. The fraction of Drell-Yan events with 2 or more jets with $E_t^{raw} > 10\,GeV$, ϵ_{2j}, can be approximated as a linear function of the dilepton mass:

$$\epsilon_{2j} = (2.5\times 10^{-4})M_{\ell\ell}(GeV) \ + \ 9.6\times 10^{-3}.$$

If ϵ_{2j}^{lo} (ϵ_{2j}^{hi}) is the fraction of 2 jet events corresponding to the average dilepton mass of the $N_{lo}(N_{hi})$ events, and ϵ_{2j}^{Z} is the similar fraction for the N_Z events, then the number of background events expected from Drell-Yan is:

$$N_{bg}^{DY} = N_Z^{pass}\frac{\epsilon_{2j}^{lo}N_{lo}+\epsilon_{2j}^{hi}N_{hi}}{\epsilon_{2j}^{Z}N_Z}. \tag{6.2}$$

This differs from the naive prediction of equation 6.1 by a factor of;

$$f_c = \frac{(\epsilon_{2j}^{lo}/\epsilon_{2j}^{Z})N_{lo}+(\epsilon_{2j}^{hi}/\epsilon_{2j}^{Z})N_{hi}}{N_{lo}+N_{hi}}.$$

[†] For previous Drell-Yan background estimates see references [61].

[*] It is assumed the $\not{E}_t$ rejection is independent of $M_{\ell\ell}$, which isn't quite true because of the correlation between $\not{E}_t$ and jet activity in Drell-Yan events.

Channel	N_{lo}	N_Z	N_{hi}	$\langle M_{\ell\ell}\rangle_{lo}$	$\langle M_{\ell\ell}\rangle_Z$	$\langle M_{\ell\ell}\rangle_{hi}$	f_c	N_Z^{pass}	N_{bg}^{DY}
ee	236	2482	80	58.5	89.6	142.1	0.91	3	0.35 ± 0.20
$\mu\mu$	252	2982	123	57.3	90.7	132.1	0.95	3	0.35 ± 0.20
$\ell\ell$	488	5464	203	57.9	90.2	136.0	0.93	6	0.70 ± 0.20

Table 6.1

Drell-Yan background calculation for $109\,pb^{-1}$ of data *before* the contribution from top is subtracted.

Note that N_{bg}^{DY} only depends on the mass dependence of ϵ_{2j}, not on the absolute predicted 2-jet fractions. However, it is of interest to note that the Monte Carlo predicted fraction of Z^0 events with at least 2 jets is 3.2 %, compared with the somewhat larger fractions seen in the data: $3.6 \pm 0.4\,\%$ in the ee channel, and $4.0 \pm 0.4\,\%$ in the $\mu\mu$ channel.

Table 6.1 gives all the relevant information needed to calculate N_{bg}^{DY} for both the ee and $\mu\mu$ channels separately. In the $109\,pb^{-1}$ of data there were 6 events (3 ee and 3 $\mu\mu$) in the Z^0 mass window that passed the dilepton $\not\!\!E_t$ and 2-jet cuts. These are shown in the $\Delta\phi(\not\!\!E_t, \ell \text{ or } jet)$ versus $\not\!\!E_t$ plots of Figure 6.3*.

The results in Table 6.1 are not the final answer. The expected contribution from $t\bar{t}$ decay in the Z^0 mass window must be subtracted from the 6 events seen. This is done in the next subsection. It should be noted that contributions from

---

*Similar plots using $\Delta\phi(\not\!\!E_t, jet)$ which motivate the $\not\!\!E_t$ cuts are shown in Figure 4.13.

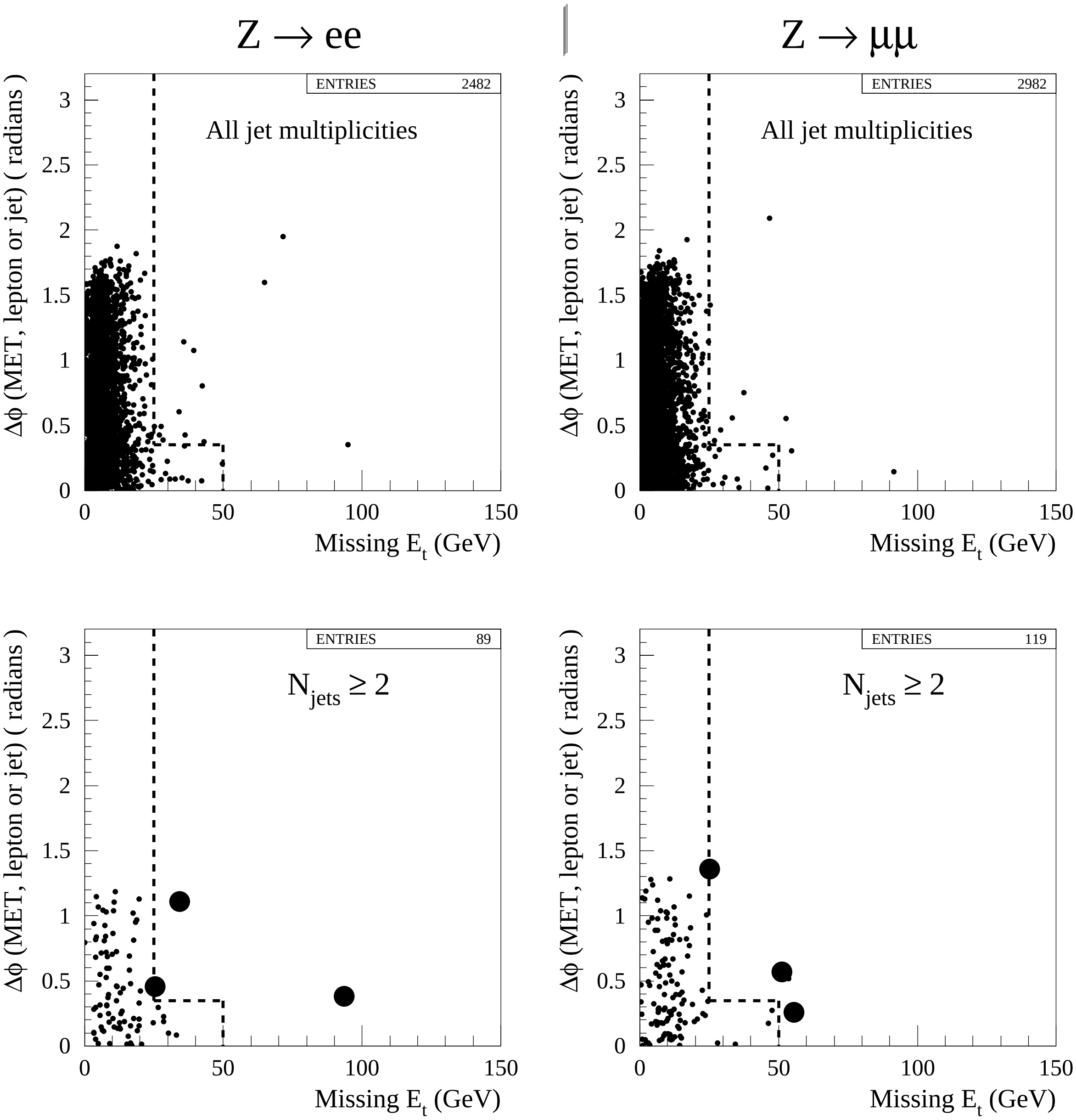

Figure 6.3

The azimuthal angle between the $\not\!\!E_t$ and the closest lepton or jet, versus the $\not\!\!E_t$, for $Z^0 \rightarrow ee$ and $Z^0 \rightarrow \mu\mu$ data. The 6 "Z^0" events passing the 2-jet and $\not\!\!E_t$ cuts are shown with larger dots.

other processes to the Drell-Yan background estimate are not taken into account, but are not expected to be significant. More specifically, one can note that after all cuts in the $ee + \mu\mu$ channels, the ratio of $t\bar{t}$ to non-Drell-Yan background is about 3 to 1, with none of these non-Drell-Yan backgrounds particularly favoring the Z^0 mass window. Nevertheless, it is noted that neglect of other sources in the Drell-Yan background calculation will result in an over-estimate of the Drell-Yan contribution to the $t\bar{t}$ signal.

6.1.1 Correction for the top contribution

Within the Z^0 mass window one expects a contribution from $t\bar{t}$ decay (see Figure 4.11), which should be subtracted from the number of Drell-Yan candidates seen within this window in order to get the expected background from Drell-Yan processes alone.

It was seen in section 5.4 that the efficiency of the Z^0 mass cut for ee and $\mu\mu$ events was $\epsilon_{mass}(ee, \mu\mu) = 0.75 \pm 0.02$, implying $(25 \pm 2)\%$ of the $t\bar{t}$ events in the ee and $\mu\mu$ channels are lost to the Z^0 invariant mass cut. Therefore, the expected number of ee and $\mu\mu$ events from $t\bar{t}$ decay in the Z^0 mass window *after all other selection cuts* is:

$$N^{Z}_{top}(ee) = 0.25 \times \mathcal{L}\sigma_{t\bar{t}}\epsilon_{total}R'_{ee}$$

$$N^{Z}_{top}(\mu\mu) = 0.25 \times \mathcal{L}\sigma_{t\bar{t}}\epsilon_{total}R'_{\mu\mu},$$

where, the integrated luminosity is $\mathcal{L} = 109\,pb^{-1}$, the most recent $t\bar{t}$ production cross-section is measured to be [63], $\sigma_{t\bar{t}} = 7.5^{+1.9}_{-1.6}\,pb^{*}$, the total $t\bar{t}$ acceptance in the dilepton channel is (section 5.6), $\epsilon_{total} = (0.77 \pm 0.08)\%$, and, $R'_{\ell\ell}$ are the ee and $\mu\mu$ acceptances relative to the total dilepton acceptance *before the Z^0 mass cut* (

---

*This the combined result from the *lepton + jets* and dilepton analyses for $109\,pb^{-1}$.

$R'_{ee} = (17 \pm 1)\%$ and $R'_{\mu\mu} = (30 \pm 2)\%$). The expected contributions from $t\bar{t}$ decay in the Z^0 mass window are, therefore;

$$N^Z_{top}(ee) = 0.27 \pm 0.08 \ \text{ events.}$$

$$N^Z_{top}(\mu\mu) = 0.47 \pm 0.14 \ \text{ events.}$$

$$N^Z_{top} = 0.74 \pm 0.22 \ \text{ events.}$$

When this is subtracted from N_Z^{pass} in equation 6.2, the expected Drell-Yan background becomes:

$$N_{bg}^{DY}(ee) = 0.32 \pm 0.19 \ ,$$

$$N_{bg}^{DY}(\mu\mu) = 0.30 \pm 0.19 \ ,$$

$$N_{bg}^{DY} = 0.62 \pm 0.30 \ .$$

6.1.2 Drell-Yan contribution before the 2-jet cut

Although the Drell-Yan background estimate has been calculated in the previous section, it is worthwhile to estimate the Drell-Yan background, and in fact all background processes, before the 2-jet cut in order to understand the 2-jet rejection factor for the background processes, and to check whether the data is showing what is expected before this cut.

Before the 2-jet cut there are 14 $Z^0 \rightarrow ee$ events and 9 $Z^0 \rightarrow \mu\mu$ events that pass the $\not\!\!E_t$ requirements. These are also shown in Figure 6.3. With no jet requirements, the number of ee events in the Z^0 mass window is 2482, and the number outside is 316. The corresponding numbers for $\mu\mu$ events are 2982 and 375 respectively. Therefore, assuming the $\not\!\!E_t$ rejection is independent of the dilepton mass, the expected numbers of Drell-Yan events before the 2-jet cut are*:

$$N_{bg}^{DY}(ee) = 1.8 \pm 0.5 \quad \text{(before 2 jet cut)}$$

$$N_{bg}^{DY}(\mu\mu) = 1.1 \pm 0.4 \quad \text{(before 2 jet cut)}$$

$$N_{bg}^{DY} = 2.9 \pm 0.6 \quad \text{(before 2 jet cut)}\ .$$

The efficiency of the 2-jet cut for dilepton events from $t\bar{t}$ decay was shown in section 5.4 to be 0.84 ± 0.02. Therefore, the expected number of events from top in the Z^0 mass window before the 2-jet cut is, 0.88 ± 0.36 $(0.74/0.84)$. When the number of Drell-Yan events seen before the 2-jet cut is corrected for this, the Drell-Yan background becomes:

$$N_{bg}^{DY} = 2.8 \pm 0.6 \quad \text{(before 2 jet cut)}\ .$$

This gives a 2-jet cut efficiency (for events that have already passed the $\not{E}_t$ cuts), for the Drell-Yan background, of:

$$\epsilon_{2-jet}^{DY} = 0.22 \pm 0.12\ .$$

6.1.3 A closer look at the six $Z^0 + \not{E} + 2\,jet$ events

As mentioned above 3 $Z^0 \to ee$ and 3 $Z^0 \to \mu\mu$ events pass all the top dilepton selection except for the fact that they fall within the Z^0 mass window. Since a $t\bar{t}$ contribution is expected in the Z^0 mass window, of 0.74 ± 0.22 events (see section 6.1.1), these events warrant closer examination.

A summary of these 6 events in the Z^0 mass window is given in Table 6.2. The sum of the transverse energies of the jets in the event which satisfy the jet requirements of section 4.10, is denoted by $\sum_j E_t$. Figure 6.4 displays some of their

---

*Using an analogous calculation to that of equation 6.1.

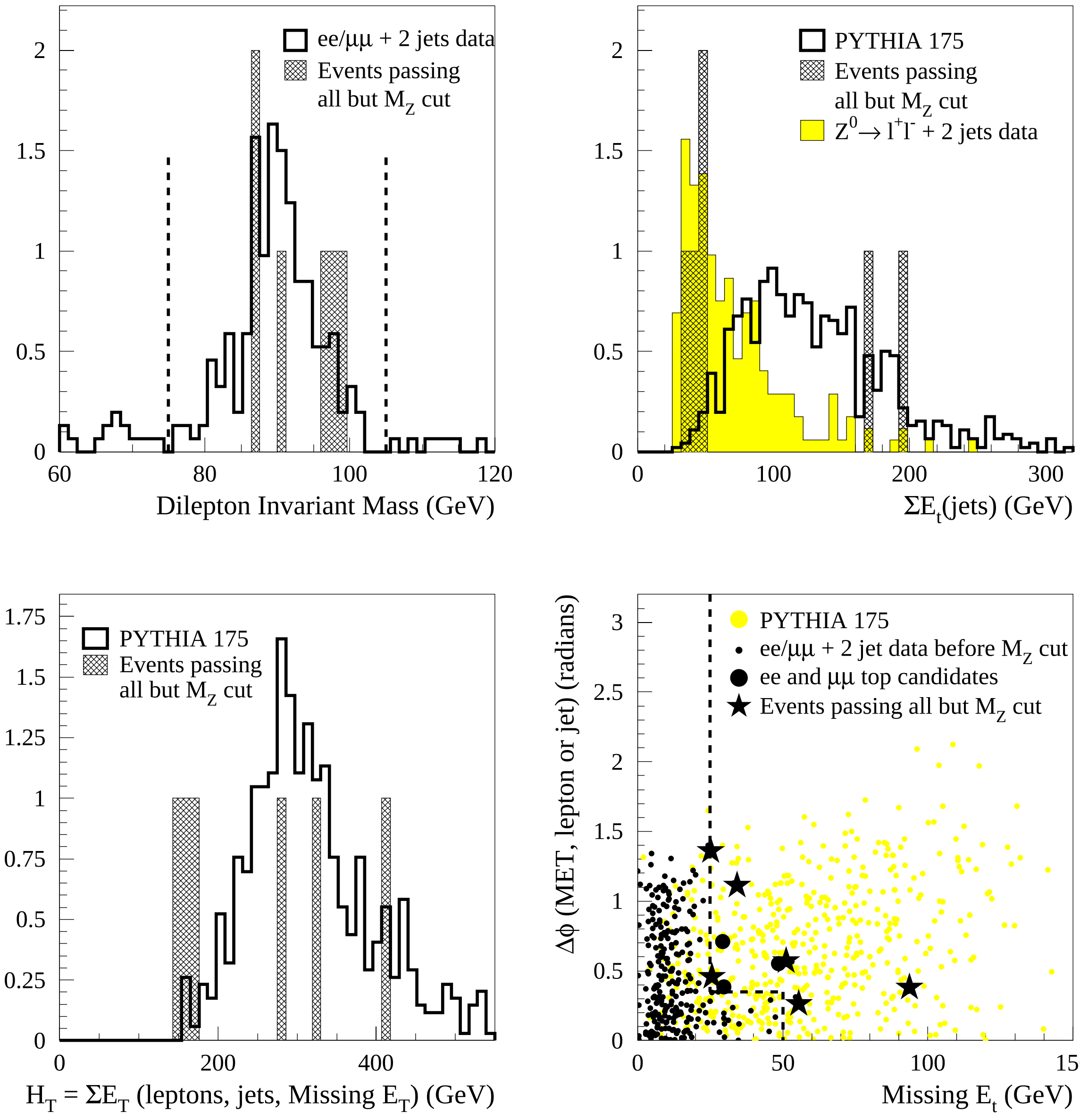

Figure 6.4

Properties of the 6 $Z^0 + \not{E}_t + 2\,jet$ events as compared to both Z^0 data and PYTHIA top 175 Monte Carlo (normalized arbitrarily). The dashed lines represent the analysis cuts. See also Table 6.2.

Run/Event	class	$P_t(\ell_1)$	$P_t(\ell_2)$	$P_t(\ell\ell)$	$M_{\ell\ell}$	$\not\!E_t$	$\sum_j E_t$	$\Delta\phi(\not\!E_t,\ell)$	$\Delta\phi(\not\!E_t,j)$
43170/198920	TCM-TCM	67.3	37.1	36.4	98.5	51.2	167	32.7°	106.4°
59699/20787	TCE-LCE	64.2	35.2	39.2	96.7	25.5	50	74.6°	26.1°
64880/570654	CMX-CMI	99.1	66.6	138.0	97.3	55.5	193	106.1°	15.1°
65004/23360	TCE-TCE	91.1	53.0	112.9	90.3	93.6	41	132.7°	21.8°
69113/171364	TCE-TCE	39.3	38.9	3.9	87.3	34.3	34	63.7°	164.7°
69709/228902	TCM-CMX	54.7	31.1	27.3	87.5	25.2	48	77.7°	105.5°

Table 6.2

Characteristics of the $Z^0 + \not\!E_t + 2\,jet$ events that pass all but the invariant mass cut. In addition 43170/198920 has a jet b-tagged in the SVX.

characteristics in comparison to what is expected from $t\bar{t}$ PYTHIA Monte Carlo with a top mass of $175\,GeV$, and Z^0 data. H_t is the sum of all the transverse energy in the event, and is defined more precisely in section 7.1.

Two of the 6 $Z^0 + \not\!E_t + 2\,jet$ events (43170/198920 and 64880/570654), both $\mu\mu$, have unusually large $\sum_j E_t$ for $Z^0 + 2\,jet$ events. In addition the event from run 1A (43170/198920) has a jet that is tagged as a b quark. However, there is expected to be some correlation between the $\not\!E_t$ and $\sum_j E_t$, so Z^0 events that pass the $\not\!E_t$ cuts have a greater probability of having a large $\sum_j E_t$. This is shown in Figure 6.5, where the ratio of the number of events that pass the $\not\!E_t$ magnitude cut to the number that fail, increases with $\sum_j E_t$ for both the 1 and $\geq$ 2 jet cases, in both the data and Monte Carlo. This effect is shown somewhat more quantitatively

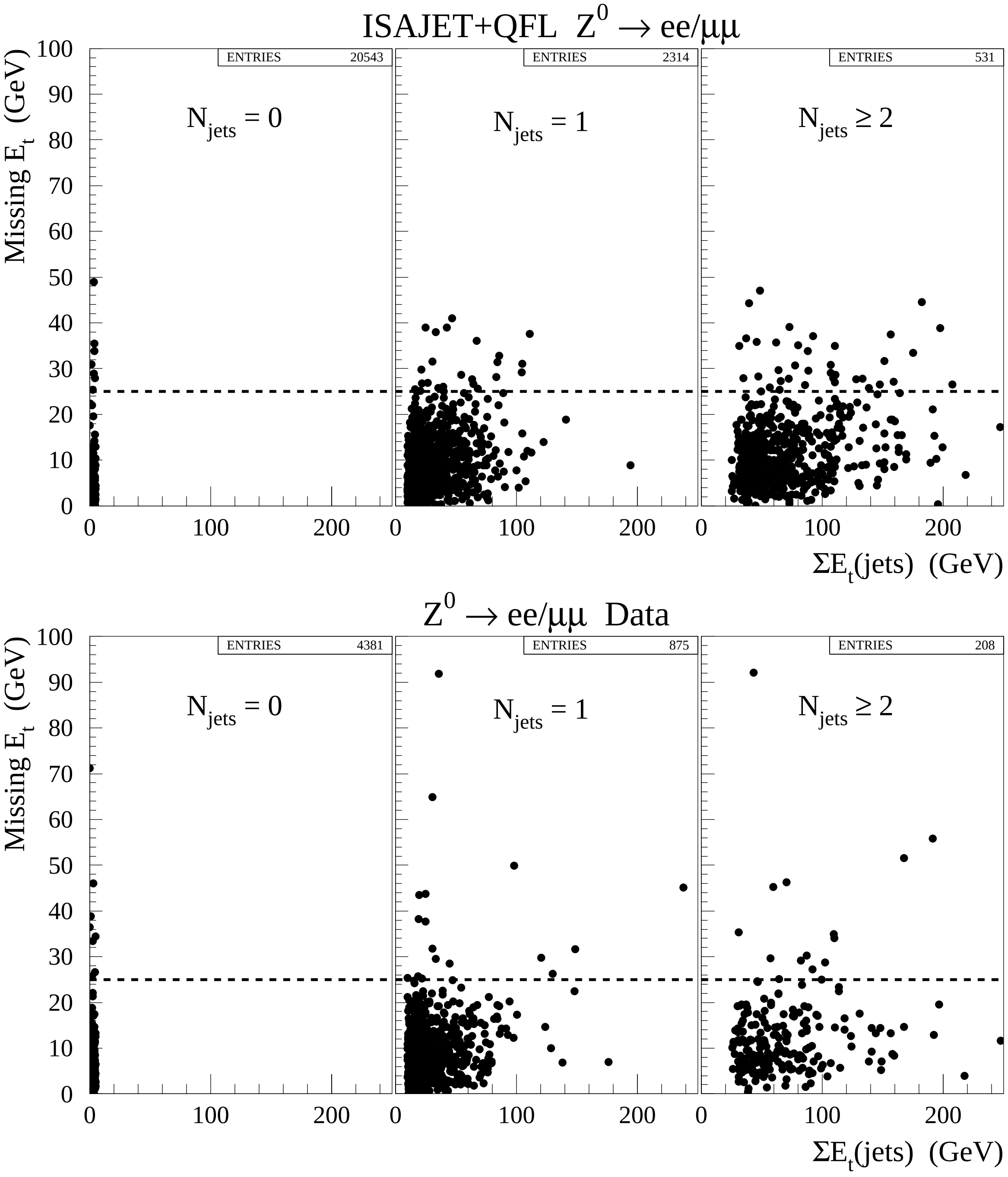

Figure 6.5

$\not{E}_t$ versus $\sum_j E_t$ for Z^0 events from Monte Carlo and data.

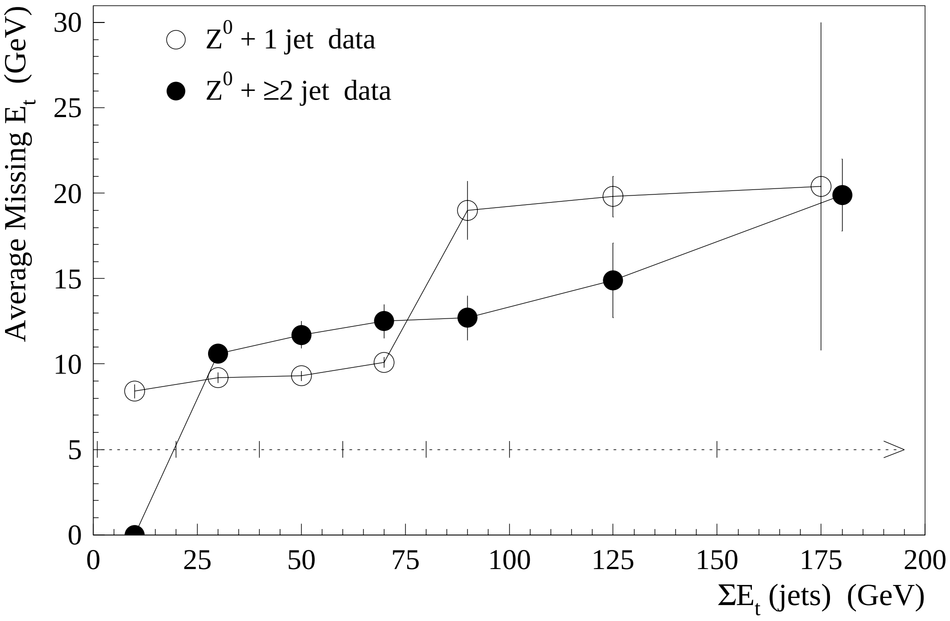

Figure 6.6

The average $\not\!\!E_t$ for events in the $Z^0 + jets$ data that fall within the $\sum_j E_t$ bins represented by the dotted line. Errors are statistical only and do not include systematic effects from non-Z^0 contributions.

in Figure 6.6 which explicitly demonstrates the increase in the average $\not\!\!E_t$ in Z^0 data events with increasing $\sum_j E_t$.

The $Z^0 + \not\!\!E_t + 2\,jet$ event with the largest $\not\!\!E_t$ at $93.6\,GeV$ (65004/23360) is, based on this alone, very unusual if interpreted as a Z^0 event. In addition the lepton pair in this event has a large combined P_t ($113\,GeV$), and relatively low energy jets*. For Z^0's which recoil off jets there will be, by conservation of momentum, a correlation between the jet E_t's and the P_t of the Z^0. This is demonstrated in

---

*Which is contrary to what is expected from Z^0 events with large $\not\!\!E_t$ as discussed above.

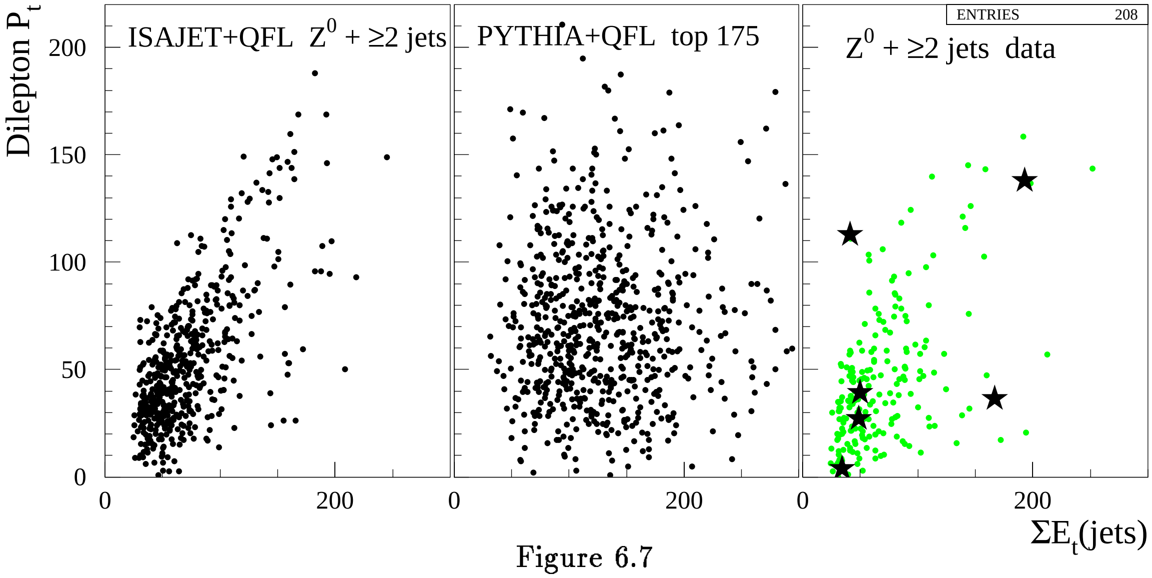

Figure 6.7

The dilepton P_t versus $\sum_j E_t$ for $Z^0 + 2\,jet$ Monte Carlo, top 175 Monte Carlo, and $Z^0 + 2\,jet$ data. The 6 data events in the Z^0 mass window which pass the $\not{E}_t$ and 2-jet requirements are represented by stars.

Figure 6.7, which shows the correlation for $Z^0 + 2\,jet$ Monte Carlo events, and the lack of such a significant correlation in $t\bar{t}$ Monte Carlo events with $m_t = 175\,GeV$. Event 65004/23360 ($\sum_j E_t = 41\,GeV, P_t(\ell\ell) = 113\,GeV$) is shown to be somewhat removed from what is expected from $Z^0 + 2\,jet$ events. The event with a b-tagged jet (43170/198920) is at ($\sum_j E_t = 167\,GeV, P_t(\ell\ell) = 36\,GeV$).

If one interprets 2 of these 6 events as coming from $t\bar{t}$ decay*, then the predicted Drell-Yan background is an overestimate, though the uncertainty is properly taken into account. The probability that the expected number of $t\bar{t}$ decays in the Z^0 mass

---

*Or from some other source besides Drell-Yan.

	Data		Monte Carlo
	Before 2-jet cut	After all dilepton selection cuts	After all dilepton selection cuts
ee	1.8 ± 0.5	0.32 ± 0.19	0.22 ± 0.07
$\mu\mu$	1.0 ± 0.4	0.30 ± 0.19	0.26 ± 0.08
$\ell\ell$	2.8 ± 0.6	$\mathbf{0.62 \pm 0.30}$	0.48 ± 0.10

Table 6.3

Summary of the Drell-Yan contribution to the dilepton signal in $109\,pb^{-1}$, corrected for the expected $t\bar{t}$ contribution. The predictions from a $500\,pb^{-1}$ ISAJET+QFL Z^0 sample are given for comparison.

window, 0.74 ± 0.22, could fluctuate to 2 or more events is 17%.

6.1.4 Summary of Drell-Yan background predictions

The Drell-Yan predictions calculated in the previous subsections are summarized in Table 6.3, with the expected top contribution in the Z^0 mass window taken into account. Recall from Table 6.1 that before the subtraction of the expected contribution from $t\bar{t}$ decay the Drell-Yan background result was 0.70 ± 0.20 events in $109\,pb^{-1}$. For comparison, the expected Drell-Yan background as predicted from Z^0 Monte Carlo is given after all dilepton selection cuts. The Monte Carlo numbers are calculated using the $500\,pb^{-1}$ ISAJET+QFL Z^0 sample for the number of events in the Z^0 mass region, and with a lower statistics ISAJET+QFL Drell-Yan sample to calculate the ratio of events outside the Z^0 mass window to that inside. The ISAJET Drell-Yan sample gives about 15% fewer events outside the Z^0 mass window than observed in the data, relative to the number of events inside the mass window.

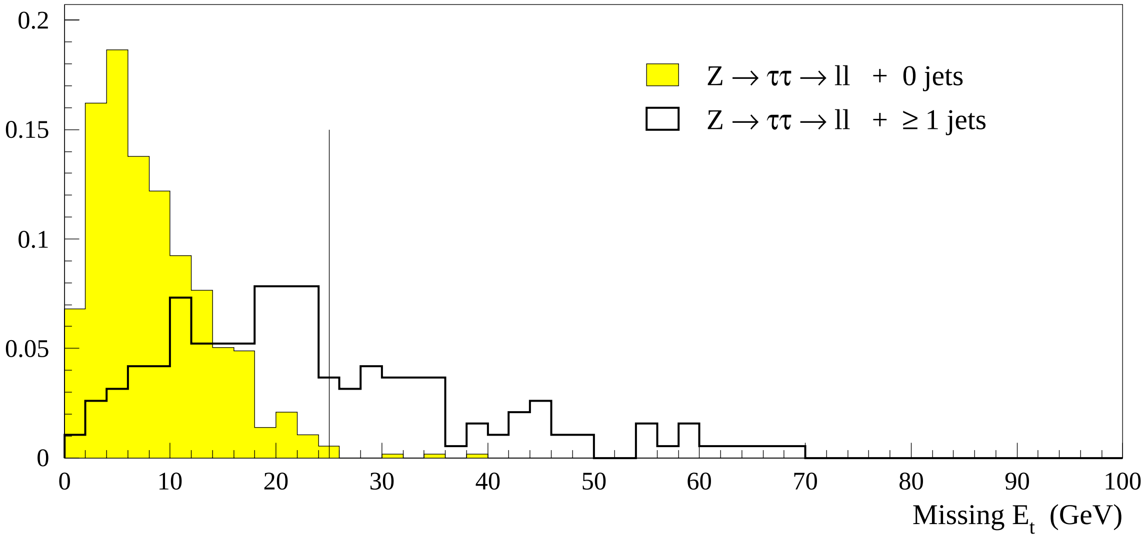

Figure 6.8

Missing transverse energy distributions in ISAJET Monte Carlo $Z^0 \rightarrow \tau^+\tau^- \rightarrow \ell^+\ell^-$ ($\ell = e$ or μ) events. The line represents the $|\not{E}_t|$ cut at $25\,GeV$. Both distributions are normalized to 1.

In the $500\,pb^{-1}$ ISAJET sample, 10 ee and 11 $\mu\mu$ events survive all dilepton cuts (except the Z^0 mass cut), giving a predicted background from Drell-Yan of 0.48 ± 0.10 events in $109\,pb^{-1}$. This number is lower but still consistent with the prediction from the Z^0 data. It should be noted that although ISAJET+QFL gives good agreement with the data for the $\not{E}_t$ and $\sum_j E_t$ distributions in Figure 6.2, the fraction of Z^0 events in the ISAJET sample with 2 or more jets is $(2.4 \pm 0.1)\%$ compared to the $(3.8 \pm 0.3)\%$ seen in the Z^0 data.

6.2 $Z^0 \rightarrow \tau^+\tau^-$

The production of Z^0 bosons in association with at least 2 QCD jets, where the Z^0 then decays to a tau pair, can be a source of dilepton background if both τ's decay leptonically. The branching ratio for the leptonic decay of a tau $BR(\tau \rightarrow \ell\nu_\ell\nu_\tau$, $\ell = e$ or $\mu)$, is 18% [64], giving BR($Z^0 \rightarrow \tau^+\tau^- \rightarrow \ell^-\overline{\nu}_\ell\nu_\tau\ell^+\nu_\ell\overline{\nu}_\tau$) = 13%. The 4 neutrinos in the event contribute to the $\not{E}_t$. However, if the two τ's are back to back, as is mostly the case if the Z^0 is not recoiling off any jet activity in the event, then the neutrino momenta will largely cancel leading to only a small $\not{E}_t$. This is demonstrated in Figure 6.8 which shows the $\not{E}_t$ distributions for $Z^0 \rightarrow \tau^+\tau^-$ events, both with no jets in the event and with at least one jet in the event. Therefore, it will be mostly those $Z^0 \rightarrow \tau^+\tau^-$ events with jets that will pass the $\not{E}_t$ cuts, thus making the jet activity very important to the level of this background.

For the $Z^0 \rightarrow \tau^+\tau^-$ background estimate presented here, a large ISAJET+QFL $Z^0 \rightarrow \tau^+\tau^-$ sample was used [65]. This estimate will be compared to the predictions from a somewhat smaller VECBOS sample, and also to previously published numbers from Run 1A which have been scaled to the full Run 1 luminosity of $109\,pb^{-1}$.

The method used in Run 1A to calculate the $Z^0 \rightarrow \tau^+\tau^-$ background utilized the $Z^0 \rightarrow e^+e^-$ data, thus bypassing the dependence on a Monte Carlo generator to correctly simulate jet activity [66, 59, 67]. In a sample of $Z^0 \rightarrow e^+e^-$ data events, the 2 electrons were replaced by 2 taus which were then decayed by ISAJET to an electron or muon, and simulated by QFL. In order to get better statistics, each $Z^0 \rightarrow e^+e^-$ data event was simulated in this way 80 times. By scaling the Run 1A ($19.3\,pb^{-1}$) background estimate to the total Run 1 luminosity ($109\,pb^{-1}$), and correcting for differences between the Run 1A and Run 1 selection [68], one gets the following expected background contributions from $Z^0 \rightarrow \tau^+\tau^-$:

$$N_{bg}^{Z\rightarrow\tau\tau}(ee+\mu\mu) = 0.28 \pm 0.08 \ \text{ events}$$

Dilepton Cut	ee	$\mu\mu$	$e\mu$	$\ell\ell$
Lepton ID	154	180	386	720
Same-Sign	154	180	386	720
Isolation	154	178	385	717
Invariant Mass	147	167	385	699
Missing E_t	6	15	31	52
$N_{jets} = 0$	1	0	0	1
$N_{jets} = 1$	1	9	18	28
$N_{jets} \geq 2$	4	3	13	20
2-jet (corrected for ϵ_{LID})	3.5	2.7	11.6	17.8

Table 6.4

Results of applying the dilepton cuts to a $Z^0 \rightarrow \tau^+\tau^-$ ISAJET+QFL Monte Carlo sample of 760 000 events.

$$N_{bg}^{Z\rightarrow\tau\tau}(e\mu) = 0.34 \pm 0.08 \quad \text{events,}$$

giving a total of 0.62 ± 0.11 expected events in the top dilepton signal.

A VECBOS+HERPRT+TAUOLA+QFL sample representing an integrated luminosity of $1140 \pm 100\,pb^{-1}$, gives a total $Z^0 \rightarrow \tau^+\tau^-$ expectation of 0.41 ± 0.20 background events. Recall from section B that VECBOS+HERPRT has been shown to give good agreement with the jet multiplicity seen in Z^0 data.

The ISAJET+QFL $Z^0 \rightarrow \tau^+\tau^-$ sample used for the current background estimate, is composed of 760 000 events with no forced decays. Using the latest CDF cross-section measurement for $Z^0 \rightarrow e^+e^-$ of $\sigma \cdot BR(Z^0 \rightarrow e^+e^-) = 0.231 \pm 0.012\,nb$[69], and assuming lepton universality in the decay of the Z^0, the ISAJET sample represents an integrated luminosity of $3300 \pm 200\,pb^{-1}$. This is over 30 times the luminosity accumulated in the data. The results of running the dilepton data analysis on this sample are given in Table 6.4. The events passing the $\not\!\!E_t$ cuts have been divided according to their jet multiplicity. The last row is the number of events passing the 2-jet cut and corrected for the discrepancy in lepton identification efficiencies between QFL and data (see section 5.3). From this table one also obtains the ISAJET+QFL predictions for the efficiencies of the $\not\!\!E_t$ and 2-jet cuts for $Z^0 \rightarrow \tau^+\tau^-$ events to be;

$$\epsilon_{\not E_t} = 0.074 \pm 0.010 \quad (\text{after Z}^0 \text{ mass cut})$$

$$\epsilon_{2-jet} = 0.38 \pm 0.08 \quad (\text{after } \not\!\!\mathrm{E}_\mathrm{t} \text{ cuts})$$

respectively. As mentioned above, the low $\not\!\!E_t$ efficiency is mainly due to 0-jet events. The effect of the $\not\!\!E_t$ cuts on $Z^0 \rightarrow \tau^+\tau^-$ events is shown in Figure 4.14. Note that in this plot the azimuthal angular separation between the $\not\!\!E_t$ and the nearest lepton is used, *not* between the $\not\!\!E_t$ and nearest lepton *or* jet, which is what is cut on. However, for $Z^0 \rightarrow \tau^+\tau^-$ events the $\not\!\!E_t$ direction is nearly always closer to a lepton direction than to a jet.

The invariant mass cut does not remove a large fraction of $Z^0 \rightarrow \tau^+\tau^-$ events, because the energy carried away by the neutrinos in the τ decays diminishes the energy available to the electrons or muons, thus shifting the dilepton invariant mass distribution lower. This is demonstrated in Figure 6.9.

The numbers from Table 6.4 are used to calculate the $Z^0 \rightarrow \tau^+\tau^-$ background

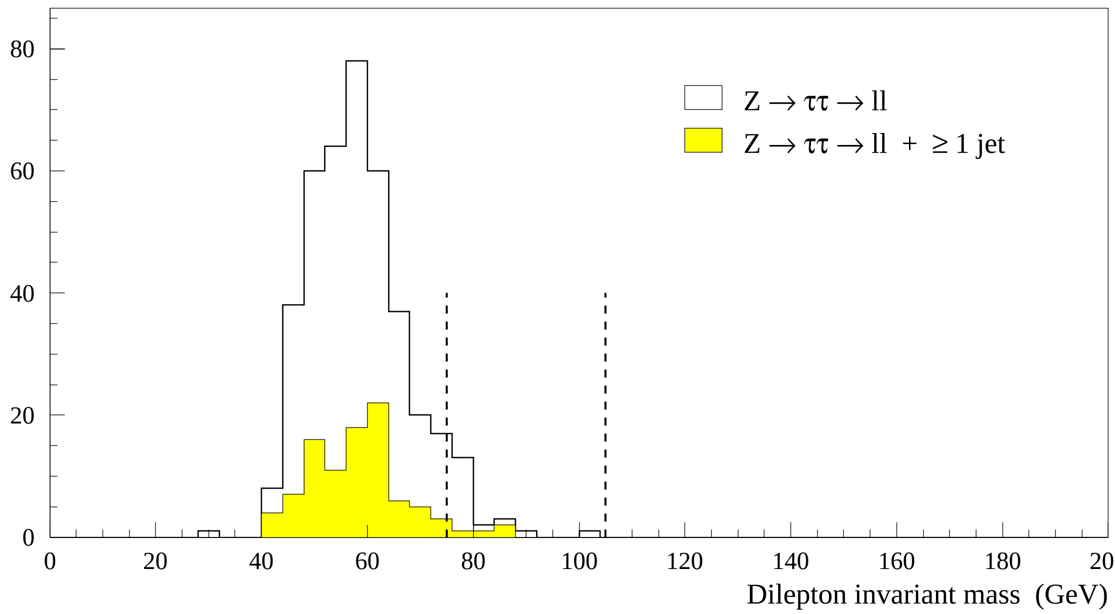

Figure 6.9

The ee and $\mu\mu$ invariant mass distribution from an ISAJET Monte Carlo sample of $Z^0 \rightarrow \tau^+\tau^- \rightarrow \ell^+\ell^-$ ($\ell = e$ or μ) events, after the lepton ID, same-sign, and isolation cuts have been applied. The vertical dashed lines represent the Z^0 mass window used for the invariant mass cut.

estimates in $109\,pb^{-1}$. These are summarized in Table 6.5, and are in good agreement with the other estimates above, obtained by scaling the Run 1A results, and from VECBOS.

The ISAJET result ignores the polarization of the tau lepton from Z^0 decay, though this effect has been shown to be small [66] (in the order of 4%).

6.3 Vector boson pair production

Boson pairs ($VV = WW, WZ^0, Z^0Z^0$) can be produced in $p\overline{p}$ collisions by the

	Before 2-jet cut	After all Dilepton cuts
$ee + \mu\mu$	0.62 ± 0.15	0.21 ± 0.08
$e\mu$	0.91 ± 0.18	0.38 ± 0.11
$\ell\ell$	1.5 ± 0.2	$\mathbf{0.59 \pm 0.14}$

Table 6.5

Summary of the expected $Z^0 \to \tau^+\tau^-$ contribution to the top dilepton signal from ISAJET Monte Carlo. Errors are statistical only.

processes illustrated in Figure 6.10, which include the t- or u-channel diagram involving boson-fermion couplings, and the s-channel diagram involving the tri-boson coupling. Only WW production is shown here, but analogous diagrams for WZ^0 production also exist. Production of Z^0 pairs can not occur through any standard model tri-boson vertex, but can occur by a diagram analogous to the first in Figure 6.10 involving the boson-fermion couplings. The tri-boson vertices contributing to WW production, the WWZ and $WW\gamma$ vertices*, are the only tri-boson vertices in the standard model. A next-to-leading-order (NLO) standard model calculation gives the following cross-sections for diboson production in $p\overline{p}$ collisions at $\sqrt{s} = 1.8\,TeV$ [70, 71, 72]:

$$\sigma(p\overline{p} \to WW) = 9.5\,pb,$$

$$\sigma(p\overline{p} \to WZ^0) = 2.5\,pb.$$

---

*The WWZ vertex also contributes to WZ^0 production.

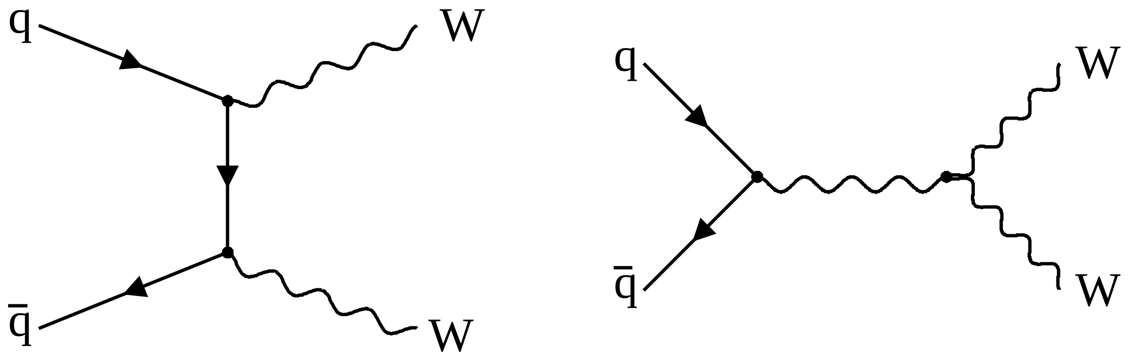

Figure 6.10

Feynman diagrams for tree level WW production in the Standard Model.

The dominant VV source of background in the $t\bar{t}$ dilepton channel is from WW production. This is discussed in the next section, with the contributions from WZ^0 and Z^0Z^0 briefly examined in section 6.3.3.

6.3.1 *WW* production

Higher order diagrams of W pair production which include at least 2 jets, can potentially satisfy the top dilepton channel criteria if both W's decay leptonically ($p\bar{p} \to W^+W^- + 2\,jets \to \ell^+\nu_\ell\ell^-\overline{\nu}_\ell + 2\,jets$). Such events contain 2 neutrinos which can supply the required $\not{E}_t$. The branching ratio for the WW dilepton decay channel is, $BR(W^+W^- \to \ell^+\nu_\ell\ell^-\overline{\nu}_\ell) = 5\%$, where, $\ell = e$ or μ. It is noted that $W \to \tau\nu_\tau$ decays will also contribute, in the order of 10%, similarly to the $t\bar{t}$ dilepton channel (see section 5.4). This is included in the WW acceptance, and in the final WW background estimate, but for the sake of clarity will be mentioned only this once.

The WW background estimate is calculated in 2 ways. The final results will be based on a similar method to that used previously [59, 68], which uses an ISAJET WW sample in conjunction with a matrix element (ME) calculation to obtain the 2-jet fraction. This result will be checked with the prediction from a large PYTHIA WW sample. The ISAJET + ME calculation is presently preferred because it is better understood than the more recent PYTHIA result. The WW ISAJET+QFL Monte Carlo sample consists of 100 000 generated events, and the PYTHIA+QFL sample represents 900 000 WW events (with no forced decays), giving much better statistics.

The expected number of WW events passing the dilepton selection can be written as:

$$N_{bg}^{WW} = \epsilon_{tot-2j}^{WW} \times \epsilon_{2j}^{WW} \times \sigma(p\overline{p} \to WW) \cdot BR(WW \to \ell\nu\ell\nu) \times \mathcal{L} \qquad (6.3)$$

where, ϵ_{tot-2j}^{WW} is the efficiency of all cuts except the 2-jet cut, and ϵ_{2j}^{WW} is the efficiency of the 2-jet cut, *after all other cuts have been applied.* The reason for separating the total acceptance, $\epsilon_{tot}^{WW} = \epsilon_{tot-2j}^{WW}\,\epsilon_{2j}^{WW}$, in this way is because an independent ME calculation is used for the 2-jet fraction in WW events, as will be discussed below. The integrated luminosity, $\mathcal{L}$, is $109\,pb^{-1}$. The theoretical cross-section $\sigma(p\overline{p} \to WW) = 9.5\,pb$ is used, and is assigned an uncertainty of 30%, resulting from theoretical uncertainties [71] and the fact that ISAJET returns a WW cross-section of $\sim 6\,pb$. A cross-section of $9.5\,pb$ implies the ISAJET sample corresponds to an integrated luminosity of $10.5\,fb^{-1}$.

The ISAJET sample was run through the top dilepton data analysis, with corrections made for lepton efficiencies as discussed previously. The number of WW events surviving each stage of the dilepton analysis is given in Table 6.6. A muon trigger simulation was applied [57], which reduced the initial number of $\mu\mu$ events by about 25% (large because most of these events do not contain jets and so are more

Dilepton Cut	ee	$\mu\mu$	$e\mu$	$\ell\ell$
Geom/P_t	234	298	640	1172
Lepton ID	197	278	575	1050
Same-Sign	196	278	575	1049
Isolation	194	274	564	1032
Invariant Mass	153	214	564	931
Missing E_t	100	149	387	636
$N_{jets} = 0$	61	86	240	387
$N_{jets} = 1$	31	43	112	186
$N_{jets} \geq 2$	8	20	35	63
2-jet (corrected for ϵ_{LID})	6.8	18.3	30.8	55.9

Table 6.6

The numbers of events surviving the consecutive dilepton cuts in a WW ISAJET+QFL Monte Carlo sample of 100 000 events.

prone to the muon prescales). The events surviving up to and including the $\not{E}_t$ cuts have been divided according to jet multiplicity. The number of WW events passing all cuts is 55.9 ± 7.5 in $10.5\, fb^{-1}$. This gives the following efficiencies (defined above) from the ISAJET sample:

$$\epsilon^{WW}_{tot-2j} = (0.56 \pm 0.02)\% \ ,$$

$$\epsilon_{2j}^{WW} = (9.9 \pm 1.2)\% \ .$$

Substituting this result in equation 6.3, together with the 30% uncertainty in the WW cross-section, gives for $109\,pb^{-1}$ of data :

$$N_{bg}^{WW} = 0.58 \pm 0.19 \ \text{ events } \quad \text{(ISAJET only)}.$$

This would be the final result if one were confident that ISAJET was calculating the correct 2-jet fraction in WW events. However, there is reason to believe that this is not the case. For instance the jet multiplicity seen in Z^0 data events is not replicated well by ISAJET, as was seen in section 6.1 (though the jet energy and $\not{E}_t$ spectra were in rather good agreement).

As an independent estimate of jet activity, a $WW + multijet$ parton level calculation was performed [73], with hard gluon radiation and jet fragmentation added using HERPRT. This gave a very different 2-jet fraction from the $(9.9 \pm 1.2)\%$ predicted from ISAJET, as will be shown below. VECBOS+HERPRT simulates the jet activity in good agreement with that seen in Z^0 data events [74], giving confidence in the independent VECBOS-like parton level calculation. In addition, using VECBOS+HERPRT, the jet activity in Z^0 events was compared to that in $Z^{0'}$ events, where the $Z^{0'}$ calculation is the same as for the Z^0 calculation but with the Z^0 mass increased to the average WW mass of $250\,GeV$.

Since the production diagrams for $Z^{0'}$ and WW are different, it is not obvious that the 2-jet fractions should be the same. However, the 2-jet fractions have been calculated for both the WW production diagrams (all of them summed) using a parton level calculation, and for the $Z^{0'}$ production diagrams using a modified version of VECBOS, and they come out identical [75].

VECBOS (with a $Z^{0'}$ mass of $250\,GeV$) predicted that the 2-jet fraction should increase by a factor of 1.44 if the Z^0 mass is increased from $91\,GeV$ to $250\,GeV$.

However this factor is sensitive to various theoretical uncertainties. For instance, the Q^2 scale used to evaluate α_s makes a significant difference, especially in processes where α_s gets squared such as $WW + 2\,jets$ production. The factor of 1.44 uses an α_s evaluated at $Q^2 = M^2_{WW}$, that is, around $(250\,GeV)^2$. If instead, Q^2 is chosen to be the average P_t^2 of the jets, then α_s is being evaluated at a scale of around $(20\,GeV)^2$ or $(30\,GeV)^2$, and it is found that the factor of 1.44 increases to 1.83. If the same procedure of increasing the Z^0 mass is performed using ISAJET, a factor of 1.61 is obtained for the increase in the 2-jet fraction. In this calculation jets are defined using GENP particles in a cone of 0.7, rather than partons. The ISAJET calculation gives a $Z^{0'}$ 2-jet fraction similar to the VECBOS+HERPRT $Z^{0'}$ 2-jet fraction, and therefore similar to the independent parton level calculation of the WW 2-jet fraction. However, ISAJET gives a WW 2-jet fraction much bigger than its $Z^{0'}$ 2-jet fraction. This is not yet understood, and it is for this reason that the ISAJET result by itself is not used. Given the observed variation in the ratio of 2-jet fractions in the $Z^{0'}$ and Z^0 calculations, this factor is taken to be 1.6 ± 0.4.

The factor of 1.6 ± 0.4 is used on the 2-jet fraction seen in the $109\,pb^{-1}$ of Z^0 data, to get the expected 2-jet fraction in WW events. The following 2-jet fractions are seen in the $Z^0 \rightarrow e^+e^-$ and $Z^0 \rightarrow \mu^+\mu^-$ data:

$$f_{2j}^{ee} = \frac{90}{2501} = (3.6 \pm 0.4)\% \ ,$$

$$f_{2j}^{\mu\mu} = \frac{120}{3028} = (4.0 \pm 0.4)\% \ ,$$

$$f_{2j}^{\ell\ell} = \frac{210}{5529} = (3.8 \pm 0.3)\% \ .$$

Therefore, the expected 2-jet fraction in WW events is:

$$f_{2j}^{WW} = (6.1 \pm 1.6)\% \ .$$

The expected WW background as obtained from ISAJET, where the 2-jet fraction was $(9.9 \pm 1.2)\%$, then needs to be scaled down by a factor of 0.62 ± 0.18. This gives for the WW background in $109\,pb^{-1}$:

$$N_{bg}^{WW}(ee + \mu\mu) = 0.16 \pm 0.07 \ \text{ events.}$$

$$N_{bg}^{WW}(e\mu) = 0.20 \pm 0.09 \ \text{ events.}$$

$$N_{bg}^{WW} = 0.36 \pm 0.16 \ \text{ events.}$$

One should note that the 2-jet fraction obtained from the Z^0 data together with the parton level Monte Carlo (6.1%) is, strictly speaking, that expected before the invariant mass and $\not{E}_t$ cuts are applied. This is in contrast to the 2-jet fraction in WW events quoted from ISAJET (9.9%), which is obtained after *all* other selection cuts. However, the 2-jet fraction observed in the WW ISAJET sample before the invariant mass and $\not{E}_t$ cuts is consistent with the 2-jet fraction in the events after these cuts ($(11.0 \pm 1.0)\%$ compared to $(9.9 \pm 1.2)\%$). That is, the 2-jet fraction in WW events is not strongly correlated with the other cuts, thus validating the above method.

As mentioned above a PYTHIA+QFL sample of 900 000 WW events, representing an integrated luminosity of $95\,fb^{-1}$, has been generated to give an independent estimate of the WW background contribution to the dilepton signal. The results from this sample are given in Table 6.7, which is analogous to the ISAJET results in Table 6.6. Note that in comparison with the 2-jet fraction from ISAJET, $(9,9 \pm 1.2)\%$), and from a VECBOS ME calculation in conjunction with Z^0 data, $(6.1 \pm 1.6)\%$, PYTHIA gives a 2-jet fraction of $(4.6 \pm 0.3)\%$, where the error is statistical only. The effects of the invariant mass and $\not{E}_t$ cuts are shown in Figures 6.11 and 6.12 respectively. The background estimates from this sample are shown for comparison in Table 6.8.

Dilepton Cut	ee	$\mu\mu$	$e\mu$	$\ell\ell$
Geom/P_t	2078	2335	5406	9819
Lepton ID	1756	2227	4681	8664
Same-Sign	1756	2223	4678	8657
Isolation	1731	2184	4604	8519
Invariant Mass	1290	1651	4604	7545
Missing E_t	897	1150	3118	5165
$N_{jets} = 0$	670	867	2386	3923
$N_{jets} = 1$	182	233	588	1003
$N_{jets} \geq 2$	45	50	144	239
2-jet (corrected for ϵ_{LID})	38.9	44.9	124.9	208.7

Table 6.7

The numbers of events surviving the consecutive dilepton cuts in a WW PYTHIA+QFL Monte Carlo sample of 900 000 events.

6.3.2 WW background before 2-jet cut

The WW dilepton signature in the 0-jet bin is rather different from the other dilepton processes, and so can provide a good check between the Monte Carlo estimate and what is seen in the data. As shown in Figure 6.12, WW events with 0 jets that pass the $\not{E}_t$ cut tend to have their leptons pointing away from the $\not{E}_t$. As the

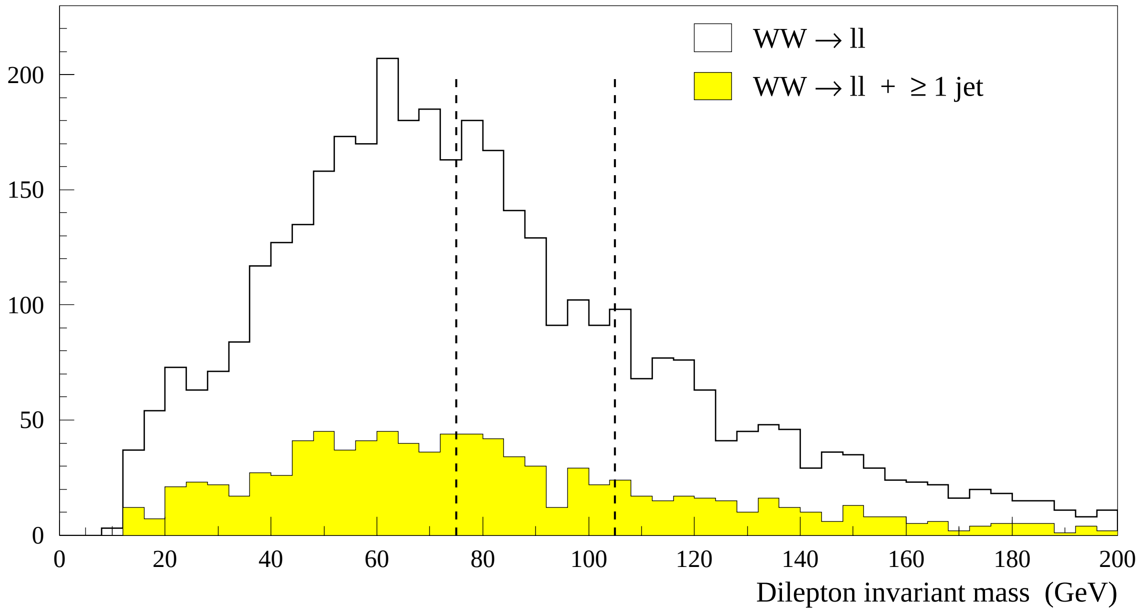

Figure 6.11

The ee and $\mu\mu$ invariant mass distribution from a PYTHIA WW sample representing $95\,fb^{-1}$, after the lepton ID, same-sign, and isolation cuts have been applied. The vertical dashed lines represent the Z^0 mass window used for the invariant mass cut.

$\not{E}_t$ increases in $WW + 0\,jet$ events, the 2 neutrinos will tend to be more aligned and thus more back-to-back with the 2 leptons. If the W pair is recoiling off some jet activity then the neutrino and lepton momenta will tend to be pointing more in the same direction, which is demonstrated in the 1 and ≥ 2 jet bins of Figure 6.12. From the analogous 0-jet data plots of Figures 4.21, 4.22, and 4.23, there are 2 $ee + 0\,jet$ events and 3 $e\mu + 0\,jet$ events (as well as 1 $\mu\mu + 1\,jet$ event) which demonstrate the topology expected from WW events, and which therefore stand out as possible WW candidates.

Using the $10.5\,fb^{-1}$ WW ISAJET sample, the results in Table 6.6 give for the

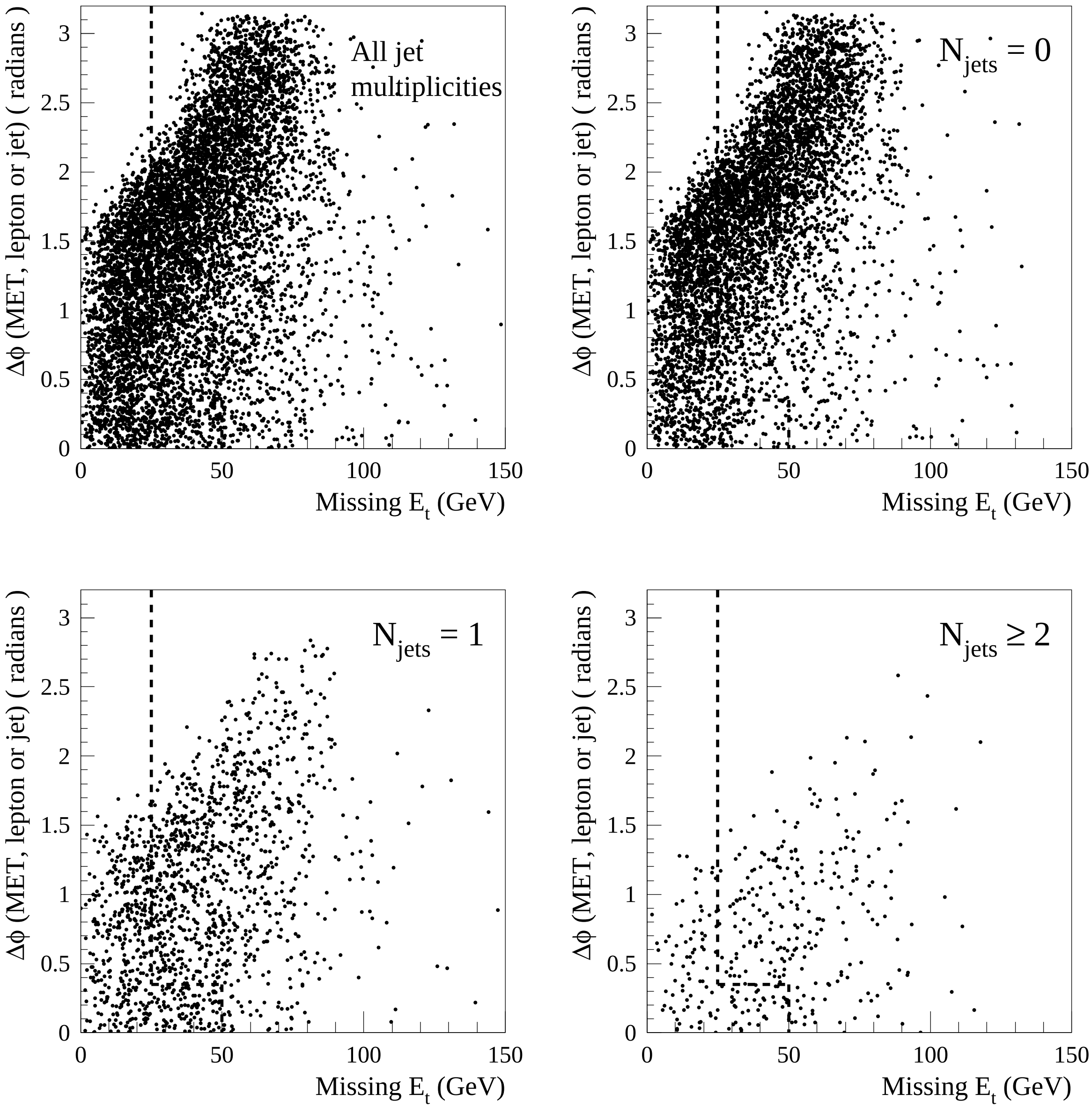

Figure 6.12

The azimuthal angular difference between the $\not\!\!E_t$ and the nearest lepton or jet, versus the $\not\!\!E_t$, for a PYTHIA WW sample representing $95\, fb^{-1}$, after the dilepton selection up to the $\not\!\!E_t$ cuts. These distributions are very similar to those seen in the ISAJET sample used for the background estimate, but have better statistics.

expected number of WW events before the 2-jet cut in $109\,pb^{-1}$:

$$N_{bg}^{WW}(ee+\mu\mu) = 2.3 \pm 0.8 \quad \text{(before 2jet cut)}.$$

$$N_{bg}^{WW}(e\mu) = 3.5 \pm 1.1 \quad \text{(before 2jet cut)}.$$

$$N_{bg}^{WW} = 5.8 \pm 1.9 \quad \text{(before 2jet cut)}.$$

These numbers have been corrected for the lepton efficiency differences seen between QFL and data. This result is consistent with what is seen in the data.

6.3.3 WZ^0 and Z^0Z^0 production

The most probable channel for a WZ^0 event to appear in the $t\bar{t}$ dilepton signal region, would be the case where the Z^0 decays leptonically, to produce the 2 high-P_t leptons, and the W hadronically, to give the required 2 jets. The branching ratio for this decay channel is about 4.5%*. However, such a WZ^0 decay has no natural source of $\not{E}_t$, and so the required $\not{E}_t$ would need to come from the mismeasurement of the jet energies. One can use $Z^0+2\,jet$ data to get a rough idea of the $\not{E}_t$ rejection factor in such WZ^0 events. This is :

$$\frac{\text{Number of } Z^0 + \not{E}_t + 2\,jet \text{ events}}{\text{Number of } Z^0 + 2\,jet \text{ events}} = \frac{6}{208} = 2.9 \pm 1.2\%.$$

If in addition one assumes the WZ^0 events are reduced by the Z^0 mass cut by about an additional factor of ~ 5 (estimated from the $Z^0+ \geq 2\,jet$ data), and that the 2-jet fraction in such events is 1 (clearly an overestimate), then, the combined efficiency of the Z^0 mass cut, the $\not{E}_t$ cuts, and the 2-jet cut is about 0.6%. Using the results of the previous sections, the same combined efficiency for WW events is about 3.7%. This combined with the differences in the WW and WZ^0 cross-sections, implies the

---

*$BR(Z^0 \to e^+e^- \text{ or } \mu^+\mu^-) = 6.8\%$ and $BR(W \to ud \text{ or } cs) = 67\%$.

WZ^0 contribution to the dilepton signal will be *at least* 25 times smaller than the WW contribution, and is therefore neglected in the VV background estimate. One might argue that WZ^0 production could contribute through the leptonic decays of both the Z^0 and the W, since this would have a greater efficiency for passing the Z^0 mass cut. However, the branching ratio is 3 times smaller, and similarly to WW production, at least 2 QCD jets will additionally be required. This gives a contribution roughly 60 times smaller than the WW contribution.

Similar arguments apply to the expected Z^0Z^0 contribution. The $p\overline{p} \rightarrow Z^0Z^0$ cross-section is $1.0\,pb$ [76], and the branching ratio for one Z^0 to decay leptonically and the other hadronically is about 9%. This together with the expected $\not{E}_t$ and Z^0 mass rejection factors gives a Z^0Z^0 contribution of the same order as the WZ^0 contribution, and is therefore also neglected in the background estimate.

6.3.4 VV background summary

Of the possible diboson background sources only W pair production is significant. A summary of the expected WW contribution to the dilepton signal, both after all cuts and before the 2-jet cut, is given in Table 6.8. Both the ISAJET+ME and PYTHIA predictions are shown. The result used is that from the ISAJET+QFL WW sample of 100 000 events ($10.5\,fb^{-1}$) with the 2-jet fraction calculated independently using a parton level ME Monte Carlo.

6.4 Fake leptons

The dilepton background contribution from events in which one lepton is *faked* by a hadronic particle is expected to come primarily from $W+ \geq 3\,jet$ events, in which the W decays leptonically. An example of such a process which could

	ISAJET + ME calculation		PYTHIA	
	Before 2-jet cut	After all dilepton cuts	Before 2-jet cut	After all dilepton cuts
$ee{+}\mu\mu$	$2.3 \pm 0.2 \pm 0.8$	$0.16 \pm 0.05 \pm 0.05$	$2.1 \pm 0.05 \pm 0.6$	$0.10 \pm 0.01 \pm 0.03$
$e\mu$	$3.5 \pm 0.2 \pm 1.1$	$0.20 \pm 0.06 \pm 0.06$	$3.1 \pm 0.06 \pm 0.9$	$0.14 \pm 0.01 \pm 0.04$
$\ell\ell$	$5.8 \pm 0.3 \pm 1.9$	$\mathbf{0.36 \pm 0.11 \pm 0.11}$	$5.2 \pm 0.08 \pm 1.5$	$0.24 \pm 0.02 \pm 0.07$

Table 6.8

Summary of the expected WW contribution to the top dilepton signal. The first error is statistical and the second is the 30% systematic error assigned to the WW cross-section.

fake the dilepton signature is shown in Figure 6.13. Charged hadrons which don't interact significantly in the calorimeters and punch through to the muon chambers, can fake the presence of a muon. Also, hadronic decays-in-flight in which a muon is produced just before or in the calorimeter can mimic a muon from the primary vertex. Electrons can be impersonated by highly electromagnetic jets, for instance jets which contain photons or π^0's can look like tracks (produced by charged particles in the jets) pointing to mostly electromagnetic clusters. The probability for a hadron to fake a lepton is very small ($\sim 10^{-4}$), therefore, the case of 2 jets faking leptons in 4-jet events is neglected.

Since a faked lepton in a $W+ \geq 3\,jet$ event will have no charge preference, there is expected to be the same level of fake background in same-sign dilepton events as in opposite-sign dilepton events. One can therefore use the same-sign dilepton results

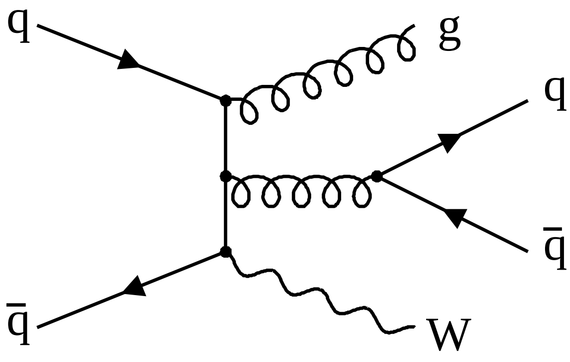

Figure 6.13

Example of W boson production in association with 3 jets.

from section 7.6 to obtain an estimate of the fake background. Before the 2-jet cut there are 3 same-sign dilepton events (1 $\mu\mu$ and 2 $e\mu$) that have passed the $\not{E}_t$ cuts. As discussed in section 7.6, the same-sign $\mu\mu$ event looks like a cosmic ray event. Of the remaining 2 $e\mu$ events, one has a b-tagged jet, and is a $t\bar{t}$ candidate in the *lepton + jets* analysis. Both same-sign $e\mu$ events pass the 2-jet cut. To obtain an estimate of the fake dilepton background using same-sign events, the 2 $e\mu$ events before the 2-jet cut are used, and the expected 2-jet cut efficiency for fake events applied to them. A jet is labelled "fakable" if it has corrected $P_t > 20\,GeV$, and $|\eta| < 1.2$. The 2-jet cut efficiency for fake events is then calculated as the ratio of the number of "$W+ \geq 2\,jet+ \geq 1\,fakable\ jet$" events to the number of "$W+ \geq 1\,fakable\ jet$" events. A W is simply selected as a tight lepton plus $\not{E}_t > 25\,GeV$. From the full Run 1 dataset, the 2-jet cut efficiency is found to be 0.12 ± 0.01. Applying this to the 2 $e\mu$ same-sign events before the 2-jet cut gives a fake dilepton background

	Before 2-jet cut	After all dilepton cuts
$ee + \mu\mu$	1.5 ± 1.2	0.21 ± 0.17
$e\mu$	1.1 ± 1.1	0.16 ± 0.16
$\ell\ell$	2.6 ± 1.9	$\mathbf{0.37 \pm 0.23}$

Table 6.9

Expected number of fake lepton background events in $109\,pb^{-1}$.

estimate in $109\,pb^{-1}$ of;

$$N_{bg}^{fake} = 0.24 \pm 0.17 \ \ \text{events} \quad (\text{from Same}-\text{Sign analysis}).$$

A second method to estimate this background uses inclusive jet samples to calculate the probability for a jet to fake a lepton, and applies this probability to the number of fakable jets found in $W+ \geq 3\,jet$ events [77, 78]. From the jet samples, real leptons from W's and Z^0's are removed, however, real leptons from heavy flavor decay have not yet been removed because of the present uncertainty in the b-jet fraction in these jet samples. Therefore, the fake background obtained in this way will be an overestimate. Table 6.9 contains the expected number of background events from fake leptons, as a result of applying the fake probabilities to a sample of $W + multijet$ events. Although the errors are large, the 2 methods for calculating the fake background give consistent results, though the latter will be used in taking a conservative approach to the background level.

6.5 b quark pair production

The $t\bar{t}$ background from $b\bar{b}$ production is the smallest of those contributing individually to the total background estimate. For the CDF top discovery PRL [2] the estimate in $67\,pb^{-1}$ was 0.03 ± 0.02 events [68]. No new estimate was made for this thesis, and so this number will simply be scaled from the PRL luminosity to obtain the estimate in $109\,pb^{-1}$. The method used in estimating the $b\bar{b}$ contribution will be briefly discussed below.

Although the cross-section for $b\bar{b}$ production is in the order of 5×10^6 times greater than for $t\bar{t}$ production, it is extremely difficult for $b\bar{b}$ decay to mimic the signal of $t\bar{t}$ decay. Kinematical arguments insist that for a b quark decaying to a high-P_t lepton[*], it must be extremely energetic, and so all its decay products will tend to be tightly collimated[†]. Therefore, a high-P_t lepton from b decay will always be surrounded by hadronic activity, giving a low lepton identification efficiency (see section 5.3 for the efficiencies of leptons from b decay in $t\bar{t}$ events). In general these leptons will not be isolated, and the neutrinos in the event will tend to be back-to-back, making it difficult for the event to pass both the isolation and $\not{E}_t$ cuts. Also, higher order QCD processes are required to produce sufficient additional jet activity for the event to meet the 2-jet requirement.

The P_t spectrum for leptons from the decay of b quarks in $b\bar{b}$ production events is rapidly falling [79], with the probability for a single b quark to produce a lepton with $P_t > 20\,GeV$ and which passes the lepton selection requirements (see sections 4.2 and 4.3), being in the order of 10^{-4}. Nevertheless, there is a small number of $b\bar{b}$ events in the data in which 2 leptons pass the identification cuts required in the

---

[*] Note that it is really the B hadron that decays, and the detected decay products are hadrons not partons, but for convenience "b decay" will usually be the term used.

[†] Note that this is in stark contrast to t decay.

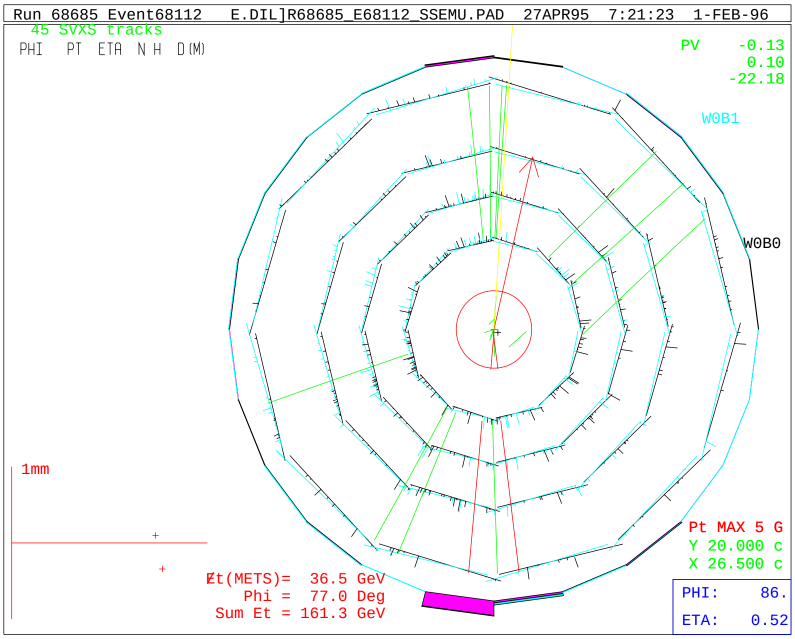

Figure 6.14

Transverse view of the tracks in the SVX from a $b\bar{b}$ event with 2 high-P_t leptons. An e^- with $E_t = 34\,GeV$ at $\phi = 264°$, and a μ^- with $P_t = 26\,GeV$ at $\phi = 86°$, both pass the lepton identification cuts. Only tracks with $P_t \geq 1\,GeV$ are shown. The arrow represents the $\not{E}_t$ before being corrected for the muon.

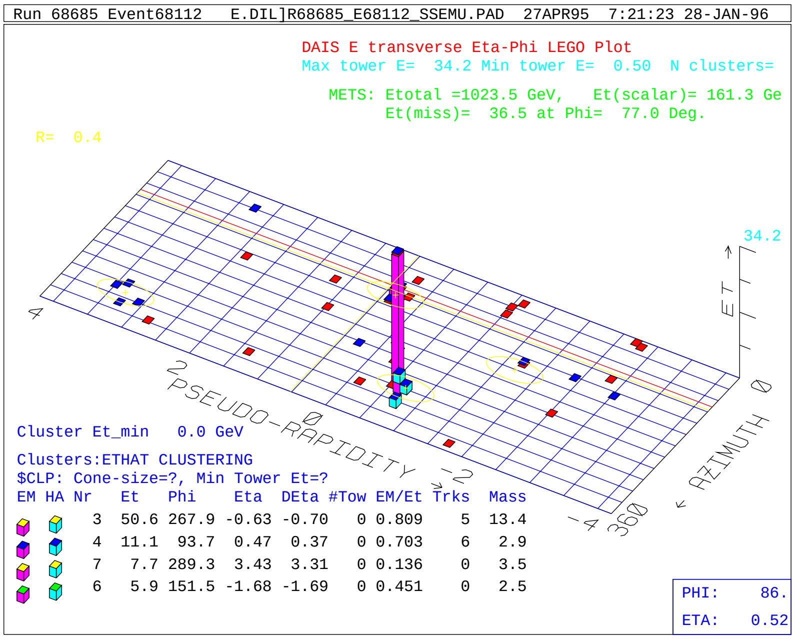

```
Cluster Et_min   0.0 GeV

Clusters:ETHAT CLUSTERING
$CLP: Cone-size=?, Min Tower Et=?
EM HA Nr    Et    Phi     Eta  DEta #Tow EM/Et Trks  Mass
          3  50.6 267.9 -0.63 -0.70   0 0.809    5  13.4
          4  11.1  93.7  0.47  0.37   0 0.703    6   2.9
          7   7.7 289.3  3.43  3.31   0 0.136    0   3.5
          6   5.9 151.5 -1.68 -1.69   0 0.451    0   2.5
```

Figure 6.15

Lego plot of the transverse energy in the calorimeter of the $b\bar{b}$ event whose tracks are shown above. The jet containing the muon is partially obscured by the electromagnetic tower of the electron.

top dilepton analysis. As an illustration of the difficulty explained above for such events to pass the subsequent dilepton selection cuts consider Figures 6.14 and 6.15 which show an $e\mu$ $b\bar{b}$ event in which both leptons pass their identification cuts; an electron with $E_t = 34\,GeV$, and a muon with $P_t = 26\,GeV$ (beam constrained). The jets containing the leptons are back-to-back, and the jet with the electron has a secondary vertex that is b-tagged by the SECVTX algorithm (see section 7.4). However, this event does not pass any of the remaining dilepton selection cuts placed on $e\mu$ events. It is of interest to note that the e and μ have the same charge resulting from either $B^0\overline{B}^0$ mixing or a cascade decay, $b \rightarrow c \rightarrow s\ell\nu_\ell$, of one of the b quarks[‡]. Neither lepton passes the isolation cuts (section 4.7), because they are both in jets, and the $\not{E}_t$ magnitude is only $13\,GeV$. The jet containing the muon has insufficient energy to pass the E_t^{raw} cut for jets (presumably since most of the b quark energy went into the muon), and jets are not counted if they are within a cone of $\Delta R = 0.4$ from electrons (see section 4.10). This results in a jet count of zero. The problems encountered by this event in passing the $t\bar{t}$ dilepton selection are expected to be typical for most $b\bar{b}$ events.

The heavy flavor background from $b\bar{b}$ production was estimated using ISAJET+-CLEO+QFL $b\bar{b}$ Monte Carlo samples, which were normalized to the low P_t $e\mu$ data of Run 1A [80, 68]. Two ISAJET samples were generated, totalling $67.5\,pb^{-1}$, both requiring at least 1 generator level (GENP) b quark with $P_t > 25\,GeV$. The generation of these samples was extremely CPU intensive, but it is hoped in the future to obtain much larger samples from which to re-study this background.

The first sample consisted of $16.3\,pb^{-1}$ of $b\bar{b}$ events in which there were required to be at least 2 leptons; at least one with $P_t > 14\,GeV$, and one with $P_t > 5\,GeV$,

---

[‡] About 35% of dilepton $b\bar{b}$ events will be same-sign because of these 2 effects [79].

	Before 2-jet cut	After all dilepton cuts
$ee + \mu\mu$	0.07 ± 0.05	0.03 ± 0.02
$e\mu$	0.05 ± 0.05	0.02 ± 0.02
$\ell\ell$	0.12 ± 0.07	$\mathbf{0.05 \pm 0.03}$

Table 6.10

Expected number of $b\bar{b}$ background events in $109\,pb^{-1}$.

which, for simplicity will be called the $(14, 5)\,GeV$ cuts. Both these cuts were at the generator level before detector simulation. This sample was used to normalize the integrated luminosity returned by ISAJET to that seen in the data. The $e\mu$ events in the data which pass $(15, 5)\,GeV$ cuts and tight lepton identification cuts, but no isolation requirement, are dominated by $b\bar{b}$ with about $20 \pm 10\%$ background [80]. The normalization factor thus obtained was applied to the full $67.5\,pb^{-1}$ of ISAJET Monte Carlo.

The second $b\bar{b}$ sample contained 2 leptons with $(10, 10)\,GeV$ cuts, and represented an integrated luminosity of $51.2\,pb^{-1}$. After the $\not{E}_t$ cuts no events are observed. To estimate the $\not{E}_t$ and 2-jet rejection factors, the P_t cuts were lowered from $20\,GeV$ to $15\,GeV$. The 2-jet rejection factor was found to be 0.43 ± 0.10, which gave the estimated $b\bar{b}$ backgrounds summarized in Table 6.10. As mentioned above, these numbers were scaled from the background estimates for the $67\,pb^{-1}$ of data used in the CDF top discovery PRL [68, 2].

6.6 Other small sources of background

The sources of dilepton events listed below were examined with the conclusion that their individual contributions are not significant to the dilepton signal. However, they will be assigned a combined contribution of 0.1 events in $109\,pb^{-1}$.

6.6.1 Radiative Z^0 bosons

Radiative Z^0 bosons, which are produced in association with an extra jet, and in which the photon meets the requirements for a jet, are a potential background if there is also $\not\!\!E_t$ in the event. At present, there is no cut to reject photons from the jet count (this will change, see Appendix D). This source of dilepton events was not anticipated, and indeed is estimated to be extremely small as will be shown below. However, the motivation to estimate this background was initiated by the observance of a $\mu\mu$ event in the $t\bar{t}$ dilepton signal region, which was very consistent with a radiative $Z^0 + 1\,jet$ event (see section 7.3). If the photon energy is large, then not only will it have a greater chance to pass the jet requirements, but it can also force the $\mu\mu$ invariant mass below the Z^0 mass window cut.

The background estimate from radiative Z^0 bosons produced in association with an extra jet has been obtained from the data as follows [81]. First the number of dilepton events in the data which have a photon of energy greater than $10\,GeV$, and for which the dilepton invariant mass is below the Z^0 mass window, are counted. This number is then scaled by 2 factors. First by the ratio of the number of $Z^0 + \geq 1\,jet$ events to the total number of Z^0 events, to give the required jet rejection, and by the ratio of the number of $Z^0 + \geq 1\,jet + \not\!\!E_t$ events to the number of $Z^0 + \geq 1\,jet$ events to get the required $\not\!\!E_t$ rejection. This gives for the estimated background from radiative Z^0 bosons in $109\,pb^{-1}$,

$$N_{bg}^{Z\gamma} = 0.07 \pm 0.04 \ \text{ events.}$$

6.6.2 $Wb\bar{b}$

The leading order diagram for $Wb\bar{b}$ production involves the formation of Wg ($q\bar{q} \rightarrow Wg$), followed by gluon splitting to a b quark pair ($g \rightarrow b\bar{b}$). The cross-section for this process multiplied by $BR(W \rightarrow e\nu \text{ or } \mu\nu)$ is in the order of $10\,pb$ [82]. To contribute to the dilepton signal the W must decay leptonically with the second lepton coming from the semi-leptonic decay of one of the b quarks. This background is not expected to contribute much to the dilepton signal because of the low detection efficiency for leptons from b decay, which is compounded by the fact that b jets from gluon splitting are generally not well separated and have extremely soft energy spectra relative that required for the production of a $20\,GeV$ lepton [82].

A HERWIG+QFL $Wb\bar{b}$ sample corresponding to an integrated luminosity of $\approx\ 10\,fb^{-1}$, was used in estimating the dilepton background from this source. This represents about 90 times more integrated luminosity than was collected in Run 1 ($109\,pb^{-1}$). No events from this $Wb\bar{b}$ sample pass all the dilepton selection cuts. However, 3 events pass all the dilepton selection except the 2-jet cut (i.e. up to and including the $\not{E}_t$ cuts), 1 with 0 jets, and 2 with 1 jet, and 13 events survive after only the lepton identification cuts. To get an estimate of the 2-jet rejection factor, the jet multiplicity of the 13 events passing lepton identification were used, because there is not expected to be a large correlation between the 2-jet cut and the other analysis requirements (mainly because the $\not{E}_t$ and an isolated lepton will result from the W decay). Of these 13 events, 5 have no jets, 6 have 1 jet, and 2 have 2 jets, giving a 2-jet rejection factor of 0.15 ± 0.11. Therefore, the expected number of dilepton events in $109\,pb^{-1}$ of data from $Wb\bar{b}$ is estimated to be:

$$N_{bg}^{Wb\bar{b}} = 0.005 \pm 0.004 \text{ events.}$$

Consequently this source of dilepton events is justifiably neglected.

The dilepton signal contribution was not calculated for the $Z^0 b\bar{b}$ process, but was assumed also to be negligible, given that the cross-section is 10 times smaller than for $Wb\bar{b}$, and even if both leptons came from the Z^0, the probability of passing both the invariant mass and $\not{E}_t$ cuts would be extremely low. This process is discussed more in section 7.5 where a trilepton event that passes all dilepton cuts except the $\not{E}_t$ cuts is identified as a possible candidate for $Z^0 b\bar{b}$ production.

6.6.3 Associated production of SM Higgs bosons

Associated Higgs boson production at $p\bar{p}$ colliders occurs through the processes, $q\bar{q} \rightarrow W^* \rightarrow W^{\pm}H^0$, and, $q\bar{q} \rightarrow Z^* \rightarrow Z^0 H^0$. The neutral Higgs boson will then preferentially decay to a $b\bar{b}$ pair, as a result of the $H \rightarrow f\bar{f}$ decay rate being proportional to the square of the fermion mass*.

A dilepton signature can result in WH^0 if the W decays leptonically ($W \rightarrow e\nu$ or $\mu\nu$) and a b quark decays semi-leptonically to produce a sufficiently high-P_t lepton. $Z^0 H^0$ production would require, $Z^0 \rightarrow e^+e^-$ or $\mu^+\mu^-$, to contribute to the dilepton signal, however, the invariant mass and $\not{E}_t$ cuts will severely reduce this possible source.

In a sample of 26 800 $Z^0H^0 + WH^0$ PYTHIA+QFL Monte Carlo events [83] (where $\sigma(WH)/\sigma(ZH) = 1/0.6$), generated with a Higgs mass of $M_H = 100\,GeV$, and with H forced to decay to $b\bar{b}$, 3 events pass the dilepton analysis selection. If the combined cross-section of WH^0 and Z^0H^0 production at $M_H = 100\,GeV$ is

---

*True only for a light Higgs: $M_H < 2M_W$.

denoted, $\sigma_{VH} = \sigma_{WH} + \sigma_{ZH}$, then, in $109\,pb^{-1}$ of data, the number of dilepton events expected from associated Higgs production is:

$$N_{bg}^{VH} = 0.01 \times \sigma_{VH} \;\; \text{events},$$

where, σ_{VH} is expressed in *pb*. Theoretical Standard Model cross-sections for WH^0 and ZH^0 production vary considerably, but assuming σ_{VH} is in the order of $\sim 1\,pb^{-1}$ for $M_H = 100\,GeV$, then associated Higgs production can be neglected as a source of dilepton events.

6.7 Top dilepton background summary

The results from the previous sections are summarized in Table 6.11, in which the expected contributions from the various backgrounds have been separated according to jet multiplicity. In addition the total background given in this table, the level of the combined contributions from the other small sources from section 6.6, is assigned a value of 0.1 events. Therefore, the total background expectation for an integrated luminosity of $109\,pb^{-1}$ in the dilepton channel of $t\bar{t}$ decay is;

$$\overline{B} = 2.1 \pm 0.4 \;\; \text{events}.$$

The expected number of $t\bar{t}$ dilepton events has been calculated using the acceptance results from chapter 5, an integrated luminosity of $109\,pb^{-1}$, and the theoretical $t\bar{t}$ production cross-sections of Berger and Contopanagos [24]*. The number of $t\bar{t}$ events expected is given for top masses of $160\,GeV$, $175\,GeV$, and $190\,GeV$, for which the cross-sections used were $8.9\,pb^{-1}$, $5.5\,pb^{-1}$, and $3.4\,pb^{-1}$ respectively. The events seen in the CDF data are discussed in the next chapter.

---

*Discussed in section 2.3.

	Before 2-jet cut	0-jet	1-jet	2-jet
$e\mu$				
Z → $\tau\tau$	0.91 ± 0.18	0.00	0.53	0.38 ± 0.11
WW	3.5 ± 1.1	2.7	0.6	0.20 ± 0.09
Fake	1.1 ± 1.1	0.5	0.5	0.16 ± 0.16
$b\bar{b}$	0.05 ± 0.05	0.01	0.02	0.02 ± 0.02
Total Background	5.6 ± 1.6	3.2 ± 1.1	1.7 ± 0.5	0.76 ± 0.21
Top 160, 175, 190	4.9, 3.3, 2.2	0.05, 0.01, 0.01	0.81, 0.43, 0.27	4.1, 2.8, 1.9
CDF data	16	4	5	7
$ee + \mu\mu$				
Drell-Yan	2.8 ± 0.6	1.0	1.1	0.62 ± 0.30
Z → $\tau\tau$	0.62 ± 0.15	0.03	0.30	0.21 ± 0.08
WW	2.3 ± 0.8	1.7	0.4	0.16 ± 0.07
Fake	1.5 ± 1.2	0.6	0.6	0.21 ± 0.17
$b\bar{b}$	0.07 ± 0.05	0.01	0.03	0.03 ± 0.02
Total Background	7.3 ± 1.6	3.3 ± 0.9	2.4 ± 0.7	1.23 ± 0.36
Top 160, 175, 190	3.3, 2.2, 1.5	0.03, 0.01, 0.01	0.54, 0.29, 0.38	2.7, 1.9, 1.3
CDF data	9	3	3	3
$ee + \mu\mu + e\mu$				
Total Background	12.9 ± 2.5	6.5 ± 1.7	4.1 ± 1.0	2.0 ± 0.4
Top 160, 175, 190	8.2, 5.5, 3.6	0.08, 0.02, 0.02	1.36, 0.72, 0.44	6.8, 4.7, 3.2
CDF data	25	7	8	10

Table 6.11

Summary of the background contributions to the $t\bar{t}$ dilepton decay channels, separated before the 2-jet cut according to jet multiplicity. In addition a combined contribution of 0.1 events is assigned from other small sources listed in section 6.6, and is to be added to the total dilepton background.

7. DILEPTON RESULTS

7.1 The $t\bar{t}$ dilepton candidate events

The results after applying the top dilepton channel selection, discussed in Chapter 4, on the $109\,pb^{-1}$ dataset are summarized in Table 7.1. The number of dilepton events surviving each of the consecutive cuts is shown for each dilepton category. The events surviving the invariant mass ($M_{\ell\ell}$) cut have been divided into their different jet multiplicity bins, as have the events surviving the following missing E_t ($\not\!\!E_t$) cut, in order to show the effect of the latter cut as a function of jet multiplicity. Note that all 7 "$e\mu$ + 2-jet" events that survive the invariant mass cut also survive the $\not\!\!E_t$ cut, demonstrating the relative purity of the $e\mu$ sample, which doesn't suffer from the same Drell-Yan background as the ee and $\mu\mu$ channels. The events in the $\geq 2\,jet$ bin that have passed the $\not\!\!E_t$ cut are the top dilepton candidates. These were first introduced in Chapter 4 when each of the selection cuts was explained in more detail and more graphically.

There are a total of 10 events passing the dilepton selection (1 ee, 2 $\mu\mu$ and 7 $e\mu$). However, recall from sections 4.10 and 6.6.1 that one of the $\mu\mu$ candidates is more consistent with being a *radiative* Z^0 + *1 jet* event, than from $t\bar{t}$ decay. This event will be discussed further in section 7.3, and will often be referred to as the "$\mu\mu\gamma$" event. Although this event has been identified as not coming from $t\bar{t}$ decay, it will be included in all the distributions shown for the dilepton candidates. Therefore, for the purposes of displaying the results, the number of candidate events will be 10,

	DILEPTON CUT										
	Lepton	Same			$N_j > 10\,GeV$				$N_j > 10\,GeV$		
Category	ID	Sign	Isolation	$M_{\ell\ell}$	0	1	≥ 2	$\not{E}_t$	0	1	≥ 2
TCE-TCE	2402	2397	2378	258	200	46	12	5	2	2	1
TCE-LCE	455	444	420	58	43	12	3	1	1	0	0
$e-e$	2857	2841	2798	316	243	58	15	4	2	1	**1**
TCM-TCM	1324	1318	1265	145	105	26	14	5	1	2	2
TCM-CMX	1047	1047	1044	113	76	28	9	1	0	1	0
CMX-CMX	191	191	181	20	13	4	3	1	0	1	0
TCM-CMI	675	673	656	73	57	11	5	0	0	0	0
CMX-CMI	217	216	211	24	16	7	1	0	0	0	0
$\mu-\mu$	3454	3445	3357	375	267	76	32	5	1	2	**2**
TCE-TCM	39	31	28	28	16	8	4	9	2	3	4
TCE-CMX	9	9	6	6	3	1	2	4	1	1	2
TCE-CMI	12	11	11	11	9	2	0	1	1	0	0
TCM-LCE	6	4	4	4	2	1	1	2	0	1	1
CMX-LCE	2	0	0	0	0	0	0	0	0	0	0
$e-\mu$	68	55	49	49	30	12	7	16	4	5	**7**
Total	6379	6341	6204	740	540	146	54	25	7	8	10

Table 7.1

Top dilepton channel analysis results in $109\,pb^{-1}$ for each of the dilepton categories. 1 ee, 2 $\mu\mu$ and 7 $e\mu$ events survive all cuts.

Category Run/Event z_{vertex}	$P_t(\ell_1)$, η_{ℓ_1}, ϕ_{ℓ_1} $(E,\vec{P})_{\ell_1}$ ℓ_1^{charge}	$P_t(\ell_2)$, η_{ℓ_2}, ϕ_{ℓ_2} $(E,\vec{P})_{\ell_2}$ ℓ_2^{charge}	$E(j_1), E_t(j_1)$, η_{j_1}, ϕ_{j_1} $E(j_2), E_t(j_2)$, η_{j_2}, ϕ_{j_2} $\vdots$	H_t $\not{E}_t$, $\phi_{\not{E}_t}$
ee				
TCE-TCE 68185/174611 41.1cm	23.4, -0.71, 310° (29.6, 14.7, -18.3, -18.2) e^+	20.5, -1.13, 32° (35.1, 17.1, 11.3, -28.5) e^-	55.1, 45.6, -0.63, 144° 84.1, 35.6, -1.51, 192°	176 50.7, 343°
$\mu\mu$				
TCM-TCM 58281/44805 44.0cm	35.2, -0.46, 318° (39.1, 26.3, -23.6, -17.0) μ^+	34.3, 0.03, 158° (34.3, -31.9, 12.7, 1.1) μ^-	26.2, 23.0, -0.52, 180° 16.3, 16.3, -0.02, 134° [23.0, 15.5, 0.95, 356°]	137 27.8, 359°
TCM-TCM 63700/272140 6.8cm	40.0, 0.29, 292° (41.8, 14.6, -37.3, 12.0) μ^-	29.3, 0.35, 147° (31.1, -24.4, 16.2, 10.5) μ^+	33.0, 29.6, 0.47, 249° 19.7, 17.9, 0.46, 77°	144 27.2, 53°
$e\mu$				
TCE-TCM 41540/127085 $-4.8cm$	22.2, 0.84, 32° (30.5, 18.7, 12.0, 21.0) e^-	47.7, 0.17, 14° (48.3, 46.3, 11.7, 7.7) μ^+	127.3, 126.5, 0.11, 353° 60.8, 52.8, -0.54, 215° [199.1, 21.1, -2.94, 113°]	384 135.0, 179°
TCM-LCE 45047/104393 7.8cm	40.8, -0.36, 116° (43.4, -18.2, 36.5, -14.9) μ^-	24.3, 0.42, 255° (26.5, -7.3, -23.2, 10.6) e^+	113.9, 62.7, -1.20, 118° 41.3, 28.6, 0.91, 118°	272 116.1, 312°
TCE-CMX 47122/38382 12.1cm	50.6, 0.93, 25° (73.9, 46.4, 20.2, 53.9) e^+	37.3, -0.74, 4° (48.0, 37.2, 2.7, -30.3) μ^-	95.1, 78.5, 0.64, 218° 30.4, 14.4, 1.37, 344° [225.5, 16.4, -3.31, 344°]	241 60.3, 150°
TCE-TCM 57621/45230 $-10.8cm$	49.0, 0.77, 340° (64.1, 45.7, -17.8, 41.4) e^+	25.4, -0.48, 115° (28.3, -10.9, 23.0, -12.5) μ^-	36.5, 32.2, 0.51, 254° 32.4, 30.4, -0.37, 190°	184 51.4, 83°
TCE-CMX 66046/380045 $-11.6cm$	105.6, -0.10, 94° (106.2, -8.2, 105.3, -10.7) e^+	52.7, 0.77, 130° (69.5, -33.8, 40.4, 45.4) μ^-	24.1, 23.8, -0.17, 325° 27.0, 21.2, -0.73, 270° 18.6, 16.8, -0.46, 294° 30.0, 18.7, -1.05, 65°	347 108.4, 273°
TCE-TCM 67581/129896 $-51.2cm$	181.8, 0.78, 131° (240.0, -116.6, 139.4, 156.7) e^+	27.2, 0.30, 25° (28.2, 24.8, 11.4, 7.3) μ^-	119.7, 82.9, 0.91, 327° 57.6, 33.7, 1.12, 359°	434 108.0, 269°
TCE-TCM 69808/639398 23.1cm	42.3, 0.64, 160° (51.2, -39.8, 14.2, 28.9) e^-	56.3, -0.39, 111° (60.4, -20.3, 52.5, -21.8) μ^+	75.0, 47.6, -1.03, 242° 52.5, 40.7, -0.74, 345° 32.1, 21.0, -0.99, 281°	239 30.9, 20°

Table 7.2

Kinematic properties of the 9 dilepton candidates. Also included is the "$\mu\mu\gamma$" event, 58281/44805. All energies and momenta are in units of GeV, with the muon momenta beam constrained. Jets in parentheses,[ ],did not satisfy the E_t^{raw} and $|\eta|$ requirements.

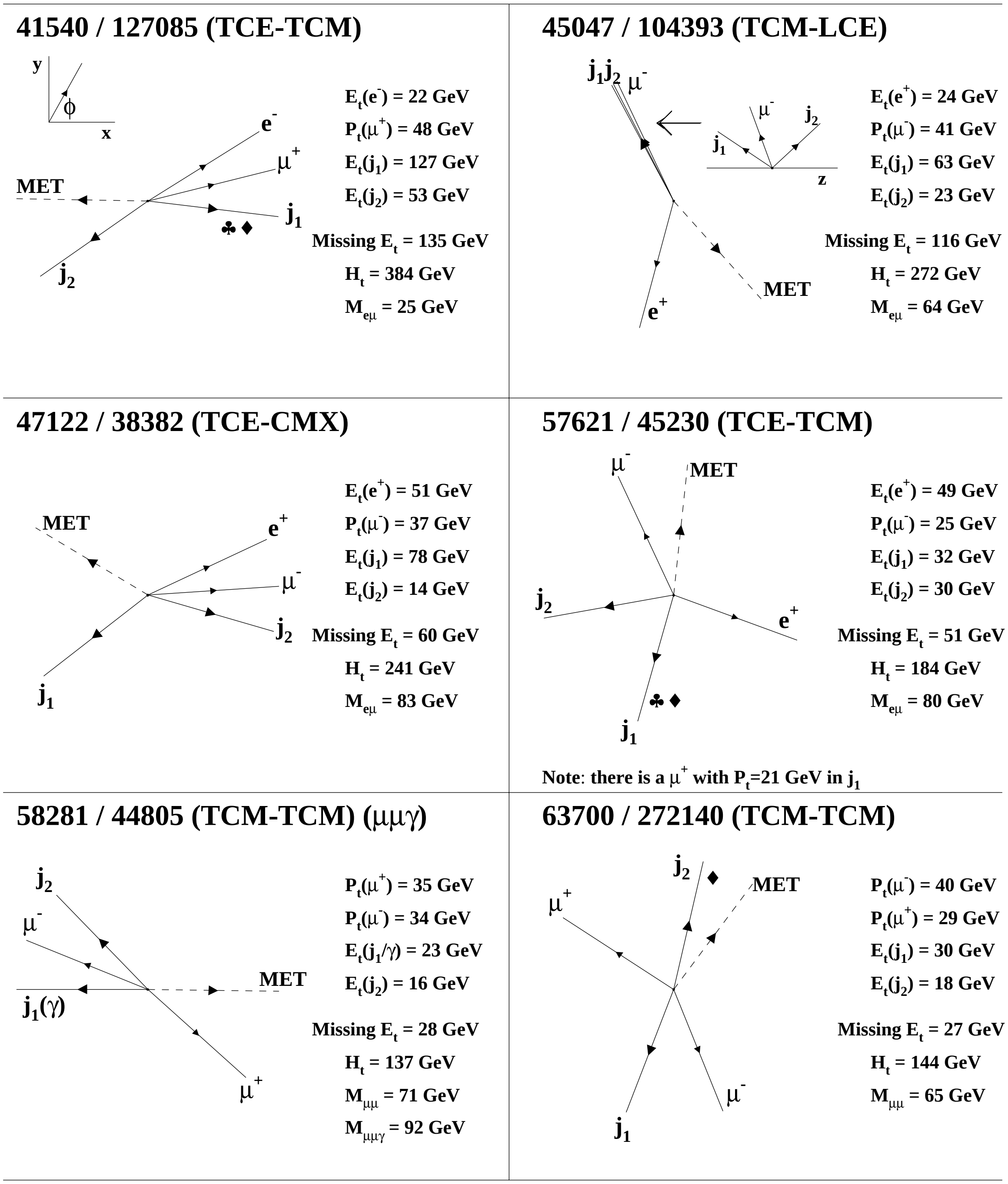

Figure 7.1

Vectorial schematics of the dilepton candidates in the transverse plane. Jets are labelled if tagged by SECVTX(♣) or SLT(♢). The candidate events are labelled by Run/Event number and dilepton category.

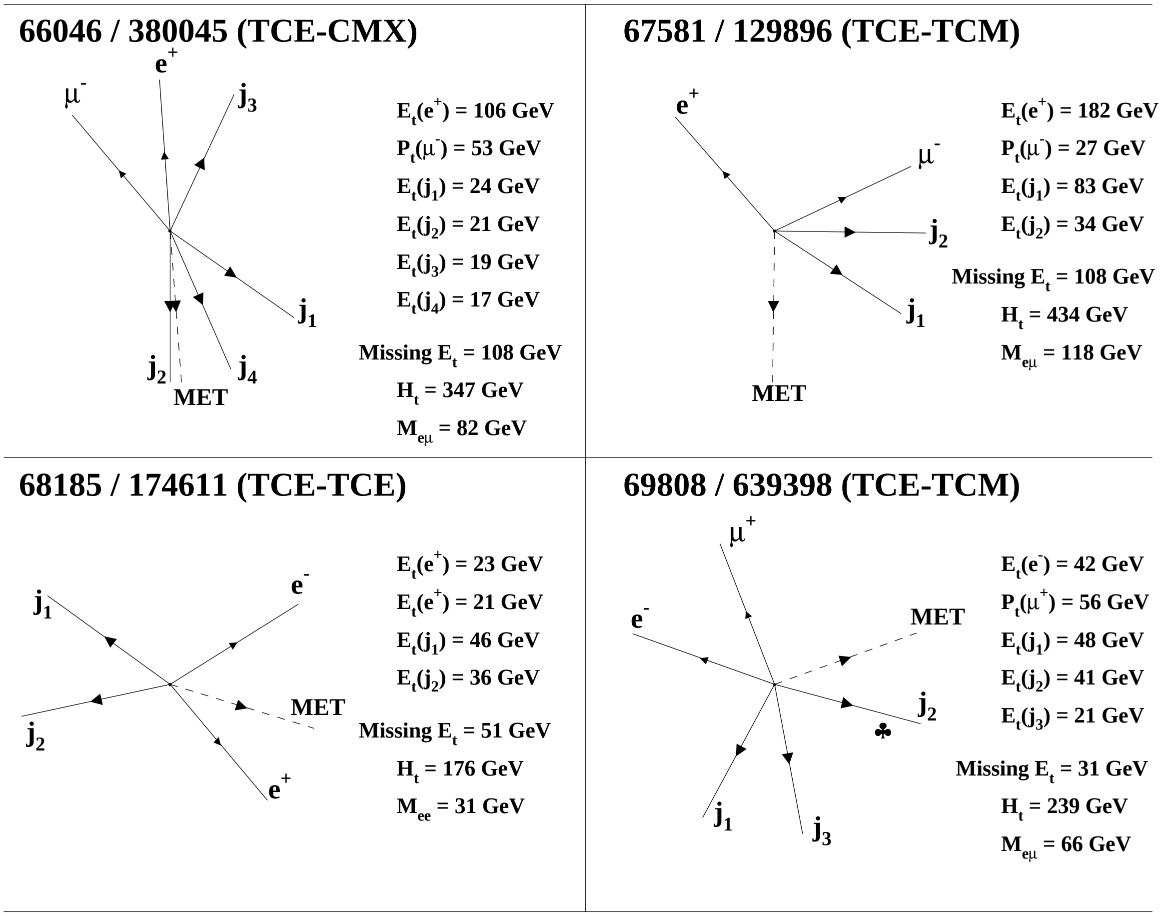

Figure 7.2

Schematics of the dilepton candidates continued from Figure 7.1.

however, in the next chapter where the significance and cross-section are calculated, the number of $t\bar{t}$ dilepton candidates will be taken as 9.

Table 7.2 lists the properties of the 10 candidate events, with their graphical representation in the transverse plane displayed in Figures 7.1 and 7.2. The actual CDF event displays of these candidates are given in Appendix E for reference. In Table 7.2, z_{vertex} is the z position of the interaction (primary) vertex, $P_t(\ell)$ is the beam constrained transverse momentum (measured by the CTC) if $\ell = \mu$ and the transverse energy (measured by the CEM) if $\ell = e$, and, $\not{E}_t$ is the missing transverse energy corrected for muons and jets as explained in section 4.9. All jet energies have been corrected in the manner described in section 4.10*. H_t is the scalar sum of all the transverse energy in the event, defined by;

$$H_t \;=\; \sum_i E_t(e_i) \;+\; \sum_i P_t(\mu_i) \;+\; \sum_i E_t(j_i) \;+\; \not{E}_t \;,$$

where, the lepton energy sums are over *every* lepton in the event which passes the fiducial, kinematic, and identification cuts discussed in sections 4.2 and 4.3. Likewise, the sum over the jet energies (corrected) is for all jets in the event that satisfy the requirements of section 4.10 ($E_t^{raw} > 10\,GeV$, $|\eta| < 2.0$). The H_t for the 10 candidates is plotted in Figure 7.3. Also shown is the H_t distribution of events in a PYTHIA $t\bar{t}$ Monte Carlo sample that have passed all dilepton selection cuts. The $t\bar{t}$ distribution has been normalized to an arbitrary value. The H_t distribution expected from the background processes is shown with twice its contribution relative to $t\bar{t}$ (assuming 2 background events, and 8 $t\bar{t}$ events). The background shape was calculated from WW Monte Carlo, $Z \rightarrow \tau\tau$ Monte Carlo, and, for the fake back-

---

*That is, using the *relative* corrections to account for detector effects. Unless explicitly stated otherwise, E_t for jets will be taken to imply corrected transverse energy.

ground, from $W + 3$-jet data where at least 1 jet was required to have $E_t > 20\,GeV$ and $|\eta| < 1.0$. With only 6 data events from which the Drell-Yan background was calculated (see section 6.1), a statistically significant H_t distribution from Drell-Yan dilepton events could not be obtained. The relative proportions of the 3 sources contributing to the background H_t distribution are the same as calculated in Table 6.11. At least two of the 10 dilepton candidate events appear to be more consistent with the background H_t shape than with the $t\bar{t}$ shape for a top mass of $175\,GeV$. One of these is the "$\mu\mu\gamma$" event. The expected H_t distribution of dilepton candidates from $t\bar{t}$ PYTHIA Monte Carlo was checked with a HERWIG sample and seen to be in good agreement.

Figures 7.4 and 7.5 show some properties of the jets and leptons respectively, in the 10 dilepton candidates and in $t\bar{t}$ events which have passed the dilepton selection. With jets as defined in section 4.10, Figure 7.4 evinces that one can expect about 40% of $t\bar{t}$ dilepton candidates to contain 3 or more jets. Of the 10 dilepton candidates in the data, 1 has 3 jets, 1 has 4 jets, and the rest have the required 2 jets*. The transverse energy sum of the jets in the 10 candidates is also shown in Figure 7.4. Again, good agreement is observed between PYTHIA and HERWIG Monte Carlo samples.

Characteristics of the two leptons in the 10 candidate events, and in $t\bar{t}$ Monte Carlo dilepton events with a top mass of $175\,GeV$, are shown in Figure 7.5. In the case of Event 45230 from Run 57621, in which there is a third good lepton (a muon) in one the jets (see Figure 7.1 and below), only the two isolated leptons are used in these plots.

Angular characteristics in the dilepton events are plotted against $\not{E}_t$ in Figure 7.6. These plots show the data and $t\bar{t}$ Monte Carlo distributions for dilepton 2-jet events

---

*Interestingly, both the 3-jet and 4-jet candidates are *b-tagged* (see section 7.4).

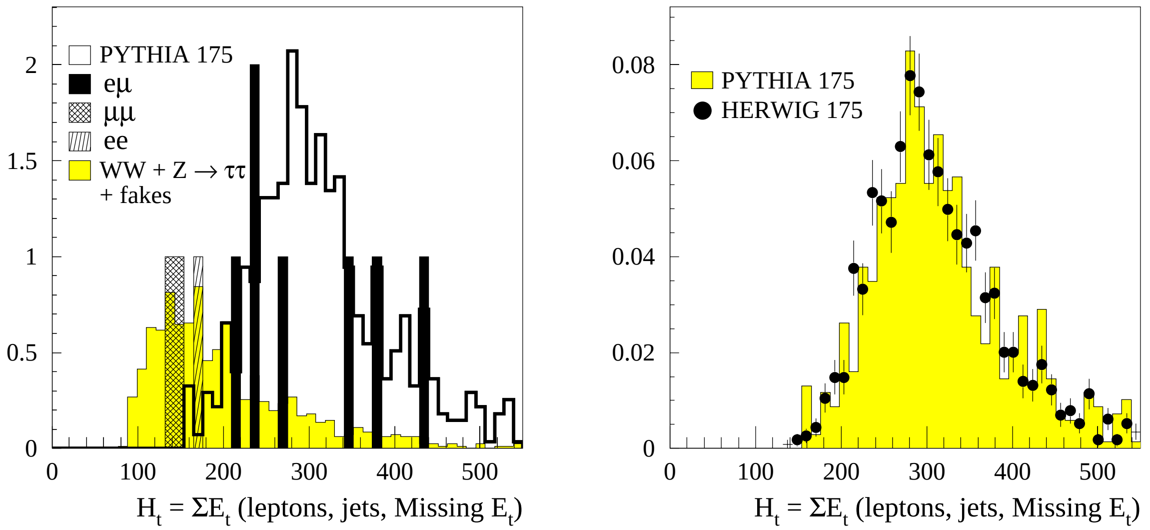

Figure 7.3

H_t (GeV) distributions of the 10 dilepton candidates, the expected background, and $t\bar{t}$ Monte Carlo with $m_t = 175\,GeV$ (left plot). The right plot shows the H_t comparison between two different Monte Carlo generators. The vertical scale is arbitrary. See the text for further explanation.

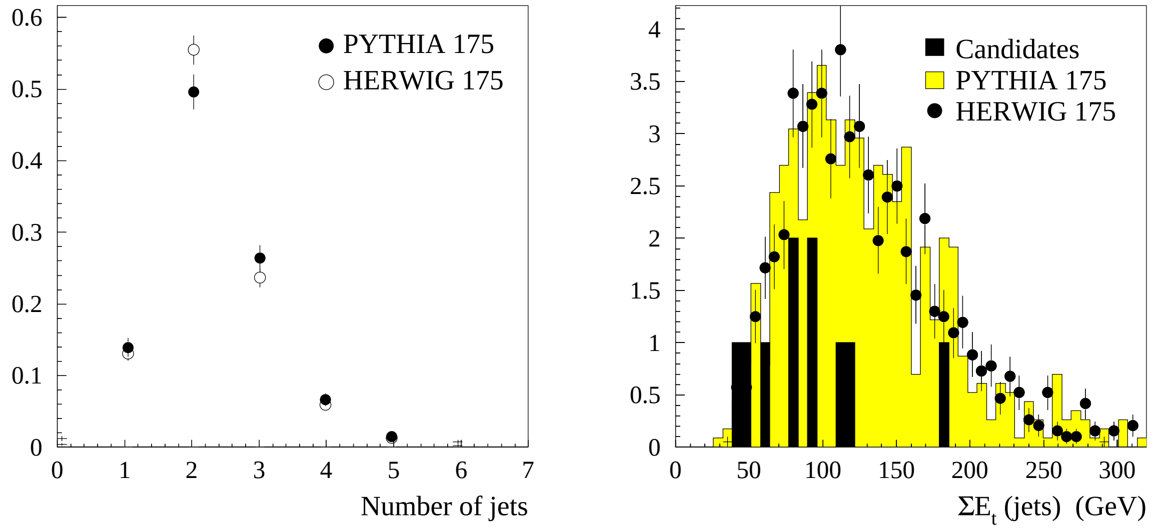

Figure 7.4

Jet multiplicity (normalized to 1) in $t\bar{t}$ Monte Carlo dilepton events with $m_t = 175\,GeV$ (left plot), and the transverse energy sum of the jets in the 10 dilepton candidate events compared with Monte Carlo distributions of arbitrary normalization (right plot).

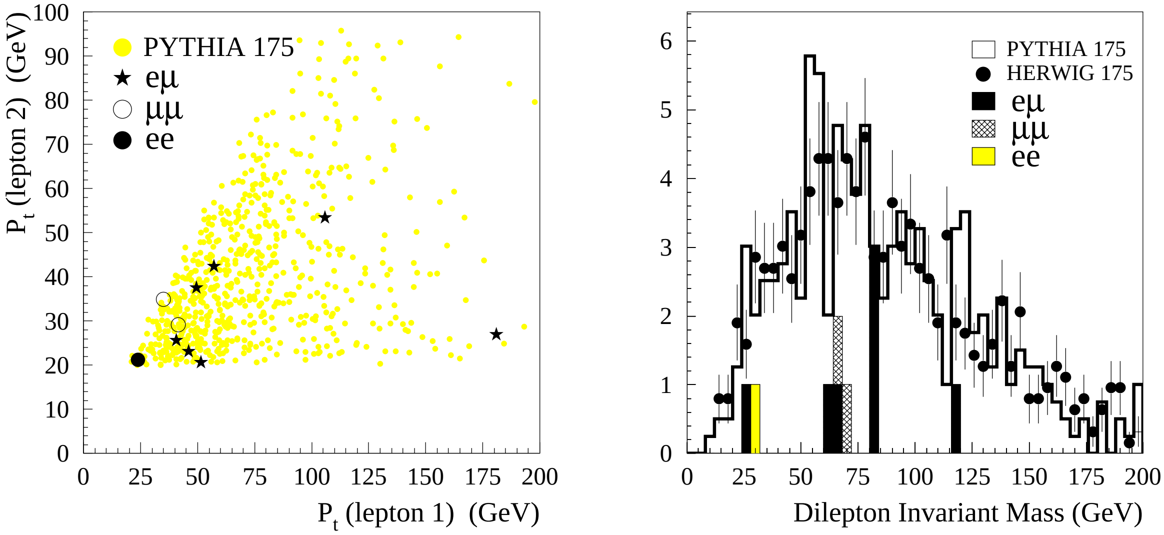

Figure 7.5

Scatter plot of lepton transverse momenta (left plot, with *lepton 1* the highest P_t lepton), and, the dilepton invariant mass distribution (right plot), for the 10 candidate events. In both plots $t\bar{t}$ Monte Carlo dilepton distributions, with $m_t = 175\,GeV$, are shown.

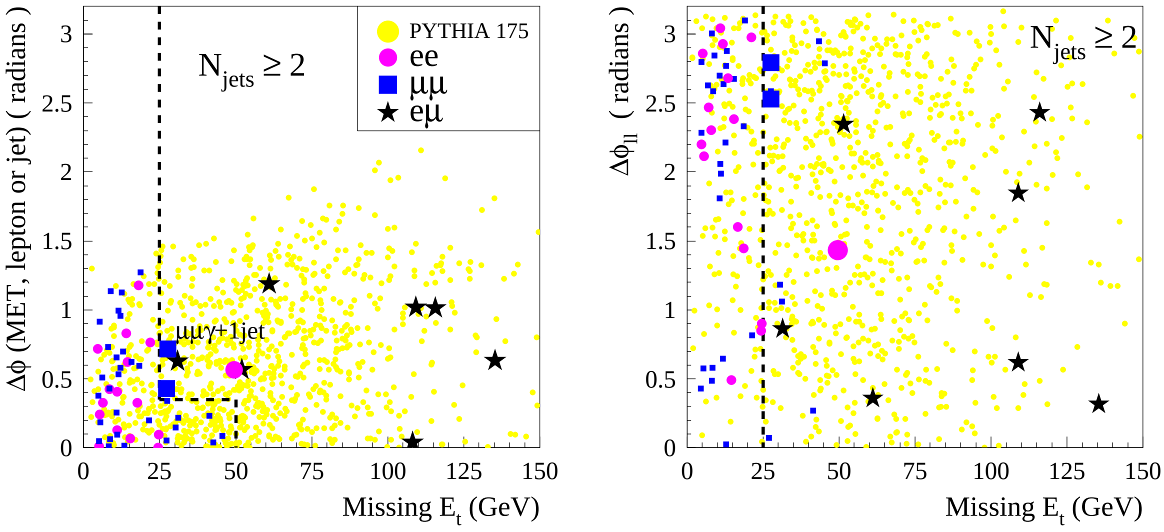

Figure 7.6

Azimuthal angle between the $\not{E}_t$ and the nearest lepton or jet versus the $\not{E}_t$ (left plot), and, the azimuthal angular separation between the two leptons versus the $\not{E}_t$ (right plot), for both the 10 candidate events and $t\bar{t}$ Monte Carlo with $m_t = 175\,GeV$. The 10 dilepton candidates are indicated by the larger symbols. The dashed lines represent the $\not{E}_t$ cuts.

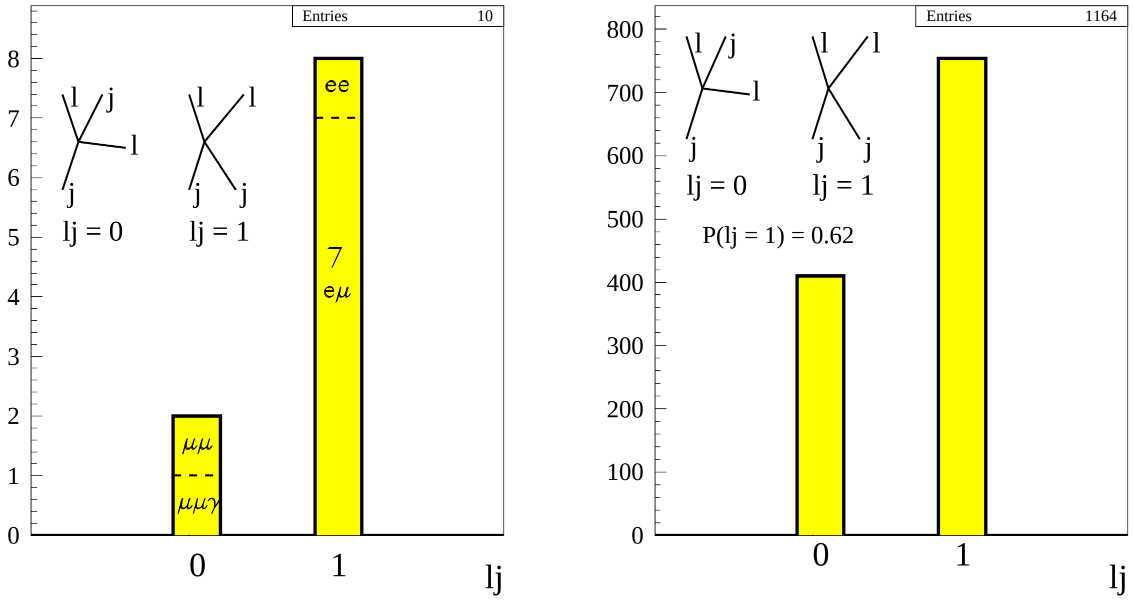

Figure 7.7

Topology of the 10 candidate events in the transverse plane (left plot), with that expected from HERWIG $t\bar{t}$ dilepton events with $m_t = 175\,GeV$.

before the $\not\!\!E_t$ cuts, which are represented by the dashed lines.

To get a more global topological insight into $t\bar{t}$ dilepton events, a variable lj is constructed. If $lj = 0$, then no 2 leptons or jets are found to be consecutive in ϕ. If $lj = 1$, then the 2 leptons (and therefore the 2 jets), are consecutive in ϕ. Only the 2 leading (i.e. highest E_t) jets are used. The variable lj is plotted for both the 10 dilepton candidate events, and for HERWIG $t\bar{t}$ Monte Carlo events that have passed all dilepton selection cuts, in Figure 7.7. HERWIG predicts the probability for a $t\bar{t}$ dilepton candidate to assume the $lj = 1$ topology to be 0.62 ± 0.02. A PYTHIA Monte Carlo sample (version 5.6, without W polarization) predicts this probability to be 0.66 ± 0.02. In the data all 7 $e\mu$ candidates and the single ee candidate have the $lj = 1$ topology, while the $\mu\mu$ candidate (and the "$\mu\mu\gamma$" event) have the $lj = 0$ topology. Although the statistics are small, the $lj = 1$ topology seems to be favored in the data.

7.2 A note on the 0 and 1 jet bins

From Table 7.1, after the $\not\!\!E_t$ cuts, there are 4 ee, 5 $\mu\mu$ and 16 $e\mu$ events remaining. As explained in section 4.10.4, there is a loose jet vertex requirement that is made before the 2-jet cut and which is therefore also reflected in the numbers in the $\not\!\!E_t$ column. This requirement removes 2 1-jet $\mu\mu$ events in which the jets in these events are seen to clearly come from a different vertex to the leptons. In addition, 1 1-jet ee event is removed for the same reason, and 1 0-jet ee event is removed because there is a jet at $\eta = 2.01$ (which is therefore not included in the jet count), that also clearly comes from a second vertex in the event. All events removed by this requirement have been verified using the event displays to contain jets which originate from a vertex different to the leptons. This requirement only affects ee and $\mu\mu$ events with 0 or 1 jets. All the 2-jet candidates, and all $e\mu$ events before the 2-jet requirement, have been verified to contain a single vertex from which both the leptons and jets originate. Further study needs to be done in order to understand these multiple interactions events, and get an estimate for its background contribution.

It is noted from Table 6.11 that the expected background plus $t\bar{t}$ contributions to the 0, 1, and 2-jet bins, are in good agreement with what is observed in the data, however, it is noted that the number of $e\mu$ events is higher than expected in both the 1 and 2-jet bins, though not statistically significant. Perhaps what is more significant, is that 2 of the 1-jet $e\mu$ events have b-tagged jets, with a second jet in the event that fails the jet requirements. This strongly suggests that at least 2 of the 5 1-jet $e\mu$ events are also from $t\bar{t}$ decay, when 0.43 are expected for a top mass of $175\,GeV$. This gives a total of 5 b-tagged $e\mu$ events. Without the requirement of b-tagging, about 3 or 4 $e\mu$ events are expected from $t\bar{t}$ decay in the 1 and 2-jet bins for a top mass of $175\,GeV$.

7.3 Comments on some candidates events

All the dilepton candidates deserve to be discussed in more detail, however, only those with somewhat problematical features will be mentioned here. Most of the candidates have and will be discussed elsewhere in this chapter.

The now infamous dilepton candidate that has come to be known as the "$\mu\mu\gamma$" event (44805/58281), has a dimuon invariant mass of $71\,GeV$. However, in this event the $23\,GeV$ jet has no stiff track pointing to an almost entirely electromagnetic cluster (the electromagnetic fraction is 0.994), suggesting that this jet is most likely a photon. This can be seen in the CTC event display of Figure 7.8. The invariant mass of the two muons *with* the "photon" is $92\,GeV$, giving a strong indication that these 3 objects came from a *radiative* Z^0 boson, with an extra jet in the event. There is in fact a third jet in the event at $\phi = 355°$ with $E_t = 15.5\,GeV$ (corrected), but with $E_t^{raw} = 9.96\,GeV$, and therefore just failing the cut at $E_t^{raw} > 10\,GeV$. As discussed in section 6.6 only about 0.07 events of this type are expected in $109\,pb^{-1}$ of data. Because such events were not anticipated, no cut was made to reject them. This will be done in future top dilepton analyses (see Appendix D), eliminating the chance for radiative Z^0 events to appear in the $t\bar{t}$ signal region. The "$\mu\mu\gamma$" event is therefore only loosely considered a candidate, and is not used in the significance or cross-section calculations.

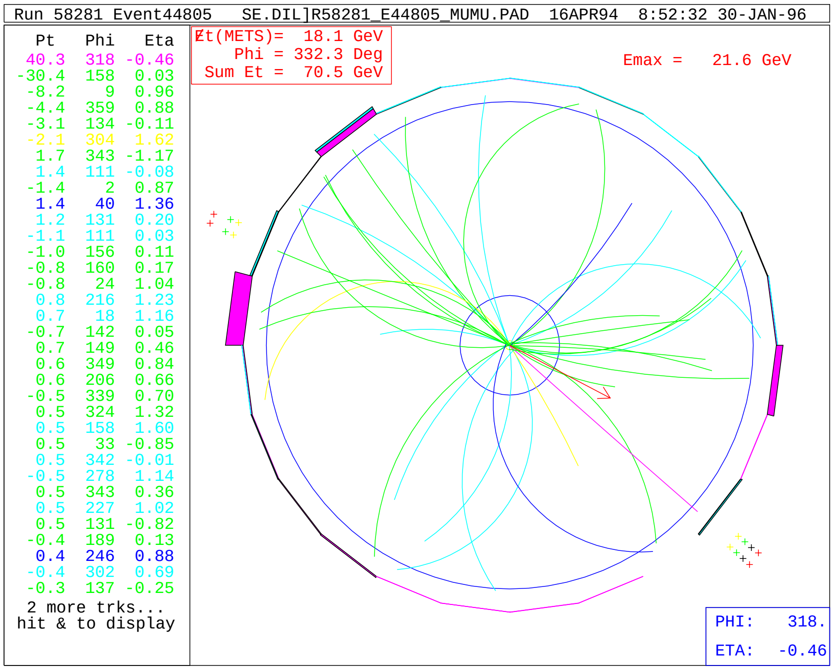

```
Run 58281 Event44805   SE.DIL]R58281_E44805_MUMU.PAD  16APR94  8:52:32 30-JAN-96

   Pt   Phi   Eta     Ɇt(METS)=  18.1 GeV
  40.3  318 -0.46         Phi = 332.3 Deg
 -30.4  158  0.03      Sum Et =  70.5 GeV
  -8.2    9  0.96
  -4.4  359  0.88                           Emax =   21.6 GeV
  -3.1  134 -0.11
  -2.1  304  1.62
   1.7  343 -1.17
   1.4  111 -0.08
  -1.4    2  0.87
   1.4   40  1.36
   1.2  131  0.20
  -1.1  111  0.03
  -1.0  156  0.11
  -0.8  160  0.17
  -0.8   24  1.04
   0.8  216  1.23
   0.7   18  1.16
  -0.7  142  0.05
   0.7  149  0.46
   0.6  349  0.84
   0.6  206  0.66
  -0.5  339  0.70
   0.5  324  1.32
   0.5  158  1.60
   0.5   33 -0.85
   0.5  342 -0.01
  -0.5  278  1.14
   0.5  343  0.36
   0.5  227  1.02
   0.5  131 -0.82
  -0.4  189  0.13
   0.4  246  0.88
  -0.4  302  0.69
  -0.3  137 -0.25
  2 more trks...
 hit & to display
                                                     PHI:    318.
                                                     ETA:   -0.46
```

Figure 7.8

CTC tracks in the "$\mu\mu\gamma$" event 58281/44805. The muon tracks point to stubs represented by groups of "+". The electromagnetic clusters are represented by the shaded areas at the radius of the CTC. The largest CEM cluster ($E_t = 23\,GeV$) at $\phi = 180°$ has no stiff track pointing to it.

Event 129896 of Run 67581 has 2 jets close in η and ϕ, an extremely large E_t isolated electron ($182\,GeV$), an isolated muon ($P_t = 27\,GeV$), and a large $\not{E}_t$ ($108\,GeV$). However, one of the jets is entirely electromagnetic, and only has a single track pointing to the calorimeter energy cluster. In fact it passes all electron identification cuts *except* the fiducial requirement because it is very close to the ϕ crack at 0°. It is, therefore, only a jet because the "electron" fails the fiducial requirement. If this were an electron then the most likely scenario is still $t\bar{t}$ decay, with the non-fiducial "electron" being associated with the nearby b jet, and the second b jet having insufficient E_t to be counted as a jet in the dilepton analysis. Using the track momenta of this "electron", it forms an invariant mass of $62\,GeV$ with the other electron.

It is also of interest to note the ratio of ee, $\mu\mu$ and $e\mu$ dilepton candidates seen in the data. From chapter 5, about 15% of candidates are expected to be ee, 25% $\mu\mu$, and 60% $e\mu$. Therefore, given 9 $t\bar{t}$ dilepton candidates, the expected numbers of ee, $\mu\mu$ and $e\mu$ are 1.35, 2.25, and 5.40, respectively. The numbers seen in the data (excluding the "$\mu\mu\gamma$" event) are 1, 1, and 7, respectively.

7.4 b-tags in the dilepton candidates

It was *not* required in this dilepton analysis for events to contain a jet that is identified as fragmenting from a b quark. It is required in the *lepton + jets* analysis in order to reduce the considerable background from $W+\geq 3$-jet events, however the dilepton channel does not suffer in the same way from this background. Nevertheless, since SM $t\bar{t}$ decay does involve 2 b quarks, it is of interest to *a posteriori* enquire whether the jets in the dilepton candidate events are identified as b-jets. In fact a dilepton candidate with a b-tagged jet could be considered a "smoking gun" signal for $t\bar{t}$ production with decay in the dilepton channel. The most popular algorithms used at CDF for b-jet identification are SECVTX [5, 84] (SECondary VerTeX), and SLT [5] (Soft Lepton Tagger).

The SECVTX algorithm uses SVX (see section 3.2.1) tracking information to search for secondary vertices from b quark decays. The secondary vertex is defined as the point of decay of a long-lived B meson[*], which originated at the primary vertex. The jet is tagged if it contains a secondary vertex formed from 2 or more

---

[*] $c\tau$ for B mesons is about $390\,\mu m$.

tracks with tight track quality cuts, or from 3 or more tracks with looser track quality cuts.

The SLT b-tagging algorithm looks for *soft* leptons (relative to the leptons from W decay) produced in direct b quark decays, $b \rightarrow c\ell\nu_\ell$, and in cascade decays, $b \rightarrow c \rightarrow s\ell\nu_\ell$, where $\ell = e$ or μ. It will also find charm decay leptons from $W \rightarrow cs$, but this is not a concern in $t\bar{t}$ dilepton events.

The efficiency for the SECVTX algorithm to b-tag at least one jet in a $t\bar{t}$ decay is $(42 \pm 5)\%$ [2]. The efficiency of the SLT algorithm to detect an extra electron or muon in a $t\bar{t}$ event consistent with coming from b decay is $(20 \pm 2)\%$ [2]*. About $\frac{3}{4}$ of the SLT tags in $t\bar{t}$ events are muons.

The dilepton candidates with b-tagged jets are listed in Table 7.3, along with details of the tagged jet. It is worth special mention that the SLT muon tag in event 57621/45230 passes all the high-P_t muon identification requirements of the dilepton analysis, and therefore contributes a third high-P_t lepton to the event. This is discussed further in the next section.

Assuming that 7 of the dilepton candidates are from $t\bar{t}$ decay (excluding the "$\mu\mu\gamma$" event, and subtracting the expected background of 2 events), then with the above b-tagging efficiencies, 2.9 ± 0.3 events are expected to contain at least one jet tagged by SECVTX, and 1.4 ± 0.1 events are expected to be tagged by the SLT algorithm. From Table 7.3, 3 events are tagged by SECVTX and 3 events by SLT, in reasonable agreement with expectations. Note that 2 of the 4 tagged events, contain a jet that is tagged by both algorithms. If just the total number of b-tagged jets is considered, then in 7 $t\bar{t}$ events, 4.3 ± 0.4 jets are expected to be tagged by at

---

*These efficiencies are actually for $t\bar{t}$ events with ≥ 3 jets, but are not expected to be very different for ≥ 2 jet events, since in both cases there can only be 2 b jets.

	SVX tagged jet			SLT tagged jet		
Run/Event	$E_t(GeV)$	ϕ_j	$c\tau$ (μm)	$E_t(GeV)$	ϕ_j	P_t(tag) (GeV)
41540/127085	127	353°	470 ± 40	127	353°	8.8 (μ)
57621/45230	32	254°	110 ± 10	32	254°	21 (μ)
63700/272140		—		18	77°	3.7 (μ)
69808/639398	41	345°	1220 ± 20		—	

Table 7.3

Dilepton candidate events which contain a b-tagged jet. For jets tagged by the SECVTX algorithm the $c\tau$ of the secondary vertex is given, and for jets tagged by the SLT algorithm, the P_t of the lepton which tagged the jet is given.

least 1 of the 2 algorithms[†], and 6 b-tagged jets are observed. The mistag rate (the probability for tagging non-heavy flavor) for the SECVTX and SLT algorithms is about 2% and 5% respectively per dilepton event. Therefore, under the assumption that the 9 $t\bar{t}$ candidates (excluding the "$\mu\mu\gamma$" event) are background, the number of b-tagged jets expected would be about 0.7. The fact that 6 jets are observed to be b-tagged is not included when calculating the significance of the dilepton result (see section 8.1).

The SVX tracks of the 2 SECVTX b-tagged dilepton candidates from Run 1B are shown in Figures 7.9 and 7.10.

[†] Assuming no correlation between the 2 algorithms.

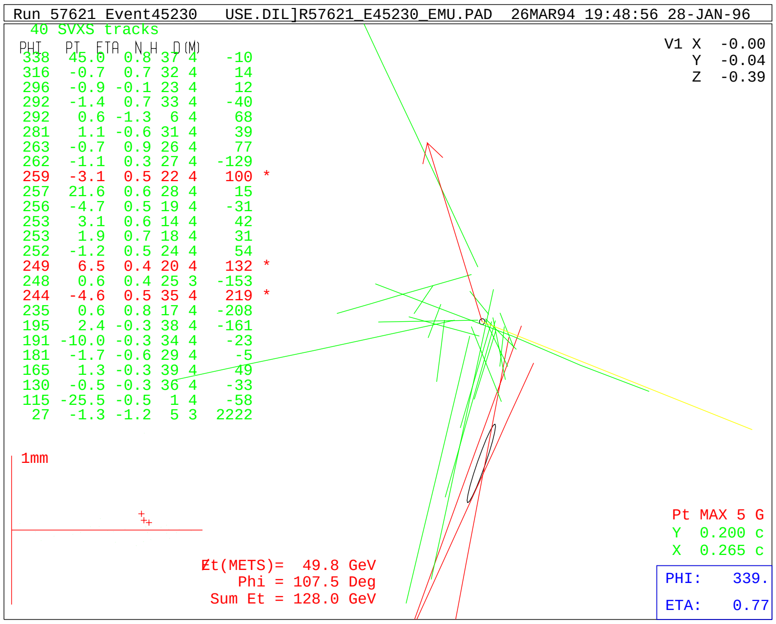

```
Run 57621 Event45230   USE.DIL]R57621_E45230_EMU.PAD  26MAR94 19:48:56 28-JAN-96
  40 SVXS tracks
 PHI   PT  ETA  N H  D(M)
 338  45.0  0.8 37 4   -10
 316  -0.7  0.7 32 4    14
 296  -0.9 -0.1 23 4    12
 292  -1.4  0.7 33 4   -40
 292   0.6 -1.3  6 4    68
 281   1.1 -0.6 31 4    39
 263  -0.7  0.9 26 4    77
 262  -1.1  0.3 27 4  -129
 259  -3.1  0.5 22 4   100 *
 257  21.6  0.6 28 4    15
 256  -4.7  0.5 19 4   -31
 253   3.1  0.6 14 4    42
 253   1.9  0.7 18 4    31
 252  -1.2  0.5 24 4    54
 249   6.5  0.4 20 4   132 *
 248   0.6  0.4 25 3  -153
 244  -4.6  0.5 35 4   219 *
 235   0.6  0.8 17 4  -208
 195   2.4 -0.3 38 4  -161
 191 -10.0 -0.3 34 4   -23
 181  -1.7 -0.6 29 4    -5
 165   1.3 -0.3 39 4    49
 130  -0.5 -0.3 36 4   -33
 115 -25.5 -0.5  1 4   -58
  27  -1.3 -1.2  5 3  2222

V1 X  -0.00
   Y  -0.04
   Z  -0.39

Pt MAX 5 G
Y  0.200 c
X  0.265 c

Ɇt(METS)=  49.8 GeV
    Phi = 107.5 Deg
 Sum Et = 128.0 GeV

PHI:    339.
ETA:    0.77
```

Figure 7.9

The SVX b-tag (at $\phi = 254°$) in the $e\mu$ candidate 57621/45230. The decay length is 0.085 *cm*

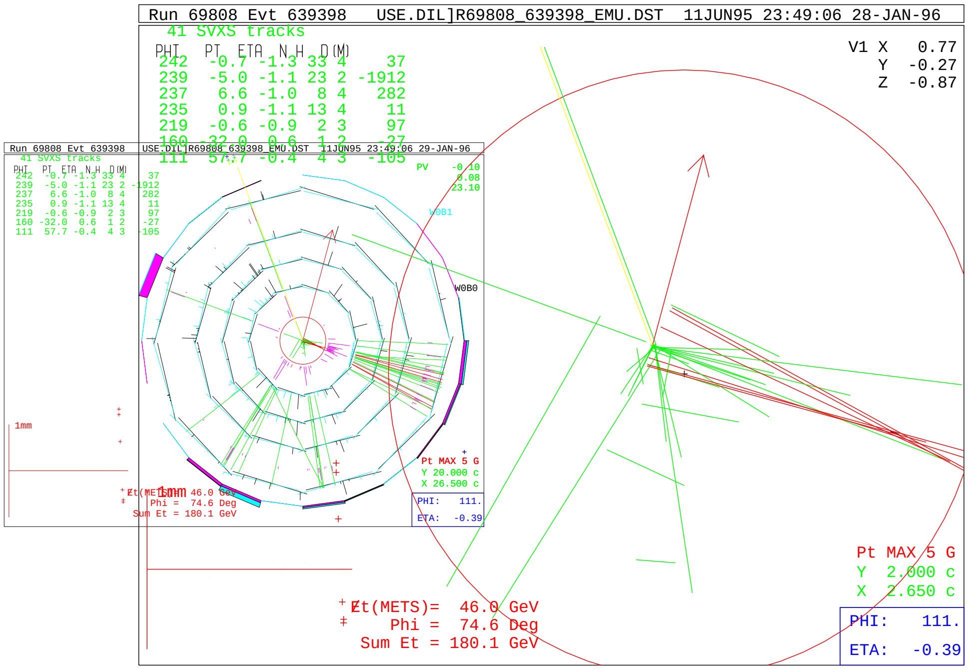

```
Run 69808 Evt 639398   USE.DIL]R69808_639398_EMU.DST  11JUN95 23:49:06 28-JAN-96
  41 SVXS tracks
 PHI   PT  ETA  N H  D(M)
 242  -0.7 -1.3 33 4    37
 239  -5.0 -1.1 23 2 -1912
 237   6.6 -1.0  8 4   282
 235   0.9 -1.1 13 4    11
 219  -0.6 -0.9  2 3    97
 160 -32.0  0.6  1 2   -27
 111  57.7 -0.4  4 3  -105

V1 X   0.77
   Y  -0.27
   Z  -0.87

Pt MAX 5 G
Y  2.000 c
X  2.650 c

Ɇt(METS)=  46.0 GeV
    Phi =  74.6 Deg
 Sum Et = 180.1 GeV

PHI:    111.
ETA:   -0.39
```

Figure 7.10

The SVX b-tag (at $\phi = 345°$) in the $e\mu$ candidate 69808/639398. The decay length is 0.81 *cm*. The transverse view of the SVX is shown as an inset for comparison. The radius of the outer layer is 7.9 *cm*.

Category Run/Event z_{vertex}	$E_t(e)$, η_e, ϕ_e $(E,\vec{P})_e$ e^{charge}	$P_t(\mu)$, η_μ, ϕ_μ $(E,\vec{P})_\mu$ μ^{charge}	$E(j_1), E_t(j_1)$, η_{j_1}, ϕ_{j_1} $E(j_2), E_t(j_2)$, η_{j_2}, ϕ_{j_2} $\vdots$	H_t $\not{E}_t$, $\phi_{\not{E}_t}$
TCE-TCE-TCM 64811/197867 $-0.7cm$	82.6, 0.30, 69° (86.4, 29.9, 77.0, 25.2) e^-	23.5, 0.57, 259° (27.4, -4.5, -23.1, 14.2) μ^-	31.2, 26.7, 0.57, 252° 25.8, 25.1, 0.24, 289°	193 1.5, 114°
	33.5, 0.53, 189° (38.3, -33.1, -4.7, 18.7) e^+			

Table 7.4

Kinematic properties of the trilepton event appearing in the dilepton analysis (other than the $t\bar{t}$ dilepton candidate). All energies and momenta are in units of GeV, and the $\not{E}_t$ has been corrected for muons and jets. The 2 electrons form an invariant mass of $91.5\,GeV$.

7.5 Trilepton events

It was shown in chapter 5 that in $t\bar{t}$ events only $(0.3\pm0.2)\%$ of dilepton candidates have a third lepton with $P_t > 20\,GeV$ and passing all lepton ID criteria. Such events can come from other sources, for instance WZ^0 production, but nevertheless events with more than two $20\,GeV$ leptons are extremely rare. It is therefore worthwhile to examine any such events closely and try to understand their origin.

After the lepton ID cuts, there are 2 events in the $109\,pb^{-1}$ of data containing 3 high-P_t leptons[*]. One of these 2 events is the dilepton candidate 57621/45230, the properties of which have already been detailed in Tables 7.2 and 7.3. Assuming a sample of 7 $t\bar{t}$ dilepton events[†], the 0.3% probability for a third lepton gives an

---

[*] That is, with each lepton having P_t(or E_t) $> 20\,GeV$ and being in one of the categories TCE, LCE, TCM, CMX or CMI, the plug region being excluded.

[†] Ten minus the "$\mu\mu\gamma$" event, minus 2 background events.

expectation of only 0.02 trilepton events in $109\,pb^{-1}$.

The properties of the other trilepton event are given in Table 7.4. This event only fails the $\not\!\!E_t$ cuts in the dilepton analysis. The almost zero $\not\!\!E_t$ together with the 2 electrons forming an invariant mass of $91.5\,GeV$ suggest that this event is a $Z^0 \rightarrow e^+e^-$ event, with 2 jets, one of the jets having a high-P_t muon in it. The muon and the close proximity of the jets give a hint that this might be a $b\bar{b}$ pair from gluon splitting. The cross section for $Z^0b\bar{b}$ production multiplied by $BR(Z^0 \rightarrow ee$ or $\mu\mu)$ is of order $1\,pb$ at the Tevatron*. The acceptance for Z^0 events in the dilepton analysis is about 10%, implying about 10 $Z^0b\bar{b}$ events are expected in the Z^0 sample using the dilepton analysis cuts. Although the probability is extremely low that a b jet from gluon splitting could produce a lepton with $P_t > 20\,GeV$, this seems the most reasonable explanation for this particular trilepton event. The dilepton background from $Z^0b\bar{b}$ was assumed negligible (see section 6.6.2). Certainly it is small, since not only would a b jet be required to produce a third high-P_t lepton (so that the invariant mass of one of the dilepton combinations would not fall into the Z^0 mass window), but the event would somehow have to generate enough $\not\!\!E_t$ to pass the $\not\!\!E_t$ cuts.

Note that this trilepton event is not interpreted as a WZ^0 candidate, where $W \rightarrow cs$ is followed by the semileptonic decay of the charm to produce the high-P_t muon, because the invariant mass of the 2 jets and the muon is only $24\,GeV$.

7.6 Same-Sign analysis

As discussed in previous sections, dilepton events in which the leptons have the same charge can only result from three main sources: fake dilepton events (see

---

*Estimated using $\sigma_{Wb\bar{b}}BR(W \rightarrow \ell\nu) \approx 10\,pb$ from section 6.6, together with the measurement of $R \equiv \sigma \cdot BR(W \rightarrow e\nu)/\sigma \cdot BR(Z^0 \rightarrow ee) = 10.9$ [85].

Dilepton Cut	ee	$\mu\mu$	$e\mu$	$\ell\ell\ell$	Total
Geom/P_t	512	711	1318	135	2676
Lepton ID	245	422	708	16	1391
Opposite Sign	18	21	31	16	86
Isolation	17	17	25	15	74
Z^0 mass	14	13	25	12	64
Missing E_t	10	7	16	9	42
2-jet	9	7	11	4	31
Corrected for lepton ID	6.4	5.2	7.9	2.4	21.9

Table 7.5

The *Same-Sign* dilepton analysis on a PYTHIA $t\bar{t}$ sample of 80 000 events with $m_t = 175\,GeV$. The 21.9 surviving events represents an acceptance of $(0.027 \pm 0.006)\%$.

section 6.4), $b\bar{b}$ (see section 6.5), and $t\bar{t}$ where one lepton comes from a W, and the other from a b decay (see section 5.4). In the dilepton analysis the $b\bar{b}$ contribution is very small (about 0.05 events expected in $109\,pb^{-1}$), and the fraction of $b\bar{b}$ pairs decaying to same-sign leptons is about 35% (see section 6.5), so the number of same-sign events in the data from this source is not expected to be significant.

After all dilepton cuts, the fraction of $t\bar{t}$ opposite-sign dilepton events in which one lepton comes from b decay is expected to be about 3% (see Table 5.8). This therefore also represents the fraction of $t\bar{t}$ same-sign dilepton events expected to pass all cuts*. The results of the dilepton analysis with the *requirement* that the leptons have the same charge, on a PYTHIA top 175 sample (introduced in section 5.1), is given in Table 7.5. This can be compared to the *standard* results on the same sample in Table 5.3. Using the same-sign $t\bar{t}$ dilepton acceptance from Table 7.5, and the opposite sign dilepton data analysis results of 9 candidate events (excluding the "$\mu\mu\gamma$" event) with a background of 2.1 ± 0.4 events, and an acceptance of $(0.77 \pm 0.08)\%$, the expected number of same-sign $t\bar{t}$ dilepton events in $109\,pb^{-1}$ of data is:

$$N_{t\bar{t}}^{SS} = 0.24 \pm 0.11 \quad \text{events.}$$

The only other contribution to the same-sign dilepton sample is from fake leptons as has already been discussed in section 6.4. The expected contribution is less than half an event in $109\,pb^{-1}$, though the errors are large.

It is therefore of interest to investigate whether the same-sign analysis produces the sparse number of events expected, not only as a check to the understanding of the data, but also because it may be a channel sensitive to new physics.

The analog to the standard dilepton analysis results in Table 7.1, for same-sign dileptons, is shown in Table 7.6. Before the invariant mass cut, there are 4 ee, 5 $\mu\mu$, and 2 $e\mu$ same-sign events. As shown in Figure 7.11, 6 of the 9 ee and $\mu\mu$ same-sign events fall within the Z^0 mass window and are therefore identified as same-sign Z^0 events. This can only happen when there has been a problem with the track reconstruction in the event. It clearly is not a common occurrence, happening about 0.1% of the time, in the total of 5535 Z^0 events in the dilepton analysis. Tracking problems also manifest themselves in same-sign events with zero dilepton invariant mass. The same-sign ee event at zero invariant mass has two overlapping tracks

---

*To be pedantic, the 0.3% of expected trilepton events should also be included.

	DILEPTON CUT										
	Lepton	Opp			$N_j > 10\,GeV$				$N_j > 10\,GeV$		
Category	ID	Sign	Isolation	$M_{\ell\ell}$	0	1	≥ 2	$\not\!\!E_t$	0	1	≥ 2
TCE-TCE	2402	5	2	0	0	0	0	0	0	0	0
TCE-LCE	455	11	2	0	0	0	0	0	0	0	0
$e - e$	2857	16	4	0	0	0	0	0	0	0	**0**
TCM-TCM	1324	6	1	1	1	0	0	1	1	0	0
TCM-CMX	1047	0	0	0	0	0	0	0	0	0	0
CMX-CMX	191	0	0	0	0	0	0	0	0	0	0
TCM-CMI	675	2	2	0	0	0	0	0	0	0	0
CMX-CMI	217	1	1	0	0	0	0	0	0	0	0
$\mu - \mu$	3454	9	4	1	1	0	0	1	1	0	**0**
TCE-TCM	39	8	2	2	0	0	2	2	0	0	2
TCE-CMX	9	0	0	0	0	0	0	0	0	0	0
TCE-CMI	12	1	0	0	0	0	0	0	0	0	0
TCM-LCE	6	2	0	0	0	0	0	0	0	0	0
CMX-LCE	2	2	0	0	0	0	0	0	0	0	0
$e - \mu$	68	13	2	2	0	0	2	2	0	0	**2**

Table 7.6

Same-sign dilepton channel analysis results in $109\,pb^{-1}$. Two same-sign $e\mu$ events pass all cuts.

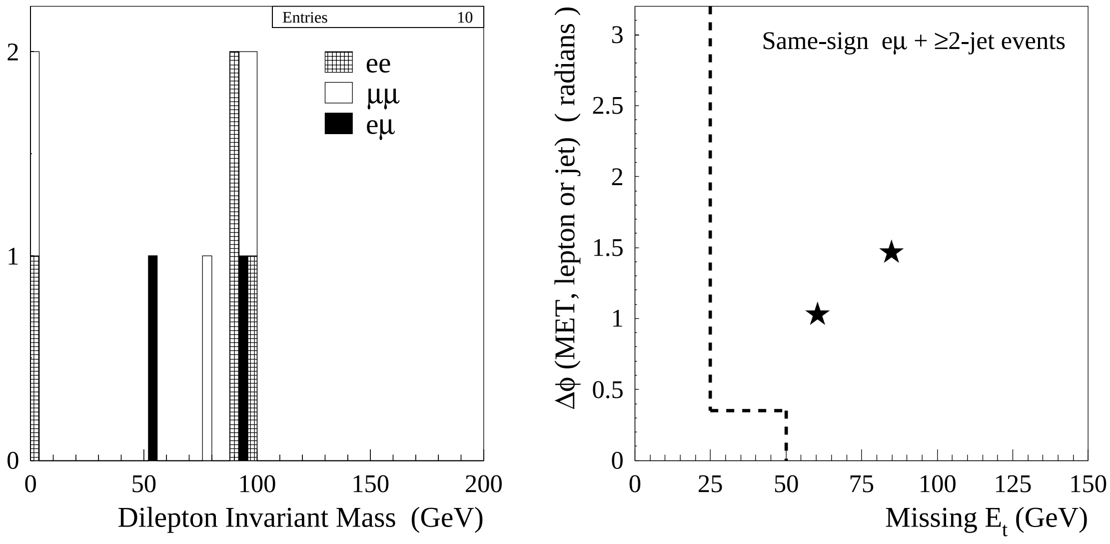

Figure 7.11

The invariant mass of same-sign dileptons in the data after the lepton ID, opposite sign, and isolation cuts (left plot), and, the $\not{E}_t$ scatter plot after the invariant mass cut for the same-sign $e\mu$ channel (right plot). Both same-sign $e\mu$ events that pass the $\not{E}_t$ cuts have ≥ 2 jets.

associated with the same electromagnetic cluster[*]. Similarly, there is a same-sign $\mu\mu$ event at almost zero invariant mass, which has two diametrically opposite stubs in the muon chambers, but only one track pointing to one them, but which has been reconstructed as two tracks. There is nothing else in the event, making it most likely that this is a cosmic ray event that has confused the tracking reconstruction algorithms. Therefore, all the same-sign ee and $\mu\mu$ events that pass up to and including the isolation cut can be accounted for by tracking problems. There are no ee or $\mu\mu$ same-sign events that pass all cuts.

---

[*] This event also fails the invariant mass cut because it is required that $M_{\ell\ell} > 0\,GeV$.

Category Run/Event z_{vertex}	$E_t(e)$, η_e, ϕ_e $(E,\vec{P})_e$ e^{charge}	$P_t(\mu)$, η_μ, ϕ_μ $(E,\vec{P})_\mu$ μ^{charge}	$E(j_1), E_t(j_1)$, η_{j_1}, ϕ_{j_1} $E(j_2), E_t(j_2)$, η_{j_2}, ϕ_{j_2} $\vdots$	H_t $\not{E}_t$, $\phi_{\not{E}_t}$
same-sign $e\mu$				
TCE-TCM 61074/103772 $-3.5\,cm$	27.9, -0.42, 120° (30.4, -15.1, 23.5, -12.2) e^-	25.1, 0.06, 318° (25.1, 18.6, -16.8, 1.3) μ^-	115.4, 104.3, 0.46, 226° 52.0, 52.0, -0.04, 92° 37.2, 37.2, 0.04, 309°	307 60.6, 34°
TCE-TCM 68592/219028 $19.6\,cm$	57.5, -0.29, 84° (60.0, 5.9, 57.2, -17.1) e^+	89.1, -0.49, 165° (101.1, -86.1, 22.7, -47.7) μ^+	55.9, 53.5, -0.30, 264° 37.2, 29.2, 0.73, 266°	314 85.3, 1°

Table 7.7

Kinematic properties of the 2 same-sign $e\mu$ dilepton candidates. All energies and momenta are in units of GeV, with the muon momenta beam constrained.

The 2 same-sign $e\mu$ events, also shown in Figure 7.11, pass all the dilepton selection cuts, one with 2 jets, and one with 3 jets. Characteristics of these 2 events are given in Table 7.7. The second of these (68592/219028), has a peculiar muon, in that it does not match very well with the z vertex (z-vertex match $= 2.5\,cm$) or with the beam position (impact parameter $= 0.25\,cm$). Although it passes both the cuts (barely), the values of both these variables are in the tails of the distributions given in Figure 4.4. In addition, the muon track momentum before beam constraining was $846\,GeV$, and the charge of the beam constrained track could not be determined. One possible scenario could therefore be that this track has been badly measured leading to an incorrect determination of its charge, and that it is in fact an opposite-sign $e\mu$ event with 2 jets*.

The other same-sign $e\mu$ (61074/103772) is well known to the *lepton + jets* anal-

---

*Neither of the 2 jets is b-tagged.

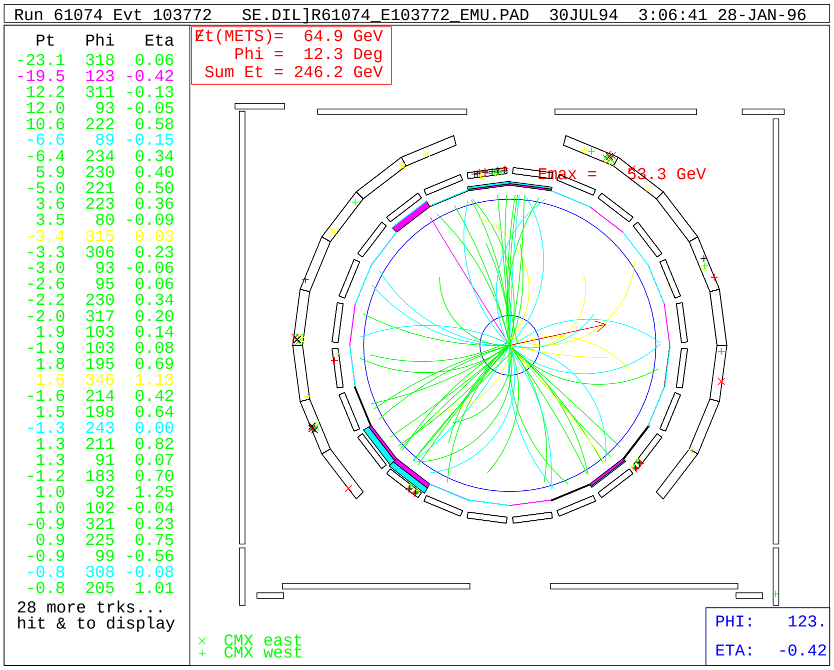

```
Run 61074 Evt 103772    SE.DIL]R61074_E103772_EMU.PAD  30JUL94  3:06:41 28-JAN-96

  Pt    Phi   Eta
-23.1   318  0.06
-19.5   123 -0.42
 12.2   311 -0.13
 12.0    93 -0.05
 10.6   222  0.58
 -6.6    89 -0.15
 -6.4   234  0.34
  5.9   230  0.40
 -5.0   221  0.50
  3.6   223  0.36
  3.5    80 -0.09
 -3.4   315  0.03
 -3.3   306  0.23
 -3.0    93 -0.06
 -2.6    95  0.06
 -2.2   230  0.34
 -2.0   317  0.20
  1.9   103  0.14
 -1.9   103  0.08
  1.8   195  0.69
  1.6   346  1.13
 -1.6   214  0.42
  1.5   198  0.64
 -1.3   243  0.00
  1.3   211  0.82
  1.3    91  0.07
 -1.2   183  0.70
  1.0    92  1.25
  1.0   102 -0.04
 -0.9   321  0.23
  0.9   225  0.75
 -0.9    99 -0.56
 -0.8   308 -0.08
 -0.8   205  1.01
28 more trks...
hit & to display

Et(METS)=   64.9 GeV
    Phi =   12.3 Deg
 Sum Et = 246.2 GeV
```

Figure 7.12

Transverse view of the CTC tracks in the same-sign $e\mu$ candidate 61074/103772. The electron is at $\phi = 120°$, and the muon at $\phi = 318°$.

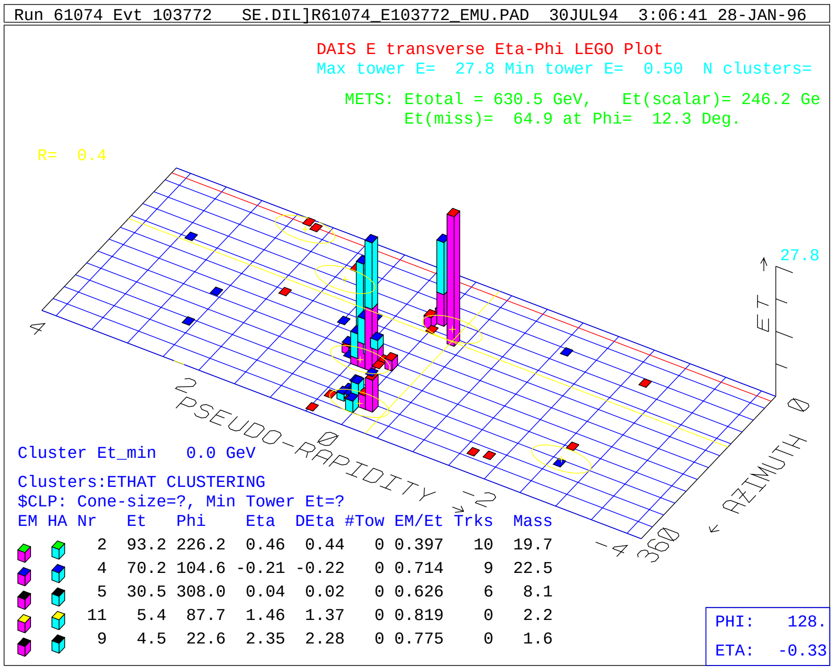

```
Run 61074 Evt 103772    SE.DIL]R61074_E103772_EMU.PAD  30JUL94  3:06:41 28-JAN-96

DAIS E transverse Eta-Phi LEGO Plot
Max tower E=  27.8 Min tower E=  0.50  N clusters=

METS: Etotal = 630.5 GeV,    Et(scalar)= 246.2 Ge
       Et(miss)=  64.9 at Phi=  12.3 Deg.

Cluster Et_min   0.0 GeV

Clusters:ETHAT CLUSTERING
$CLP: Cone-size=?, Min Tower Et=?
EM HA Nr   Et   Phi    Eta  DEta #Tow EM/Et Trks  Mass
        2  93.2 226.2  0.46  0.44   0 0.397   10  19.7
        4  70.2 104.6 -0.21 -0.22   0 0.714    9  22.5
        5  30.5 308.0  0.04  0.02   0 0.626    6   8.1
       11   5.4  87.7  1.46  1.37   0 0.819    0   2.2
        9   4.5  22.6  2.35  2.28   0 0.775    0   1.6
```

Figure 7.13

Lego plot showing the calorimeter transverse energy in the same-sign $e\mu$ candidate 61074/103772. The electromagnetic and hadronic energy is represented by the darker and lighter shade respectively.

ysis. The 27.9 GeV electron is isolated, and the 25.1 GeV muon is in the jet at $\phi = 309°$. This jet, and the one at $\phi = 92°$, are *both* b-tagged by the SECVTX algorithm, giving strong evidence for this event being a *lepton + jets* $t\bar{t}$ candidate in which one of the b quarks decays to give a high-P_t muon that passes the lepton identification of the dilepton analysis. It was calculated above that about 0.24 events of this type are expected from $t\bar{t}$ decay. The event displays of this same-sign $e\mu$ candidate are shown in Figures 7.12 and 7.13.

8. DILEPTON CHANNEL SIGNIFICANCE AND CROSS SECTION

8.1 Statistical significance

It was shown in chapters 7 and 6 that the dilepton analysis sees 10 events and expects 2.1 ± 0.4 events from the known background processes. It was also pointed out that one of these events (the "$\mu\mu\gamma$" event) was identified as a radiative Z^0+ 1-jet event, even though the expected contribution from this source is extremely small (see section 6.6.1). As discussed in Appendix D, such events in the future will be cut by the requirement that photons are not included in the jet count, without any loss to the $t\bar{t}$ acceptance. Therefore, for the purposes of the statistical significance and cross-section measurement, this event will not be considered a candidate event.

It is important to quantify the significance of observing of 9 events when the expectation from background processes alone is 2.1 ± 0.4 events. To do this the following *null hypothesis* is tested: "the observed number of events arose solely from the background sources [86]". That is, the probability that the estimated background, $\overline{B}$, could fluctuate to give at least the observed signal, N, is calculated. Let this probability be denoted by $\mathcal{P}(N,\,\overline{B})$. If, for simplicity, the background uncertainty is ignored, $\mathcal{P}(N,\,\overline{B})$ is given by the following sum of Poisson probabilities:

$$\mathcal{P}(N,\,\overline{B}) \;=\; \sum_{n=N}^{\infty} \frac{\overline{B}^{\,n}}{n!}\,e^{-\overline{B}} \;=\; 1 - \sum_{n=0}^{N-1} \frac{\overline{B}^{\,n}}{n!}\,e^{-\overline{B}}\,. \tag{8.1}$$

The Poisson distribution, $P(n;\,\overline{B})$, with mean $\overline{B} = 2.1$, is shown in Figure 8.1.

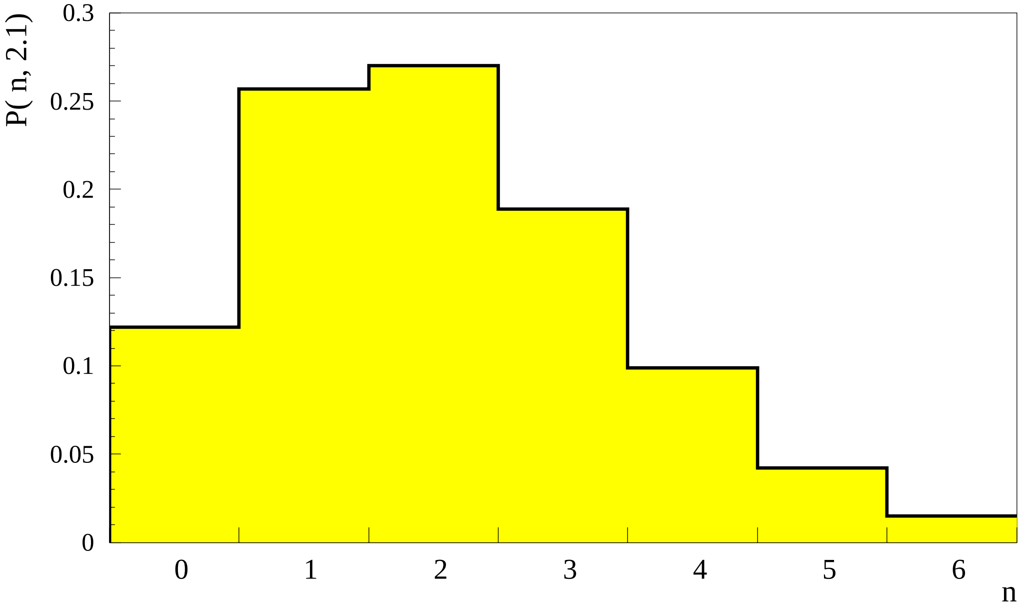

Figure 8.1

Poisson probability distribution with a mean equal to the expected dilepton background, $\overline{B} = 2.1$ events.

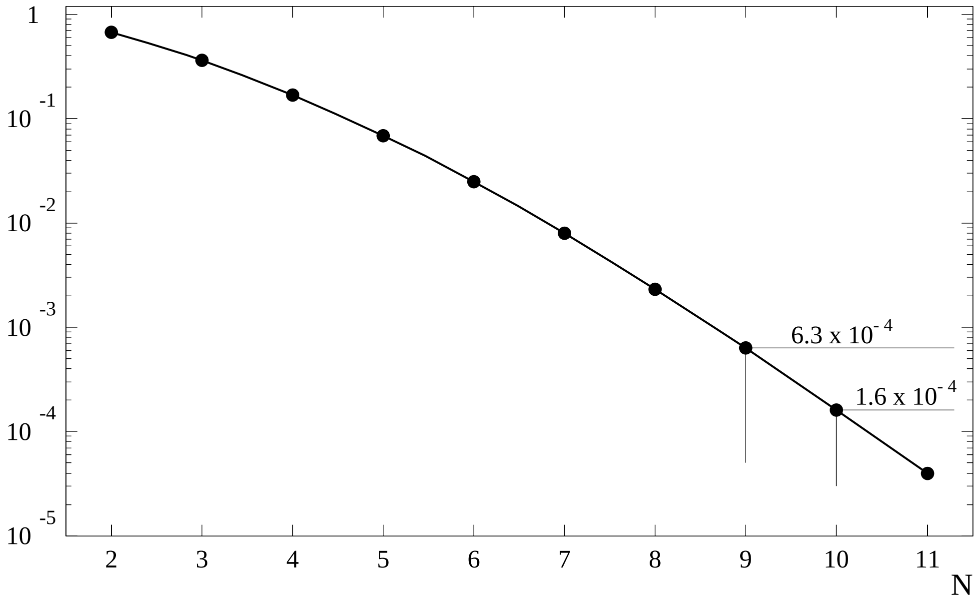

Figure 8.2

Probability that $\overline{B} = 2.1 \pm 0.4$ could fluctuate to give N observed events or more. Labelled are probabilities for $N = 9$ and $N = 10$ observed events.

Evaluating equation 8.1 for 9 observed dilepton events yields:

$$\mathcal{P}(N=9,\,\overline{B}=2.1)=3.4\times10^{-4}\ .$$

The uncertainty in the background estimate is taken into account by smearing the above Poisson distribution, $P(n;\,\overline{B})$, for observing n independent events when the expected number of events is $\overline{B}$, with a Gaussian distribution, $G(\overline{B},\,\sigma_{\overline{B}})$, with mean $\overline{B}$ and width $\sigma_{\overline{B}}$*. Explicitly, the following loop is performed a large number of times: a random number is generated from the $G(0,\,\sigma_{\overline{B}})$ distribution and added to $\overline{B}$, to give a mean $\overline{B}'$, from which it is randomly determined if the Poisson distribution $P(n;\,\overline{B}')$ returns a value of $n\geq N$. By accounting for the uncertainty in the background in this way, the probability obtained is:

$$\mathcal{P}(N=9,\,\overline{B}=2.1\pm0.4)=6.3\times10^{-4}\ .$$

Therefore, the pure background (or null) hypothesis is only 0.063% probable for 9 observed events. The probabilities for an upward fluctuation of 2.1 ± 0.4 events, to at least N events is plotted in Figure 8.2, for a range of N from 2 to 11, with the observed number of dilepton candidates indicated. It can be noted that for a Gaussian probability distribution (which this clearly is not), a probability of 0.063% correspond to an excess of 3.2σ.

This significance does not include the fact that the dilepton candidate events contain b-tagged jets, since the dilepton selection did not *a-priori* require a b-tag. As discussed in section 7.4, under the *null hypothesis* that all the dilepton events observed are background, the number of b-tagged jets expected would be about 0.7. Six tags are observed.

---

*Given by the background uncertainty, which in this case is 0.4.

8.2 The $t\bar{t}$ cross section

In the previous chapters all the components necessary to calculate the $t\bar{t}$ production cross section using the dilepton decay channel, have been evaluated. The cross section for $p\bar{p} \rightarrow t\bar{t}$ is calculated in the dilepton channel from:

$$\sigma_{t\bar{t}} = \frac{N - \overline{B}}{\epsilon_{dil}\mathcal{L}} \tag{8.2}$$

where;

$N =$ number of observed events $= 9$ (Chapter 7).

$\overline{B} =$ expected number of background events $= 2.1 \pm 0.4$ (Chapter 6).

$\epsilon_{dil} =$ total dilepton channel acceptance $= (0.77 \pm 0.08)\%$ (Chapter 5).

$\mathcal{L} = \int L\, dt =$ the total integrated luminosity $= 109.4 \pm 7.2\, pb^{-1}$ (section 1.2).

To correctly enumerate the error in $\sigma_{t\bar{t}}$ a likelihood function, L_{dil}, is formed from the Poisson probability of observing N events when the expected number of events is $(\sigma_{t\bar{t}}\, \epsilon_{dil}\, \mathcal{L} + \overline{B})$ for a given value of $\sigma_{t\bar{t}}$, smeared by the Gaussian distributions for $\mathcal{L}$, $\overline{B}$, and ϵ_{dil}, with widths given by their respective uncertainties. That is, the likelihood function,

$$L_{dil} = G(\mathcal{L},\, \sigma_{\mathcal{L}}) \cdot G(\epsilon_{dil},\, \sigma_{\epsilon_{dil}}) \cdot G(\overline{B},\, \sigma_{\overline{B}}) \cdot P(N,\, \sigma_{t\bar{t}}\, \epsilon_{dil}\, \mathcal{L} + \overline{B})$$

is maximized to calculate the $t\bar{t}$ production cross section [*], with the uncertainties on $\sigma_{t\bar{t}}$ calculated as the $\Delta \ln L = \frac{1}{2}$ points of the likelihood function [5, 87]. The results is:

$$\boxed{\sigma_{t\bar{t}} = 8.2^{+4.3}_{-3.3}\, pb\ .}$$

Figure 8.3 displays the $t\bar{t}$ production cross section measurement in the dilepton channel, with that expected from the NLO calculation with soft gluon resummation

---

[*] Of course, L_{dil} is trivially maximized by equation 8.2.

of Laenen, Smith and van Neerven [22]. The light point also displayed is the $t\bar{t}$ cross section measured in the lepton+jets channel using the SVX b-tagging algorithm. This represents the latest value of $\sigma_{t\bar{t}} = 6.8^{+2.3}_{-1.8}\,pb$ [63], using the full $109\,pb^{-1}$ dataset. The number hasn't changed from the top discovery PRL [2], which used $67\,pb^{-1}$ of data, but the errors have been reduced. The dotted line represents the central values of $\sigma_{t\bar{t}}$ measured in the dilepton channel with 9 observed candidate events, as a function of top mass. The negative slope is the effect of the increasing $t\bar{t}$ acceptance in the dilepton channel with increasing top mass (see Figure 5.10).

It is of interest to note that if the $e\mu$ channel only is used, with 7 candidate events, over a background of 0.74 ± 0.21 events, and an acceptance of $(0.45 \pm 0.05)\%$, the cross section obtained is:

$$\sigma_{t\bar{t}} = 12.7^{+6.5}_{-4.9}\,pb \qquad (e\mu \text{ channel only}).$$

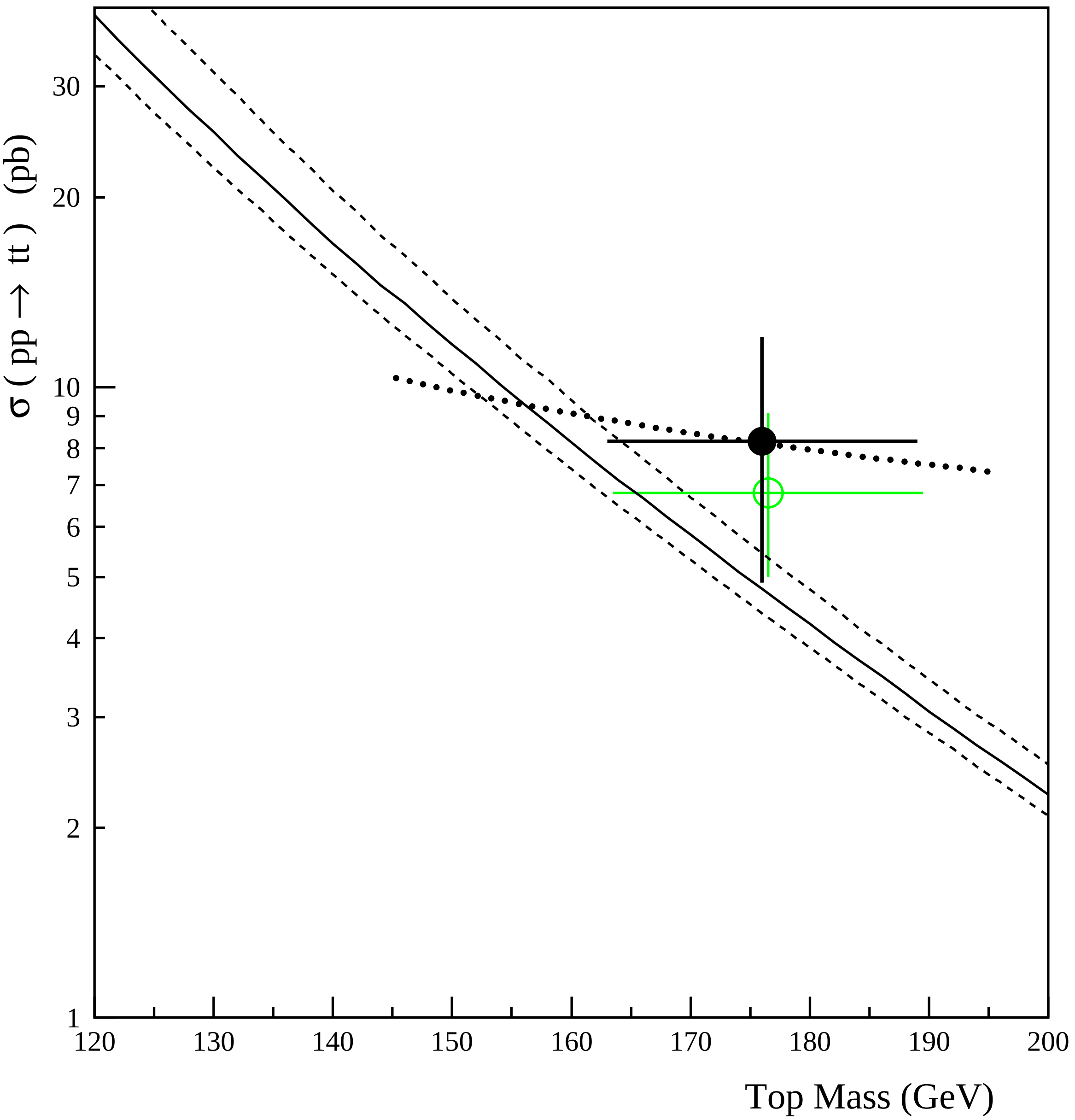

Figure 8.3

The $t\bar{t}$ production cross section as measured in the dilepton channel (dark point), plotted at a top mass of $176 \pm 13\, GeV$. Also shown are, the theoretical curves of Laenen et al. (the one solid and two dashed curves), the cross section measured in the lepton + jets channel (light point), and, $\sigma_{t\bar{t}}$ for 9 observed events as a function of top mass (dotted line).

9. CONCLUSIONS

Production of $t\bar{t}$ pairs has been observed in the dilepton decay channel ($t\bar{t} \rightarrow W^+bW^-\bar{b} \rightarrow \ell^+\nu_\ell b\ell^-\bar{\nu}_\ell\bar{b}$, where $\ell = e$ or μ), based on 9 observed candidate events with an expected background of 2.1 ± 0.4 events. The probability of a background fluctuation to give the observed number of events is 6.3×10^{-4}. The $t\bar{t}$ production cross-section from the dilepton channel is measured to be:

$$\sigma_{t\bar{t}} = 8.2^{+3.8}_{-3.3}\, pb\ .$$

Of the 9 candidates, 1 was observed in the ee decay channel, 1 in the $\mu\mu$, and 7 in the $e\mu$. One additional $\mu\mu$ event that passed all dilepton cuts was identified as a radiative Z^0 event. Four of the 9 candidate events have jets identified as resulting from b quark fragmentation, strengthening the significance of the dilepton result.

It is important that the properties of the top measured in the *lepton + jets* channel [2], can be verified from a different decay channel. The cross-section measured in the *lepton + jets* channel is consistent with the dilepton result above, however, a measurement of the top mass in the dilepton channel would be an important verification of this electroweak parameter that is not predicted by the Standard Model. Certainly, the present CDF dataset will be the most useful source for at least a few years to study the top quark properties, in particular its mass, branching fractions, production cross-section and various kinematic distributions. A more precise and detailed understanding of these properties may shed some light on the role of the top quark in electroweak symmetry breaking, and perhaps provide some clues of what lies beyond the Standard Model.

BIBLIOGRAPHY

BIBLIOGRAPHY

1. The Standard Model, an SU(3) × SU(2) × U(1) gauge invariant theory of the strong and electroweak forces, is discussed in numerous references: personal favorites include; D. Griffiths, *Introduction to Elementary Particles*, Harper & Row Publishers, 1987 ; F. Halzen and A. Martin, *Quarks & Leptons: An Introductory Course in Modern Particle Physics*, John Wiley & Sons, 1984 ; V. Barger and R. Phillips, *Collider Physics*, Addison Wesley Publishing Company, 1987.

2. F. Abe et al. Observation of Top Quark Production in $\overline{p}p$ Collisons with the Collider Detector at Fermilab. *Phys. Rev. Lett.*, **74**:2626, 1995.

3. C. Grosso-Pilcher et al. Luminosity for the Top PRL. CDF internal note 3021, 1995.

4. S. Herb et al. Observation of a Dimuon Resonance at 9.5 GeV in 400-GeV Proton-Nucleus Collisions. *Phys. Rev. Lett.*, **39**:252, 1977.

   W. Innes et al. Observation of Structure in the Υ Region. *Phys. Rev. Lett.*, **39**:1240, 1977.

5. F. Abe et al. Evidence for top quark production in $p\overline{p}$ collisions at $\sqrt{s} = 1.8$ TeV. *Phys. Rev. D*, **50**:2966, 1994.

6. F. Abachi et al. Observation of the Top Quark. *Phys. Rev. Lett.*, **74**:2632, 1995.

7. Measurements of electroweak parameters made at LEP using the 1989-1993 data can be found in: B. Jocobsen, Top Mass from Electroweak Measurements, presented at the XXIXth Rencontres de Moriond, March 19-26, 1994.

8. W. Bartel et al. A measurement of the electroweak induced charge aymmetry in $e^+e^- \rightarrow b\overline{b}$. *Phys. Lett. B*, **146**:437, 1984.

9. P. Abreu et al. Measurement of the forward-backward asymmetry of $e^+e^- \rightarrow Z \rightarrow b\overline{b}$ using prompt leptons and a lifetime tag. *Z. Phys. C*, **65**:569, 1995.

10. R. Akers et al. A measurement of the forward-backward asymmetry of $e^+e^- \rightarrow$

$b\bar{b}$ by applying a jet charge algorithm to lifetime tagged events. *Z. Phys. C*, **67**:365, 1995.

11. G. Kane and M. Peskin. A constraint from B decay on models with no t quark. *Nucl. Phys.*, **B195**:29, 1982.

12. S. Glashow, J. Iliopoulos, and L. Maina. Weak Interactions with Lepton-Hadron Symmetry. *Phys. Rev. D*, **2**:1285, 1970.
    Recall that the GIM mechanism requires all left- and right-handed quark components of the same electric charge in different families to have the same weak isospin.

13. A. Bean et al. Improved upper limit on flavor-changing neutral-current decays of the b quark. *Phys. Rev. D*, **35**:3533, 1987.

14. J. Rosner. Electroweak measurements and the top quark. *Rev. Mod. Phys.*, **64**:1151, 1992.

15. W. Hollik. Electroweak precision observables - an indirect access to the top quark. Karlsruhe preprint KA-TP-2-1995 (electronic archive: hep-ph/9503410).

16. S. Errede. The M_W vs. M_{Higgs} Relation from Electroweak Radiative Corrections. CDF/ANAL/ELECTROWEAK/CDFR/3372. 1995.

17. C. Albajar et al. Search for new heavy quarks at the CERN proton-antiproton collider. *Z. Phys. C*, **37**:505, 1988.

18. F. Abe et al. Top-quark search in the electron+jets channel in proton-antiproton collisions at $\sqrt{s} = 1.8\,\text{TeV}$. *Phys. Rev. D*, **43**:664, 1991.

19. F. Abe et al. Lower Limit on the Top-Quark Mass from Events with Two Leptons in $p\bar{p}$ collisions at $\sqrt{s} = 1.8\,\text{TeV}$. *Phys. Rev. Lett.*, **68**:447, 1992.

    F. Abe et al. Limit on the top-quark mass from proton-antiproton collisions at $\sqrt{s} = 1.8\,\text{TeV}$. *Phys. Rev. D*, **45**:3921, 1992.

20. S. Abachi et al. Search for the Top-Quark in $p\bar{p}$ collisions at $\sqrt{s} = 1.8\,\text{TeV}$. *Phys. Rev. Lett.*, **72**:2138, 1994.

21. R. Meng, G.A. Schuler, J. Smith, and W.L. van Neerven. *Nucl. Phys.*, **B339**:325, 1990.

22. E. Laenen, J. Smith, and W. L. van Neerven. Top quark production cross

section. *Phys. Lett. B*, **321**:254, 1994.

23. R. K. Ellis. Rates for Top Quark Production. *Phys. Lett. B*, **259**:492, 1991.

24. E. Berger and H. Contopanagos. Perturbative gluon resummation of the top-quark production cross section. *Phys. Lett. B*, **361**:115, 1995.

25. S. Catani, M.L. Mangano, P. Nason, and L. Trentadue. The Top Cross Section in Hadronic Collisions. CERN preprint, CERN-TH/96-21 (electronic archive: hep-ph/9602208).

26. I. Bigi et al. Production and decay properties of ultra-heavy quarks. *Phys. Lett. B*, **181**:157, 1986.

27. F. Abe et al. Measurement of the W boson mass. *Phys. Rev. Lett.*, **75**:11, 1995.

28. M. Jeżabek and J. H. Kühn. Top quark width: Theoretical update. *Phys. Rev. D*, **48**:1910, 1993.

29. V. Barger, J. Ohnemus, and R.J.N. Phillips. Spin correlation effects in the hadroproduction and decay of very heavy top quark pairs. *J. Mod. Phys.*, **A4**:617, 1989.

30. G.L. Kane, G.A. Ladinsky, and C.-P. Yuan. Using the top quark for testing standard-model polarization and CP predictions. *Phys. Rev. D*, **45**:124, 1992.

31. S. Parke. Summary of Top Quark Physics. FERMILAB-Conf-94/322-T. Presented at DPF'94, University of New Mexico, NM, August 2-6, 1994.

    G. Eilam, J. Hewett and A. Soni. Rare decays of the top quark in the standard and two-Higgs-doublet models. *Phys. Rev. D*, **44**:1473, 1991.

32. T. Han, R.D. Peccei, and X. Zhang. Top-Quark Decay Via Flavor-Changing Neutral Currents at Hadron Colliders. FERMILAB-PUB-95/160-T. June 1995. See also the references contained within.

33. T. LeCompte. Top decay physics at CDF and measurement of the CKM element V_{tb}. CDF/PUB/TOP/PUBLIC/3465, 1995. Also published as Fermilab conference proceedings, FERMILAB-CONF-96/021-E.

34. T. Baumann, J. Konigsberg and M. Franklin. A top dilepton analysis using hadronic taus. CDF/ANAL/TOP/CDFR/2325, 1994.

S. Leone. Search for the top quark at CDF in events with two charged leptons, neutrinos and hadronic jets. PhD thesis, University of Pisa, February 1994.

M. Gallinaro and H. Grassmann. Top Analysis with Lepton + Isolated Track. CDF/ANAL/TOP/CDFR/3132, 1995.

M. Gallinaro and M. Hohlmann. Observation of top dileptons with hadronically decaying tau leptons. CDF/ANAL/TOP/CDFR/3461, 1995.

35. P. Azzi et al. Observation of $t\bar{t}$ Production in the All-Hadronic Channel. CDF/ANAL/TOP/CDFR/3429, 1995.

36. W. Bokhari, L. Rosenson, and P. Sphicas. Search for the Top Quark in the multijet channel with double SVX tagging. CDF/ANAL/TOP/CDFR/3088, 1995.

37. Some accelerator parameters can be found on WWW at the URL address: http://www-fermi3.fnal.gov/.

38. F. Abe et al. The CDF Detector: an overview. *Nucl. Inst. Meth. Phys. Res.*, **A271**:387, 1988.

39. D. Amidei et al. The CDF Silicon Vertex Detector. *Nucl. Inst. Meth. Phys. Res.*, **A350**:73, 1994.

40. D. Amidei et al. SVX$'$: The New CDF Silicon Vertex Detector. *Nucl. Inst. Meth. Phys. Res.*, **A360**:137, 1995.

41. F. Bedeschi et al. Design and construction of the CDF Central Tracking Chamber. *Nucl. Inst. Meth. Phys. Res.*, **A268**:50, 1988.

42. L. Balka et al. The CDF Central Electromagnetic Calorimeter. *Nucl. Inst. Meth. Phys. Res.*, **A267**:272, 1988.

43. S. Bertolucci et al. The CDF Central and Endwall Hadron Calorimeter. *Nucl. Inst. Meth. Phys. Res.*, **A267**:301, 1988.

44. G. Ascoli et al. CDF Central Muon Detector. *Nucl. Inst. Meth. Phys. Res.*, **A268**:33, 1988.

45. G. Foster et al. A Fast Hardware Track-Finder for the CDF Central Tracking Chamber. *Nucl. Inst. Meth. Phys. Res.*, **A269**:93, 1988.

46. D. Glenzinski and P. Schlabach. Validation of the Run 1B, Stream A, High P_t, Central, Inclusive Muon Data Set. CDF/ANAL/MUON/CDFR/2715, 1994.

47. CDF Top Group. Sample Selection for Run 1B Top Search. CDF/ANAL/TOP-/CDFR/2966, 1995.

48. D. Gerdes. Study of Conversion Removal for the Lepton + Jets Sample. CDF/ANAL/TOP/CDFR/2903, 1995.

49. CDF Dilepton Working Group. Event Selection for the Top Dilepton Analysis. CDF/DOC/TOP/CDFR/2862, 1995.

50. R. Field and R. Feynman. *Nucl. Phys.*, **B136**:1, 1978.

51. L. Garren. Herwig at F.N.A.L. Fermilab Publication PU124, 1993. See also the references contained within.

    G. Marchesini and B. R. Webber. Simulation of QCD jets including soft gluon interference. *Nucl. Phys.*, **B238**:1, 1984.

    B. R. Webber. A QCD model for jet fragmentation including soft gluon interference. *Nucl. Phys.*, **B238**:492, 1984.

52. F. Abe et al. Topology of three-jet events in $p\overline{p}$ collisions at $\sqrt{s} = 1.8\,\mathrm{TeV}$. *Phys. Rev. D*, **45**:1448, 1992.

53. F. Abe et al. Study of four-jet events and evidence for double parton interactions in $p\overline{p}$ collisions at $\sqrt{s} = 1.8\,\mathrm{TeV}$. *Phys. Rev. D*, **47**:4857, 1993.

54. S. Kuhlmann. The 10% Solution. CDF/PHYS/TOP/CDFR/2506, 1994.

55. The PYTHIA top 175 $t\bar{t}$ sample wes created by Marcus Hohlmann at the University of Chicago.

56. The HERWIG $t\bar{t}$ samples were created by Carla Grosso-Pilcher at the University of Chicago.

57. T. Liss. A Fast Muon Trigger Simulation. CDF/DOC/TOP/CDFR/2998, 1995.

58. D. Cronin-Hennessy et al. Measurement of $Z \rightarrow e^+e^-+$ N Jet Cross Sections in 1.8TeV $\overline{p}p$ Collisions. CDF/DOC/TOP/CDFR/3360, 1995.

59. T. Chikamatsu et al. Top Dilepton Analysis. CDF/ANAL/HEAVYFLAVOR/-CDFR/1975, 1993.

60. S. Drell and T.-M. Yan. Massive Lepton-Pair Production in Hadron-Hadron Collisions at High Energies. *Phys. Rev. Lett.*, **25**:316, 1970.

61. M. Contreras and J. Wang. Estimate of the Drell-Yan background in the Top Dilepton Analysis. CDF/ANAL/TOP/CDFR/2261, 1993.

    J. Konigsberg. Drell-Yan backgrounds for the Top Dilepton Analyis in $100\,pb^{-1}$. CDF/DOC/TOP/CDFR/3208, 1995.

62. F. Berends et al. *Nucl. Phys.*, B357:32, 1991. Michelangelo Mangano performed the calculations used here.

63. T. Liss and R. Roser. $t\bar{t}$ Production Cross Section for $110\,pb^{-1}$. CDF/ANAL/TOP/CDFR/3481, 1996.

64. Physical Review D, Particles and Fields, Review of Particle Properties, Volume 50, 1 August 1994, page 1193.

65. The ISAJET sample used for the $Z \rightarrow \tau\tau$ background estimate was created by Toshiharu Uchida.

66. J. Wang and M. Contreras. Estimate of $Z^0 \rightarrow \tau^+\tau^-$ background in the Top Dilepton Analysis. CDF/ANAL/TOP/CDFR/2108, 1993.

67. J. Romano, Ph.D. dissertation, University of Chicago, August 1995.

68. T. Chikamatsu et al. Top Dilepton Analysis - Run 1. CDF/ANAL/TOP/-CDFR/2851, 1995.

69. F. Abe et al. Measurement of $\sigma \cdot B(W \rightarrow e\nu)$ and $\sigma \cdot B(Z^0 \rightarrow e^+e^-)$ in $p\overline{p}$ collisions at $\sqrt{s} = 1.8\,tev$. *Phys. Rev. Lett.*, 1996. To be published.

70. K. Hagiwara, J. Woodside, and D. Zeppenfeld. Measuring the WWZ coupling at the Fermilab Tevatron. *Phys. Rev. D*, **41**:2113, 1990.

71. J. Ohnemus. Order-α_s calculation of hadronic W^-W^+ production. *Phys. Rev. D*, **44**:1403, 1991.

72. J. Ohnemus. Order-α_s calculation of hadronic $W^{\pm}Z$ production. *Phys. Rev. D*, **44**:3477, 1991.

73. Much of the WW matrix element work was done by Chris Wendt using a VECBOS style Monte Carlo program written by Tao Han.

74. A. Goshaw, S. Hauger, W. Kowald, and W. Robertson. Properties of Jets in Z Boson Events from 1.8 TeV $p\overline{p}$ Collisions. CDF/ANAL/ELECTROWEAK/-CDFR/2711, 1994.

75. Chris Wendt, private communication.

76. J. Ohnemus and J. F. Owens. Order-α_s calculation of hadronic ZZ production. *Phys. Rev. D*, **43**:3626, 1991.

77. J. Romano and M. Contreras. Background due to Hadron Misidentification in the Top Dilepton Search. CDF/ANAL/TOP/CDFR/2107, 1993.

    P. Yeh, M.T. Cheng, and G.P. Yeh. Top Dilepton Background from Fake Leptons. To be published as a CDF note, 1996.

78. D. Bortoletto et al. Top Dilepton Analysis - June 1995 Update. CDF/ANAL/TOP/CDFR/3203, 1995.

79. F. Abe et al. Measurement of $B^0\overline{B}^0$ Mixing at the Fermilab Tevatron Collider. *Phys. Rev. Lett.*, **67**:3351, 1991.

80. L. Song, G.P. Yeh, and Q.F. Wang. Study of Top Dilepton Background from $b\overline{b}$ Sources. CDF/ANAL/TOP/CDFR/2106, 1993.

81. Milciades Contreras, CDF meeting presentations and private communication.

82. G. Unal. W$b\overline{b}$ and W$c\overline{c}$ Backgrounds in the Top SVX Channel. CDF/ANAL/TOP/CDFR/3389, 1995.

83. G. Apollinari et al. Preliminary evidence for a $b\overline{b}$ state of mass $105\,GeV$ produced in association with a W or a Z boson: findings of a study of top production and a search for the higgs in W, $Z+\geq 1$ jet events. CDF/ANAL/TOP/CDFR/3431, 1996.

84. B-Tag Working Group. Update of SECVTX Tagging in Run 1B Data. CDF/DOC/SEC_VTX/CDFR/3178, 1995.

85. F. Abe et al. Measurement of the ratio $\sigma B(p\overline{p} \rightarrow W \rightarrow e\nu)/\sigma B(p\overline{p} \rightarrow Z^0 \rightarrow ee)$ in $p\overline{p}$ collisions at $\sqrt{s} = 1800\,\mathrm{GeV}$. *Phys. Rev. D*, **52**:2624, 1995.

86. T. Liss, G. Unal, and P. Sinervo. Estimating the Statistical Significance of a Top Quark Search Counting Experiment. CDF/ANAL/TOP/CDFR/2370, 1994.

87. R. Hughes, B. Winer, and T. Liss. Combining the SVX, SLT, and Dilepton $t\bar{t}$ Cross Sections. CDF/ANAL/TOP/CDFR/3111, 1995.

88. F. E. Paige and S. D. Protopopescu. A Monte Carlo Generator for pp and $p\bar{p}$ Reactions. BNL report No. 38034, 1986 (unpublished). At CDF this can be found in ISAJET$DOC:ISAJET_NOTE.TXT .

89. T. Sjöstrand. High-energy-physics event generation with PYTHIA 5.7 and JETSET 7.4. *Computer Physics Communications*, **82**:74, 1994.

90. F.A. Berends, W.T. Giele, H. Kuijf, and B. Tausk. On the production of a W and jets at hadron colliders. *Nucl. Phys.*, **B357**:32, 1991.

91. J. Benlloch, A. Caner, T. Rodrigo, and M. Mangano. On transforming partons into jets: HERPRT, a new interface between ME MC and fragmentation models. CDF/DOC/MONTECARLO/1823, 1992.

92. J. Lewis and P. Avery. CLEOMC: The CDF Interface to the CLEO Monte Carlo (QQ). CDF/DOC/MONTECARLO/PUBLIC/2724, 1994.

93. S. Jadach, Z. Wąs, R. Decker, and J.H. Kühn. The τ decay library TAUOLA, version 2.4. *Computer Physics Communications*, **76**:361, 1993.

94. C. Loomis. Using TAUOLA, A Decay Library for Polarized τ Leptons, at CDF. CDF/DOC/EXOTIC/CDFR/2796, 1994.

95. M. Shapiro et al. A User's Guide to QFL. CDF/ANAL/MONTECARLO/-PUBLIC/1810, 1992.

96. A. Caner. CDFSIM + QFL Simulation of the CDF Detector. CDF/ANAL/-MONTECARLO/PUBLIC/2177, 1993.

APPENDICES

APPENDIX A: CALCULATING LEPTON IDENTIFICATION EFFICIENCIES

To calculate high-P_t electron and muon identification efficiencies, $Z^0 \rightarrow ee$ and $Z^0 \rightarrow \mu\mu$ events in the data are used, because of the very little background expected under the Z^0 peak. Events are selected which have one *tight* lepton (see sections 4.2 and 4.3), and a second lepton in the fiducial region* with a transverse energy greater than $20\,GeV$. In addition, the two leptons must combine to form an invariant mass consistent with coming from a Z^0 decay: $80 < M_{\ell\ell} < 100\,GeV$. For ee events, the second electron is also required not to come from a photon conversion [48, 49], and, for $\mu\mu$ events the second muon is required to be inconsistent with coming from a cosmic ray [49]. The number of "second" leptons that pass all the lepton identification requirements is then used to calculate the efficiency for the appropriate lepton type.

A.1 Total ID efficiency

The total lepton ID efficiency for a given lepton type (TCE, LCE, TCM, CMX or CMI) is the probability that, given a high-P_t fiducial lepton, it passes all the required selection criteria (see chapter 4). Let ϵ_{ID} be that probability, and let $\mathcal{X}$ represent a lepton of a given type that has passed all the selection cuts, and $\mathcal{O}_{\mathcal{X}}$ represent a lepton, of the same type, that has failed at least one of the selection cuts. Then, all Z^0 events, with two true leptons, can be categorized as follows, with each category shown with the probability that a given Z^0 event falls into it.

---

*Defined by the lepton geometrical requirements given in subsections 4.2.1 and 4.3.1.

	Category	Probability
(a)	$\mathcal{X}-\mathcal{X}$	ϵ_{ID}^2
(b)	$\mathcal{X}-\mathcal{O}_{\mathcal{X}}$	$\epsilon_{ID}(1-\epsilon_{ID})$
(c)	$\mathcal{O}_{\mathcal{X}}-\mathcal{X}$	$(1-\epsilon_{ID})\epsilon_{ID}$
(d)	$\mathcal{O}_{\mathcal{X}}-\mathcal{O}_{\mathcal{X}}$	$(1-\epsilon_{ID})^2$

By construction of the Z^0 sample described above, only categories (a), (b) and (c) will be present in the data. These categories are used to calculate the given lepton efficiency as follows. If,

$N_{\mathcal{X}\mathcal{X}}$ = the number of dilepton Z^0 events in which both leptons pass all the selection cuts (the number of events in category (a)), and,

$N_{\mathcal{X}\mathcal{O}}$ = the number of dilepton Z^0 events in which one and only one lepton passes all the selection cuts (the number of dileptons in categories (b) and (c)),

then, the total lepton ID efficiency is given by:

$$\epsilon_{ID} = \frac{2N_{\mathcal{X}\mathcal{X}}}{2N_{\mathcal{X}\mathcal{X}} + N_{\mathcal{X}\mathcal{O}}} \ . \tag{A.1}$$

This is easily verified by substituting for $N_{\mathcal{X}\mathcal{X}}$ and $N_{\mathcal{X}\mathcal{O}}$ in equation A.1, their respective probabilities in the above list of categories. It should be stressed that equation A.1 is only valid when dealing with Z^0 events of the same lepton type (i.e. TCE-TCE, LCE-LCE, TCM-TCM, CMX-CMX). For the case of CMI muons, there will be no CMI-CMI Z^0 events because there is no CMI event trigger (see section 2.3 and subsection 4.3.1). However, because CMI muons come in on other triggers, one can calculate the CMI efficiency by using TCM-CMI Z^0 events. If the TCM and CMI efficiencies are ϵ_{TCM} and ϵ_{CMI} respectively, and $\mathcal{X}_{TCM}$ ($\mathcal{X}_{CMI}$) represents a TCM (CMI) that has passed the selection criteria, with $\mathcal{O}_{TCM}$ ($\mathcal{O}_{CMI}$) representing a TCM (CMI) that has failed at least one of it's selection cuts, then the Z^0 events that will be seen in the data will fall into one of two categories: $\mathcal{X}_{TCM} - \mathcal{X}_{CMI}$ with probability $\epsilon_{TCM}\epsilon_{CMI}$, and $\mathcal{X}_{TCM} - \mathcal{O}_{CMI}$ with probability $\epsilon_{TCM}(1-\epsilon_{CMI})$. The CMI efficiency is then simply given by:

$$\epsilon_{CMI} = \frac{N_{\mathcal{X}\mathcal{X}}}{N_{\mathcal{X}\mathcal{X}} + N_{\mathcal{X}\mathcal{O}}} \ .$$

The results from the lepton efficiency calculations are given in section 4.4.

A.2 A second method for calculating efficiencies

A limitation in the method of calculating lepton efficiencies given in the previous section is the necessity that the lepton requirements be the same for both legs of the Z^0[*]. This is particularly evident when wanting to calculate the efficiencies for non-isolated leptons, as is done in section 5.3, where the above method would not be able to provide sufficient statistics, because the probability for both leptons in a Z^0 event to be non-isolated is very small. To avoid this problem, and calculate the efficiencies of muons (MU) and electrons (EL) with any desired requirements, one can use TCM-MU and TCE-EL Z^0 events by employing the following method.

- Look for dimuon or dielectron Z^0 events[†] where only the geometrical and P_t requirements have been imposed on both leptons.
- Randomly pick one of the leptons and check if it passes the tight lepton cuts (i.e. check to see if it is a TCM or TCE lepton).
- If it does not pass the tight lepton cuts, reject the event, otherwise, if it does, check to see if the second lepton passes the desired requirements for MU or EL.
- If N_{total} is the total number of events for which the second lepton was checked,

---

[*] Except for calculating CMI efficiencies as explained above.

[†] That is, events for which $80\,GeV < M_{\ell\ell} < 100\,GeV$.

and N_{pass} is the number for which the second lepton satisfied the desired cuts, then the MU or EL lepton efficiency is simply:

$$\epsilon = \frac{N_{pass}}{N_{total}} \ .$$

Although this method substantially increases the statistics when calculating efficiencies such as for non-isolated leptons, the method of section A.1 gives about twice the statistics for TCM, TCE and LCE leptons. Also, as a result of a significantly greater number of TCM-CMX Z^0's than CMX-CMX Z^0's, this second method provides better statistics for calculating ϵ_{CMX}. The results of the lepton efficiency calculations, using both methods, are given in Table 4.5. The efficiency calculation methods of sections A.1 and A.2 with henceforth be referred to as "method 1" and "method 2" respectively.

A.3 Effect of the trigger bias

In the methods described above to calculate lepton efficiencies, the effects of the event triggers have been neglected. This will cause an upward bias on the lepton efficiencies because the lepton which triggered the Z^0 event will have already passed certain identification cuts required in the level 3 trigger (see section 4.1). This will have a greater effect the lower the trigger efficiency, and so will be more pronounced in the muon identification efficiencies. To check the effect of the muon triggers, the muon efficiencies were recalculated *after* requiring the level 3 conditions (see Table 4.1) on *every* muon in the event. This gives the identification efficiencies for muons that have passed the trigger requirements, ϵ_μ^{trg}. The results are given in Table A.1, and compared with the observed muon efficiencies, ϵ_μ^{obs}, for both TCM and CMX muons (CMI muons are unaffected because they can not trigger an event). The TCM efficiencies are calculated using method 1 above, and the CMX efficiencies

	ϵ_μ^{obs}	ϵ_μ^{trg}
TCM	0.917 ± 0.007	0.934 ± 0.006
CMX	0.914 ± 0.010	0.946 ± 0.008

Table A.1

Identification efficiencies for muons that have passed the level 3 trigger requirements, ϵ_μ^{trg}, and the observed muon efficiencies, ϵ_μ^{obs}, calculated by ignoring which muon triggered the event.

are from method 2 (because the statistics are about 5 times greater).

The muon efficiencies after the trigger requirements are imposed, imply that the measured TCM efficiencies should be about 2% lower, and the measured CMX efficiency about 3.5% lower, in order to obtain the true muon efficiencies. To eliminate the trigger effect, one can calculate the efficiencies using method 2 above, by additionally requiring that the muon picked at random also be the one that triggered the event. However, for the efficiency results of section 4.4 this was not done.

A.4 Efficiency errors

When either the overall or the individual cut efficiency can be written in the form;

$$\epsilon = \frac{2N_x}{2N_x + N_o} ,$$

where N_x is the number of *pass* events and N_o the number of *fail* events, then the error in ϵ, $\delta\epsilon$, can be written as:

$$\delta\epsilon = \frac{2\delta p}{(1+p)^2}, \qquad \delta p = \sqrt{\frac{p(1-p)}{N}},$$

where, $N = N_x + N_o$, is the total number of Z^0 events seen, and $p = N_x/N$.

Proof

We can write ϵ in terms of p thus;

$$\epsilon = \frac{2}{\frac{1}{p}+1}.$$

Then;

$$\delta\epsilon = \left|\frac{\partial\epsilon}{\partial\left(\frac{1}{p}\right)}\right|\delta\left(\frac{1}{p}\right) = \frac{2}{\left(\frac{1}{p}+1\right)^2}\frac{\delta p}{p^2} = \frac{2\delta p}{(1+p)^2}.$$

If the probability of observing N_x of the N events to *pass* is represented by a binomial distribution, and the probability of a single event b in this *pass* state is given by p then δp is given by;

$$\delta p = \sqrt{\frac{p(1-p)}{N}}.$$

Note that when the efficiency is written in the form; $\epsilon = \frac{N_x}{N_x+N_o}$, as is the case when calculating CMI efficiencies (see above), the error is trivially, $\delta\epsilon = \delta p$.

APPENDIX B: MONTE CARLO SIMULATION PROGRAMS

Throughout the text various Monte Carlo simulations are referred to, for which this appendix serves as an introduction. Event generators (ISAJET, HERWIG, PYTHIA, etc.) simulate the desired process with the events being written to a *generator level data bank* called a GENP bank. The GENP bank contains momentum, parent, and daughter information for every particle created in the event process, with the format being standardized to a CDF particle database system. CDF detector simulations (QFL, CDFSIM) use the GENP banks as input to create the fully simulated CDF data banks for each event. The following list provides an introduction to the Monte Carlo simulations used, together with the references of where to find more detailed reviews.

ISAJET. A Monte Carlo program which simulates pp and $p\overline{p}$ collisions at high energies [88]. Unless otherwise stated the version used is v7.06. ISAJET is based on perturbative QCD, with phenomenological models used for parton and beam jet fragmentation. QCD initial and final state radiative corrections are added in the leading log approximation. Partons, including the top quark, are fragmented into hadrons. This means that even though the top quark is known to decay as a free spin-$\frac{1}{2}$ quark, ISAJET will decay it mostly as a spin-0 meson.

HERWIG. HERWIG (Hadron Emission Reactions With Interfering Gluons) simulates high energy hadronic processes, with one of it's strengths being it's detailed simulation of QCD jets which includes color coherence effects between initial and final partons [51]. Unless otherwise stated the version used is v5.6.

PYTHIA. The PYTHIA Monte Carlo [89] can be made to generate hard or soft processes at e^+e^-, ep, and pp colliders. The PYTHIA $t\bar{t}$ samples used in this analysis utilized the default leading order (LO) CTEQ2L structure functions. Parton fragmentation was carried out using the string fragmentation model for the light quarks and the Peterson fragmentation model for the heavier quarks (c, b, and t). Version 5.6 of the PYTHIA code was mostly used. This has the known problem of ignoring the polarization of W bosons from top decay, and hence models the W decay as isotropic. Version 5.7 of the PYTHIA code includes the W polarization, but was not installed at CDF at the time most of the Monte Carlo samples were made for this analysis.

VECBOS. A Matrix Element (ME) Monte Carlo for $W + jets$ events [90]. As a ME calculation, it only provides the four momenta of the partons involved in the scattering process, and the weight (or probability) for each event. VECBOS is used extensively at CDF with HERPRT (see below) for $V + multijet$ ($V = W$ or Z) studies, because of it's good agreement with the $V + jet$ characteristics seen in the data.

HERPRT. In order to turn partons into jets for events created from ME Monte Carlo generators such as VECBOS, the color coherent fragmentation model used in HERWIG is often used at CDF, the interface for which is called HERPRT [91].

QQ(CLEO). QQ is the Monte Carlo generator used at CLEO for the decay of bottom and charm particles [92]. It is used at CDF by removing all particles in a generated event that descend from bottom and charm particles (typically B mesons in top events), and then redecaying them using QQ.

TAUOLA. A library of Monte Carlo routines that simulate the decay of polarized τ leptons [93]. In order to decay τ's in a consistent and correct manner for all Monte Carlo generators, an interface at CDF is used to redecay τ's created in the GENP banks using the TAUOLA library [94].

QFL. QFL is a fast simulation of the CDF detector [95, 96]. It's speed is achieved from using parameterizations of detector response, rather than deriving the response from first principles as in GEANT based detector simulations. All simulated events used in this analysis were generated with QFL (as opposed to CDFSIM).

APPENDIX C: Run 1C $\mu\mu$ candidate !

After the conclusion of Run 1B, and a shutdown of several months, the Tevatron was scheduled to continue running for a short time, before being switched for use by the fixed target experiments. If Run 1C ends when it is scheduled to on February 20, 1996, it will accumulate about $8\,pb^{-1}$ at $1.8\,TeV$. During the first few pb^{-1}'s of Run 1C a new dilepton candidate has been found; a $\mu\mu$ event with large $\not\!\!E_t$, and 2 high-E_t jets (with another extremely energetic jet in the forward region which doesn't pass the jet $|\eta|$ requirement). The details of this event are given in Table C.1.

Run/Event : 75326/48051		$z_{vertex} = -12.5\,cm$	
μ_1	$P_t = 34.8\,GeV$	$\phi = 120°$	$\eta = -0.02$
μ_2	$P_t = 20.1\,GeV$	$\phi = 3°$	$\eta = 0.59$
jet 1	$E_t = 47.2\,GeV$	$\phi = 358°$	$\eta = 0.59$
jet 2	$E_t = 32.2\,GeV$	$\phi = 51°$	$\eta = -0.06$
"jet 3"	$E_t = 55.4\,GeV$	$\phi = 260°$	$\eta = -2.41$
$\not\!\!E_t$	$E_t = 65.3\,GeV$	$\phi = 202°$	

Table C.1

Characteristics of the Run 1C $\mu\mu$ candidate. Muon P_t values are beam constrained, jet E_t values have been relatively corrected, and the $\not\!\!E_t$ has been corrected for muons and jets. Note that "jet 3" fails to pass the jet $|\eta|$ requirement.

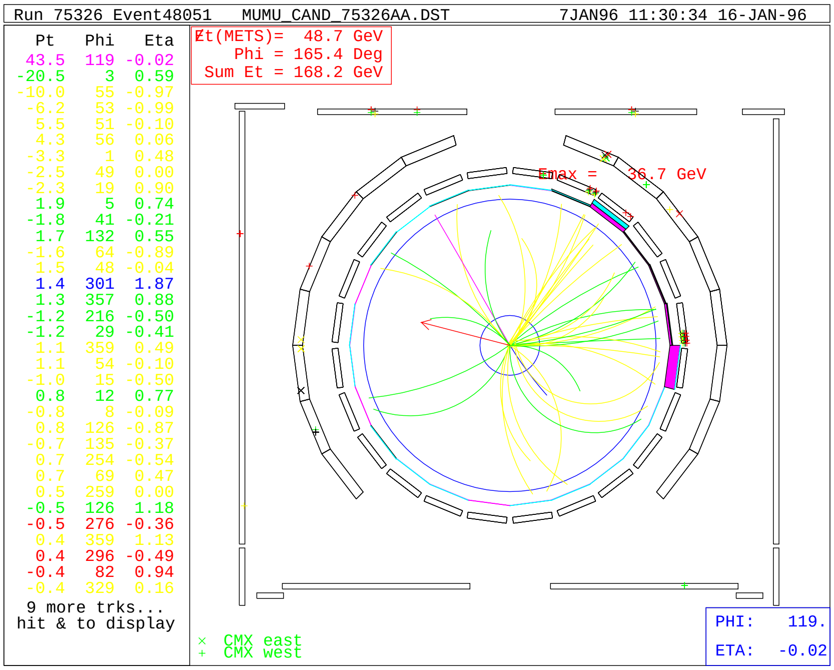

```
Run 75326 Event48051    MUMU_CAND_75326AA.DST          7JAN96 11:30:34 16-JAN-96
```

```
  Pt    Phi   Eta
 43.5   119 -0.02
-20.5     3  0.59
-10.0    55 -0.97
 -6.2    53 -0.99
  5.5    51 -0.10
  4.3    56  0.06
 -3.3     1  0.48
 -2.5    49  0.00
 -2.3    19  0.90
  1.9     5  0.74
 -1.8    41 -0.21
  1.7   132  0.55
 -1.6    64 -0.89
  1.5    48 -0.04
  1.4   301  1.87
  1.3   357  0.88
 -1.2   216 -0.50
 -1.2    29 -0.41
  1.1   359  0.49
  1.1    54 -0.10
 -1.0    15 -0.50
  0.8    12  0.77
 -0.8     8 -0.09
  0.8   126 -0.87
 -0.7   135 -0.37
  0.7   254 -0.54
  0.7    69  0.47
  0.5   259  0.00
 -0.5   126  1.18
 -0.5   276 -0.36
  0.4   359  1.13
  0.4   296 -0.49
 -0.4    82  0.94
 -0.4   329  0.16
 9 more trks...
hit & to display
```

```
Et(METS)=   48.7 GeV
    Phi = 165.4 Deg
 Sum Et = 168.2 GeV
```

Figure C.1

Transverse view of the CTC tracks in the Run 1C $\mu\mu$ candidate. The muons are at $\phi = 119°$ and $\phi = 3°$, and the jets at $\phi = 358°$ and $\phi = 51°$.

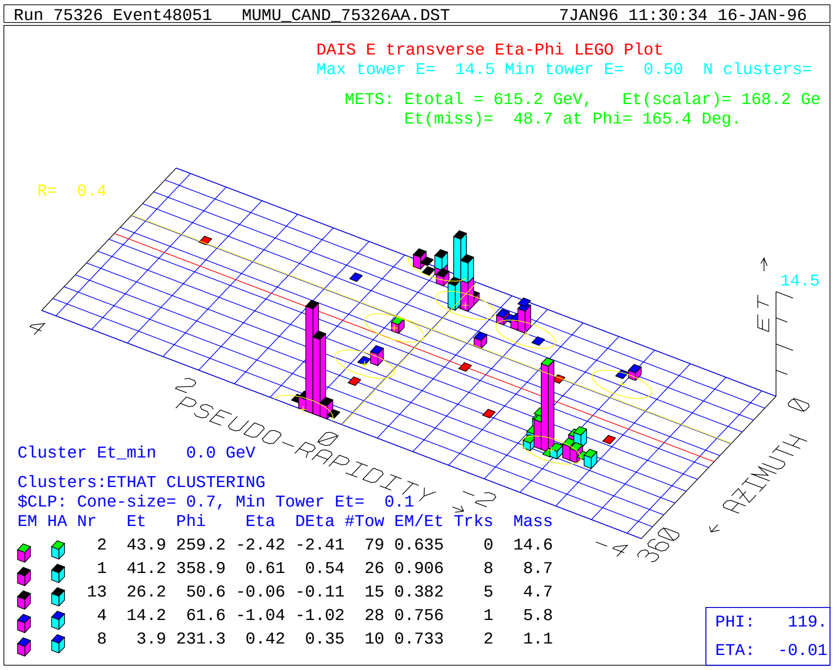

```
Run 75326 Event48051    MUMU_CAND_75326AA.DST          7JAN96 11:30:34 16-JAN-96
```

```
DAIS E transverse Eta-Phi LEGO Plot
Max tower E=  14.5 Min tower E=  0.50  N clusters=
   METS: Etotal = 615.2 GeV,    Et(scalar)= 168.2 Ge
         Et(miss)=  48.7 at Phi= 165.4 Deg.
```

```
Cluster Et_min   0.0 GeV

Clusters:ETHAT CLUSTERING
$CLP: Cone-size= 0.7, Min Tower Et=  0.1
EM HA Nr    Et   Phi    Eta  DEta #Tow EM/Et Trks  Mass
        2  43.9 259.2 -2.42 -2.41   79 0.635    0  14.6
        1  41.2 358.9  0.61  0.54   26 0.906    8   8.7
       13  26.2  50.6 -0.06 -0.11   15 0.382    5   4.7
        4  14.2  61.6 -1.04 -1.02   28 0.756    1   5.8
        8   3.9 231.3  0.42  0.35   10 0.733    2   1.1
```

Figure C.2

Lego plot showing the calorimeter E_t in the Run 1C $\mu\mu$ candidate. The jet at $(\eta, \phi) = (-2.41, 260°)$ has $E_t^{corr} = 55\,GeV \Longrightarrow E^{corr} = 309\,GeV$.

Figures C.1 and C.2 show the CTC and lego event displays respectively for the $\mu\mu$ candidate. The muon at $\phi = 120°$ is "CMP only" in that it goes through a ϕ crack between the CMU chambers. The other muon at $\phi = 3°$ is "CMU only", so neither muon has hits in both the CMU and CMP chambers. The dimuon invariant mass is $48\,GeV$. Jet 2 is tagged by the SECVTX algorithm as a b jet. This jet also has a muon stub, but no track matching well enough to it to be identified as a soft muon in the SLT b-tagging algorithm. The $20.1\,GeV$ muon appears to be associated with jet 1, suggesting that this is in fact a *lepton+jets* event passing the dilepton selection. Recall from chapter 5 that $\sim 3\%$ of the dilepton acceptance is expected from $t\bar{t}$ decays in the *lepton + jets* channel. If in fact both jet-1 and jet-2 are b jets, then the presence of an extra jet with an energy of $\sim 300\,GeV$ at high η, is another unusual feature of this event, if it is indeed from $t\bar{t}$ decay.

With this event, the same-sign dilepton candidate (see section 7.6), and the dilepton candidate 57621/45230 (see Table 7.2), all containing high-P_t leptons in b jets, it becomes an interesting question as to how many such events are expected, assuming these events are indeed from $t\bar{t}$ decay. From sections 7.5 and 7.6, it is expected in $109\,pb^{-1}$ that 0.5 ± 0.2 events from $t\bar{t}$ decay will contain a high-P_t lepton from b decay, and pass the dilepton analysis cuts excluding the same-sign cut. Three such events are observed.

APPENDIX D: PROPOSED IMPROVEMENTS TO THE DILEPTON ANALYSIS

The following are targeted as improvements to future $t\bar{t}$ standard (i.e. not including τ's) dilepton analyses. Now that the top quark is discovered and its mass measured, many of the dilepton cuts that were initially designed for a simple counting experiment, can be optimized and expanded towards the now known properties of top.

- With a top mass of $175\,GeV$, the total transverse energy in an event, H_t (defined in section 7.1), is an excellent variable for which to separate signal and background (see Figure 7.3). An H_t cut (at around $200\,GeV$) would significantly enhance the $t\bar{t}$ dilepton signal over the background.
- The $\not\!\!E_t$ cuts need reviewing. The $\Delta\phi(\not\!\!E_t, nearest\ lepton) < 20^\circ$ cut does not significantly reject any backgrounds after the 2-jet requirement is imposed, and the $\Delta\phi(\not\!\!E_t, nearest\ jet) < 20^\circ$ cut should be abolished in the $e\mu$ channel where there is not expected to be much Drell-Yan contamination.
- A better method of removing Z^0 events and retrieving the top contribution in the Z^0 window needs to be addressed.
- The dilepton isolation cut, which requires at least 1 lepton to be tight (TCE, TCM or CMX) and isolated, was shown to be 95% efficient for $t\bar{t}$ dilepton events. Requiring both leptons to be isolated, still keeps this an efficient cut (especially for the case where both leptons come from W decay), while essentially eliminating backgrounds involving leptons from b decay, and fake leptons, which although small, are difficult to estimate.
- As shown in Figure 4.19, for a top mass of $175\,GeV$, the jet E_t^{raw} cut could be increased on the leading jet without any significant loss in acceptance. The effect

of this needs to be studied for dilepton backgrounds.

- A photon algorithm needs to be applied to all jets, with jets identified as photons being removed from the jet list. This will eliminate the radiative Z^0 contribution to the dilepton signal. However, this background should still be completely understood. As has been discussed one radiative Z^0 event appeared in the dilepton signal region in the present analysis.
- The dilepton *same-sign* analysis (see section 7.6) should be scrutinized more carefully, because it provides an invaluable probe into a deeper understanding of the dilepton events, especially the backgrounds to $t\bar{t}$ events, and may even be sensitive to new physics.
- The effect of multiple interactions needs to be understood. This is related to the requirement that the jets and leptons come from the same vertex (see section 4.10.4).

APPENDIX E: EVENT DISPLAYS OF THE DILEPTON CANDIDATES

This appendix is intended to serve as a supplement to 7. For each $t\bar{t}$ dilepton candidate event, the CTC and *lego* event displays are given. The former shows the transverse view of the tracks in the event, and the latter the transverse energy deposited in the calorimeter towers. The reader is referred to Table 7.2 and Figures 7.1 and 7.2 from Chapter 7 for more detailed information on each event. Here, each candidate will simply be labelled by its run and event numbers, and displayed in chronological order.

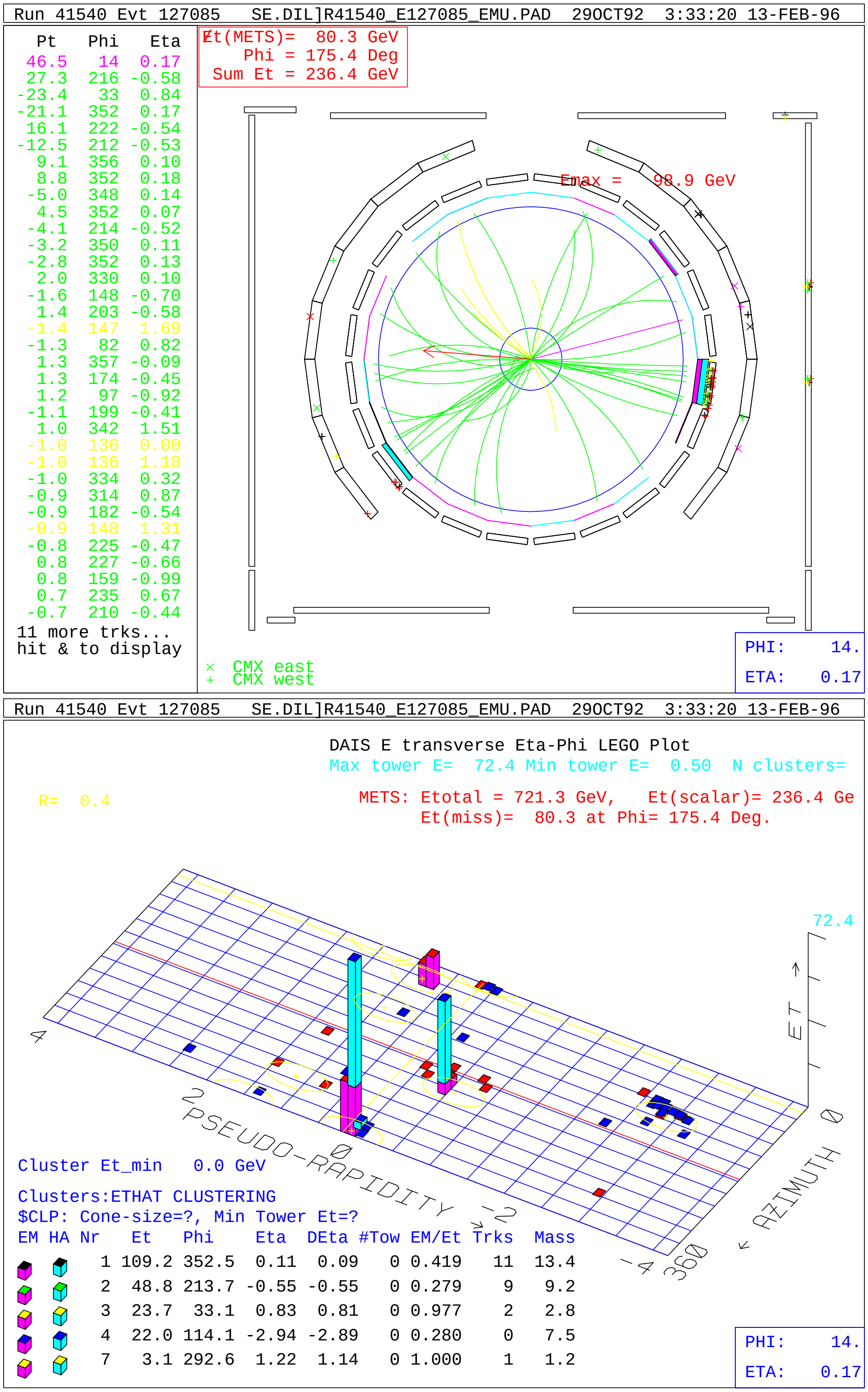

```
Run 41540 Evt 127085   SE.DIL]R41540_E127085_EMU.PAD   29OCT92   3:33:20 13-FEB-96
```

```
  Pt   Phi   Eta
 46.5   14  0.17
 27.3  216 -0.58
-23.4   33  0.84
-21.1  352  0.17
 16.1  222 -0.54
-12.5  212 -0.53
  9.1  356  0.10
  8.8  352  0.18
 -5.0  348  0.14
  4.5  352  0.07
 -4.1  214 -0.52
 -3.2  350  0.11
 -2.8  352  0.13
  2.0  330  0.10
 -1.6  148 -0.70
  1.4  203 -0.58
 -1.4  147  1.69
 -1.3   82  0.82
  1.3  357 -0.09
  1.3  174 -0.45
  1.2   97 -0.92
 -1.1  199 -0.41
  1.0  342  1.51
 -1.0  136  0.00
 -1.0  136  1.18
 -1.0  334  0.32
 -0.9  314  0.87
 -0.9  182 -0.54
 -0.9  148  1.31
 -0.8  225 -0.47
  0.8  227 -0.66
  0.8  159 -0.99
  0.7  235  0.67
 -0.7  210 -0.44
11 more trks...
hit & to display
```

```
Et(METS)=   80.3 GeV
    Phi = 175.4 Deg
 Sum Et = 236.4 GeV
```

```
Run 41540 Evt 127085   SE.DIL]R41540_E127085_EMU.PAD   29OCT92   3:33:20 13-FEB-96
```

```
DAIS E transverse Eta-Phi LEGO Plot
Max tower E=  72.4 Min tower E=  0.50  N clusters=

METS: Etotal = 721.3 GeV,   Et(scalar)= 236.4 Ge
      Et(miss)=  80.3 at Phi= 175.4 Deg.
```

```
Cluster Et_min   0.0 GeV

Clusters:ETHAT CLUSTERING
$CLP: Cone-size=?, Min Tower Et=?
EM HA Nr   Et   Phi    Eta   DEta #Tow EM/Et Trks  Mass
        1 109.2 352.5  0.11  0.09    0 0.419   11  13.4
        2  48.8 213.7 -0.55 -0.55    0 0.279    9   9.2
        3  23.7  33.1  0.83  0.81    0 0.977    2   2.8
        4  22.0 114.1 -2.94 -2.89    0 0.280    0   7.5
        7   3.1 292.6  1.22  1.14    0 1.000    1   1.2
```

Figure E.1

41540/127085 : e^- at $\phi = 310°$, $\eta = -0.71$: μ^+ at $\phi = 14°$, $\eta = 0.17$.

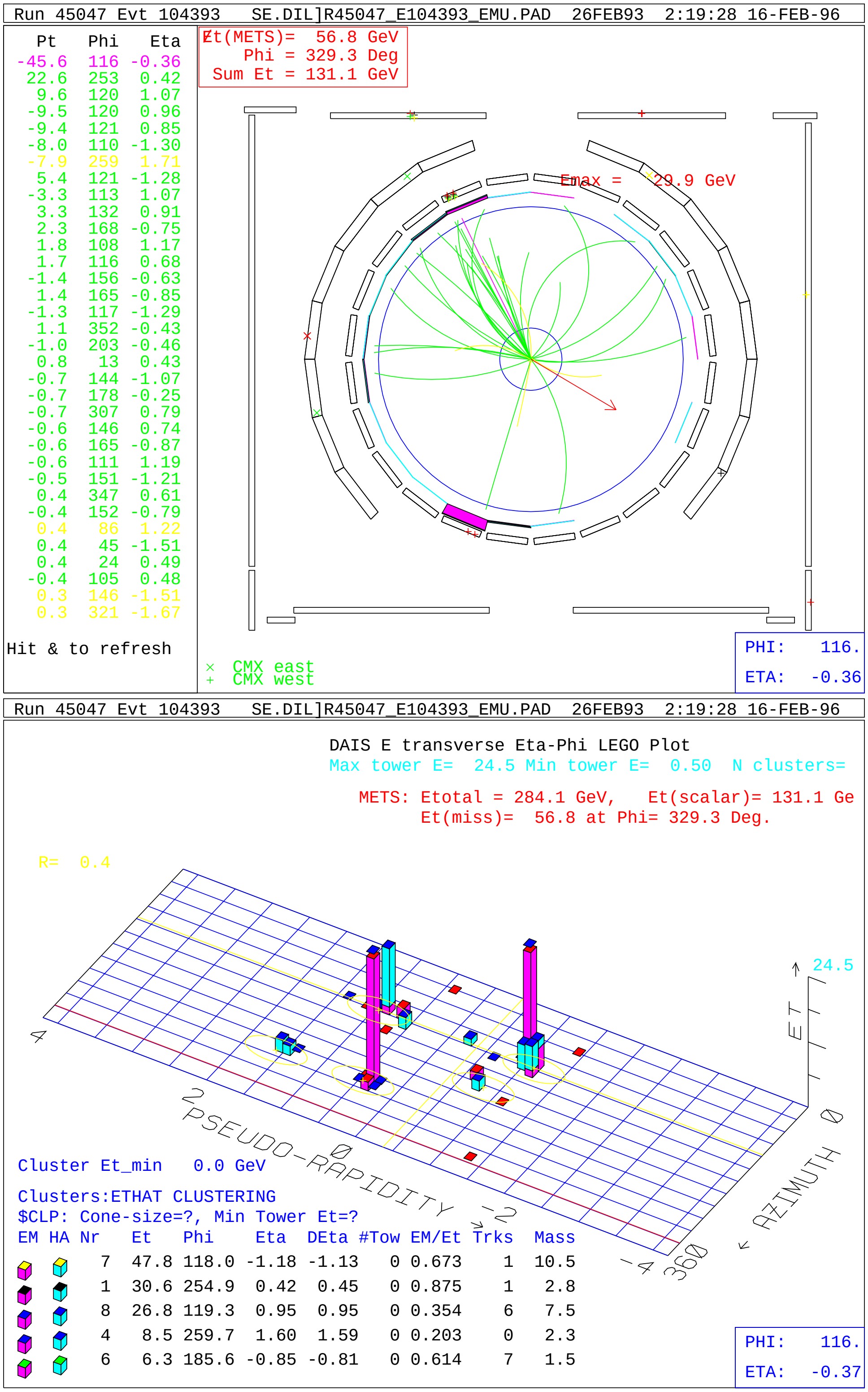

```
Run 45047 Evt 104393    SE.DIL]R45047_E104393_EMU.PAD   26FEB93   2:19:28 16-FEB-96
   Pt    Phi    Eta
-45.6   116  -0.36
 22.6   253   0.42
  9.6   120   1.07
 -9.5   120   0.96
 -9.4   121   0.85
 -8.0   110  -1.30
 -7.9   259   1.71
  5.4   121  -1.28
 -3.3   113   1.07
  3.3   132   0.91
  2.3   168  -0.75
  1.8   108   1.17
  1.7   116   0.68
 -1.4   156  -0.63
  1.4   165  -0.85
 -1.3   117  -1.29
  1.1   352  -0.43
 -1.0   203  -0.46
  0.8    13   0.43
 -0.7   144  -1.07
 -0.7   178  -0.25
 -0.7   307   0.79
 -0.6   146   0.74
 -0.6   165  -0.87
 -0.6   111   1.19
 -0.5   151  -1.21
  0.4   347   0.61
 -0.4   152  -0.79
  0.4    86   1.22
  0.4    45  -1.51
  0.4    24   0.49
 -0.4   105   0.48
  0.3   146  -1.51
  0.3   321  -1.67

Hit & to refresh

Et(METS)=   56.8 GeV
     Phi = 329.3 Deg
  Sum Et = 131.1 GeV
```

```
Run 45047 Evt 104393    SE.DIL]R45047_E104393_EMU.PAD   26FEB93   2:19:28 16-FEB-96

                         DAIS E transverse Eta-Phi LEGO Plot
                         Max tower E=  24.5 Min tower E=  0.50  N clusters=

                            METS: Etotal = 284.1 GeV,    Et(scalar)= 131.1 Ge
                                  Et(miss)=  56.8 at Phi= 329.3 Deg.

Cluster Et_min   0.0 GeV

Clusters:ETHAT CLUSTERING
$CLP: Cone-size=?, Min Tower Et=?
EM HA Nr    Et    Phi     Eta   DEta #Tow EM/Et Trks  Mass
        7  47.8 118.0 -1.18 -1.13    0 0.673    1  10.5
        1  30.6 254.9  0.42  0.45    0 0.875    1   2.8
        8  26.8 119.3  0.95  0.95    0 0.354    6   7.5
        4   8.5 259.7  1.60  1.59    0 0.203    0   2.3
        6   6.3 185.6 -0.85 -0.81    0 0.614    7   1.5
```

Figure E.2

45047/104393 : e^+ at $\phi = 255°$, $\eta = 0.42$: μ^- at $\phi = 116°$, $\eta = -0.36$.

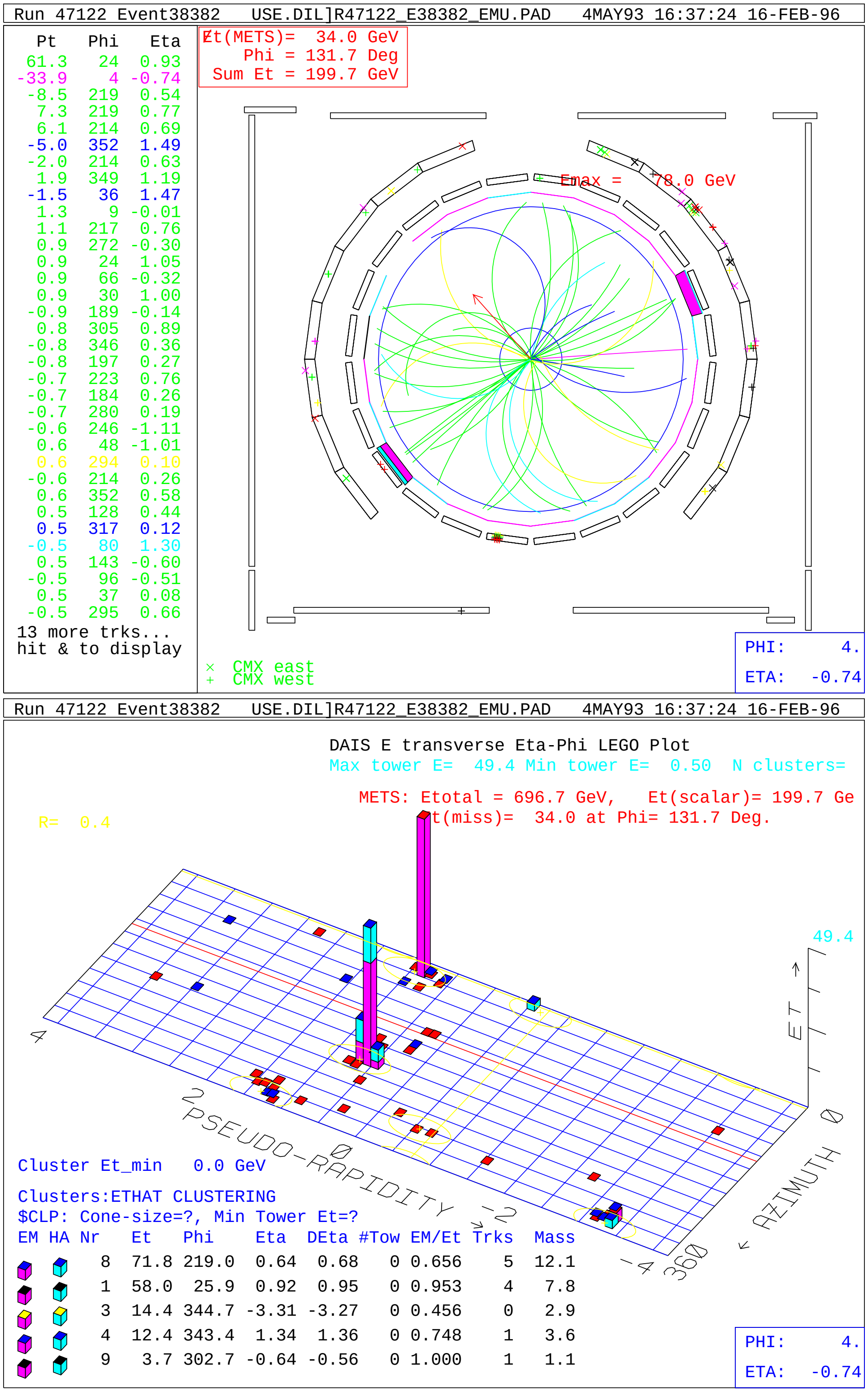

```
Run 47122 Event38382   USE.DIL]R47122_E38382_EMU.PAD   4MAY93 16:37:24 16-FEB-96

  Pt    Phi   Eta      Et(METS)=   34.0 GeV
 61.3    24  0.93          Phi = 131.7 Deg
-33.9     4 -0.74       Sum Et = 199.7 GeV
 -8.5   219  0.54
  7.3   219  0.77
  6.1   214  0.69
 -5.0   352  1.49
 -2.0   214  0.63
  1.9   349  1.19
 -1.5    36  1.47
  1.3     9 -0.01
  1.1   217  0.76
  0.9   272 -0.30
  0.9    24  1.05
  0.9    66 -0.32
  0.9    30  1.00
 -0.9   189 -0.14
  0.8   305  0.89
 -0.8   346  0.36
 -0.8   197  0.27
 -0.7   223  0.76
 -0.7   184  0.26
 -0.7   280  0.19
 -0.6   246 -1.11
  0.6    48 -1.01
  0.6   294  0.10
 -0.6   214  0.26
  0.6   352  0.58
  0.5   128  0.44
  0.5   317  0.12
 -0.5    80  1.30
  0.5   143 -0.60
 -0.5    96 -0.51
  0.5    37  0.08
 -0.5   295  0.66
13 more trks...
hit & to display
                                                               PHI:      4.
                                                               ETA:   -0.74

Run 47122 Event38382   USE.DIL]R47122_E38382_EMU.PAD   4MAY93 16:37:24 16-FEB-96

                         DAIS E transverse Eta-Phi LEGO Plot
                         Max tower E=  49.4 Min tower E=  0.50  N clusters=

                            METS: Etotal = 696.7 GeV,   Et(scalar)= 199.7 Ge
                                  Et(miss)=  34.0 at Phi= 131.7 Deg.

Cluster Et_min   0.0 GeV

Clusters:ETHAT CLUSTERING
$CLP: Cone-size=?, Min Tower Et=?
EM HA Nr   Et   Phi    Eta  DEta #Tow EM/Et Trks  Mass
         8  71.8 219.0  0.64  0.68   0 0.656   5  12.1
         1  58.0  25.9  0.92  0.95   0 0.953   4   7.8
         3  14.4 344.7 -3.31 -3.27   0 0.456   0   2.9
         4  12.4 343.4  1.34  1.36   0 0.748   1   3.6
         9   3.7 302.7 -0.64 -0.56   0 1.000   1   1.1
                                                               PHI:      4.
                                                               ETA:   -0.74
```

Figure E.3

47122/38382 : e^+ at $\phi = 25°$, $\eta = 0.93$: μ^- at $\phi = 4°$, $\eta = -0.74$.

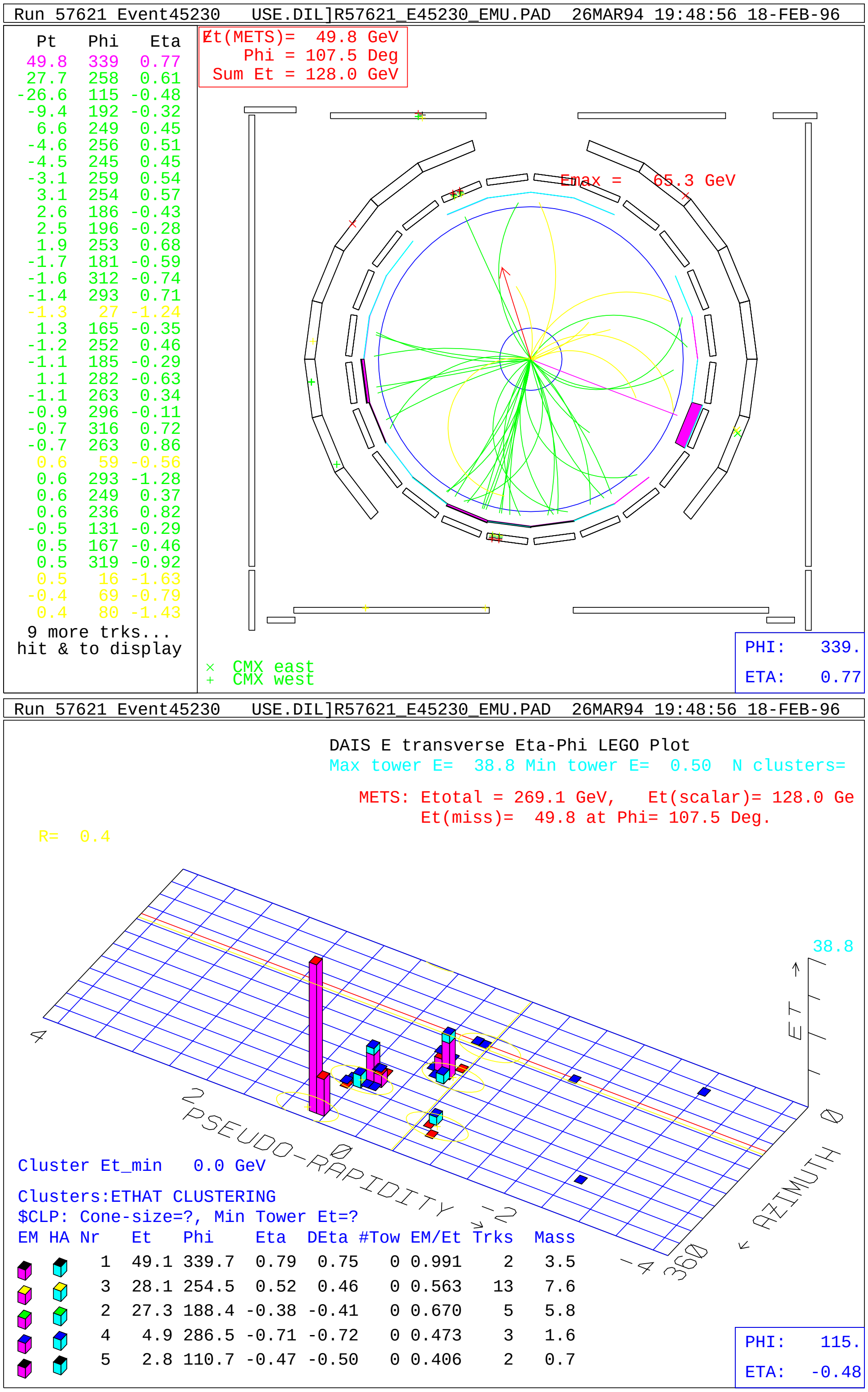

```
Run 57621 Event45230   USE.DIL]R57621_E45230_EMU.PAD  26MAR94 19:48:56 18-FEB-96

  Pt    Phi    Eta
 49.8   339   0.77
 27.7   258   0.61
-26.6   115  -0.48
 -9.4   192  -0.32
  6.6   249   0.45
 -4.6   256   0.51
 -4.5   245   0.45
 -3.1   259   0.54
  3.1   254   0.57
  2.6   186  -0.43
  2.5   196  -0.28
  1.9   253   0.68
 -1.7   181  -0.59
 -1.6   312  -0.74
 -1.4   293   0.71
 -1.3    27  -1.24
  1.3   165  -0.35
 -1.2   252   0.46
 -1.1   185  -0.29
  1.1   282  -0.63
 -1.1   263   0.34
 -0.9   296  -0.11
 -0.7   316   0.72
 -0.7   263   0.86
  0.6    59  -0.56
  0.6   293  -1.28
  0.6   249   0.37
  0.6   236   0.82
 -0.5   131  -0.29
  0.5   167  -0.46
  0.5   319  -0.92
  0.5    16  -1.63
 -0.4    69  -0.79
  0.4    80  -1.43
  9 more trks...
 hit & to display

Et(METS)=   49.8 GeV
    Phi = 107.5 Deg
 Sum Et = 128.0 GeV

PHI:    339.
ETA:    0.77

Run 57621 Event45230   USE.DIL]R57621_E45230_EMU.PAD  26MAR94 19:48:56 18-FEB-96

DAIS E transverse Eta-Phi LEGO Plot
Max tower E=  38.8 Min tower E=  0.50  N clusters=

METS: Etotal = 269.1 GeV,   Et(scalar)= 128.0 Ge
      Et(miss)=  49.8 at Phi= 107.5 Deg.

Cluster Et_min    0.0 GeV

Clusters:ETHAT CLUSTERING
$CLP: Cone-size=?, Min Tower Et=?
EM HA Nr    Et    Phi    Eta   DEta #Tow EM/Et Trks  Mass
       1  49.1 339.7   0.79   0.75   0 0.991    2   3.5
       3  28.1 254.5   0.52   0.46   0 0.563   13   7.6
       2  27.3 188.4  -0.38  -0.41   0 0.670    5   5.8
       4   4.9 286.5  -0.71  -0.72   0 0.473    3   1.6
       5   2.8 110.7  -0.47  -0.50   0 0.406    2   0.7

PHI:    115.
ETA:   -0.48
```

Figure E.4

57621/45230 : e^+ at $\phi = 340°$, $\eta = 0.77$: μ^- at $\phi = 115°$, $\eta = -0.48$.

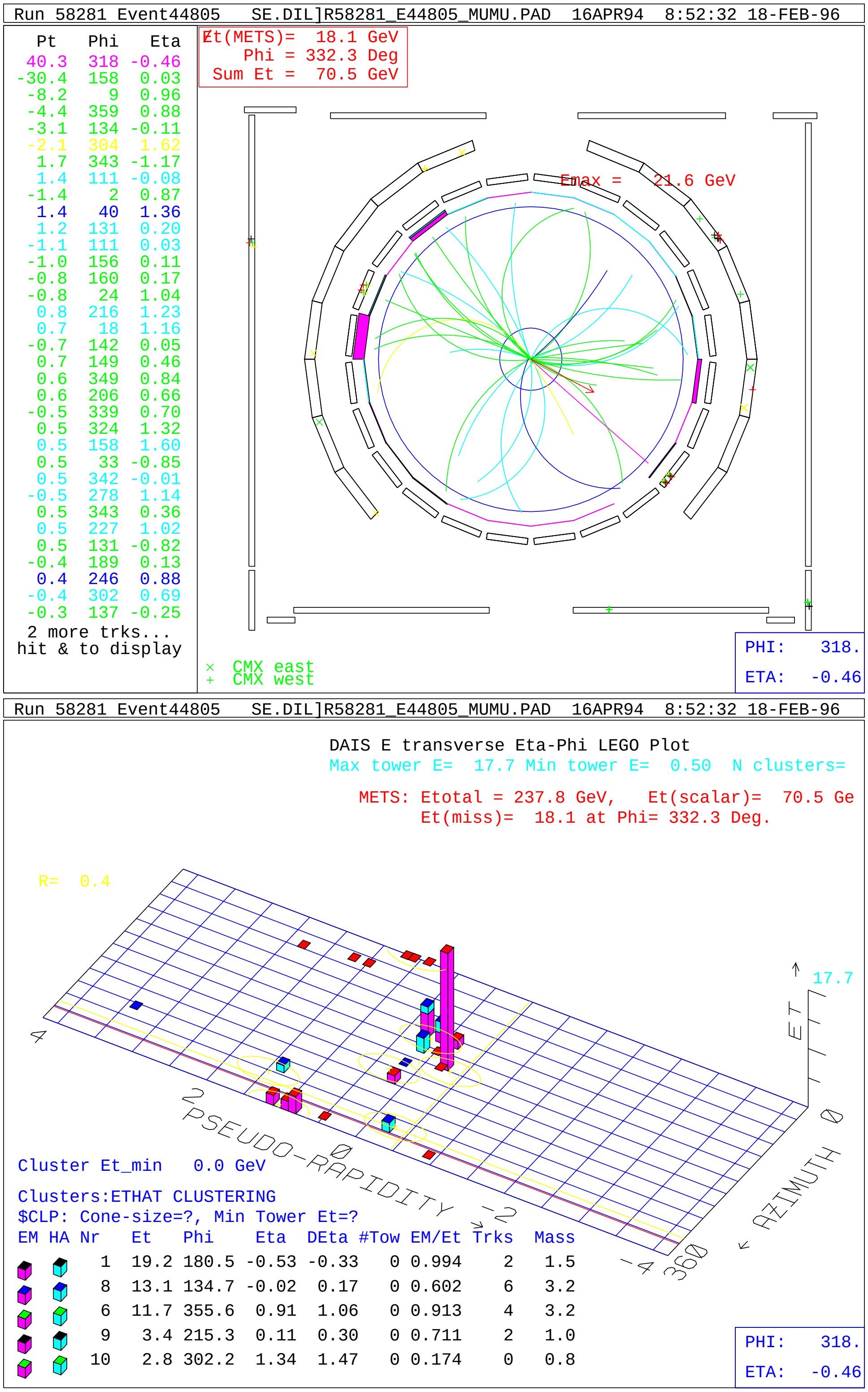

```
Run 58281 Event44805   SE.DIL]R58281_E44805_MUMU.PAD  16APR94   8:52:32 18-FEB-96
```

```
  Pt   Phi   Eta
 40.3  318 -0.46
-30.4  158  0.03
 -8.2    9  0.96
 -4.4  359  0.88
 -3.1  134 -0.11
 -2.1  304  1.62
  1.7  343 -1.17
  1.4  111 -0.08
 -1.4    2  0.87
  1.4   40  1.36
  1.2  131  0.20
 -1.1  111  0.03
 -1.0  156  0.11
 -0.8  160  0.17
 -0.8   24  1.04
  0.8  216  1.23
  0.7   18  1.16
 -0.7  142  0.05
  0.7  149  0.46
  0.6  349  0.84
  0.6  206  0.66
 -0.5  339  0.70
  0.5  324  1.32
  0.5  158  1.60
  0.5   33 -0.85
  0.5  342 -0.01
 -0.5  278  1.14
  0.5  343  0.36
  0.5  227  1.02
  0.5  131 -0.82
 -0.4  189  0.13
  0.4  246  0.88
 -0.4  302  0.69
 -0.3  137 -0.25
 2 more trks...
hit & to display
```

```
Et(METS)=  18.1 GeV
    Phi = 332.3 Deg
 Sum Et =  70.5 GeV
```

```
Run 58281 Event44805   SE.DIL]R58281_E44805_MUMU.PAD  16APR94   8:52:32 18-FEB-96
```

```
DAIS E transverse Eta-Phi LEGO Plot
Max tower E=  17.7 Min tower E=  0.50  N clusters=

METS: Etotal = 237.8 GeV,   Et(scalar)=  70.5 Ge
      Et(miss)=  18.1 at Phi= 332.3 Deg.
```

```
Cluster Et_min   0.0 GeV

Clusters:ETHAT CLUSTERING
$CLP: Cone-size=?, Min Tower Et=?
EM HA Nr   Et   Phi    Eta  DEta #Tow EM/Et Trks  Mass
        1  19.2 180.5 -0.53 -0.33   0 0.994    2   1.5
        8  13.1 134.7 -0.02  0.17   0 0.602    6   3.2
        6  11.7 355.6  0.91  1.06   0 0.913    4   3.2
        9   3.4 215.3  0.11  0.30   0 0.711    2   1.0
       10   2.8 302.2  1.34  1.47   0 0.174    0   0.8
```

Figure E.5

58281/44805 $(\mu\mu\gamma)$: μ^+ at $\phi = 318°$, $\eta = -0.46$: μ^- at $\phi = 158°$, $\eta = 0.03$.

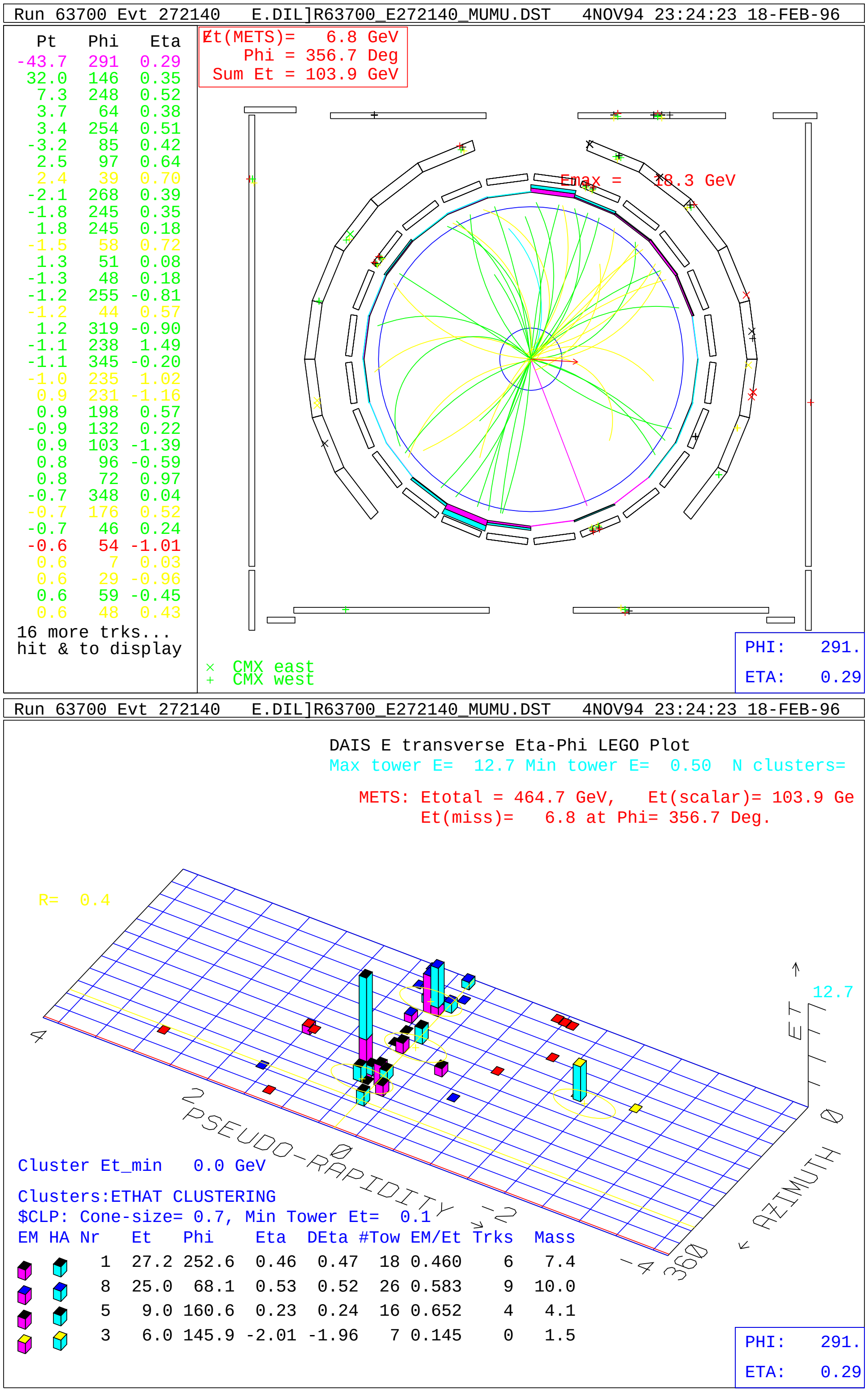

```
Run 63700 Evt 272140    E.DIL]R63700_E272140_MUMU.DST    4NOV94 23:24:23 18-FEB-96
  Pt    Phi    Eta
-43.7   291   0.29
 32.0   146   0.35
  7.3   248   0.52
  3.7    64   0.38
  3.4   254   0.51
 -3.2    85   0.42
  2.5    97   0.64
  2.4    39   0.70
 -2.1   268   0.39
 -1.8   245   0.35
  1.8   245   0.18
 -1.5    58   0.72
  1.3    51   0.08
 -1.3    48   0.18
 -1.2   255  -0.81
 -1.2    44   0.57
  1.2   319  -0.90
 -1.1   238   1.49
 -1.1   345  -0.20
 -1.0   235   1.02
  0.9   231  -1.16
  0.9   198   0.57
 -0.9   132   0.22
  0.9   103  -1.39
  0.8    96  -0.59
  0.8    72   0.97
 -0.7   348   0.04
 -0.7   176   0.52
 -0.7    46   0.24
 -0.6    54  -1.01
  0.6     7   0.03
  0.6    29  -0.96
  0.6    59  -0.45
  0.6    48   0.43
16 more trks...
hit & to display
```

```
Et(METS)=    6.8 GeV
    Phi = 356.7 Deg
 Sum Et = 103.9 GeV
```

```
Run 63700 Evt 272140    E.DIL]R63700_E272140_MUMU.DST    4NOV94 23:24:23 18-FEB-96
DAIS E transverse Eta-Phi LEGO Plot
Max tower E=  12.7 Min tower E=  0.50  N clusters=
METS: Etotal = 464.7 GeV,   Et(scalar)= 103.9 Ge
      Et(miss)=   6.8 at Phi= 356.7 Deg.
```

```
Cluster Et_min   0.0 GeV

Clusters:ETHAT CLUSTERING
$CLP: Cone-size= 0.7, Min Tower Et=  0.1
EM HA Nr   Et   Phi    Eta  DEta #Tow EM/Et Trks  Mass
       1  27.2 252.6  0.46  0.47  18 0.460    6   7.4
       8  25.0  68.1  0.53  0.52  26 0.583    9  10.0
       5   9.0 160.6  0.23  0.24  16 0.652    4   4.1
       3   6.0 145.9 -2.01 -1.96   7 0.145    0   1.5
```

Figure E.6

63700/272140 : μ^- at $\phi = 292°$, $\eta = 0.29$: μ^+ at $\phi = 147°$, $\eta = 0.35$.

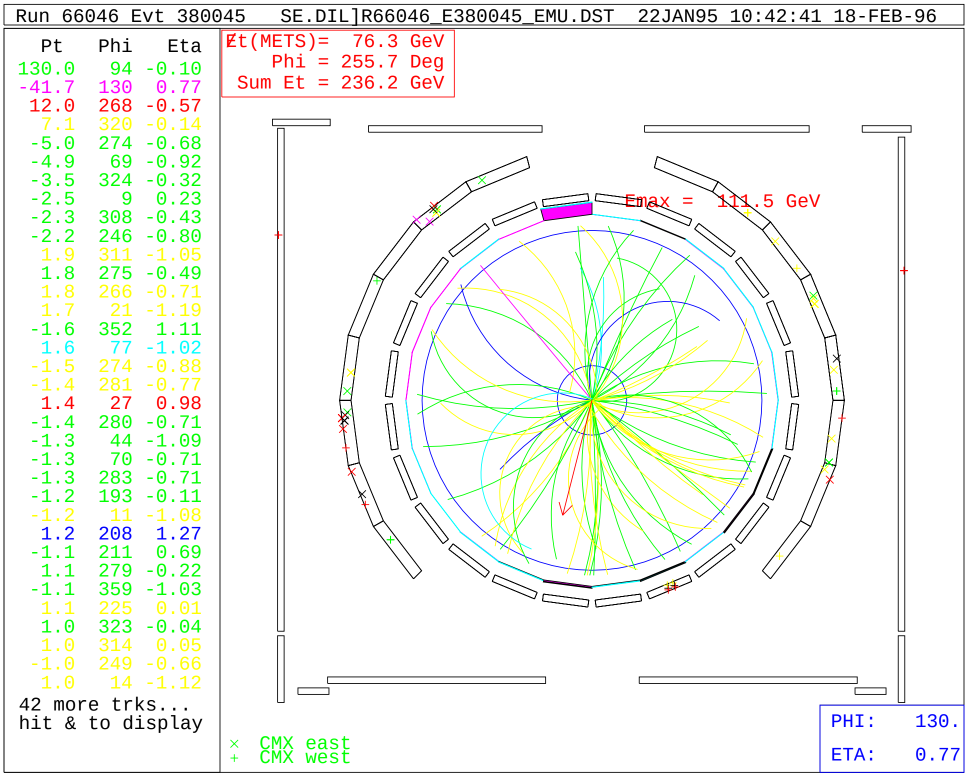

```
Run 66046 Evt 380045   SE.DIL]R66046_E380045_EMU.DST   22JAN95 10:42:41 18-FEB-96
```

```
  Pt    Phi   Eta
130.0   94  -0.10
-41.7  130   0.77
 12.0  268  -0.57
  7.1  320  -0.14
 -5.0  274  -0.68
 -4.9   69  -0.92
 -3.5  324  -0.32
 -2.5    9   0.23
 -2.3  308  -0.43
 -2.2  246  -0.80
  1.9  311  -1.05
  1.8  275  -0.49
  1.8  266  -0.71
  1.7   21  -1.19
 -1.6  352   1.11
  1.6   77  -1.02
 -1.5  274  -0.88
 -1.4  281  -0.77
  1.4   27   0.98
 -1.4  280  -0.71
 -1.3   44  -1.09
 -1.3   70  -0.71
 -1.3  283  -0.71
 -1.2  193  -0.11
 -1.2   11  -1.08
  1.2  208   1.27
 -1.1  211   0.69
  1.1  279  -0.22
 -1.1  359  -1.03
  1.1  225   0.01
  1.0  323  -0.04
  1.0  314   0.05
 -1.0  249  -0.66
  1.0   14  -1.12
42 more trks...
hit & to display
```

```
Et(METS)=   76.3 GeV
     Phi =  255.7 Deg
  Sum Et =  236.2 GeV
```

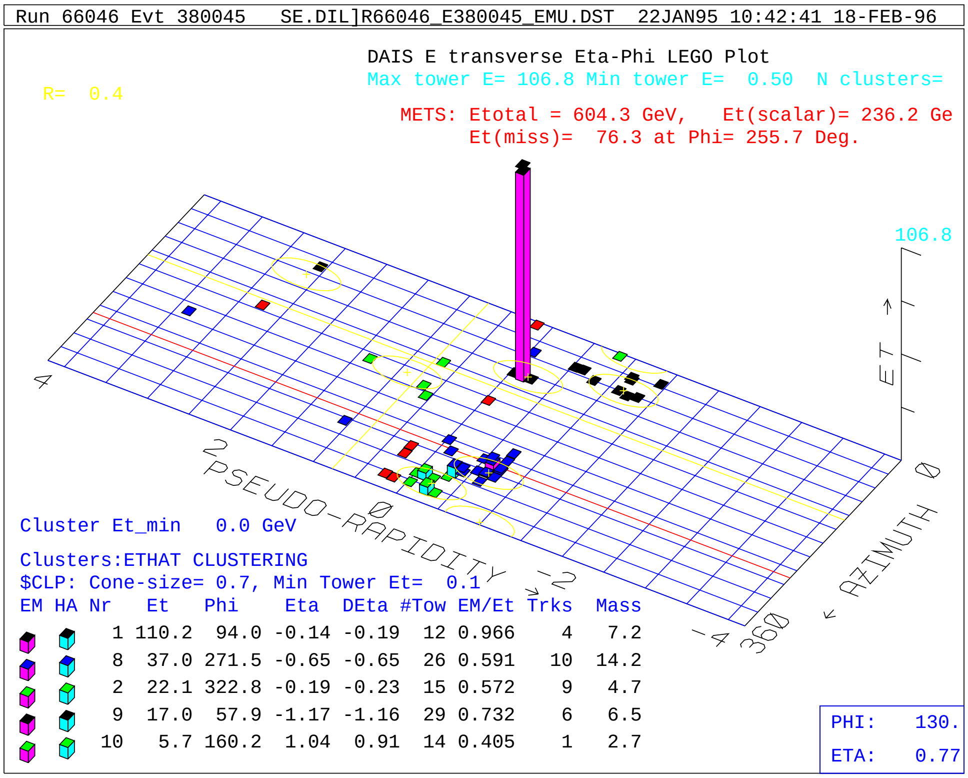

```
Run 66046 Evt 380045   SE.DIL]R66046_E380045_EMU.DST   22JAN95 10:42:41 18-FEB-96
```

```
DAIS E transverse Eta-Phi LEGO Plot
Max tower E= 106.8 Min tower E=  0.50  N clusters=
METS: Etotal = 604.3 GeV,    Et(scalar)= 236.2 Ge
      Et(miss)=  76.3 at Phi= 255.7 Deg.
```

```
Cluster Et_min    0.0 GeV

Clusters:ETHAT CLUSTERING
$CLP: Cone-size= 0.7, Min Tower Et=  0.1
EM HA Nr    Et    Phi     Eta   DEta #Tow EM/Et Trks   Mass
        1 110.2   94.0 -0.14 -0.19   12 0.966    4    7.2
        8  37.0 271.5 -0.65 -0.65   26 0.591   10   14.2
        2  22.1 322.8 -0.19 -0.23   15 0.572    9    4.7
        9  17.0  57.9 -1.17 -1.16   29 0.732    6    6.5
       10   5.7 160.2  1.04  0.91   14 0.405    1    2.7
```

Figure E.7

66046/380045 : e^+ at $\phi = 94°$, $\eta = -0.10$: μ^- at $\phi = 130°$, $\eta = 0.77$.

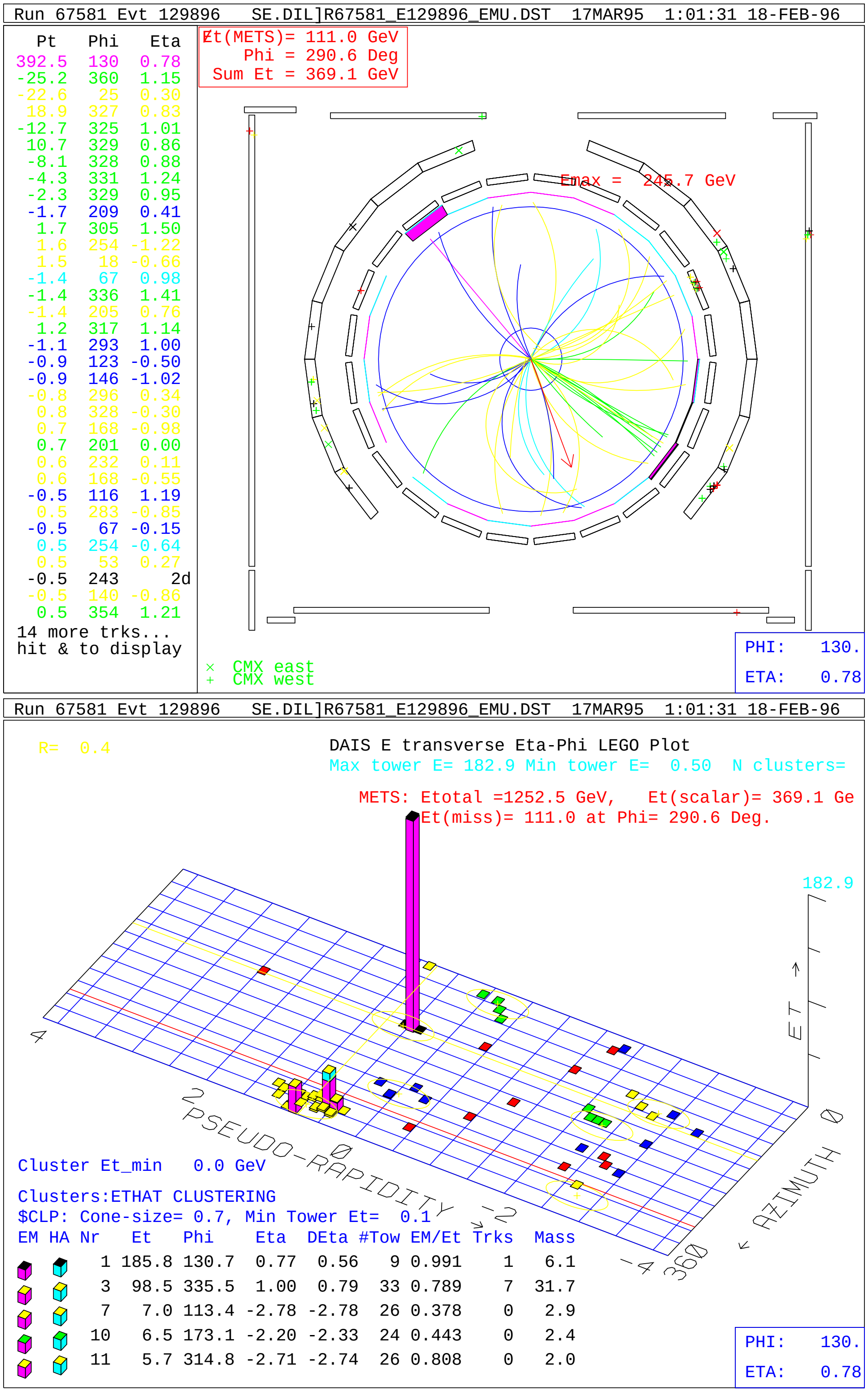

Run 67581 Evt 129896 SE.DIL]R67581_E129896_EMU.DST 17MAR95 1:01:31 18-FEB-96

Pt	Phi	Eta
392.5	130	0.78
-25.2	360	1.15
-22.6	25	0.30
18.9	327	0.83
-12.7	325	1.01
10.7	329	0.86
-8.1	328	0.88
-4.3	331	1.24
-2.3	329	0.95
-1.7	209	0.41
1.7	305	1.50
1.6	254	-1.22
1.5	18	-0.66
-1.4	67	0.98
-1.4	336	1.41
-1.4	205	0.76
1.2	317	1.14
-1.1	293	1.00
-0.9	123	-0.50
-0.9	146	-1.02
-0.8	296	0.34
0.8	328	-0.30
0.7	168	-0.98
0.7	201	0.00
0.6	232	0.11
0.6	168	-0.55
-0.5	116	1.19
0.5	283	-0.85
-0.5	67	-0.15
0.5	254	-0.64
0.5	53	0.27
-0.5	243	2d
-0.5	140	-0.86
0.5	354	1.21

14 more trks...
hit & to display

E̸t(METS)= 111.0 GeV
Phi = 290.6 Deg
Sum Et = 369.1 GeV

PHI: 130.
ETA: 0.78

Run 67581 Evt 129896 SE.DIL]R67581_E129896_EMU.DST 17MAR95 1:01:31 18-FEB-96

R= 0.4

DAIS E transverse Eta-Phi LEGO Plot
Max tower E= 182.9 Min tower E= 0.50 N clusters=

METS: Etotal =1252.5 GeV, Et(scalar)= 369.1 Ge
Et(miss)= 111.0 at Phi= 290.6 Deg.

Cluster Et_min 0.0 GeV

Clusters:ETHAT CLUSTERING
$CLP: Cone-size= 0.7, Min Tower Et= 0.1

EM	HA	Nr	Et	Phi	Eta	DEta	#Tow	EM/Et	Trks	Mass
■	■	1	185.8	130.7	0.77	0.56	9	0.991	1	6.1
■	■	3	98.5	335.5	1.00	0.79	33	0.789	7	31.7
■	■	7	7.0	113.4	-2.78	-2.78	26	0.378	0	2.9
■	■	10	6.5	173.1	-2.20	-2.33	24	0.443	0	2.4
■	■	11	5.7	314.8	-2.71	-2.74	26	0.808	0	2.0

PHI: 130.
ETA: 0.78

Figure E.8

67581/129896 : e^+ at $\phi = 131°$, $\eta = 0.78$: μ^- at $\phi = 25°$, $\eta = 0.30$.

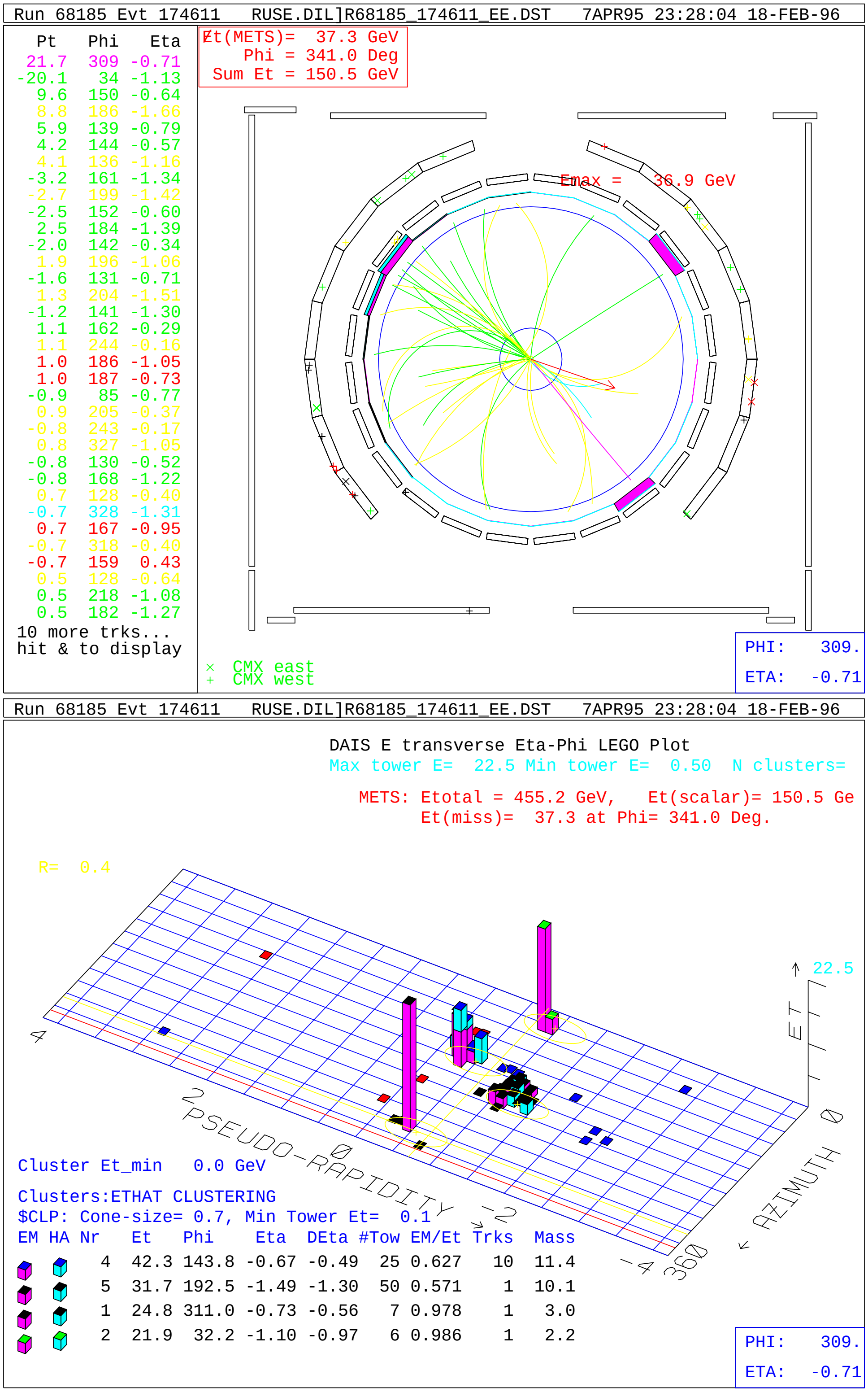

```
Run 68185 Evt 174611   RUSE.DIL]R68185_174611_EE.DST   7APR95 23:28:04 18-FEB-96

  Pt    Phi   Eta
 21.7   309 -0.71
-20.1    34 -1.13
  9.6   150 -0.64
  8.8   186 -1.66
  5.9   139 -0.79
  4.2   144 -0.57
  4.1   136 -1.16
 -3.2   161 -1.34
 -2.7   199 -1.42
 -2.5   152 -0.60
  2.5   184 -1.39
 -2.0   142 -0.34
  1.9   196 -1.06
 -1.6   131 -0.71
  1.3   204 -1.51
 -1.2   141 -1.30
  1.1   162 -0.29
  1.1   244 -0.16
  1.0   186 -1.05
  1.0   187 -0.73
 -0.9    85 -0.77
  0.9   205 -0.37
 -0.8   243 -0.17
  0.8   327 -1.05
 -0.8   130 -0.52
 -0.8   168 -1.22
  0.7   128 -0.40
 -0.7   328 -1.31
  0.7   167 -0.95
 -0.7   318 -0.40
 -0.7   159  0.43
  0.5   128 -0.64
  0.5   218 -1.08
  0.5   182 -1.27
10 more trks...
hit & to display

Et(METS)=  37.3 GeV
    Phi = 341.0 Deg
 Sum Et = 150.5 GeV
```

```
Run 68185 Evt 174611   RUSE.DIL]R68185_174611_EE.DST   7APR95 23:28:04 18-FEB-96

DAIS E transverse Eta-Phi LEGO Plot
Max tower E=  22.5 Min tower E=  0.50  N clusters=

METS: Etotal = 455.2 GeV,   Et(scalar)= 150.5 Ge
      Et(miss)=  37.3 at Phi= 341.0 Deg.

Cluster Et_min   0.0 GeV

Clusters:ETHAT CLUSTERING
$CLP: Cone-size= 0.7, Min Tower Et=  0.1
EM HA Nr   Et    Phi    Eta  DEta #Tow EM/Et Trks  Mass
        4  42.3 143.8 -0.67 -0.49  25 0.627   10  11.4
        5  31.7 192.5 -1.49 -1.30  50 0.571    1  10.1
        1  24.8 311.0 -0.73 -0.56   7 0.978    1   3.0
        2  21.9  32.2 -1.10 -0.97   6 0.986    1   2.2
```

Figure E.9

68185/174611 : e^+ at $\phi = 310^\circ$, $\eta = -0.71$: e^- at $\phi = 32^\circ$, $\eta = -1.13$.

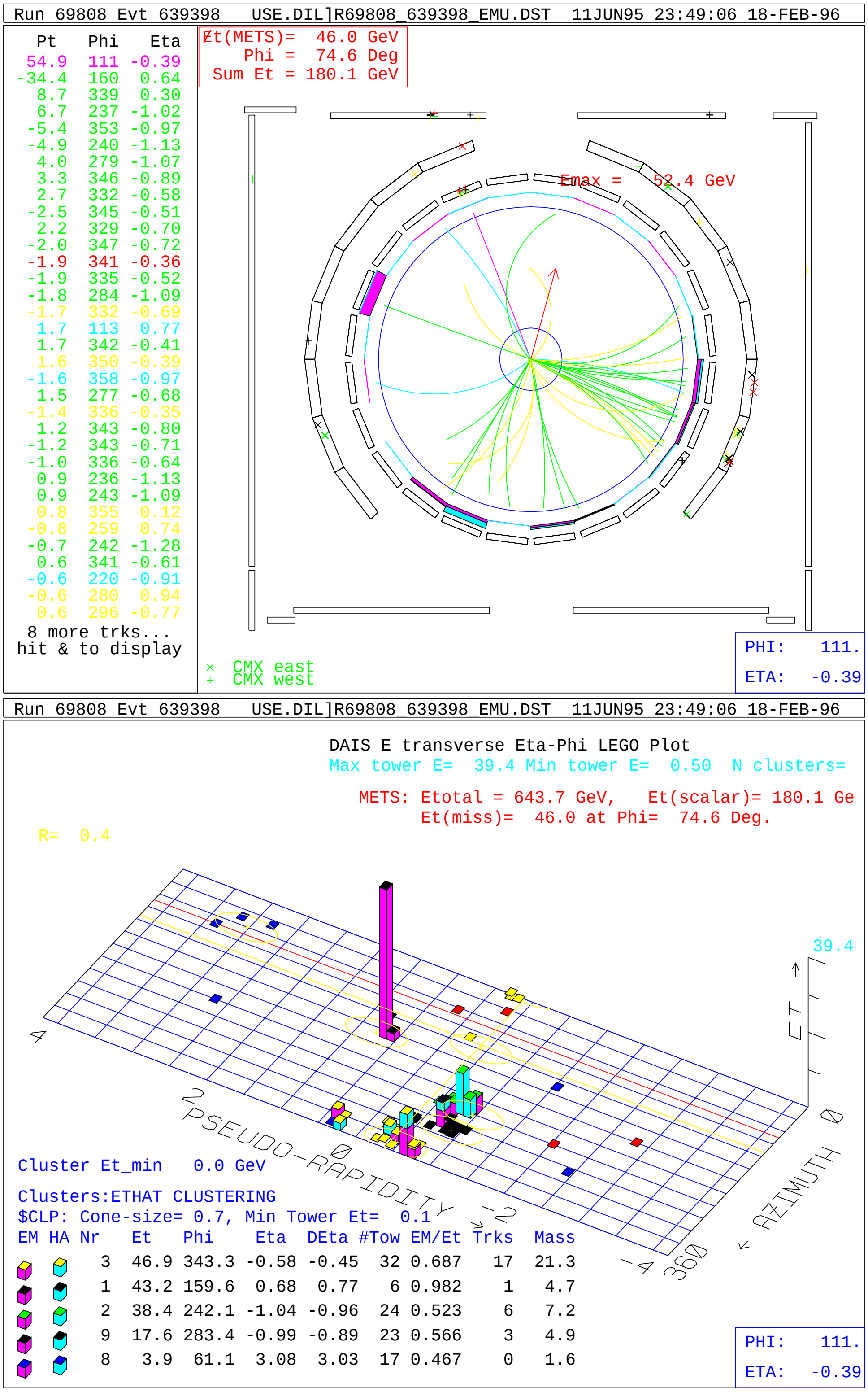

```
Run 69808 Evt 639398    USE.DIL]R69808_639398_EMU.DST   11JUN95 23:49:06 18-FEB-96
  Pt    Phi    Eta
 54.9   111  -0.39
-34.4   160   0.64
  8.7   339   0.30
  6.7   237  -1.02
 -5.4   353  -0.97
 -4.9   240  -1.13
  4.0   279  -1.07
  3.3   346  -0.89
  2.7   332  -0.58
 -2.5   345  -0.51
  2.2   329  -0.70
 -2.0   347  -0.72
 -1.9   341  -0.36
 -1.9   335  -0.52
 -1.8   284  -1.09
 -1.7   332  -0.69
  1.7   113   0.77
  1.7   342  -0.41
  1.6   350  -0.39
 -1.6   358  -0.97
  1.5   277  -0.68
 -1.4   336  -0.35
  1.2   343  -0.80
 -1.2   343  -0.71
 -1.0   336  -0.64
  0.9   236  -1.13
  0.9   243  -1.09
  0.8   355   0.12
 -0.8   259   0.74
 -0.7   242  -1.28
  0.6   341  -0.61
 -0.6   220  -0.91
 -0.6   280   0.94
  0.6   296  -0.77
 8 more trks...
hit & to display

Et(METS)=   46.0 GeV
    Phi =   74.6 Deg
 Sum Et = 180.1 GeV
```

```
Run 69808 Evt 639398    USE.DIL]R69808_639398_EMU.DST   11JUN95 23:49:06 18-FEB-96
DAIS E transverse Eta-Phi LEGO Plot
Max tower E=  39.4 Min tower E=  0.50  N clusters=
METS: Etotal = 643.7 GeV,   Et(scalar)= 180.1 Ge
        Et(miss)=  46.0 at Phi=  74.6 Deg.
Cluster Et_min   0.0 GeV

Clusters:ETHAT CLUSTERING
$CLP: Cone-size= 0.7, Min Tower Et=  0.1
EM HA Nr   Et   Phi    Eta   DEta #Tow EM/Et Trks  Mass
       3  46.9 343.3 -0.58 -0.45  32 0.687   17  21.3
       1  43.2 159.6  0.68  0.77   6 0.982    1   4.7
       2  38.4 242.1 -1.04 -0.96  24 0.523    6   7.2
       9  17.6 283.4 -0.99 -0.89  23 0.566    3   4.9
       8   3.9  61.1  3.08  3.03  17 0.467    0   1.6
```

Figure E.10

69808/639398 : e^- at $\phi = 160°$, $\eta = 0.64$: μ^+ at $\phi = 111°$, $\eta = -0.39$.

VITA

VITA

Mark Kruse was born in Auckland, New Zealand on December 22, 1964. He completed his high school education at Penrose High School in Auckland in 1982. In 1983 he embarked on a Bachelor of Science degree at Auckland University, graduating with a B.Sc. in Physics in May 1986. He continued to study at Auckland University towards a Masters degree in Nuclear Physics, for which he conducted his thesis research at the *Pelletron Collider* at the Australian National University in Canberra, Australia during the year of 1987, as the student of Alan Poletti. In August 1988 he graduated with an M.Sc. in Physics with first class honours. With the desire to experience life outside the constructs of academia, he decided to accept an offer to work as a Scientist at the National Radiation Laboratory in Christchurch, New Zealand, where he remained until mid 1990. In August 1990 he made his first venture into the Northern Hemisphere, starting a Ph.D. in physics at Purdue University in West Lafayette, Indiana. He joined the CDF collaboration at Fermilab, as the student of Arthur Garfinkel and Daniela Bortoletto, where he conducted his thesis research until receiving his Ph.D. in Physics in February 1996.